Impact ejecta and crater formation on asteroid surfaces

Sabina D. Raducan

Department of Earth Science and Engineering
Imperial College London

Submitted in part fulfilment of the requirements for the degree of Doctor Doctor of Philosophy in Planetary Science and Diploma of Imperial College

May 2020

Declaration of Originality

The work presented in this thesis was conducted and the thesis written during my time as a PhD student at Imperial College London. I confirm that everything presented in here is my own, except where clearly referenced, or otherwise noted. All results presented in this thesis were interpreted jointly by myself and my supervisors, Gareth Collins and Thomas Davison.

Copyright Declaration

The copyright of this thesis rests with the author. Unless otherwise indicated, its contents are licensed under a Creative Commons Attribution-Non Commercial 4.0 International Licence (CC BY-NC). Under this licence, you may copy and redistribute the material in any medium or format. You may also create and distribute modified versions of the work. This is on the condition that: you credit the author and do not use it, or any derivative works, for a commercial purpose. When reusing or sharing this work, ensure you make the licence terms clear to others by naming the licence and linking to the licence text. Where a work has been adapted, you should indicate that the work has been changed and describe those changes.

Please seek permission from the copyright holder for uses of this work that are not included in this licence or permitted under UK Copyright Law.

Abstract

Asteroids in the Solar System are numerous and have varied composition. Analysis of impact crater sizes and morphologies on asteroids can provide a direct diagnosis of the surface material properties and near-surface structures. This thesis describes numerical simulations of impacts into low-gravity asteroid surfaces using the iSALE shock physics code to inform this diagnosis.

Asteroids may pose a future catastrophic threat to Earth and to avoid it, the incoming asteroid can be deflected by a spacecraft impact. However, the efficiency of the deflection is determined by target properties. This work considered different target scenarios to determine the sensitivity of crater morphology, ejecta mass-velocity distribution and momentum transferred, to asteroid surface properties and shallow structures. For homogeneous targets, the surface cohesion, initial porosity, and internal friction were found to greatly influence ejecta mass/velocity distributions and the amount an asteroid can be deflected. In a two-layer target scenario, the presence of a less porous, stronger lower layer can cause both amplification and reduction of ejected mass and momentum relative to the homogeneous case. Impacts into targets with decreasing porosity with depth only produced an enhancement in the ejected momentum for sharp exponential decreases in porosity. Using reasonable estimates for the material properties of the Double Asteroid Redirection Test (DART) asteroid target, the simulations show that the ejecta produced from the impact can enhance the deflection 2 to 4 times.

Simulations of impacts into possible target structures on Psyche show large diversity in possible crater morphologies that the 'Psyche' mission could encounter. If Psyche's interior is homogeneous, then the mission will find simple bowl-shaped craters, with a depth-diameter ratio diagnostic of rock or iron. If Psyche has a layered structure, the spacecraft could find craters with more complex morphologies, e.g. concentric or flat-floored craters. Based on 3-4 proposed large craters on Psyche's surface, model size-frequency distributions suggest that Psyche could be at least 3 billion years old if rocky and more than 4 billion years old if metal-rich.

Acknowledgements

Firstly, I would like to thank my supervisor, Gareth Collins, for the incredible amount of support and the lengthy weekly meetings, without which all of this work would not have been possible. I also want to thank Tom Davison for always making time to answer my many questions whenever I knocked on his door, sometimes even several times a day.

A big thanks to the girl's night club, Branwen, Zoe and Rachel, for their amazing friendships and all the nice evenings spent together. I also want to thank the rest of my friends at Imperial, Mariana, Sarah, Natalia and Lucas. I especially want to thank Simon for sharing a desk with me for most of my PhD. I know it must have been difficult at times.

Outside of Imperial, I want to thank my old friends from Kent, Gaj and Chris.

I want to thank Uca Marinescu and Marin Bica, along with Florin Munteanu and the rest of the Centre for the Complexity Studies, for encouraging me to pursue a career in science.

Also special thanks to Chris, who was by my side all the way through my PhD.

Finally, I want to thank my parents and sister for always supporting me and my ideas, even my crazier ones, and for encouraging me to follow my passion, even if it was difficult at times.

Thank you.

Contents

List of Tables

List of Figures

Symbols

C_0	Scaling constant
C_1	Scaling constant
C	Coupling parameter
D	Damage
E_0	Initial energy (in front of the shock wave)
E_s	Internal energy (behind the shock wave)
E	Energy
F_i	External body forces per unit mass
H_1	Scaling constant
H_2	Scaling constant
J_2	Second invariant of the deviatoric cress tensor
K_{R1}	Scaling constant
K_{R2}	Scaling constant
P_0	Initial pressure
P_s	Pressure in the solid matrix
P	Pressure
R	Crater radius
T	Temperature
U_s	Velocity of the shock wave
U	Impact velocity
V_0	Initial specific volume

V_s	Volume in the solid matrix
V_v	Volume of void space
Y_0	Cohesion (yield strength at zero pressure)
Y	Yield stress
Δt	Time step
Δx	Cell size
α	Distension
β	Momentum enhancement factor
$\mathbf{p_{ej}}$	Impactor momentum
$\mathbf{p_{imp}}$	Impactor momentum
δ	Impactor density
$\dot{\epsilon}'_{ij}$	Deviatoric strain rate
$\dot{\epsilon}$	Strain rate
ϵ_{ij}	Strain
ϵ	Strain
μ	Velocity scaling exponent
ν	Density scaling exponent
ϕ_0	Initial target porosity
π_3	Strength scaled impact size
π_4	Densities ratio
π_R	Cratering efficiency
ρ_0	Initial (uncompressed) density (e.g. in front of a shock)
ρ_s	Density of solid matrix
ρ	Density
σ_{ij}	Stress tensor
σ	Stress
θ	Impact angle (^{o})
a	Impactor radius
c	Sound speed in the material

f_i	Coefficient of internal friction for intact material
f	Coefficient of internal friction
m	Impactor mass
n_1	Constant
n_2	Constant
p	Scaling constant
r_{ic}	Radius of the isobaric core
s	Stress
t	Time
u_p	Particle velocity behind the shock wave
v	Velocity (m/s)
x	Position/distance in the x-direction

Chapter 1

Introduction

1.1 Motivation

Asteroids represent a unique opportunity to study the building blocks and mechanisms that led to the formation of planets in the Solar System, including Earth. Their surface material properties, such as cohesion, porosity or internal friction coefficient can vary significantly from one body to another. Impact cratering is probably the most ubiquitous geological process in the Solar System, having shaped the surfaces of all the solid bodies (Fassett and Minton, 2013). The aim of this thesis is to determine the influence of target properties, surface and subsurface structures on the cratering process, namely on the crater size, the crater morphology and the crater ejecta.

The size and morphology of an impact crater on a planetary surface is determined by both the projectile's properties (e.g. mass, velocity), and the target's properties (e.g. strength, gravity, porosity, structure). Therefore, crater sizes and morphologies on an asteroid surface can provide a direct diagnosis of the surface material properties and near-surface asteroid structure. Such studies can answer questions about the composition and structures of some of the most unique asteroids in the Solar System. This thesis studies the impact craters formed on a diversity of asteroid surfaces, which can potentially be used to survey asteroid surfaces, such as Asteroid (16) Psyche.

A major process involved in the impact crater formation is the ballistic ejection

of material out of the crater (Melosh, 1989). Besides providing an insight into the Solar System formation and composition, asteroids may pose a future threat of colliding with Earth, with severe or even catastrophic consequences. Dangerous asteroids can be deflected by a kinetic impactor and the efficiency of the deflection depends on the momentum carried away by the ejecta. However the crater ejecta has been shown to be greatly influenced by the impact target (Holsapple and Housen, 2012; Jutzi and Michel, 2014; Stickle et al., 2015; Cheng et al., 2016; Syal et al., 2016). The main aim of this thesis is to study the crater ejecta mass-velocity distribution in the context of the kinetic deflection of potentially hazardous asteroids. This thesis seeks to show how the asteroid surface and subsurface properties and structure influence the impact crater size, morphology, ejecta formation and momentum transferred by the ejecta.

1.2 Thesis structure

The thesis is structured in 7 chapters aimed at determining the influence of the target properties, surface and subsurface structures on cratering events on asteroids.

Chapter 2 introduces the reader to the theory and relevant literature on the formation of asteroids in the Solar System and the impact processes that have shaped them to their current state. The chapter also describes the possible threat of asteroids to impacting the Earth and outlines several deflection techniques.

Chapter 3 describes the iSALE shock physics code and other numerical methods used in this thesis. The chapter ends with validation tests of impacts into sand.

Chapter 4 presents iSALE numerical simulations that highlight the importance of the asteroid properties, such as porosity, cohesion and internal friction on crater formation and ejecta distribution, and ultimately to the efficiency of deflection of an incoming asteroid.

Chapter 5 shows the effects of target subsurface structures on crater size, morphology and ejecta mass, velocity and momentum distribution.

Chapter 6 presents numerical simulations of impacts into a variety of possible

target structures on asteroid Psyche and shows the possible crater morphologies the asteroid might reveal. These studies were then used to determine possible ages of the surface.

Chapter 7 summarises the findings of this thesis and outlines future work.

1.3 Declaration of Originality

The work presented in this thesis was conducted and the thesis written during my time as a PhD student at Imperial College London. I confirm that everything presented in here is my own, except where clearly referenced, or otherwise noted. Large parts of Chapters 4 and 5 have been used in manuscripts published in peer-reviewed journals. Parts of the work presented in Chapter 6 is included in a manuscript currently under review. My contributions to the numerical code used in this thesis include adding automatic regridding to iSALE-2D and ejecta recording to iSALE-3D. All numerical simulations included here have been performed by me, except the CHESS Monte-Carlo results in Chapter 6, which were generated by Thomas Davison. The post-processing Python scrips used to create the figures in this thesis were generated by me, except Figure 4.2 which was generated using an adaptation of a python script written by Gareth Collins. All results presented in this thesis were interpreted jointly by myself and my supervisors, Gareth Collins and Thomas Davison.

1.4 Publications

1. **Raducan, S.D.**, Davison, T.M. and Collins, G.S. Morphological diversity of impact craters on asteroid (16) Psyche, as derived form numerical models. (In review)

2. Davison, T.M., **Raducan, S.D.**, Collins, G.S. and Bland, P.A. Constraining the age and strength of Bennu and Ryugu using collisional history modelling. (In preparation)

3. **Raducan, S.D.**, Davison, T.M. and Collins, G.S. (2020) The effects of asteroid

layering on ejecta mass-velocity distribution and implications for impact momentum transfer, *Planetary and Space Science*. DOI:10.1016/j.pss.2019.104756

4. **Raducan, S.D.**, Davison, T.M., Luther, R. and Collins, G.S. (2019) The role of asteroid strength, porosity and internal friction in impact momentum transfer, *Icarus*. DOI:10.1016/j.icarus.2019.03.040

1.5 Conference and Workshop Contributions

1. **Raducan, S.D.**, Davison, T.M. and Collins, G.S. (2020) Impact Crater Sizes and Morphologies on Asteroid (16) Psyche — Insight from Numerical Modelling. *Lunar and Planetary Science Conference 51*, Houston, TX. #2162

2. Stickle, A. M., Agrusa, H. F., DeCoster, M., Graninger, D., Owen, J. M., **Raducan, S.D.**, Rosch, T., Collins, G. S., Bruck Syal, M. (2020) Effects of Spaceraft Geometry on Potential Deflection by Kinetic Impactor.*Lunar and Planetary Science Conference 51*, Houston, TX. #2339

3. **Raducan, S.D.**, Davison, T.M. and Collins, G.S. (2020) Numerical simulations for planetary defence missions. *2nd British Planetary Science Conference*, Oxford, UK.

4. **Raducan, S.D.**, Davison, T.M. and Collins, G.S. (2019) Numerical simulations of the DART impact. *AIDA International Workshop*, Rome, Italy.

5. **Raducan, S.D.**, Davison, T.M. and Collins, G.S. (2019) Numerical modelling of the DART impact and the importance of the Hera mission. *2019 IAA Planetary Defense Conference*, Washington, DC.

6. **Raducan, S.D.**, Davison, T.M. and Collins, G.S. (2019) Numerical Modelling of Impacts into Asteroid (16) Psyche Analogues. *Lunar and Planetary Science Conference 50*, Houston, TX. #1798

7. **Raducan, S.D.**, Collins, G.S. and Davison, T.M. (2019) Numerical modelling of the DART impact and the importance of the Hera mission. *Lunar and Planetary Science Conference 50*, Houston, TX. #1799

8. Davison, T.M., **Raducan, S.D.**, Collins, G.S. and Bland, P.A. (2019) Collisional Histories of Small Planetesimals: Implications for Constraining the Age of the Surface of OSIRIS-REx Target, Bennu. *Lunar and Planetary Science Conference 50*, Houston, TX. # 2385

9. **Raducan, S.D.**, Collins, G.S. and Davison, T.M. (2018) Numerical modelling of impacts into asteroid surfaces and implications for impact momentum transfer. *ESE PhD Conference*, Imperial College London, UK.

10. **Raducan, S.D.**, Collins, G.S. and Davison, T.M. (2018) The effects of asteroid layering on ejecta mass-velocity distribution and implications for impact momentum transfer. *9th Workshop on Catastrophic Disruption in the Solar System*, Kobe, Japan.

11. Stickle, A.M., Rainey, E.S.G., Owen, J.M., **Raducan, S.D.**, Bruck Syal, M. et al. (2018) Modeling Momentum Enhancement from Impacts into Rubble Pile Asteroids *Lunar and Planetary Science Conference 49*, Houston, TX. #1576

12. **Raducan, S.D.**, Collins, G.S. and Davison, T.M. (2017) The role of asteroid strength, porosity and internal friction in impact momentum transfer *15th Early Career Planetary Scientists' Meeting*, Glasgow, UK.

13. **Raducan, S.D.**, Collins, G.S. and Davison, T.M. (2017) The role of asteroid strength and porosity in impact momentum transfer. *Lunar and Planetary Science Conference 48*, Houston, TX. #2077

Chapter 2

Background

This chapter aims to introduce the reader to the theory and relevant literature on the formation of asteroids in the Solar System and the impact processes that have shaped them to their current state. The chapter begins with a brief introduction to Solar System formation and evolution, followed by the dynamical classification of the small bodies and a discussion about their physical properties. The subsequent sections of this chapter introduce the reader to shock wave physics concepts, impact cratering processes and impact crater and ejecta scaling relationships. The chapter then ends with an overview of the impact threat posed to Earth by small bodies and means of deflecting such a threat.

2.1 Formation and evolution of the Solar System

Our current understanding of the formation of the Solar System comes mainly from the present day shape and orbits in the Solar System, from the structure and composition of meteorites found on Earth and from observations of other young planet forming systems and proto-planetary disks. There are several theories describing Solar System formation, such as the Accretion theory (Lyttleton, 1961), the Protoplanet theory (McCrea, 1960; McCrea, 1988), the Capture theory (Woolfson and Lipson, 1964; Woolfson, 2019), or the Modern Laplacian theory (Prentice, 1984), however the most widely accepted theory is known as the Nebular hypothesis (Lissauer, 1993; Weidenschilling and Cuzzi, 2006; Cuzzi and Weidenschilling, 2006). Here, a short introduction to Solar System formation and

asteroids in the Solar System is given, as described by the Nebular hypothesis.

Today it is generally accepted that the Solar System began forming 4.56 billion years ago when a cloud of interstellar gas and dust, initially in hydrostatic equilibrium, reached a critical mass that caused its self gravity to dominate over the gas pressure. The molecular cloud then becomes unstable and started collapsing into a rotating protoplanetary disc, with a growing protostar at the centre. To conserve angular momentum, the cloud's rotation rate increased as it collapsed further, and the protoplanetary disc flattened. At this stage, the gravitational energy was converted to kinetic energy and the disk become opaque and increasingly hotter. Then, as the disk material was accreted into the protoSun and blown away by solar winds, the disk gradually cleared and then cooled. The clearing process is believed to have taken about 10 million years.

The formation of planets and asteroids is generally divided into several stages of evolution (Weidenschilling and Cuzzi, 2006; Cuzzi and Weidenschilling, 2006). Each stage is summarised below.

2.1.1 From gas to planetesimals

The cooling of the gaseous cloud around the Sun allowed for dust grains to condense and accrete, beginning the process of planetesimal formation. As the gas cooled down, different materials condensed from the gas at different distances from the Sun. Nearer to the Sun, the temperatures were still high (> few hundred K) and refractory materials, such as sillicates and iron, were the first materials to condense into solid grains. Towards the outer edge of the nebular disk, about 4 AU[a] from the Sun, the temperatures were much lower and volatiles, such as water ice, condensed in large quantities. Figure 2.1 shows the average temperature in the solar nebula and the condensation regions.

The dust and solid particles in the cloud were forced by the vertical component of the disk's gravity field to slowly settle towards the midplane of the disk. During their descent, the particles aggregated in low-velocity collisions, due to compaction of the particles and van der Waals forces. This process accounts for solid particle's growth up

[a]AU = Astronomical Unit, defined as the mean distance between the Earth and the Sun, 1 AU = 1.496×10^8 km.

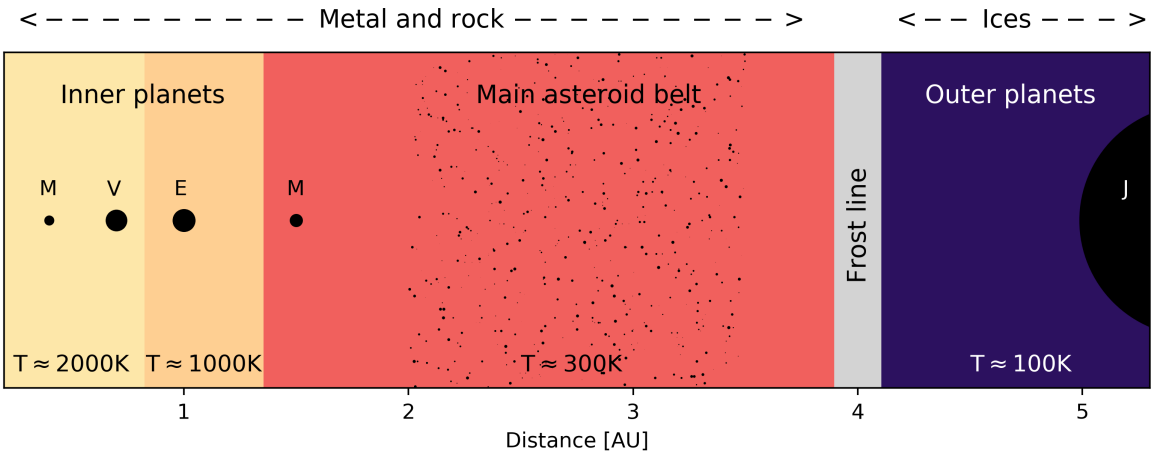

Figure 2.1: Schematic representation of the average temperatures (T) in the solar nebula, as a function of distance from the protoSun. Closer to the Sun, the temperatures were high and the refractory materials condensed into solid grains, forming the inner planets and the main asteroid belt. Beyond the 'Frost line', the temperatures were low enough (average temperature $\approx$ 100 K) for volatiles to condense into ice grains, forming the gas and the ice giant planets. The current position of inner planets, the main asteroid belt and the outer planets is also shown.

to mm and cm sizes.

The growth of solid bodies from cm size to km size is not well understood. Because the gas in the protoplanetary disk experienced a pressure gradient which exerted a force in the radial direction from the Sun, the gas' circular velocity was less rapid than the Keplarian rate for circular orbits. Small particles, of less than about 1 m, would be strongly coupled to the gas and thus were less affected. However, metre scale boulder sized particles would encounter a headwind that would cause them to slow down and spiral inwards, towards the Sun. For example, a metre sized object in the terrestrial planet region would have spiralled into the Sun in just 100 years. This size threshold between particles is often refereed to as the 'meter size barrier'. Kilometre-sized objects would experience less drag force due to their small ratio of surface area to mass. It is therefore believed the large particles might have accreted into kilometre sized objects over a very short period of time, before they spiralled inwards. Alternatively, the growth of solid bodies from small particles to planetesimals must have been induced by a different mechanism. Some of the proposed theories debate whether the solar nebula was affected by turbulences, and if it was, whether they were weak or strong (Safronov, 1972; Goldreich

and Ward, 1973; Cuzzi et al., 1993; Weidenschilling and Cuzzi, 2006).

In a nonturbulent nebula scenario, the small, centimetre to metre sized particles would settle into a dense midplane disk. The dense layer would have been accelerated to Keplarian velocities, reducing the effects of the headwind. At the same time, the relative velocities between particles would be low, allowing for the rapid growth of objects over the metre size barrier. For particles in the asteroid region, kilometre scale planetesimals would form in about 1000 years.

In a turbulent nebula, clumps of particles would form in the stagnating regions between turbulent eddies. These regions would have a high solid to gas ratio, with less gas drag and many collisions. This would reduce the relative velocity between the particles in the clump, allowing for the boulders to grow quickly over the metre size barrier.

Alternative models of how particles grew to km-sized objects are discussed in Cuzzi and Weidenschilling (2006); Morbidelli et al. (2009).

2.1.2 From planetesimals to embryos

Once the metre sized barrier was overcome, further growth of the kilometre sized object was achieved by gravitational interactions and low velocity accretional collisions. This stage in planetary formation is referred to as 'Runaway growth'. The planetesimals experienced frequent low velocity encounters, which aided their mass growth. The relative velocities remained low due to the low gravity. Once a body grew larger than its neighbours, it would sweep up and accrete all the nearby smaller planetesimals, growing into a planetary embryo.

After most of the planetesimal population was accreted into the larger bodies, the planetary embryos continued to grow, however at a slower rate, during an 'oligarchic growth' phase. Due to their increasing size, the planetary embryo started experiencing higher relative velocities, comparable to their escape velocities, decreasing the accretion efficiency. The runaway and oligarchic growth stages of the planetary formation are estimated to have lasted for several million years (Bottke et al., 2005).

Planetary embryos of a few hundred km in size were then able to perturb the

velocities of the smaller planetesimals, for up to several km/s. Collisions between bodies at such high velocities could then be disruptive. For example, due to Jupiter's migration (Walsh et al., 2011), planetesimals in orbital resonance with the planet were excited to high orbital velocities, of up to 10 km/s (Weidenschilling et al., 1998). Collisions between such planetesimals were very energetic and most of them did not lead to accretion.

2.1.3 From embryos to planets

In the last stage of planetary formation, the planetary embryos, which were now about Moon to Mars size, experienced high velocity collisions with one another and with remnant planetesimals. During this time, due to the gravitational interactions between Jupiter and other planetary embryos, the primordial bodies residing between the orbits of Jupiter and Mars, initially in quasi-circular orbits, were excited to high eccentricities and inclinations. As a result, more than 99% of the small bodies in the main asteroid region were ejected, leaving a much smaller population of bodies orbiting the Sun (Petit et al., 2001; Bottke et al., 2005). This process is expected to have lasted a very short time, on the order of only a few million years.

2.1.4 Giant collisions

During the late stages of planetary formation, giant collisions between similarly-sized planetesimals were common. Depending on the impact kinetic energy, the collision could result in three different outcome categories: cratering, disruption and dispersion (Benz and Asphaug, 1999). Cratering events form a topographic crater and material is ejected, but without destroying the target body. On the other hand, in a 'disruptive' collision the target body is broken into separate pieces. The last category includes so called 'hit-and-run' collision (Asphaug et al., 2006). Hit-and-run collisions are believed to have been common at this stage in the Solar System formation, and were more effective at removing the silicate mantles of differentiated planetary bodies than classic impacts. Giants impacts include the Moon-forming event or the event that formed the Martian crustal dichotomy (Wilhelms and Squyres, 1984), while hit-and-run collisions are thought

to be responsible for Mercury's thin mantle (Asphaug et al., 2006), and the formation of metal asteroids, such as asteroid (16) Psyche.

2.2 Asteroids in the Solar System

Asteroids, along with comets, are direct remnants from Solar System formation. They contain a relatively pristine record of the initial conditions present in the solar nebula, 4.6 billion years ago. However, the fraction of the asteroid population that has survived since that time has experienced numerous collisional, dynamical and thermal events, which have shaped their structure and orbital properties. For this reason, asteroids represent a unique opportunity to study the building blocks and mechanisms that led to the formation of planets, including Earth. In addition, asteroids may pose a future threat of colliding with Earth, with severe or even catastrophic consequences. A good understanding of asteroids can help us prevent such events.

2.2.1 Dynamical classification of small bodies in the Solar System

Asteroids in the inner Solar System are mainly found within three regions: the asteroid belt, the Jupiter trojans and the near-Earth asteroids.

Most of the known asteroids have nearly-circular orbits with a semi-major axis between 2 and 3.2 AU, located between the orbits of Mars and Jupiter, and are known as the Main Belt Asteroid (MBAs) (Fig. 2.2). The Main Belt contains more than 200 asteroids larger than 100 km in diameter, and more than 1 million larger than 1 km in diameter. The largest objects are (1) Ceres (945 km in diameter), (2) Pallas (545 km), (4) Vesta (525.4 km) and (10) Hygiea (444 km). Together, the mass of these four most massive asteroids accounts for about half of the total mass of the asteroid belt.

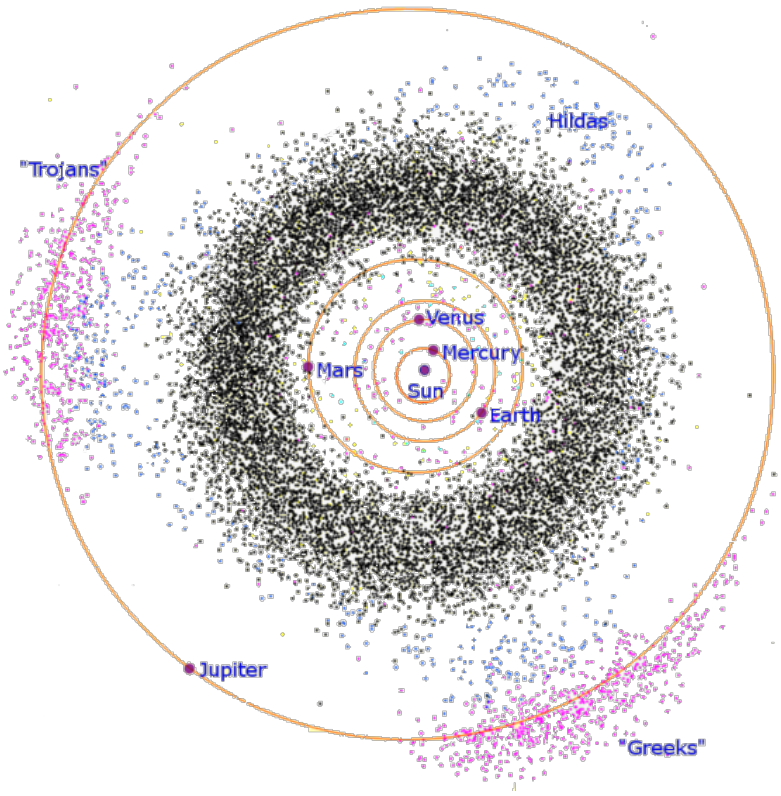

Figure 2.2: Schematic representation of the locations of asteroid populations in the inner Solar System, between the orbits of Mars and Jupiter. Main belt asteroids, shown in black, contains most of the known asteroids. Jupiter's trojans reside in the stable Lagrange points L_4 ('Greeks') and L_5 ('Trojans'), shown in pink. Hildas, which are in a 3:2 mean-motion resonance with Jupiter, are shown in blue. Adapted from Murray and Dermott (2000).

Another large population of asteroids are the Trojans (Fig. 2.2), which are found in the Jupiter's stable Lagrange points L_4 ('Greeks') and L_5 ('Trojans'). Finally, small objects that have orbits with a semi major axis of less than 1.3 AU are characterised as Near Earth Objects (NEOs).

Outside the inner Solar System, other small body populations include Centaurus (objects with orbits between Jupiter and Neptune), the Kuiper Belt (icy bodies located beyond the orbit of Neptune) and the Oort cloud (a spherical cloud of objects residing at the boundary of the Solar System and source of long period comets).

2.2.2 Near-Earth Asteroids

Currently there are over 15,000 known near-Earth asteroids (NEAs), which include all known asteroid compositions. The largest of them is asteroid (1036) Ganymed, which measures about 30 km in diameter. The NEA's are divided into four main populations, based on their orbital properties: the Atens, the Apollos, the Amors and the Atiras.

The Atens have semi-major axis less than 1 AU and aphelion distances greater than 1 AU, while the Apollos have semi-major axis greater than 1 AU and aphelion distances smaller than 1 AU. Therefore, the orbits of both of these asteroid populations frequently intersect Earth's orbit. The Amors have perihelion distances larger than 1 AU, and less than 1.3 AU, meaning that they are not crossing Earth's orbit, but can cross Mars' orbit. The Atiras have orbits that are entirely inside Earth's orbit.

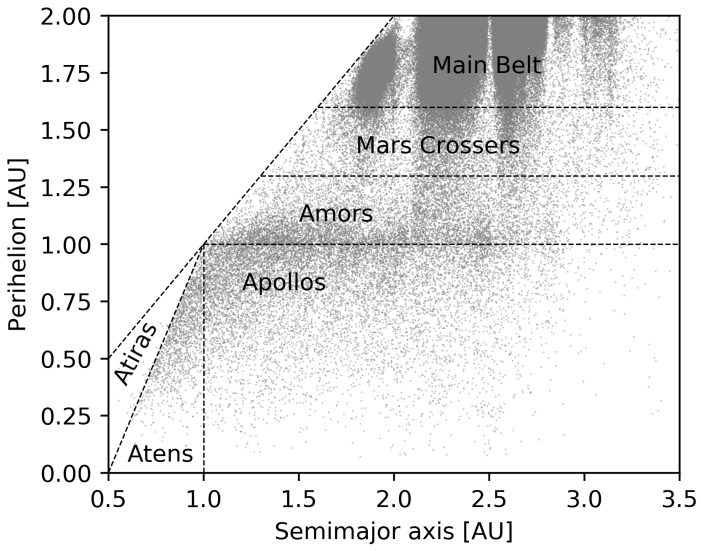

Figure 2.3: Orbital distribution of near-Earth objects. Adapted from Binzel et al. (2015)

2.2.3 Asteroid taxonomic classification

Though asteroids represent a very small fraction of the Solar System mass (about 4% of the mass of Earth's Moon), they are numerous and can have a very diverse composition. Chapman et al. (1975) introduced a small bodies classification system based on observations of the optical properties of the surface, such as emission spectra, albedo and colour. They defined three main categories, labelled with the alphabetical letters C, S and U.

Class C was assigned to dark carbonaceous objects and contained the asteroids with very low albedo. These are the most common asteroids in the Solar System and their spectra was matched to carbonaceous chondrite meteorites studied in the laboratory. Class S was attributed to stony, silicaceous objects. These objects have a spectrum that has a moderate slope (Fig. 2.4) and absorption features corresponding to olivine or pyroxene. The albedo of S-type objects is also slightly brighter than for the C-type. Class U was assigned to unclassifiable objects.

Bowell et al. (1978) further developed this taxonomic classification by introducing the M, E and R-types. The spectra from Class M asteroids is generally featureless and matches the iron-nickel rich meteorites. The E-type asteroids have high reflectivity (Fig. 2.4) and their spectra matches the enstatite meteorites, while the R-type asteroids are moderately bright, with distinct olivine and pyroxene feautures. Figure 2.4 shows the spectra of sunlight reflected from the surface of several types of asteroids: C, M, S, E-type and from asteroids (4) Vesta. These asteroid spectra can be matched to those obtained in the laboratory, from meteorites.

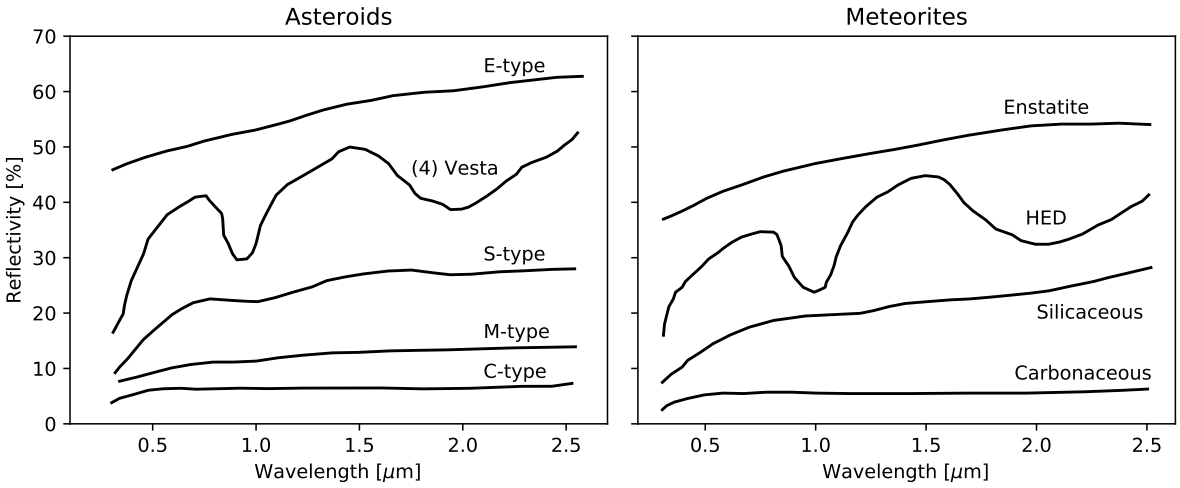

Figure 2.4: Spectra of reflected light observed from different asteroid types (left) matched with spectra obtained in laboratory from meteorites with different composition (right). For example, Asteroid (4) Vesta (V-type) has a specific reflectance signature that matches the HED (howardite–eucrite–diogenite) meteorites observed in laboratory. Adapted from Morrison et al. (1995).

Today there are several classification systems in use and depending on the classification criteria a specific asteroid can belong to different classes. However, the most

widely used classification systems are the Tholen and the SMASS systems.

The Tholen classification system was developed by Tholen (1989) and it is based on the albedo and broad band spectra measurements taken by the Eight-Color Asteroid Survey (Zellner et al., 1985). The classification systems contains 14 types, which are divided into three major groups. The C group contains the dark, carbonaceous objects and are further divided into the B, F, G and C classes. The S group contains the silicaceous objects and are divided into the A, Q, R, and V classes. X-group contains the featureless M, E and P classes.

The SMASS systems is based on the Small Main-Belt Asteroid Spectroscopic Survey II (SMASSII) (Bus and Binzel, 2002) and the Small Main-Belt Asteroid Spectroscopic Survey in the near-infrared (SMASSIR) (Burbine and Binzel, 2002). The classification system was built up on the previous classifications, keeping the same three major groupings (the S-, C-, and X-complexes), and defined a total of 26 classes, based on the presence or absence of specific spectral features.

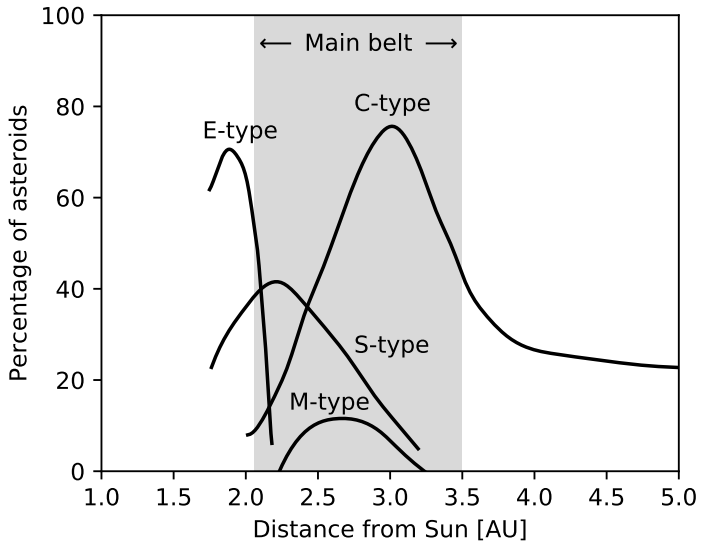

Figure 2.5: Percentage of known asteroids as a function of their orbital distance from the Sun, in AU. Different part of the main belt are dominated by asteroids of different types and therefore, composition. Adapted from Gradie and Tedesco (1982).

The distribution of asteroids of different types (and compositions) is not uniform in the Solar System. Figure 2.5 shows the percentage of asteroids that belong to the C, E, M and S-type, as a function of their mean distance to the Sun. C-type asteroids, which

are considered primitive asteroids that have suffered very little thermal alteration, are mainly found in the outer main belt and their population density peaks at about 3 AU. (Fig. 2.2). S-type asteroids, which are considered to be more evolved, are found mainly in the inner part of the main belt, peaking at about 2.2 AU. M-type asteroids, which are believed to be metallic asteroids that have been subject to differentiation, can generally be found in the middle part of the main belt.

2.2.4 Densities of Asteroids

Mass density is a fundamental property for asteroids (Britt et al., 2002). The taxonomic class of an asteroid inferred from spectra can indicate its surface composition, however it might not necessarily indicate the bulk composition of the body (Elkins-Tanton et al., 2011). The bulk density of an asteroid is defined as the mass of the body divided by its volume, and can be different from the mean grain density of the individual constituents. Only a small fraction of the known asteroids have well defined bulk densities, as this requires both the mass and the volume of the body to be known, and such measurements are often unavailable.

The mass of an asteroid can be measured directly from the orbital deflection during a close encounter of a spacecraft, another asteroid or a planet of known mass. For binary asteroid systems, the mass of the primary and secondary can also be determined indirectly, from their orbital period. The volume estimates are most often derived from from optical, infrared and radio observations (Carry, 2012).

In asteroids, a percentage of the bulk volume is usually occupied by void space, representing the porosity. The porosity can be estimated from the bulk density and its assumed grain density of the asteroid. Grain density estimates are based on laboratory measurements of spectroscopically similar meteorites (Britt et al., 2002). However a large number of observed asteroids have no link to any known meteorites, which makes their characterisation more difficult.

Porosity can be divided into macroporosity, defined as macroscopic void space and fractures within a body, and micropososity, defined as voids and pores on the scale of

tens of micrometers, similar to the porosity found in meteorites. The amount of porosity in an asteroid is directly related to the collisional evolution of the body.

Large bodies, larger than about 400 km in diameter, tend to have little to no macroporosity (Carry, 2012), because their internal pressure is greater than the lithostatic pressure. While these bodies can still have a porous surface layer, the internal cracks and voids get compressed at pressures higher than 10 MPa, which are reached at just a few km below the surface (Britt et al., 2002). For example, Figure 2.6 shows a clear threshold between the low porosity asteroids (e.g. Ceres, 2 Pallas and 4 Vesta), and the highly porous asteroids, at a mass of about 10^20 kg (about 400 km in diamter). Furthermore, due to their large size, these asteroids are more likely to survive large impacts (Britt et al., 2002).

On the other hand, asteroids between about 200 m and 10 km in diameter (Walsh et al., 2019) tend have large fractures and cracks or being accumulations of disrupted material, held together by gravity (rubble-piles) (Richardson et al., 2002).

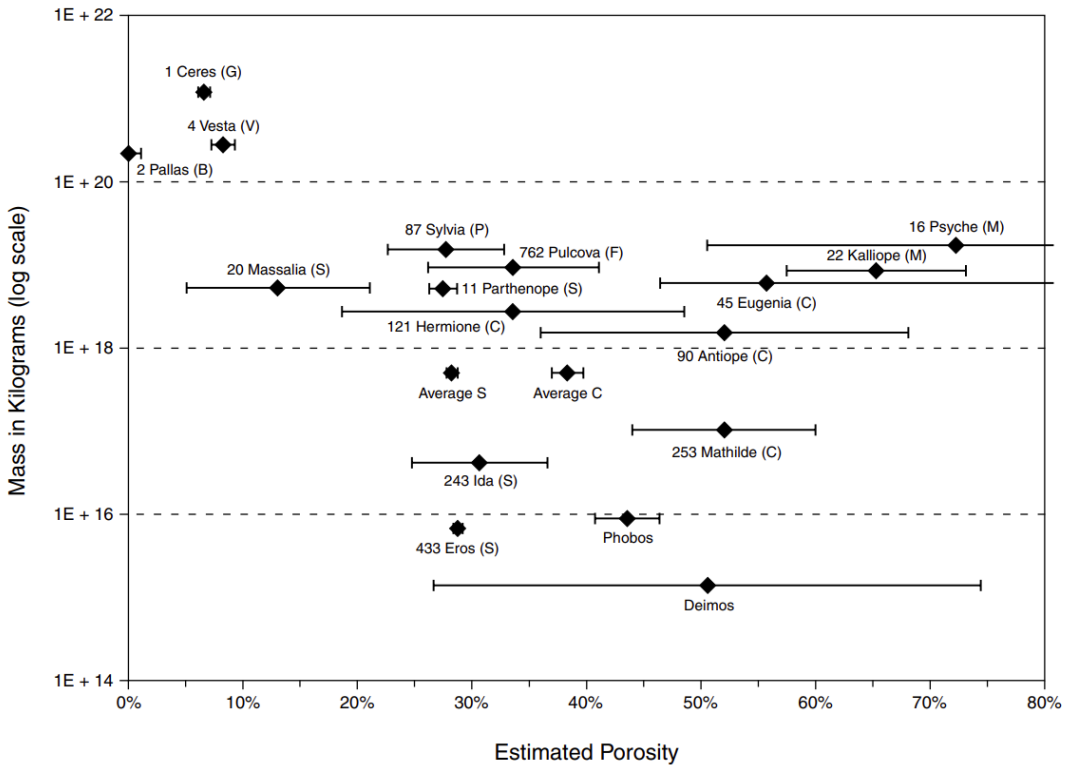

Figure 2.6: Solar System objects with their estimated porosity. From Britt et al. (2002)

Figure 2.6 shows the estimated porosity as a function of mass, for a number of

large objects ($D > 10$ km). For example, the bulk density of the C-type asteroid 253 Mathilde, which was visited by the NEAR spacecraft, was estimated at about 1.3 g/cm^3. This estimate is much lower than the density range measured for carbonaceous chondrites meteorites, of about 2.1 - 3.4 g/cm^3 (Mason, 1963). If Mathilde has a similar composition and structure to CM chondrites, then it has bulk porosity of about 50%. Asteroid Bennu, a B-type (a subgroup of the C-class) asteroid, visited by the OSIRIS-REx mission in 2019, is believed to be a rubble pile with a 40± 10% bulk porosity (Lauretta et al., 2019). Similarly, asteroid Ryugu is believed to be around 50% porous (Watanabe et al., 2019).

More primitive C-type asteroids tend to have a larger macroporosity than basaltic S-type asteroids (Britt et al., 2002), however there are large variations in porosity even for asteroids belonging to the same taxonomic class. For example, several studied S-type asteroids, such as Ida or Eros (Thomas et al., 2002; Veverka et al., 2001), have an estimated bulk porosity of about 20%, while asteroid Itokawa (Yano et al., 2006) has an estimated bulk porosity of about 40%.

2.2.5 Strength of Asteroids

The physical evolution of an asteroid is dependant on its mechanical strength (Scheeres et al., 2010). Some measure of strength, along with gravity determines whether an impact into a small body produces a crater or causes disruption. However the strength of an asteroids is difficult to estimate from observations and spacecraft flybys alone.

Firstly, it is important to distinguish between the many different types of strength. A geological material can have a tensile strength, a compressive strength, a shear strength, a crush strength and so on. Each of these strengths determines the material's ability to withstand a different type of stress state. The tensile strength of a material is determined by the value of the tensile principal stress at which the specimen breaks. The compressive strength is the material's ability to withstand compressive uniaxial stress. The shear strength is determined by the ability of a material to withstand pure shear. A material with no tensile strength (e.g. granular materials) can still have a significant amount of shear strength, which comes from the ability of the interlocking particles to move apart

and slide over one another. The shear strength measured at zero pressure is often referred to as cohesion.

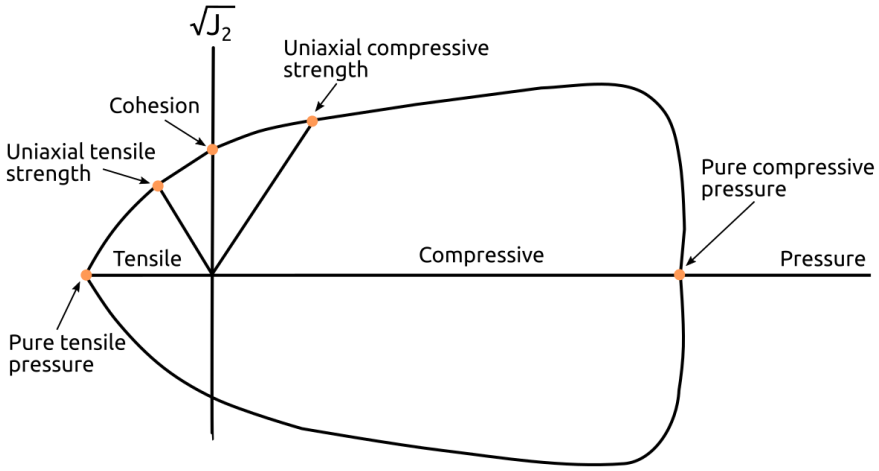

Figure 2.7: Graphic representation of a general strength/failure envelope, showing how shear, measured by $\sqrt{J_2}$ depends on pressure. Each point on the plot corresponds to different state stress. The five highlighted points represents different measures of strength. Adapted from Holsapple (2009)

Each of these strengths represents a different part of a 'failure envelope' or 'strength envelope', defined as the maximum stress a material can withstand before it undergoes plastic (irreversible) deformation (Fig.2.7). The failure envelope can be described mathematically by a yield criterion for ductile materials (e.g. metals) or by a failure criterion for brittle materials (e.g. rocks).

Two commonly used yield criteria for metals are the Tresca criterion and the von Mises criterion (Holsapple, 2009). In the Tresca criterion, the yield occurs when the maximum shear stress (in any direction) reaches a critical value. In the von Mises criterion, the shear stress is replaced by the second invariant J_2 of the deviatoric stress tensor. Both criteria are independent of pressure.

For geolological materials, due to the interlocking of the granular particles, the allowable shear depends on the confining pressure. The failure or rock materials is often described by a Mohr-Coulomb or a Drucker-Prager criterion. In a general case, the average stress (pressure P) is written using the three principal stresses of a three dimensional

stress state σ_1, σ_2 and σ_3[b],

$$P = \frac{1}{3}(\sigma_1 + \sigma_2 + \sigma_3). \tag{2.1}$$

The maximum shear stress is determined by the square root of the second invariant of the deviatoric stress tensor,

$$\sqrt{J_2} = \frac{1}{\sqrt{6}}\sqrt{[(\sigma_1 - \sigma_2)^2 + (\sigma_2 - \sigma_3)^2 + (\sigma_3 - \sigma_1)^2]}. \tag{2.2}$$

Figure 2.7 shows a plot of the square root of the second invariant as a function of pressure. There are five points along the strength envelope that define the failure caused by different stress loading. The fist point is the pure tensile pressure, which represents the maximum negative pressure applied by three equal tensile principal stresses, at which failure occurs. The next point is the uniaxial tensile strength, which represents the maximum stress applied by stretching or pulling in one direction, before breaking. Mathematically, the pressure is written in terms of a stress, s, pulling in one direction

$$P = \frac{\sigma_T}{3}. \tag{2.3}$$

The $\sqrt{J_2}$ is then expressed as

$$\sqrt{J_2} = \frac{\sqrt{2\sigma_1^2}}{\sqrt{6}} = \frac{\sigma_T}{\sqrt{3}}, \tag{2.4}$$

where $\sigma_2 = \sigma_3 = 0$ and $\sigma_1 = \sigma_T$. The slope between the origin and the uniaxial tensile strength point is then $-\sqrt{3}$.

The uniaxial compressive strength is the maximum compressive stress that can be applied in one direction, before breaking. Similarly the pressure is written in terms of the stress, s, as

$$P = \frac{\sigma_c}{3}. \tag{2.5}$$

and the $\sqrt{J_2}$ is expressed mathematically as

$$\sqrt{J_2} = \frac{\sqrt{2\sigma_1^2}}{\sqrt{6}} = \frac{\sigma_c}{\sqrt{3}}, \tag{2.6}$$

where $\sigma_2 = \sigma_3 = 0$ and $\sigma_1 = -\sigma_c$. The slope of the line between the origin and the uniaxial compressive strength is $\sqrt{3}$.

[b]The sign is positive in tension and negative in compression.

The point between the uniaxial tensile strength and the uniaxial compresive strength is the cohesion. For a material with no cohesion, the tensile strength is also zero and both points would be at origin, while the compressive strength can be non-zero.

The last point on the strength envelope is the pure compressive pressure represents the maximum compressive pressure applied by three equal tensile principal stresses, before failure.

The strength values on a strength envelope are usually determined from laboratory measurements in 'tri-axial' tests[c] For example, for a meteorite, each of these types of strength can be measured in laboratory. However they are not necessarily representative of the parent body's strength (Popova et al., 2011) due to scale effects and sample size.

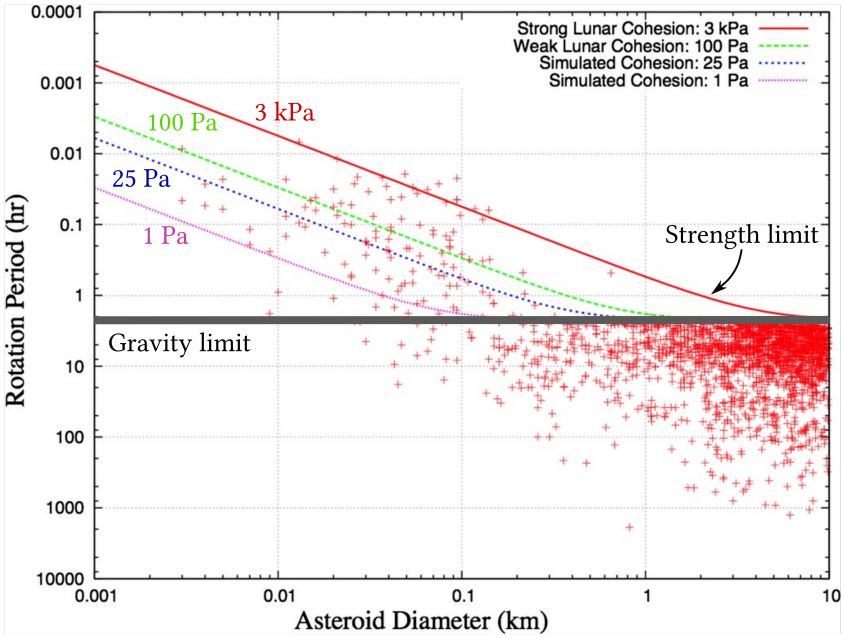

Figure 2.8: Size and spin rate distribution of small bodies in the Solar System. The lines represent different theoretical spin limits calculated assuming no cohesion (gravity limit) or fixed cohesions of 1 Pa, 25 Pa, 100 Pa and 3 kPa (strength limits), and a 90° friction angle. Adapted from Sánchez and Scheeres (2014).

The spin rates of small bodies in the Solar System can provide us with an estimate of the lowest cohesion an asteroid can have without being deformed or disrupted (Pravec and Harris, 2000). A simple analysis based on a body with a mean density of 2.5 g/cm^3 and zero tensile strength (Harris, 1996) led to a rotation period limit of 2.1 hours. This value is smaller than the rotation period of most large asteroids observed to date.

[c]Tests in which a uniform pressure is applied to a specimen in all directions.

Figure 2.8 shows the size and spin rate distribution of known small bodies in the Solar System (Sánchez and Scheeres, 2014). Most bodies larger than ≈ 120 m have a rotation period larger than 2.2 hours, which is the spin limit at which a cohesionless body can rotate and still retain its shape. Due to this strong threshold on the asteroid's rotation period, it is widely believed that most small bodies larger than about 100 m are rubble piles, cohesionless aggregates held together only by gravity. Asteroids smaller than ≈ 120 m can rotate much faster than the gravity limit. Figure 2.8 shows the theoretical spin limits for bodies with fixed cohesions of 1 Pa, 25 Pa, 100 Pa and 3 kPa. The figure suggests that some of the fast rotating bodies must have a cohesion of at least 3 kPa in order to maintain their shape, which would be similar to the upper limit of cohesion measured for the regolith on the Moon.

Bodies larger than about 10 km have a collisional lifetime similar to the age of the Solar System (Bottke et al., 2005). These bodies are expected to have survived any disruptive collision, setting an upper size limit on asteroids that are expected to be rubble piles (Walsh et al., 2019).

2.2.6 Cohesion of rubble piles

Due to the hard limit on the rotation period of asteroids larger than 120 m is tempting to assume that rubble piles have no strength. However several pieces of evidence suggest that rubble pile asteroids might instead a have a small, yet finite tensile strength (Scheeres and Sánchez, 2018).

Based on the boulder cumulative size frequency distribution on Itokawa Sánchez and Scheeres (2014) proposed that the asteroid's interior is likely to have a much larger number of fine grains, which create a matrix around the large boulders. Applying the classical theory for cohesion in dry powders, they estimated that the cohesion would decrease with increasing grain size, but that the large boulders on asteroids could be held in place by the cohesion within the small grain regolith matrix.

One example that supports this theory is the 1.1 km in diameter fast rotating asteroid (29075) 1950 DA, which belongs to the NEO Apollo family. The asteroid's physical

properties have been studied extensively due its potential threat to Earth. Hirabayashi and Scheeres (2014) found that a minimum global cohesion of 75–85 Pa is required for the body to retain its shape during rotation.

Another example is the astronomical observations of asteroid 2013 P/R3 during its disruption process. The asteroid was observed fragmenting into several distinct clusters, which allowed for the cohesion of the original parent body to be estimated between 40 and 210 Pa (Jewitt et al., 2014).

2.3 Shock wave physics

During the entire history of the Solar System, small bodies repeatedly collided with each other and with other planets. As a result of an impact event, stress waves are generated that propagate through the colliding bodies, with different amplitudes and directions of motion. Understanding how these stress waves generate, propagate and decay is vital in the study of impact cratering. A detailed description of the shock wave physics involved in impact cratering is given by Melosh (1989) and Zel'dovich and Raizer (2002). Here a brief background is included.

2.3.1 Hugoniot equations

An impact event generates a shock wave that travels at speeds higher that the material specific speed of sound. The shock front tends to be abrupt and is often represented as a discontinuous jump in pressure, particle velocity, density and internal energy.

The shock front is described by a set of three equations, known as the Rankine-Hugoniot equations, which define the conservation of mass, momentum and energy and relate the state of the material before and after the shock wave.

$$\text{Conservation of mass:} \quad \rho_s \left(U_s - u_p\right) = \rho_0 U_s \tag{2.7}$$

$$\text{Conservation of momentum:} \quad P_s - P_0 = \rho_0 u_p U_s \tag{2.8}$$

$$\text{Conservation of energy:} \quad E_s - E_0 = \left(P_s + P_0\right) \frac{1}{2} \left(\frac{1}{\rho_0} - \frac{1}{\rho_s}\right) \tag{2.9}$$

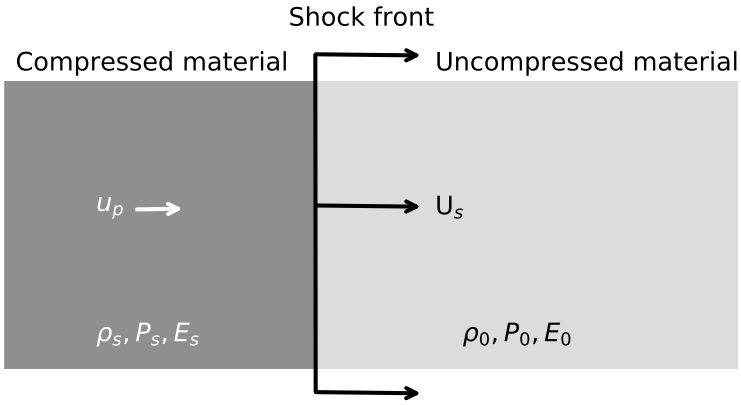

Figure 2.9: Shock wave through a material. The shock from moves at velocity U_s. The other quantities describe the state of the material before and after the shock wave has passed through. Adapted from Melosh and Sonett (1986) and Sharp and de Carli (2006).

where ρ_s and ρ_0 are the compressed and uncompressed densities, respectively, u_p is the particle velocity behind the shock, U_s is the velocity of the shock wave, P_s and P_0 are the pressures after and before the shock wave and E_s and E_0 are the specific internal energies on either side of the shock wave, respectively.

The system of equations has five unknown quantities, so a fourth equation is needed to solve the system and define the shock wave state. The fourth equation relates the pressure to the specific volume and specific internal energy and is known as the equation of state. A more detailed discussion is included in Section 3.3.

The results from shock wave studies can be presented as pressure-volume ($P-V$) diagrams or wave velocity - particle velocity (U_s - u_p) diagrams. The most commonly used is the $P-V$ diagram, which is shown schematically in Figure 2.10a. As the shock wave passes through the material, the material jumps from an unshocked state to a shocked one. Each point on the Hugoniot curve represents an individual shock event. The curve itself can be derived from a series of shock physics experiments and its shape is dependent on several material parameters, such as type, pre-shock temperature or porosity. The Rayleigh is a straight line between the initial state of the material and the state on the Hugoniot. For example, in Figure 2.10a, material with an initial pressure P_0 and initial volume V_0 (position A) jumps to a to a shocked state P_s, along the Rayleigh line, to point C on the Hugoniot curve.

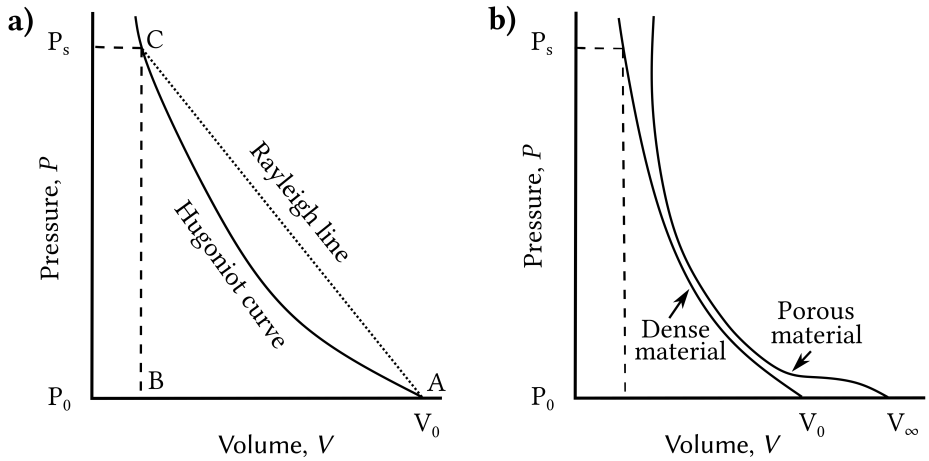

Figure 2.10: Pressure-volume Hugoniot diagrams for solid and porous materials. a) During a shock event, the material jumps from an initial state P_0, V_0, along the Rayleigh line, to a shocked state P_s, on the Hugoniot curve. b) During a shock event in a porous material, the porosity is firstly crushed until it reaches the material's solid density, then it jumps on a Hugoniot curve that lies above the Hugoniot of the non-porous material. Adapted from Melosh (1989) and Sharp and de Carli (2006).

Figure 2.10b) shows the Hugoniot curve for the same target material with and without porosity. Initial porosity in the target material causes a kink in the Hugoniot curve. The pore collapse occurs at relatively low shock pressures, however the Hugoniot curve will always lie above the curve of the non-porous material. The compressed porous material is hotter compared to the initially non-porous material, therefore it requires more PdV work to reach the same volume.

2.3.2 Release waves

After the passage of the shock wave, the decompressed material rarely returns to its initial state. Even weak shock waves can cause fracturing in brittle materials and the compaction of pores in porous targets, resulting in irreversible changes.

Material is only shocked for a short time, after which the propagation of a release or 'rarefaction' wave releases material from high pressures. The release wave propagates from the free surface into the shocked material, generally at greater speeds than the shock wave. After the passage of the release wave, the shock pressure declines to near zero, however small residual particle velocity sets material into motion. Figure 2.11 shows a schematic representation of the direction of the particle velocity. The material

is accelerated by the sharp pressure gradient at the shock front, resulting in a shock particle velocity pointing radially away from the origin. The rarefaction wave reflects at the free surface and accelerates down the target particles. The net particle velocity after the passage of the shock and the release wave is the sum of shock particle velocity and rarefaction particle velocity.

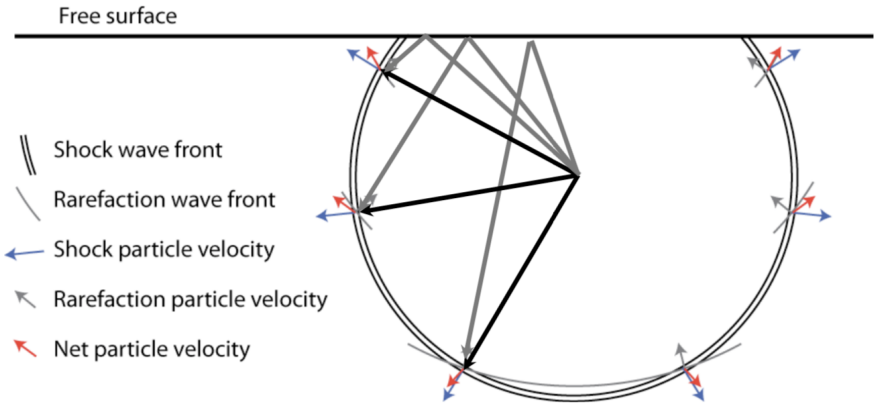

Figure 2.11: Schematic representation of the direction of the particle velocity. Figure courtesy of Gareth Collins.

The residual particle velocity after both the shock and the rarefaction waves have passed over the target material initiate the excavation flow field that leads to the opening of the crater. The crater formation processes are further discussed below.

2.4 Impact cratering processes

The process of impact cratering has been studied extensively from theoretical studies of shock waves (e.g. Melosh, 1989), laboratory experiments (e.g. Gault et al., 1963; Cintala et al., 1999; Holsapple and Schmidt, 1982; Housen et al., 1983; Holsapple and Schmidt, 1987), geological studies of large craters on Earth (e.g. Shoemaker et al., 1969) or from images of impact craters on other planetary surfaces (Gault et al., 1975; Pike, 1980; Schultz and Frey, 1990). This section briefly summarises the impact cratering processes, however more detailed discussions are provided by Melosh (1989), French (1998) and Osinski and Pierazzo (2012).

The cratering process consists of a rapid succession of events and is often divided into three main stages (Gault et al., 1968): the contact and compression stage, when the projectile first hits the target; followed by an excavation stage, during which material is displaced and removed from inside the crater; and the modification stage, which is characterised by modifications due to gravity, or erosion.

2.4.1 Contact and compression stage

The fist stage of the impact cratering process begins when the impactor hits the target surfaces at velocities higher than the speed of sound in the target/impactor material, which is typically more than a few km/s for a non-porous target. As the impactor penetrates the target, it forces target material out of its path, compressing and accelerating it to a large fraction of the impact velocity (Fig. 2.12a). At the same time, the impactor is decelerated by the target's resistance to penetration. Due to these velocity changes, shock waves are created at the boundary between the impactor and target material, which then propagate into the target, in a hemispherical fashion. The shock pressures can reach up to several hundreds GPa, much higher than the yield strength of either the target or the projectile. The highest pressure experienced by the material is roughly evenly distributed over a volume approximately equivalent to the impactor volume, called the 'isobaric core'. Outside the isobaric core, the shock peak pressure, $P(d)$, decreases with distance d, as the shock wave travels away from the impact point, roughly following an inverse power law

$$P(d) = P_{max} \left(\frac{r_{ic}}{d} \right)^n , \tag{2.10}$$

where r_{ic} is the radius of the isobaric core and n is a constant that can take values between 2 and 4.5, depending on the strength of the shock wave (Ahrens and Okeefe, 1977). The shock wave travels at very high speeds, usually exceeding the speed of sound into the target material.

During this stage highly shocked material is jetted out from the contact point, in a

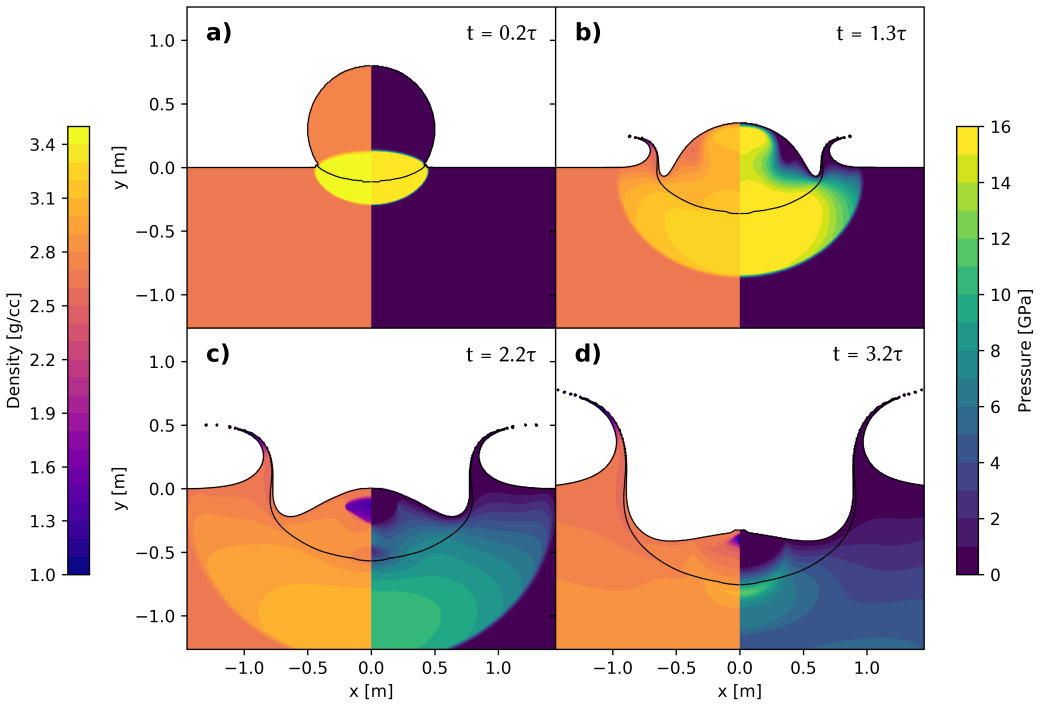

Figure 2.12: Contact and compression stage of the cratering process. Crater profiles of a 1 m aluminium sphere impacting a basalt target, at 5 km/s, showing the density (in g/cc) and pressure (in GPa) of the first stages of the cratering process. The times are shown in terms of the compact and compression stage duration, $\tau = L/U$, where L is the impactor diameter and U is the vertical component of the impact velocity. a) As the impactor hits the target, a thin region of high shocked and compressed material develops along the contact interface. b) The shock (and release) wave reaches the backside of the impactor. c) The sock wave is reflected as a rarefaction wave, leaving low pressures in the impactor. d) The sock wave propagates hemispherically through the target, followed by the rarefaction wave.

process called 'jetting'. This process can eject up to 40% of the projectiles mass[d] (Melosh and Sonett, 1986), carrying away much of the original energy and momentum. The jet velocity can reach values as high as five times the impact velocity (Kieffer, 1977), depending on the angle between the converging surface of the projectile and target (Johnson et al., 2014).

The contact and compression stage is very short, only lasting until the shock wave reaches the back side of the projectile (Fig. 2.12b). Once the shock wave reaches the back side of the projectile, a rarefaction (or release) wave travels back through the projectile and into the target, in the shape of a hemisphere (Fig. 2.12c, d). Behind the rarefaction

[d]For impact velocities higher than 11 km/s.

wave, the material is decompressed, resulting in melting and, for high impact speeds, vaporisation.

Understanding this stage of crater formation is important as it is during this stage that much of the kinetic energy of the impactor is transferred to the target, resulting in the acceleration of material away from the impact point.

2.4.2 Excavation stage

Following the contact and compression stage, there is the excavation stage of crater formation. In this stage the shock wave propagates through the target medium in a roughly hemispherical shape, weakening it and setting it into motion. As the shock wave expands, its strength decreases and it decays to a plastic wave and then to an elastic wave. The centre of the approximately hemispherical wave is located at some depth below the impact surface, at a so called 'depth of penetration'. The shock waves that travelled upwards reflect at the free surface and generate rarefaction waves. The material in the region where the shock waves and the rarefaction waves interfere, called the 'interference zone', experiences shock pressures less than those experienced by material located at the same radial distance, but directly beneath the impact point. This material is lightly shocked and is ejected early in the cratering process, and at very high velocities (Osinski and Pierazzo, 2012).

The shock wave and the subsequent rarefaction wave set material into motion, producing the 'excavation flow', which then generates the transient crater (Fig. 2.13). The material above the flow lines that intersect the transient crater rim is ejected beyond the final crater rim, and originates from a so called 'excavation zone' (orange shaded area in Fig. 2.13). The velocity vectors in the material are connected by curved lines called 'streamlines'. The streamlines originate from the inner surface of the growing crater cavity and follow paths that are parallel to the velocity vectors. Near the crater rim, the streamlines curve upwards and outwards. The streamlines originating from larger depths curve down before turning up to the free surface, whilst the streamlines originating from the growing crater floor never reach the surface and displace the material downward.

The material on streamlines that cross the free surface is ejected when it rises above the pre-impact level. The ejecta material contains a mixture of vapour, melt and weakly, and highly shocked material, depending on where it originated in the excavation zone, relative to the impact point and the free surface. The material below the 'excavation zone' is initially accelerated downward and outward, forming the base of the expanding crater cavity (grey shaded area in Fig. 2.13).

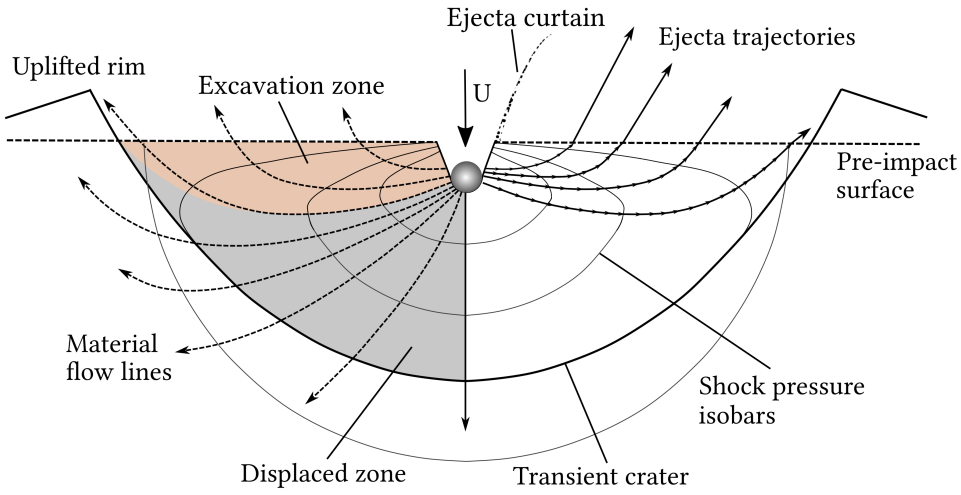

Figure 2.13: Schematic representation of the excavation stage of the cratering process. The originally spherical projectile, with an impact velocity U, penetrates the target and causes peak shock pressures to propagate as hemispherical isobars. The shock waves and the subsequent rarefaction waves set the material into motion, in the direction of the material flow lines. The upper part of the excavated material (orange) gets ejected beyond the crater rim, in an ejecta curtain, while the lower part (grey) gets displaced and does not reach the surface. Adapted from French (1998).

The excavation process described here applies to impact craters into homogeneous targets, however the presence of layering or pre-existing structures in the target may affect this process. The end of the excavation process is dictated by the dominant opposing force that decelerates and stops the excavation flow. Generally, for large craters the dominating force is gravity, while for small craters the dominating force is the strength of the target, however this is dependant on the target body. During the excavation stage the crater reaches its maximum size, called the 'transient crater'. This stage is important for ejection studies as most of the ejecta mass gets ejected during this stage.

Crater ejecta

During the excavation stage, as the crater expands, material is ejected out of the crater on a nearly parabolic trajectories. The ejected material forms a cone of material, called the 'ejecta curtain'. The characteristics of the ejecta curtain are dictated by the ejection velocity, angle, and time, which are themselves determined by the projectile and target properties. The point at which a particle crosses the pre-impact surface is called 'launch position'. The ejection velocity decreases with crater growth and early impact experiments (e.g. Piekutowski, 1980) showed that particles that are ejected at the same launch positions have similar ejection velocities. In a vertical impact, the ejection angle is about 45°, however deviations from this value exists for very early ejecta (Hermalyn and Schultz, 2011) or for specific target properties (Luther et al., 2018).

As the impact cratering ejecta represents one of the focus of this thesis, different aspects of the ejecta are discussed throughout the following chapters.

2.4.3 Modification stage

The last stage in crater formation, the modification stage, starts after the material has already been ejected from the crater and the transient crater has formed. Therefore, this stage does not play a role in ejecta formation.

In the modification stage, depending on the size of the crater and the target properties, the transient crater can be modified into three types of crater structures (Fig. 2.14): simple craters, complex craters, and multiring basins.

Small transient craters form bowl-shaped simple craters (Fig.2.14a). During this stage, due to gravity, loose debris can slide back into the crater and create a false floor. For craters with a diameter larger than a critical diameter, the crater morphology transitions from a 'simple' to a 'complex' one. Complex craters are characterised by a central uplift, a flat floor and coherent collapse of the crater rims. They are larger than the simple craters and have a smaller depth to diameter ratio. The critical diameter above which complex craters form is specific to the impacted target, and it scales as an inverse power of the surface gravity and surface target material. On the Moon, the critical diameter is

about 15 km.

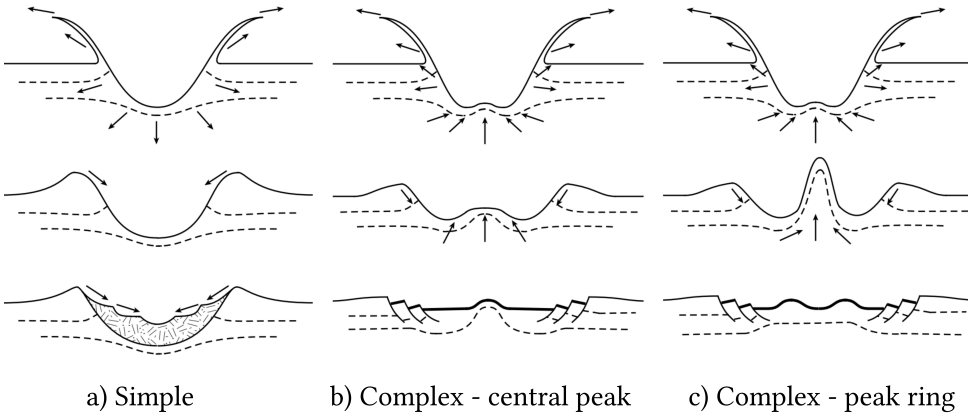

Figure 2.14: Schematic representation of the crater growth for a) simple and b) complex with a central peak and c) complex with peak ring craters. The top row shows the growth of the transient crater, the middle row shows the beginning of the modification stage and the bottom row shows the final crater morphology. Complex craters. From Davison, (2010), adapted from Melosh (1989) and French (1998).

During large impact events, the energy release is large enough to overcome the target strength over a large volume below the transient crater, causing complex interactions between the shock wave, gravity, strength and the structure of the target. These interactions result in the rise of the rocks beneath the crater and to the formation of a central uplift. The rocks around the edge of the transient crater collapse downward and inward, forming a peak ring or a series of terraces (Fig. 2.14b and c).

The duration of the modification stage depends on the size of the crater. Major changes in the crater morphology can occur for up to several minutes for km-sized impacts, however other geological processes such as erosion or sedimentation can occur over much larger timescales, with no definite end time.

2.5 Impact crater scaling relationships

The outcomes of planetary cratering, such as the size of the crater and the speed and mass of ejecta, can be predicted empirically if the impactor and target properties are known (Schmidt and Holsapple, 1982). Scaling laws assume that the impact can be approximated as a point-source of energy and momentum, which are released in a small

region, usually at some depth in the target, called the 'coupling zone' (Holsapple and Schmidt, 1987). Then the far-field/late-stage properties of the impact can be determined by a single variable, known as the coupling parameter, C (Holsapple and Schmidt, 1987), given by

$$C = aU^{\mu}\delta^{\nu} \tag{2.11}$$

The coupling parameter depends on the properties of the impactor (radius a, density δ and velocity U) (Fig. 2.15). The density scaling exponent, ν, has thus far been assumed to be independent of the material type (Housen and Holsapple, 2011) and previous experimental studies suggest $\nu \approx 0.4$ (Schmidt, 1980). The velocity scaling exponent, μ (often called the 'velocity exponent'), however, depends on the target material properties and its value lies between two theoretical limits (Holsapple and Schmidt, 1982): $\mu = 1/3$ if the crater formation is influenced by the impactor momentum alone or $\mu = 2/3$ if the it is influenced by the impactor energy alone.

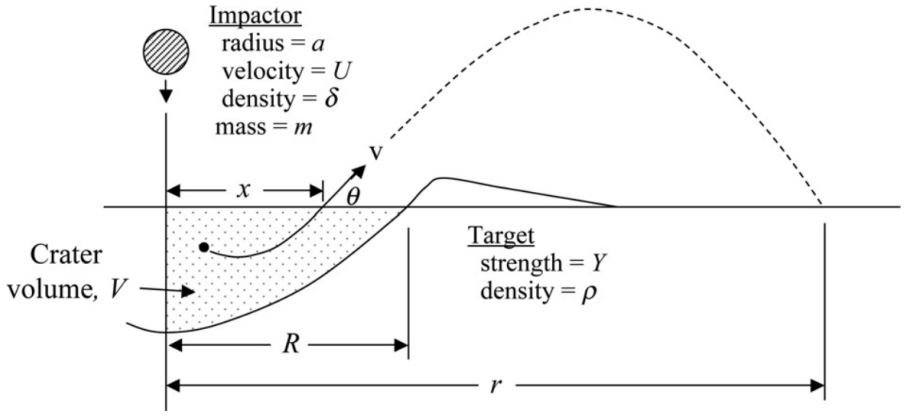

Figure 2.15: Definition of variables used in the scaling laws. Source: (Housen and Holsapple, 2011).

For known impact conditions, when considering a spherical impactor of mass m and density δ, impacting a target of density ρ and strength Y, at a velocity U, the radius of the crater (measured at the preimpact surface), R, can be expressed in terms of the widely used dimensionless π scaling parameters (Holsapple, 1993). The most general form of the scaling relationship for crater radius, R, is given by:

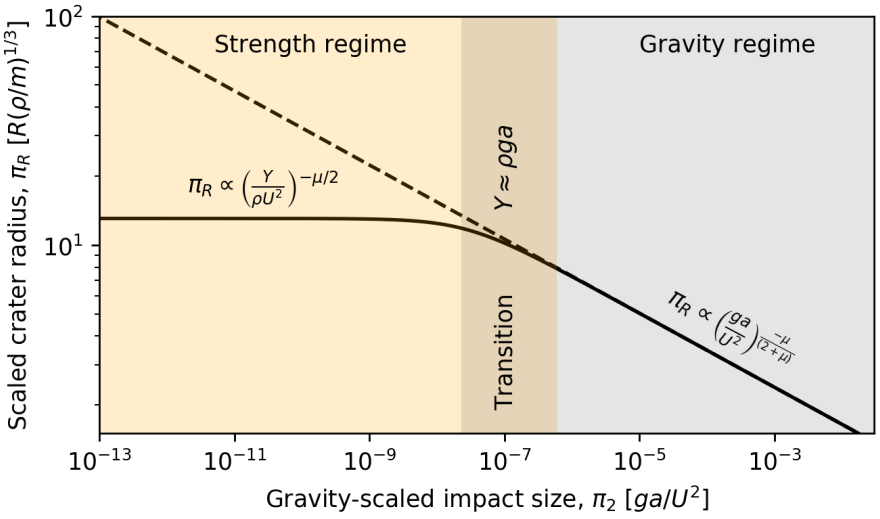

Figure 2.16: Scaled crater radius as a function of the gravity-scaled impact size. The shaded areas represent the different crater formation regimes. In the strength regime, cratering is independent of gravity, while in the gravity regime, the cratering efficiency has a power law decrease with increasing impact size. The transition between the two regimes occurs at $Y \approx \rho ga$. Adapted from Holsapple (1993).

$$R\left(\frac{\rho}{m}\right)^{1/3} = K_{R1}\left\{\frac{ga}{U^2}\left(\frac{\rho}{\delta}\right)^{\frac{(6\nu-2-\mu)}{3\mu}} + \left[K_{R2}\left(\frac{Y}{\rho U^2}\right)\left(\frac{\rho}{\delta}\right)^{\frac{(6\nu-2)}{3\mu}}\right]^{\frac{2+\mu}{2}}\right\}^{\frac{-\mu}{2+\mu}} \tag{2.12}$$

where μ, ν, K_{R1} and K_{R2} are empirically determined constants.

The cratering process occurs in the so-called strength regime (Fig. 2.16) if the dominant resisting force to crater growth is the target's cohesive strength and in this case, the scaling parameters $\pi_3 = \frac{Y}{\rho U^2}$ and $\pi_4 = \frac{\rho}{\delta}$ dictate the cratering efficiency π_R

$$R\left(\frac{\rho}{m}\right)^{1/3} = H_2\left(\frac{\rho}{\delta}\right)^{(1-3\nu)/3}\left(\frac{Y}{\rho U^2}\right)^{-\mu/2} \quad \text{(strength)}. \tag{2.13}$$

On the other hand, if the weight of the excavated material dominates over strength, then the crater forms in the gravity regime (Fig. 2.16) and the crater efficiency is expressed in terms of the $\pi_2 = \frac{ga}{U^2}$ parameter and π_4:

$$R\left(\frac{\rho}{m}\right)^{1/3} = H_1\left(\frac{\rho}{\delta}\right)^{(2+\mu-6\nu)/[3(2+\mu)]}\left(\frac{ga}{U^2}\right)^{-\mu/(2+\mu)} \quad \text{(gravity)}, \tag{2.14}$$

where $H_1 =$ and $H_2 = K_{R1}K_{R2}^{-\mu/2}$ are constants determined from laboratory experiments. Note that in both cases, the exponent in the power-law is a function of the material-dependent velocity exponent μ. When the ratio of the mass densities, π_4, is close to

unity, the density term disappears from the equation. For larger density differences and assuming $\nu \approx 0.4$, the density term is close to 1. To note the the meaning of strength is not well defined. Here Y is the effective 'cratering' strength, which can be different from the quasi-static measures (Holsapple, 1993; Güldemeister et al., 2015). Previous experimental (Poelchau et al., 2013) and numerical (Güldemeister et al., 2015) studies showed that Y can be up to five orders of magnitude below the quasi-static measures, however further studies are needed to understand these discrepancies.

2.5.1 Ejecta scaling relationships

Using the point-source approximation and dimensional analysis, Housen et al. (1983) developed a number of power-law scaling equations that relate properties of ejecta to the initial impact conditions. For instance, in one such ejecta scaling relation, the speed of ejecta normalised by the impactor velocity, v/U, is expressed as a power-law of normalised launch position, x/a, and impactor and target properties (Housen et al., 1983; Housen and Holsapple, 2011):

$$\frac{v(x)}{U} = C_0 \left[\frac{x}{a} \left(\frac{\rho}{\delta} \right)^{\nu} \right]^{-\frac{1}{\mu}} \tag{2.15}$$

where ν and μ are as previously defined, and C_0 is an empirically determined constant. However, laboratory experiments have shown that ejecta velocity distributions deviate from a simple power-law form close to the impact point and near the final crater rim. To address the deviation of ejecta scaling from a simple power law near the crater rim, where the ejection flow is increasingly affected by gravity and strength, ultimately reducing the ejection speed to zero, Housen and Holsapple (2011) proposed a simple empirical modification to Eq. 2.15, such that the ejection velocity drops to zero near the crater edge, at a distance proportional to the crater radius, R:

$$\frac{v(x)}{U} = C_1 \left[\frac{x}{a} \left(\frac{\rho}{\delta} \right)^{\nu} \right]^{-\frac{1}{\mu}} \left(1 - \frac{x}{n_2 R} \right)^{p} \tag{2.16}$$

where C_1 and p are constants determined by fitting the equation to empirical data. The velocity cut-off takes place at $x = n_2 R$, where n_2 is a material dependent constant, but previous studies suggest that it holds a value of approximately 1.0 (Housen and Holsapple, 2011).

The power-law also breaks down for the very fast ejecta, launched at distances $x < n_1 a$, where n_1 is a constant dependent on the projectile shape, material and impact velocity (Housen and Holsapple, 2011). The material below the impactor is driven downwards and does not get ejected, while the material close to the contact zone between the impactor and target is ejected at very low angles, by the 'jetting' process (Yang and Ahrens, 1995). Due to the very high velocities involved, this process is very hard to measure in laboratory based experiments and not enough data is available. Hermalyn and Schultz (2010) performed a series of impact experiments into sand, measuring the early-time high-speed ejecta produced by projectiles of different densities. They found that the projectile density affects the coupling time and the penetration depth. However, the current ejecta model does not account for these effects.

The ejection speed decreases as the launch distance x increases, so Housen and Holsapple (2011) also defines the mass ejected at speeds larger than v, $M(> v)$, as the mass of material $M(< x)$ launched at distances from within x, where

$$\frac{M(< x)}{m} = \frac{3k}{4\pi}\frac{\rho}{\delta}\left[\left(\frac{x}{a}\right)^3 - n_1^3\right]. \tag{2.17}$$

From Eq. (2.15) and Eq. (2.17), the mass ejected at speeds larger than v, $M(> v)$, can be defined in terms of impactor properties as (Housen and Holsapple, 2011)

$$\frac{M(> v)}{m} = \frac{3k}{4\pi} C_1^{3\mu}\left[\frac{v}{U}\left(\frac{\rho}{\delta}\right)^{\frac{3\nu-1}{3\mu}}\right]^{-3\mu}. \tag{2.18}$$

The scaling laws presented here have several more limitations. For very low impact velocities or for very low impactor densities, the final crater diameter is only slightly larger than the projectile. In these scenarios, the size of the coupling zone is comparable to the crater volume and the point-source approximation does not hold (Holsapple and Schmidt, 1987; Housen and Holsapple, 2011). Furthermore, laboratory experiments (Anderson et al., 2004) have shown that a stationary point source is not appropriate for oblique impacts.

2.5.2 Ejecta scaling constants from laboratory experiments and numerical simulations

Numerous past impact experiments have studied the ejecta behaviour in laboratory-scale impacts. Housen and Holsapple (2011) gives a comprehensive summary of ejecta data from the literature, for a variety of target materials.

For example, Gault et al. (1963) recorded the mass-velocity distribution of ejecta from impacts into strong basalt. Housen (1992) recorded the ejecta mass from impacts into two material mixtures, weakly cemented basalt (WCB), and crushed basalt and fly ash. These materials had tensile strengths of <1 MPa and were about 20% porous. Housen and Holsapple (2003) reported ejecta distributions from impacts into mixtures of sand and fly-ash, which were weaker and highly porous (32–96% porosity) and more representative of an asteroid environment. Cintala et al. (1999) and Anderson et al. (2003) conducted impact experiments into sand, for the purpose of measuring ejecta launch position and velocity. These experiments are discussed in Chapter 3.

Housen and Holsapple (2011) used these and a number of other experiments to analyse how the ejecta mass-velocity-launch position distribution depends on impact conditions and target properties. Each experiment presented had a different impactor size, speed or different target properties and they concluded that the ejecta distribution is most sensitive to target properties such as strength and porosity. It is however difficult to quantify the influence of these properties independently from laboratory experiments alone, or to test low cohesion low gravity environments.

Numerical simulations have the advantage over laboratory experiments that a larger range of events, which are more relevant to planetary science can be tested. Such suite of numerical simulations was conducted by Prieur et al. (2017), using iSALE, to quantify the sensitivity of crater size to target porosity and internal friction coefficient. They produced a numerical study of gravity-dominated impact craters under lunar conditions and observed that point-source scaling parameters such as μ or H_2 vary systematically with target porosity and coefficient of internal friction.

Similarly, Luther et al. (2018) used iSALE to conduct a systematic numerical

parameter study of the effects of cohesion, porosity and internal friction coefficient on the angle, speed and mass of ejecta, in the gravity regime. They showed that increasing the target porosity or internal friction coefficient reduces the ejection velocity, while reducing the target cohesion changes the ejecta velocity distribution only close to the crater rim.

2.6 Impacts and collisions in the present Solar System

Although impacts today are much less frequent and less energetic than during the early Solar System, they still occur. Earth is continuously impacted by space debris and small asteroids, and, while large asteroid impacts are very rare (Brown et al., 2002; Bland and Artemieva, 2005), they have the potential to cause severe damage.

The Chelyabinsk event in February 2013 (Popova et al., 2013), when a meteoroid entered Earth's atmosphere and exploded in the vicinity of Chelyabinsk, Russia, raised public awareness of the risks and frequency of such events (Avramenko et al., 2014). The asteroid was only about 20 m in diameter (Artemieva and Shuvalov, 2016), but the damage produced was extensive.

The only other large meteoroid airbust recorded in the last century (in 1908), Tunguska, produced even more extensive damage, flattening approximately 2000 square km of forest (Artemieva and Shuvalov, 2016). The impactor, believed to have been between 30 to 50 m in diameter (Artemieva and Shuvalov, 2016), catastrophically disrupted 6-10 km above Siberia, in Russia, an area with a very low population density. As a result, few casualties were reported, however, the energy produced would have been capable of causing extensive damage and fatalities in a large metropolitan area, such as London or New York.

2.7 Impact hazard and asteroid deflection

The damage associated with Chelyabinsk and Tunguska was caused by a blast wave in the atmosphere generated by an airbust. Neither event produced an impact crater. However, there are more than 190 confirmed impact craters on Earth. One of the most famous such impact craters is perhaps the ≈150 km Chicxulub crater (Morgan et al., 1997, 2016), in the Gulf of Mexico. The impact is estimated to have occurred 66 million years ago, causing catastrophic environmental effects, such as extended darkness, global cooling, or acid rain. The Chicxulub event has been linked to the mass extinction of dinosaurs (Schulte et al., 2010).

Efforts to detect and to asses the dangers of asteroid impacts are led by both Europe, with the NEOShield project (Harris et al., 2013; Perna et al., 2015) and the US, with projects such as the Panoramic Survey Telescope and Rapid Response System (Pan-STARRS) or the Asteroid Terrestrial-impact Last Alert System (ATLAS) (Vereš et al., 2009; Tonry, 2011; Denneau et al., 2013; Landis and Johnson, 2018). Although 90% of Near-Earth objects (NEO) larger than 1 km have been already discovered and do not pose an immediate threat (Fig. 2.17), smaller asteroids are much harder to detect and their discovery rate is considerably lower (Schunová-Lilly et al., 2017). The Chelyabinsk event lowered the asteroid size threshold of what is considered to be a potentially hazardous asteroid, from 1 km to few hundred meters (Micheli et al., 2018), which has prompted efforts to constrain the population of NEOs larger than ≈140 m (Tonry, 2011).

Figure 2.17 shows the number of NEOs discovered and predicted, as a function of size. The top axes shows the expected damage produced by different size objects, while the right-hand axis shows the estimated frequency of such objects impacting Earth. The Chelyabinsk, Tunguska and Chicxulub events are shown for comparison. Asteroids smaller than few meters in diameter would produce no damage or airbusts. Larger asteroids, however, could produce regional or even global damage.

If an asteroid of a few hundred meters is detected in advance to be on an Earth-colliding trajectory, an appropriate action can be taken to deflect its orbit. However,

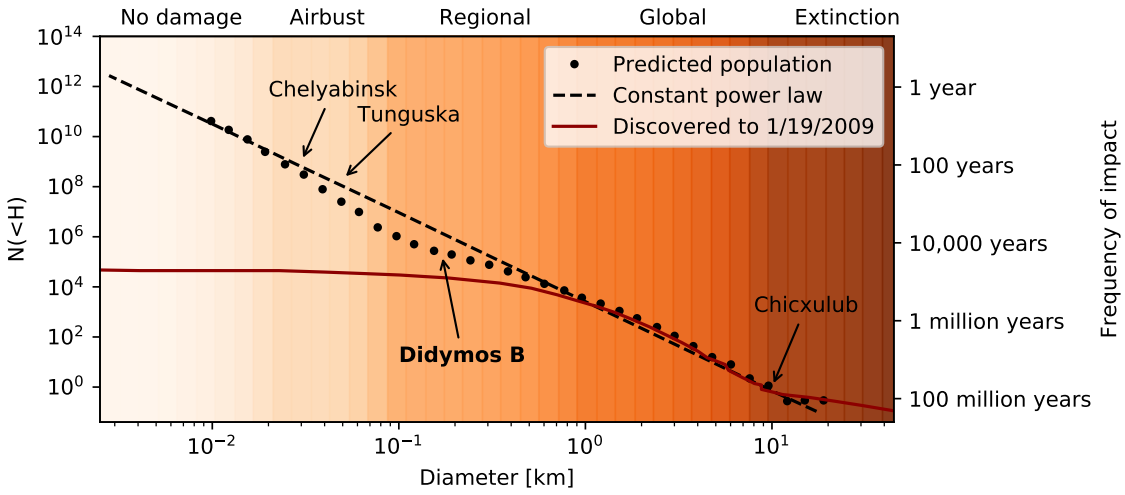

Figure 2.17: Size frequency distribution of the discovered and predicted NEO's population. The cumulative number of near-Earth asteroids, N, brighter than an absolute magnitude of H, as a function of the object diameter. The top exes shows the potential damaged if impacting Earth. The right-hand axes shows an approximate frequency of such objects impacting Earth. The Cheliabinsk, Tunguska and Chicxulub events are plotted for comparison. The DART mission is planning test the deflection of an $\approx$ 160 m in diameter asteroid. Modified from Harris and D'Abramo (2015).

when a new potentially hazardous asteroid is discovered, due to the large uncertainties associated with its orbit, it has a very low probability of impact. The impact probability is only refined after subsequent observations, which in some cases can take years.

Asteroid deflection methods include approaches such as nuclear explosions (Ahrens and Harris, 1992), gravity tractors (Lu and Love, 2005) or kinetic impactors (Melosh et al., 1994). A large factor in deciding what deflection method to use is the time warning time, which here we define as the time between the moment a decision to act is made and the time of impact. Figure 2.18 shows the regimes of applicability of different deflection methods.

2.7.1 Civil defence

As discussed previously, objects smaller than *approx* 20 m in diameter would only produce localised damage and, depending on the warning time, evacuating the area would be the most feasible option.

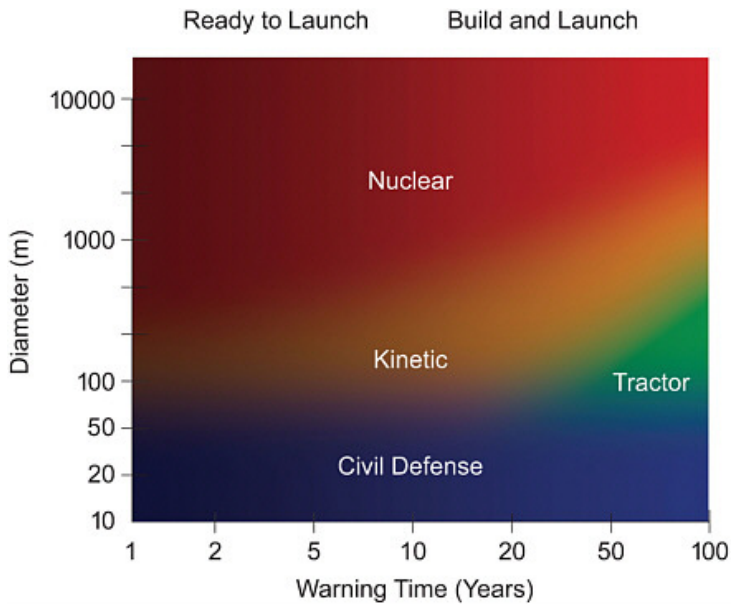

Figure 2.18: Regimes of applicability of four types of mitigation: civil defence, gravity tractor, kinetic and nuclear. The various methods work best for different combinations of asteroid diameters and warning times. For warning times less than 5-10 years, the spacecraft had to be already built and ready to launch. Source: T. Warchocki (2010), NRC report.

2.7.2 Nuclear explosion

A nuclear explosion detonated in the proximity of an asteroid would transmit large amounts of energy to the surface, in the form of neutrons and X-rays, irradiating it. The irradiated material, located in the outer layers of the asteroid, then evaporates, imparting the rest of the asteroid with the necessary impulse for deflection. The nuclear blast approach might be the most effective method of deflection. However, due to the hazards associated with handling nuclear material on Earth, before and during the launch, and due to the many political implications of arming a spacecraft with a nuclear warhead, this would not be the preferred option. Nevertheless, for very large asteroids, larger than about 1 km in diameter, or for very short warning times, a nuclear deflection is probably the only viable option (Figure 2.18).

2.7.3 Gravity tractor

Another deflection method is the gravity tractor. This method uses the gravitational force of the spacecraft to change the trajectory of an incoming asteroid. The gravity tractor

only requires the mass of the asteroid to be known in order to predict the outcome of the deflection, unlike the nuclear explosion mitigation for example, where the shape of the asteroid can influence the outcome (e.g. the shape of the asteroid will determine the area irradiated by the nuclear explosion). This method is however limited by the mass of the spacecraft (or spacecrafts for a combined gravity tractor) and by the warning time. To be efficient, the spacecraft needs to orbit the hazardous asteroid for a long time and fuel issues would need to be considered.

2.7.4 Kinetic impactor

For objects of a few hundred metres in diameter, which are the objects we are most likely to encounter that could cause substantial and widespread damage, the kinetic impactor approach seems to be the most straightforward solution. As the kinetic impactor mitigation is investigated in detail in this thesis, this deflection method is introduced in more detail below.

2.7.5 Kinetic impactor and momentum transfer

In a high velocity impact event the momentum transferred to the asteroid has two components: the momentum that is directly imparted from the impactor, and an additional momentum transferred to the target by the thrust in the opposing direction of crater ejecta that escapes the gravitational attraction of the target body.

The change in linear momentum of the asteroid as a result of the impact, $\Delta\mathbf{p}$, is therefore equal to the impactor momentum $\mathbf{p_{imp}}$ plus the resultant momentum of the escaping ejecta $\mathbf{p_{ej}}$. Assuming that $\mathbf{p_{imp}}$ and $\mathbf{p_{ej}}$ are anti-parallel, which is true for a vertical impact on a planar surface, the magnitude of the momentum change is given by:

$$\Delta\mathbf{p} = \mathbf{p_{imp}} + \mathbf{p_{ej}}, \tag{2.19}$$

$$\Delta\mathbf{p} = \beta\mathbf{p_{imp}} = \beta mU, \tag{2.20}$$

where m is the impactor mass and U is the impactor speed, $\mathbf{p_{ej}}$ is the magnitude of the

ejected momentum in the opposite direction to the impact and β is known as the momentum multiplication factor (Housen and Holsapple, 2011) — a measure of the efficiency of momentum transfer. The ratio of ejecta momentum to the impactor momentum can also be expressed in terms of β,

$$\beta - 1 = \frac{\mathbf{p_{ej}}}{mU}. \tag{2.21}$$

If the ejected momentum makes no contribution to the total imparted momentum $\beta = 1$. $\beta > 2$ implies a larger contribution to the overall momentum from the crater ejecta than the impactor itself (Fig. 2.19). $\beta < 1$ would mean that more material is spalled from the backside of the asteroid than from inside the crater. The momentum imparted by the spalled ejecta from the rear side would work against the momentum from the projectile (Fig. 2.19). While theoretically possible, $\beta < 1$ is considered very unlikely for an asteroid.

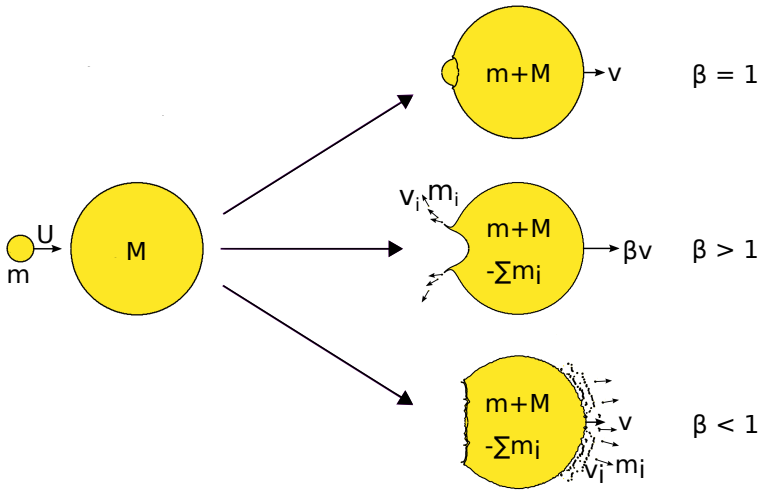

Figure 2.19: Schematic representation of the kinetic impactor mitigation. A projectile with mass m impacts a target with mass M, at a velocity U. The outcome of the impact can be: $\beta = 1$ if the crater produces no ejecta; $\beta > 1$ if the ejecta imparts an additional momentum to the target; $\beta < 1$ if the momentum of the backside spall overcomes the momentuum of the crater ejecta.

2.7.6 Ejecta scaling relationships

The total momentum carried away by the ejecta, which is of paramount importance for impact momentum transfer and asteroid deflection, can be found from integrating the mass dM ejected within a radial range dx for $0 < x < R$. Although this integration must

be done numerically, Cheng et al. (2016) showed that the cumulative ejecta momentum, normalised by the impactor momentum, $\beta - 1$, is well approximated by the analytical expression

$$\beta - 1 \approx \frac{9kC_1}{4\pi\sqrt{2}} \left(\frac{\rho}{\delta}\right)^{\frac{(\mu-\nu)}{\mu}} \frac{\mu}{3\mu - 1} \left[\left(0.74 n_2 \frac{R}{a}\right)^{\frac{(3\mu-1)}{\mu}} - n_1^{\frac{(3\mu-1)}{\mu}} \right]. \tag{2.22}$$

One goal of the present work is to verify whether this expression is also a good approximation of ejected momentum in impact simulations. Note also that, as with the crater size scaling relationships (Eqs. (6.3),(6.4)), the power-law exponents in the crater ejecta scaling relationships are functions of the same material-dependent velocity exponent μ. An accurate characterisation of μ for impacts on asteroid surfaces is therefore crucial for predictions of impact ejecta behaviour and momentum transfer.

2.8 The AIDA collaboration

Whilst a kinetic impactor seems to be the most forward solution to deflect a potentially hazardous asteroid, a technology demonstration has yet to be implemented to gain confidence that NEO deflection techniques work as predicted. In response, the Asteroid Impact and Deflection Assesment (AIDA) (Michel et al., 2016), an international cooperation between Europe and the US, was created. The AIDA collaboration comprises of NASA's DART mission and ESA's Hera mission.

2.8.1 The DART mission

NASA's Double Asteroid Redirection Test (DART) mission aims to impact the smaller component of the 65803 Didymos double asteroid system, 'Didymoon'. DART is planned to launch in 2021 (Cheng et al., 2016), and the impact is planned to occur in October 2022, during the close approach of Didymoon to Earth. The impact is expected to cause a change in the rotation period of the asteroid system of at lease 7 minutes (Cheng et al., 2018), an amount that could be detectable from Earth's observatories (Michel et al., 2016). Because the asteroid system is an eclipsing binary as seen from Earth, the

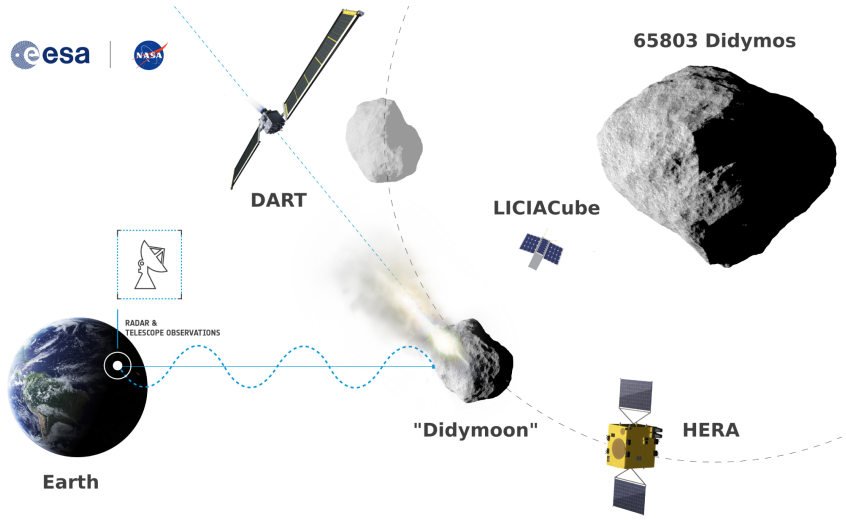

Figure 2.20: Schematic representation of the AIDA collaboration. Source ESA/NASA.

telescopes will be able to monitor the changes in the light curve before and after the impact.

The impacting spacecraft weights about 525 kg (Cheng et al., 2018) and will impact Didymoon's surface at about 7 km/s. The spacecraft bus measures $1.14 \times 1.24 \times 1.32$ m and has 22 m^2 roll-out solar arrays (Figure 2.20).

The DART mission is equipped with a narrow angle visible imager, DRACO, derived from New Horisons LORRI instrument (Cheng et al., 2008). The camera activity is divided into three operational phases. The first phase, the long-range phase, will start about 30 days before the impact. During this phase the Didymos system is not resolvable but the observations will provide useful lightcurve information, complementary to the Earth based measurements. The terminal phase begins about 4 hours before the impact when the spacecraft will use the imager for autonomous navigation. At this time, both the primary and the secondary asteroids are in the frame. The final phase begins about 2 minutes before the impact. The images taken during this phase will have the highest resolution, achieving 50 cm/pixel or better at 17 seconds before the impact. Higher resolution images will be acquired until the impact and the spacecraft will downlink the data to Earth in real time. It is expected that the last image will be acquired just 5 seconds before the impact.

The observations taken by the DRACO imager before the impact will help re-

fine the rotational period of Didymos A, determine the shape of Didymos B, as well as constrain and characterise the geology and properties of the impact location.

2.8.2 LICACube

LICIA (Light Italian Cubesat for Imaging of Asteroids), is the Italian Space Agency (ASI) contribution to the DART mission. The CubeSat will be carried by the DART spacecraft and will be released in the vicinity of the Didymos system, before the impact. LICIACube will be equipped with dual imaging system and propulsion capabilities, which will enable it to perform an autonomous fly-by of the binary Didymos system during the final part of the DART mission, monitoring the crater and the evolution of the ejecta plume and downlinking the images directly to Earth.

The main aims of the CubeSat are to take at least three images of the ejecta plume, over a range of phase angles, take at least three images of the DART impact site with a resolution of 1 m/pixel or better and take at least three images of the non-impacted surface of Didymoon. These sets of images are intended to help determine the motion of the slow ejecta and the density of the ejecta plume, estimate the size and morphology of the DART crater, and estimate of the shape and volume of target asteroid.

2.8.3 The Hera mission

To better understand the target properties of Didymoon, ESA will send a rendezvous mission, Hera (Michel et al., 2018; Cheng et al., 2018), that has a 2024 planned launch and will arrive at Didymoon several years after the DART impact. The Hera spacecraft will be equipped with a camera inherited from the Down mission, the Asteroid Framing Camera, which will provide information about the dynamics and physical characteristics of the system. The spacecraft will also carry a Lidar laser altimeter to measure the shape of the two bodies and constrain their mass, and a thermal imager. In addition, two CubeSats will be dedicated to asteroid characterisation. These measurements will provide detailed characterisation of the Didymoon volume and surface properties, as well as measure the outcome of the DART impact, including the new binary system orbit and

the volume and morphology of the DART impact crater.

2.9 Previous numerical studies of asteroid deflection

Previous work has shown that β and hence the efficiency of momentum transfer in hypervelocity cratering is strongly dependent on the impact speed and the asteroid composition and structure (Cheng et al., 2016; Jutzi and Michel, 2014; Stickle et al., 2015; Syal et al., 2016). Properties such as porosity, internal structure and cohesive strength can vary significantly from one asteroid to another, and without a close approach, these properties cannot be accurately estimated. Numerical simulations allow for a wide range of initial conditions to be used and provide an accurate method to determine the asteroid's response to a DART-scale impact.

Jutzi and Michel (2014) used Smoothed Particle Hydrodynamics (SPH) to investigate DART-scale momentum transfer into porous targets. They modelled a 400 kg aluminium spherical projectile impacting targets with $Y_0 = 100$ kPa and varying micro and macro porosity, at 10 km/s. They found that the amount of porosity in the target changes the momentum transfer efficiency, β, by more than 50%: β decreased from 2.3 for a 15% porous target, to about 1.5 for a 70% porous target (Fig. 2.21). However, they also found that whether using micro-porosity or macro-porosity does not influence the deflection.

Syal et al. (2016) also used an SPH code to simulate impacts into a 500 m asteroid, and tracked the centre of mass of the target after the impact, in order to determine β. They found that the momentum transferred increases with decreasing target cohesion, but that the difference between β for a 1 kPa target and a 100 kPa target was very small (less than 4%). On the other hand, the difference between *beta* for a 100 kPa target and a 1 MPa target was more than 85%. Syal et al. (2016) also investigated the role of porosity on the impact outcome. The β values from impacts into targets with a fixed cohesion ($Y_0 = 1$ kPa and 100 MPa) decreased with increasing target porosity (Fig. 2.21).

Stickle et al. (2015) modelled realistic DART-scale impacts using CTH simulations of the asteroid, as a 300 kg aluminium projectile, impacting a basalt target at about 6 km/s. For a 40% porosity target, they predicted β values between 1 and 2.

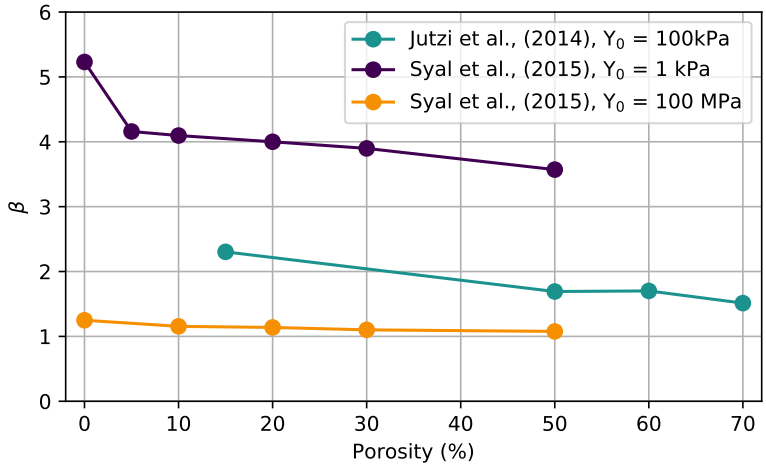

Figure 2.21: Momentum transfer efficiency, β, as a function of porosity from Syal et al. (2016) and Jutzi and Michel (2014) impact simulations studies. In all cases, the impact velocity was 10 km/s.

Past numerical studies have investigated momentum transfer in impacts on very strong targets, therefore one of the aims of this thesis is to investigate momentum transfer in impacts on weaker targets, that are more representative of asteroid surface strength.

2.10 Conclusions

Asteroids are direct remnants of Solar System formation and contain a relatively pristine record of the primordial solar nebula. Even though they represent only a very small fraction of the Solar System mass, they are numerous and have a varied composition, e.g. can be carbonaceous, siliceous or even metal. They also exhibit large variations in surface material properties, such as strength, porosity, internal friction coefficient, or structure.

Impact cratering is probably the most ubiquitous geological process in the Solar System and analysis of crater sizes and morphologies on asteroids can provide a direct diagnosis of the surface material properties and near-surface asteroid structure. Such studies can answer questions about the composition and structures of some of the most unique asteroids, such as asteroid (16) Psyche. In addition, asteroids may pose a future

threat of colliding with Earth. Impact ejecta plays an important role in asteroid deflection and a good understanding of the asteroid deflection mechanisms can help us prevent a future catastrophic event. Past laboratory experiments and numerical simulations have shown that ejecta mass-velocity distribution–and momentum– can vary significantly for the same impact depending on the asteroid properties and structure. However, while there have been several studies on the effects of target properties on crater size and momentum transfer, these focused on impacts in the gravity regime (e.g. Prieur et al., 2017; Luther et al., 2018) or in the strength regime but into strong homogeneous targets (e.g. Jutzi and Michel, 2014; Stickle et al., 2015; Syal et al., 2016). More studies are needed in the strength regime, for weak asteroid targets, to properly characterise momentum transfer and asteroid deflection.

Experimentally derived point-source scaling laws for the crater ejecta mass-velocity-launch position are widely used and they are useful in determining a quick approximation of the ejecta distribution and momentum transferred for known impact conditions. However, these scaling laws are not well constrained for fast ejecta (in the coupling zone) and only apply to vertical impacts.

The main aims of this thesis are therefore to investigate the influence of asteroid surface and subsurface properties and structure, on impact crater size, morphology and ejecta formation, and to expand the current scaling laws to more regimes of applicability (e.g. close to the crater rim for vertical impacts and for oblique impacts).

Chapter 3

Numerical Methods

This chapter introduces the numerical models and the methods used in this thesis. All the numerical simulations described in this thesis were performed using iSALE-2D and -3D, and the results were analysed using pySALEPlot. The chapter begins with a brief description of the iSALE numerical code and of the material models and the $\epsilon - \alpha$ porous-compaction model included in iSALE. The chapter then includes a description of different numerical approaches used in the work, such as ejecta measurements or spatial mesh regridding. The chapter ends with a suite of validation tests of high velocity impacts into different types of sand.

3.1 Shock physics codes

Hydrocodes can be defined as a set of codes designed to solve large deformation, finite strain transient problems that take place over a short period of time. Early hydrocodes did not include strength and they were mostly used to model fluids, but today they have a wider applicability, being used in many scientific areas (Benson, 1992). Codes used to model impact cratering include material models that account for material strength and porosity, and are often referred to as shock physics codes (Pierazzo et al., 2008).

3.2 The iSALE code

The iSALE2D shock physics code is a multi-material, multi-rheology extension of the SALE (Simplified Arbitrary Lagrangian Eulerian) hydrocode (Amsden et al., 1980). The original version of SALE, developed at Los Alamos National Lab, could only model flow of a single, strengthless material, such as Newtonian fluid flow. In later modifications, the code was enhanced to include an elasto-plastic constitutive model, a fragmentation algorithm and several equations of state, including the Tillotson EoS (Tillotson, 1962; Melosh et al., 1992). Ivanov et al. (1997) implemented free surface and material interface tracking in Eulerian mode, and later the Semi-Analytical EoS, ANEOS (Thompson and Lauson, 1972). Ivanov's improved SALE code became known as SALEB, and was capable of simulating impact events (Ivanov and Deutsch, 1999; Ivanov and Artemieva, 2002; Ivanov, 2005). Collins et al. (2002) introduced a wider range of rheologic models to the primarily Lagrangian version of SALE, which was released as SALES-2. Wünnemann and Lange (2002) rewrote large parts of the code to include the improvements developed by Ivanov et al. and extended the code to be able to model a third material (Wünnemann and Ivanov, 2003; Wünnemann et al., 2005). Today, iSALE includes strength models suitable for impacts into geologic targets (Collins et al., 2004) and a porous compaction model, the $\epsilon - \alpha$ model (Wünnemann et al., 2006; Collins et al., 2011). Thomas Davison later developed pySALEPlot, a python and matplotlib library of functions for post-processing iSALE data and producing plots.

3.3 Fundamental equations

In a computational simulation of mechanical deformation, the area under study is divided into a predefined mesh, containing material. To describe the dynamics of a compressible continuous medium, a numerical simulation uses a set of differential equations which describe the conservation of momentum, mass and energy from a macroscopic point of view. There are two fundamental ways of describing the deformation of the continuum:

the Lagrangian description, also known as the material description, where the reference frame moves along with the material; and the Eulerian description, also known as the spatial description, where the reference frame remains fixed as the material moves.

The form of the differential equations solved by a computer code for modelling material dynamics depends on which reference frame is adopted. In the Lagrangian description, the conservation laws take the form:

$$\text{Conservation of Mass} \qquad \frac{D\rho}{Dt} = -\rho\frac{\partial v_i}{\partial x_i} \tag{3.1}$$

$$\text{Conservation of Momentum} \qquad \rho\frac{Dv_i}{Dt} = F_i + \frac{\partial \sigma_{ji}}{\partial x_j} \tag{3.2}$$

$$\text{Conservation of Energy} \qquad \frac{DE}{Dt} = -\frac{P}{\rho}\frac{\partial v_i}{\partial x_i} + \frac{1}{\rho}s_{ij}\dot{\epsilon}'_{ij} \tag{3.3}$$

where v_i is the velocity, ρ is the material density, x is the position in space, t is time, E is the specific internal energy, σ_{ij} is the stress tensor, which is composed of a hydrostatic part, the pressure P, and a deviatoric part, s_{ij}. F_i is the external body force per unit volume, and $\dot{\epsilon}'_{ij}$ is the deviatoric strainrate. The subscripts represent standard tensorial notation for the coordinate directions and summation over repeated indices is implied.

In the Eulerian description, the equations take the form:

$$\text{Conservation of Mass} \qquad \frac{\partial \rho}{\partial t} + v_i\frac{\partial \rho}{\partial x_i} = -\rho\frac{\partial v_i}{\partial x_i} \tag{3.4}$$

$$\text{Conservation of Momentum} \qquad \frac{\partial \rho v_i}{\partial t} = F_i + \frac{\partial \sigma_{ji}}{\partial x_j} \tag{3.5}$$

$$\text{Conservation of Energy} \qquad \frac{\partial \rho E}{\partial t} = -P\frac{\partial v_i}{\partial x_i} + s_{ij}\dot{\epsilon}'_{ij}. \tag{3.6}$$

The iSALE shock physics code has the ability to solve these equations in an arbitrary reference frame, which means that it can use either a Lagrangian description, a Eulerian description or some other reference frame. To achieve this, iSALE uses a combination of the Lagrangian and Eulerian descriptions, known as the Arbitrary Lagrangian Eulerian (ALE) solution. For the work presented in this thesis, iSALE was used in the Eulerian mode. The solution algorithm for this model first solves the system of equations in a Lagrangian reference frame, then translates the solution into the Eulerian reference frame.

The conservation equations represent the material as a continuum, however a computer has a finite memory allocation. To apply the equations describes above, a computer model divides the spatial domain into a set of nodes on a grid. In iSALE, the spatial domain is divided into rectangular cells, with 4 corners in 2D or 8 corners in 3D. Physical properties such as pressure, density, energy or mass are known at the centre of each cell, while other quantities, such as velocity and position are known at the cell vertices.

In the Lagrangian description the grid points are attached to the material and move with the material velocity. Fields such as pressure, temperature or density are recorded as the time advances in the continuum. In the Eulerian description, the velocity, pressure, temperature etc. are measured at fixed points on the grid, as time progresses. While the grid points remain fixed with time, mass, energy and momentum flow from one cell to another.

For example, the conservation of mass equation is given in both its Lagrangian and Eulerian forms:

$$\text{Lagrangian} \qquad \frac{D\rho}{Dt} = -\rho\frac{\partial v_i}{\partial x_i} \tag{3.7}$$

$$\text{Eulerian} \qquad \frac{\partial\rho}{\partial t} + v_i\frac{\partial\rho}{\partial x_i} = -\rho\frac{\partial v_i}{\partial x_i} \tag{3.8}$$

From a numerical perspective, the two descriptions of conservation of mass are linked by the relationship between the Lagrangian and Eulerian of conservation of mass. The density in a cell is $\rho = M/V$, where M is the mass in the cell and V is the cell volume. In the Lagrangian description, mass in the cell remains constant and the changes in cell density are due to cell deformation over time, and the derivative is $\frac{D\rho}{Dt}$. In the Eulerian description, the density in a cell is determined by the mass flowing in and out of the cell, during a time-step Δt. The spatial derivative of mass per unit volume is $\frac{\partial\rho}{\partial t}$. The difference between the derivatives from the two descriptions is a term that describes the advection of mass per unit volume, $v_i\frac{\partial\rho}{\partial x_i}$, known as the advective derivative, such that:

$$\frac{D\rho}{Dt} = \frac{\partial\rho}{\partial t} + v_i\frac{\partial\rho}{\partial x_i}. \tag{3.9}$$

If the Lagrangian derivative is known (or solved for), the Eulerian derivative can

be found by accounting for the advective derivative. This can be achieved by considering the first-order forward-euler time-discretisation of the conservation of mass (Eqs.(3.7) and (3.8)). The Lagrangian equation discretised in time is:

$$^{L}\rho_{n+1} = \rho_n - \rho_n F(v_i, x_i)\Delta t \tag{3.10}$$

where ρ_n is the density of a computational cell at the beginning of a short interval of time Δt, $F(v_i, x_i)$ is a discrete version of the divergence operator over the cell and $^{L}\rho_{n+1}$ is the new density of the same cell at the end of the time interval. Density is given the superscript L to signify that this is the density of the material in the Lagrangian reference frame. A similar discretisation of the Eulerian equation is:

$$^{E}\rho_{n+1} = \rho_n - \rho_n F(v_i, x_i)\Delta t - v_i G(\rho_i, x_i)\Delta t \tag{3.11}$$

where $v_i G(\rho_i, x_i)$ is a discrete version of the advective derivative in the cell and $^{E}\rho_{n+1}$ (with the superscript E to signify Eulerian) is the updated density in the Eulerian reference frame. In both equations ρ_n was assumed to be the same, so that the time interval begins with the same initial conditions (same volume of material in space). Combining these discrete equations, allows for the formulation of a two-step approach to derive an Eulerian solution: first solve Eq. (3.10) to find the Lagrangian solution and then compute

$$^{E}\rho_{n+1} = {}^{L}\rho_{n+1} - v_i G(\rho_i, x_i)\Delta t \tag{3.12}$$

to account for the advection of mass and determine the Eulerian solution. By modifying the advective derivative, an entire suite of solutions between a Lagrangian and Eulerian solution can be defined:

$$^{ALE}\rho_{n+1} = {}^{L}\rho_{n+1} - {}^{R}v_i.G(\rho_i, x_i)\Delta t \tag{3.13}$$

where $^{ALE}\rho_{n+1}$ is the new density in an arbitrary Lagrangian Eulerian reference frame and $^{R}v_i$ is the relative velocity between the material velocity v_i and the computational grid velocity $^{G}v_i$, $^{R}v_i = v_i - {}^{G}v_i$. If the grid velocity is the same as the material velocity $^{R}v_i = 0$ and the Lagrangian solution is recovered (Eq. (3.10)); if the grid velocity is zero for a fixed reference frame, $^{R}v_i = v_i$, and the Eulerian solution is recovered (Eq. (3.12)). On

the other hand, the grid velocity can also be defined using some other criteria to provide a solution in an arbitrary reference frame that is neither Lagrangian nor Eulerian.

In addition to the conservation equations, two more equations are required to solve all the unknown variables. The fourth equation, the equation of state (EoS), relates the pressure to deformation (or volume) and internal energy

$$\text{Equation of state:} \quad P = P(V, E). \tag{3.14}$$

The EoS is material specific and is determined from the thermodynamic properties of each material during high-strain laboratory experiments. A more detailed discussion of specific EoS can be found in Section 3.6.1.

The final equation is the constitutive model (or strength model), which describes the effect of deformation (the stress required to withstand deformation), σ_{ij}, as a function of a combination of strain ϵ_{ij}, strain rate, $\dot{\epsilon}'_{ij}$, pressure, P, energy, E, temperature, T, or damage, D:

$$\text{Constitutive equation:} \quad \sigma_{ij} = f(\epsilon_{ij}, \dot{\epsilon}_{ij}, E, D). \tag{3.15}$$

3.4 The Lagrangian and Eulerian description

3.4.1 The Lagrangian description

In the Lagrangian description each body is defined at the start of the calculation and is discretised in the form of a body-fitted mesh. Each element of the mesh has a volume and it can only contain one material. As the numerical simulation progresses, external forces cause the mesh to deform. The same mass of material as in the initial state remains associated with each cell for the whole duration of the simulation. Changes in a cell's volume cause density changes in that respective cell. Figure 3.1a shows one moment during crater formation from a numerical simulation using the Lagrangian description. The cells close to the impact point are distorted while the cells away from the growing cavity are less affected. The Lagrangian reference frame is very efficient and accurate for many dynamics problems, however problems appear when the mesh experiences extreme

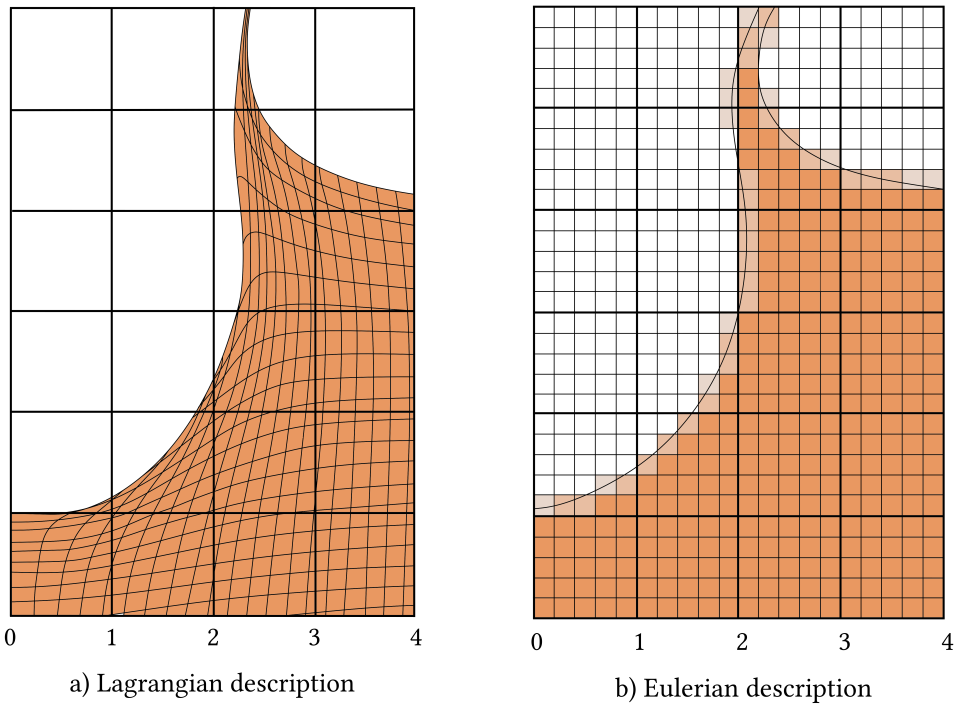

Figure 3.1: Schematic representation of the (a) Lagrangian and (b) Eulerian schemes for numerical impact simulations. (a) In the Lagrangian description, the computational mesh moves with the material. (b) In the Eulerian description, the material flows through the mesh cells. Mid-colour cells at the boundary between the target and void are partially filled cells. Adapted from Collins et al. (2012).

deformations. In such cases, the mesh becomes so distorted that aberration, such as negative cell volumes, can occur. Moreover, the time-step —which depends on the cell size— becomes very small, which can effectively terminate the simulation.

3.4.2 The Eulerian description

The Eulerian description uses a grid that remains stationary for the duration of the simulation. The material flows through the mesh, so it is not affected by extreme deformations. Unlike the Lagrangian description, each cell in the grid can contain more than one material. As a result, the material needs to be transported from one cell to another. Eulerian simulations typically need a larger grid to represent the same problem as a Lagrangian simulation, which require more computational memory. Figure 3.1b shows the same moment during crater formation from a numerical simulation using the Eulerian description. The mid-colour cells at the boundary between the target and the void are

cells that are only partially filled by material. This introduces problems associated with how to treat material.

Impact calculations involve high material deformations, making the Eulerian description preferable over the Lagrangian description. Therefore the87 numerical simulations presented in this thesis use iSALE in Eulerian mode, and simulate a spherical object impacting a planar target, which uses cylindrical coordinates in two-dimensions and Cartesian coordinates in three-dimensions.

3.5 Spatial and temporal discretisation of the continuum model

iSALE-2D can employ either cartesian (x-y) or cylindrical (r-z) coordinates. In 2D cylindrical coordinates, the left boundary is the axis of symmetry, about which the mesh is rotated. The computational mesh contains a high-resolution domain of equally-spaced cells and user defined sizes (Δx, Δy).

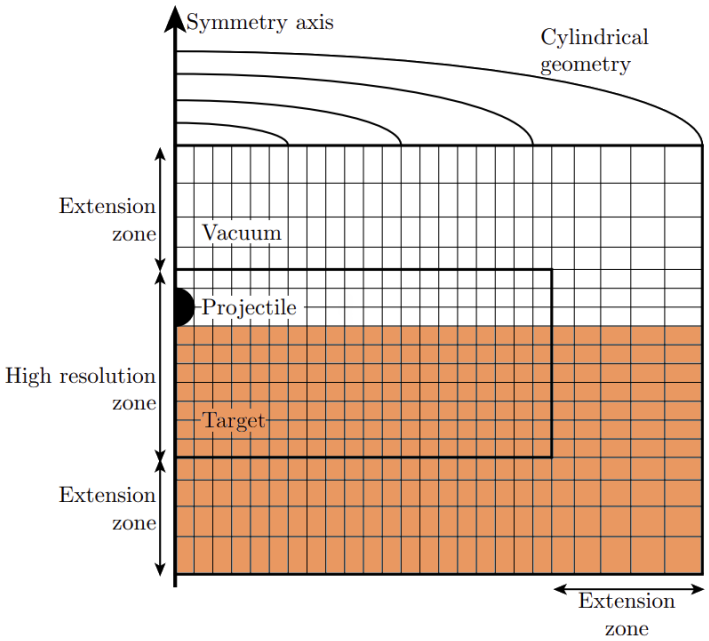

Figure 3.2: Schematic representation of the iSALE-2D mesh geometry. The inner area of the mesh represents the high-resolution zone. To the top, bottom and the right of the high-resolution zone there are added extension zones. In two dimensional simulations, the mesh is rotated around the axis of symmetry. Adapted from Davison (2008) and Wünnemann and Lange (2002).

Extension zones can be added to the high-resolution domain (HRD) to efficiently increase the mesh size. The extension zones have a proportionally increasing cell size that follows a geometric progression, compared to the high-resolution domain. The extension zones are useful to simulate the boundaries of the computational domain further away from the area of interest (e.g. the impact site), without massively increasing the computational cost. Figure 3.2 shows a schematic representation of the iSALE-2D mesh geometry

iSALE-3D employs cartesian coordinates (x-y-z). The computational domain is modelled as a half-space, with a symmetry axis along the horizontal component of the projectile velocity, in the x-z plane. Modelling only half the domain helps reduce the computational cost. Similar to iSALE-2D, extension zones can be added in all directions, except in the direction of the symmetry plane. Note that in iSALE-3D the coordinate system is x-y-z, with the z component along the vertical, which is different from iSALE-2D. Figure 3.3 shows the schematic representation of iSALE-2D and iSALE-3D domains. These coordinate systems have been used throughout this thesis to plot the simulation domain.

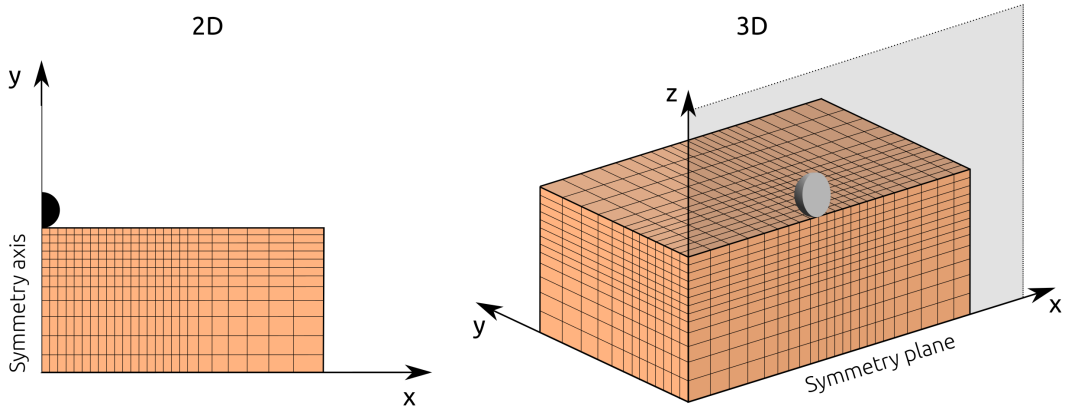

Figure 3.3: Schematic representation of the iSALE-2D and iSALE-3D mesh geometry.

iSALE uses an explicit forward euler time-step integration, explicit approach, which means that new cell values are calculated from known values at the current time. To remain stable, no information can propagate over an entire cell Δx, in a time-step Δt, known as the Courant-Friedrichs-Levy (CFL) condition. In practice, in iSALE a more

restrictive condition is applied, where no information can propagate more than 20% of the cell. The maximum time-step in the simulation must therefore be:

$$\text{Lagrangian:} \quad \Delta t \leq 0.2\frac{\Delta x}{c}, \tag{3.16}$$

$$\text{Eulerian:} \quad \Delta t \leq 0.2\frac{\Delta x}{c + |v|}, \tag{3.17}$$

where c is the sound speed in the material and v is the material velocity.

3.5.1 Lagrangian tracer particles

A major drawback of using the Eulerian description in numerical calculations of impacts is that the material flows across cell boundaries, making it difficult to track the movement and thermodynamic history of material. Therefore, only the histories of the state at a fixed point can be recorded, whereas in the Lagrangian description material history is easily recorded through time.

To overcome this limitation, iSALE uses tracers (Pierazzo et al., 1997; Pierazzo and Melosh, 2000; Ivanov and Artemieva, 2002) to record material histories. By default the tracers are placed in every cell in the high-resolution domain at the beginning of the simulation. As the simulations progresses, the tracers move through the mesh using the interpolated velocity at their current position. The tracers are able to track certain material physical parameters, such as pressure, temperature, velocity, distension or volumetric strain. In the work presented in this thesis, tracers are used to track the properties and trajectories of the ejected particles (Chapter 4 and 5) and determine peak shock pressures and temperatures experienced by the impactor and the target material (Chapter 6).

3.6 Material models

3.6.1 Equation of state (EoS)

An Equation of State (EoS) is an equation or set of equations (or a table) that relates three thermodynamic variables, e.g. pressure, P, density, ρ and energy, E. It connects the theoretical predictions of microstructural models to experimental observations and is

used to study material behaviour. For example, the ideal gas EoS relates the pressure to the specific volume and temperature. If two of these variables are known values, the third can be found. There are two types of EoS: complete and incomplete. A complete EoS is capable of describing the thermodynamic state of a material while the incomplete EoS requires an additional equation. The EoS used in shock physics are usually incomplete and relate stress to deformation and to internal energy or temperature. There is no theory that predicts the behaviour of a material from its atomic constituents and as a result, laboratory experiments, usually incident plate impact experiments, are used to calibrate the EoS.

3.6.2 Tillotson EoS

The Tillotson EoS represents a simple EoS model that approximates phase change processes in low and high pressure regions. It allows the prediction of the shocked and release phases of materials under high velocity impact conditions (Melosh, 1989). The Tillotson EoS was initially derived for hypervelocity impacts into metals (Tillotson, 1962), but today it is widely used for high velocity planetary impact calculations for many materials. The original model, which was developed in the early 1960's, included separate regions for compression (high pressures) and expansion (low pressures).

The Tillotson EoS takes two different forms. One form is valid when the material is cold or compressed to a high density, higher than the material's initial density, ρ_0, while the other form applies when the material is hot and extended to lower density. In the compression region ($\rho \geq \rho_0$) and when the energy density is less than the incipient vaporisation energy ($E < E_{iv}$), the pressure is

$$P = \left[a + \frac{b}{(E/(E_0\eta^2) + 1)}\right] \rho E + A(\eta - 1) + B(\eta - 1)^2, \tag{3.18}$$

where $\eta = \rho/\rho_0$, E is the specific internal energy and a, b, A, B and E_0[a] are material specific, experimentally derived Tillotson parameters. This expression for pressure is also valid for cold expanded state, where the specific internal energy is lower than the energy of incipient vaporisation ($E < E_{iv}$).

[a] E_0 is not the initial internal energy, but a parameter which is often similar to the vaporisation energy.

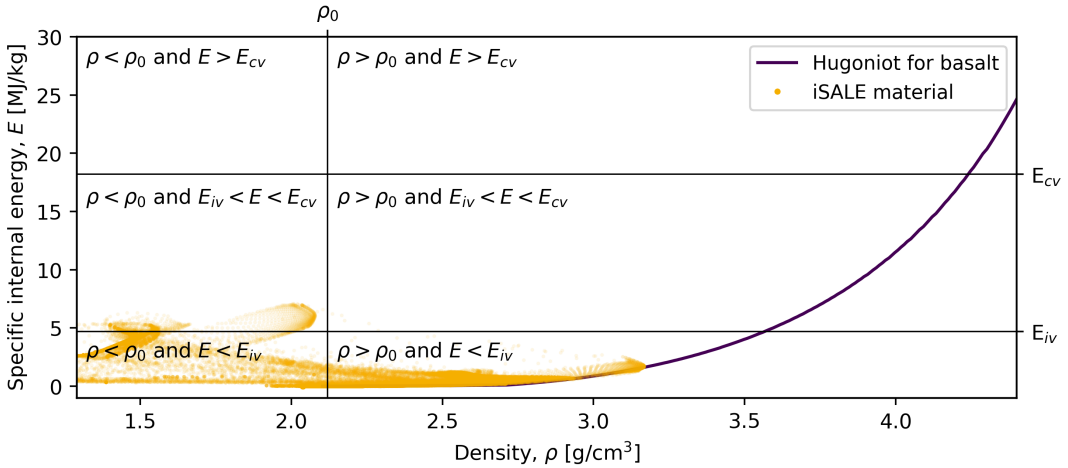

Figure 3.4: Density – Specific internal energy space for Tillotson EoS. Most of the material from an iSALE simulation of an impact into a 20% porous basalt target has a specific internal energy less than the incipient vaporisation energy for basalt ($E < E_{iv}$).

When the material is expanded ($\rho/\rho_0 \leq 1$) and the internal energy exceeds the energy of complete vaporisation ($E > E_{cv}$), the pressure takes the form (Melosh, 1989):

$$P = \alpha + \left[\frac{b}{[E/(E_0\eta^2 + 1]} + A(\eta - 1)e^{-\beta[(1-\eta)/\eta]}\right] e^{-\alpha[(1-\eta)/\eta]^2}, \tag{3.19}$$

where α and β are constants. When $\rho = \rho_0$, the pressure defined by Eq. (3.19) and its first derivative are continuous to Eq. (3.18). Problems with the Tillotson EoS appear in the partial vaporisation regime, where the material is expanded ($\rho/\rho_0 < 1$) and the internal energy is $E_{iv} < E < E_{cv}$. In this region, the pressure is calculated from both the compression form, P_c (Eq. (3.18)), and the expansion form, P_e (Eq. (3.19)), creating a smooth transition between the two:

$$P = \frac{(E - E_{iv})\, P_e - (E_{cv} - E)\, P_c}{E_{cv} - E_{iv}}. \tag{3.20}$$

While the Tillotson EoS is a relatively simple model, it is not always thermodynamically consistent. One main limitation is its inability to accurately represent the pressure in a two-phase region, for example when gas and liquid coexist (Melosh, 1989). In this thesis, the Tillotson EoS was used to represent the porous basalt targets in Chapters 4 and 5. Figure 3.4 shows the different regimes described by the Tillotson EoS in the density – specific internal energy space. The Hugoniot for basalt and cell data from an iSALE simulation of an impact into a 20% porous target were plotted for comparison.

For clarity, the iSALE data was sampled over time during the crater formation (every 10 time-steps). Due to the impact conditions used in this work (e.g. low impact velocity) most of the simulation data resides in the region where $E < E_{iv}$. As mentioned, the Tillotson EoS is not accurate in the partial vaporisation regime, however only a very small amount of the simulated material is in this regime.

Table 3.1 lists the Tillotson EoS input parameters for a series of materials used in this work.

Table 3.1: Tillotson EoS input parameters. Tillotson parameters α and β were set to 5 for all materials.

Material	ρ_0 (g/cm^3)	a	b	A (GPa)	B (GPa)	E_0 (MJ/kg)	E_{iv} (MJ/kg)	E_{cv} (MJ/kg)
Aluminium[a]	2.7	0.5	1.63	75	65	5.0	3.0	13.9
Iron[a]	7.8	0.5	1.50	128	105	9.5	2.4	8.67
Basalt[b]	2.65	0.5	1.50	53	53	4.9	4.7	18.2

[a] Tillotson (1962).
[b] Benz and Asphaug (1999).

3.6.3 ANEOS EoS

The ANalytical Equation Of State or ANEOS (Thompson and Lauson, 1974; Melosh, 2007) is a semi-analytical EoS model designed to use different physical approximations and equations in different domains of validity. Originally, ANEOS used tables to describe pressure, temperature and density in the regions where experimentally derived data existed, and analytical extensions for regions of density and temperature not covered by the tables. Due to the difficulties of locating phase boundaries in a tabular EoS, ANEOS was further improved to use analytic functions throughout.

Unlike Tillotson, ANEOS is guaranteed to be thermodynamically consistent, as the pressure, temperature and density are derived from Helmholtz free energy[b]. A detailed description of the analytical extensions used by ANEOS is given by Melosh (2007). Coupling the ANEOS codes to a shock physics code is computationally expensive. For iSALE simulations, ANEOS is used to construct EoS tables for specific materials, which are then imported into the code. The iSALE simulations presented in this work used the

[b] Helmholtz free energy = the work obtained from an isothermal and isochoric system (F≡ U-TS)

ANEOS tables for basalt (Pierazzo et al., 2005), dunite (Benz and Asphaug, 1999) and iron (Ivanov, 2000; unpublished).

3.6.4 Tillotson EoS vs ANEOS EoS

The ANEOS EoS provides a more realistic representation of the material behaviour over a large range of conditions, however, due to its simpler form, the Tillotson EoS is sometimes preferred. Figure 3.5a shows the pressure-specific volume ($P-V$) Tillotson and ANEOS Hugoniot for a non-porous basalt target. Shock data from laboratory experiments from Ahrens and Gregson (1964), Jones et al. (1968), Van Thiel (1977) and Nakazawa et al. (1997) is plotted for comparison. To account for high pressure phase changes for several minerals in basalt, the ANEOS EoS includes an artificial phase transition. In the tabular version of basalt ANEOS, this is represented as a significant density jump at the solid-solid phase transition, at about 5 GPa. However, in reality, the shock and release behaviour is significantly more complex than assumed by ANEOS. The Tillotson EoS approximates the behaviour accurately at low pressures, while the material at high pressures is not well represented. However for the impact scenarios considered in this thesis, only the low pressure region is of interest. In this region, the material behaviour is well represented by both the Tillotson and the ANEOS EoS.

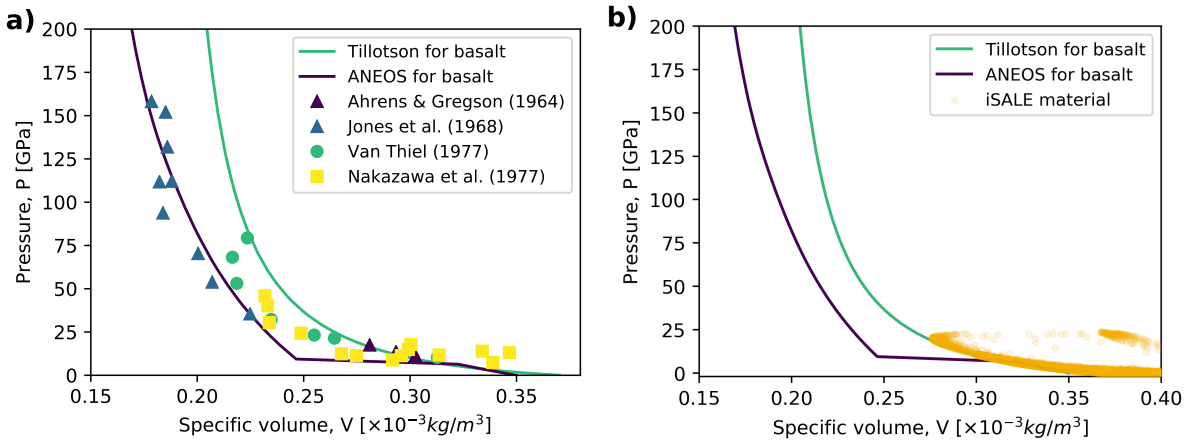

Figure 3.5: a) Tillotson and ANEOS Hugoniot for an impact into a non-porous basalt target in the pressure–specificvolume (P-V) space compared to shock data from Ahrens and Gregson (1964), Jones et al. (1968), Van Thiel (1977) and Nakazawa et al. (1997). b) iSALE simulation data from an impact into a non-porous basalt target compared to the Tillotson and ANEOS Hugoniot.

Figure 3.5b shows the Tillotson and ANEOS Hugoniot for a non-porous basalt target. Also shown are specific volumes and pressures experienced by material in an iSALE simulation of a porous aluminium projectile striking a non-porous basalt target at 7 km/s. The maximum pressure experienced by the target material is less than 10 GPa.

In numerical simulations, depending on the simulated problem, using the Tillotson EoS can be significantly less computationally expensive than using the ANEOS EoS and produce similar results. For example, Figure 3.6a shows the pressure-volume (P-V) Tillotson and ANEOS Hugoniot for a 20% porous basalt target. At high pressures, the two curves exhibit very different behaviour. The kink in the ANEOS curve at high pressure represents a solid-solid phase transition, which is not included in the Tillotson EoS. Similarly, at high particle velocities, the Tillotson EoS and the ANEOS EoS plot parallel to each other Figure 3.6b.

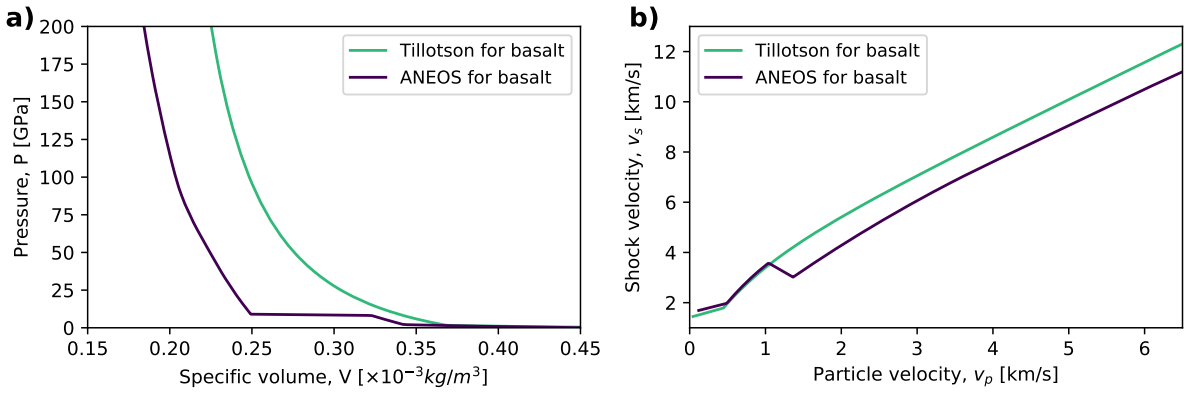

Figure 3.6: Tillotson and ANEOS Hugoniot for a 7 km/s impact into a 20% porous basalt tagert. a) Pressure-volume (P-V) Hugoniot. b) Shock velocity - particle velocity (v_s–v_p) Hugoniot.

Although the Hugoniot is different at high pressures and high particle velocities, for impacts at speeds typical of asteroid-asteroid collision, most of the target material experiences shock pressures of less than 10 GPa and particle velocities of less than 1 km/s, so using the Tillotson EoS is a good enough approximation of the basalt target behaviour. Figure 3.7a and b show the crater volume and the ejecta momentum from the same 7 km/s impact into a 20% basalt target, modelled using the Tillotson EoS and the ANEOS EoS. In this scenario, the difference in crater volume between the two simulations was less than 4%, while the difference in ejecta momentum between the two was less than

6%. However, the simulation using the Tillotson EoS took about 10% less time to run.

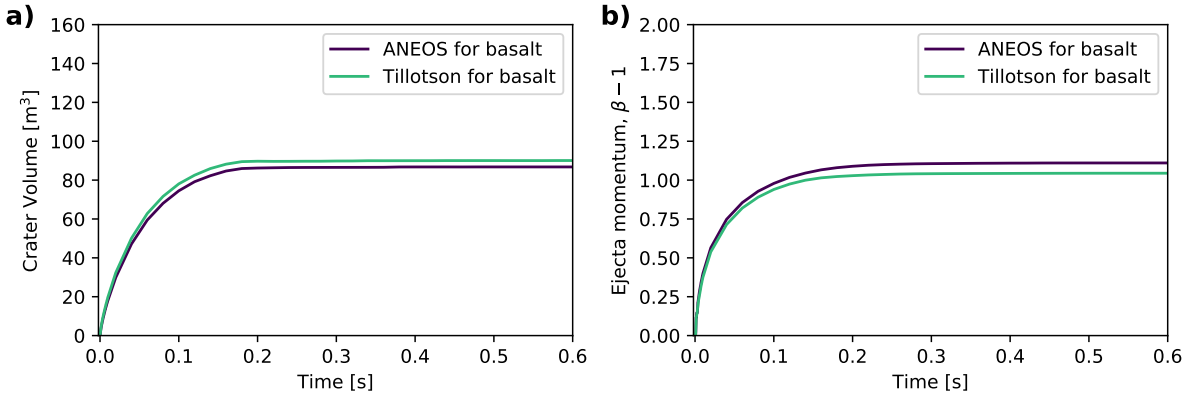

Figure 3.7: Crater growth for a spherical impact, at 7 km/s, into a 20% porous basalt target, modelled using the ANEOS EoS and the Tillotson EoS. a) Crater volume; b) Total ejecta momentum ($\beta - 1$).

3.6.5 Strength models

Materials under high-velocity impact conditions experience extremely high stress levels. As the shock wave travels away from the impact zone, it decays and separates into an elastic and a plastic deforming wave. The material has a different response to the two waves. When the material is engulfed by an elastic wave, the local stress is less than the material strength and deformation is reversible. On the other hand, when the material is engulfed by a plastic wave, the local stresses exceed the material strength and deformation occurs permanently.

In order to obtain a realistic solution to an impact into an asteroid surface, an EoS alone is not enough to describe the material response to stress and strength models have to be considered. Strength models are a set of equations that define the relation between stress, σ, strain, ϵ, strain rate, $\dot{\epsilon}$, pressure, P and internal energy or temperature, T. They can also define the onset of fracture (or damage), D,

$$\sigma_{ij} = f(\epsilon_{ij}, \dot{\epsilon}_{ij}, T, D). \tag{3.21}$$

Stress is measured by a symmetric tensor, which has six independent components in three dimensions. In iSALE, in each cell the square root of the second invariant of the

deviatoric stress tensor, J_2, is compared against the yield strength in that cell. J_2 can be written as

$$J_2 = \frac{1}{6}\left[(\sigma_1 - \sigma_2)^2 + (\sigma_2 - \sigma_3)^2 + (\sigma_3 - \sigma_1)^2\right], \tag{3.22}$$

where σ_1, σ_2 and σ_3 are principal stresses. If $\sqrt{J_2} > Y$, then shear failure occurs and each term in the stress tensor is reduced so that stress state does not exceed the yield envelope. In iSALE, the updated elastic deviatoric stress components are multiplied by the factor $Y/\sqrt{J_2}$ (Collins et al., 2016).

von Mises

The simplest strength model implemented in iSALE is the von Mises model, which was initially developed for ductile materials. The EoS assumes that the yield stress, Y, has a constant value, Y_0:

$$Y = Y_0. \tag{3.23}$$

In this work, the von Mises strength model was used to simulate the impactor material in the 3D simulations described in Chapter 4.

Johnson-Cook

The Johnson-Cook model is a particular type of von Mises strength model. Developed by Johnson and Cook using experimental data (Johnson and Cook, 1983), the model takes into account strain hardening, rate hardening and thermal softening often exhibited by metallic materials. In this case, yield stress is defined as:

$$Y = \left(A + B\epsilon^N\right)\left(1 + C\ln\dot{\epsilon}\right)\left[1 - \left(\frac{T - T_{ref}}{T_m - T_{ref}}\right)^M\right], \tag{3.24}$$

where ϵ is the equivalent plastic strain, $\dot{\epsilon}$ is the strain rate and T is the temperature. A, B, c, n and m are material specific constants.

The Johnson Cook strength model is commonly used to model impacts into ductile targets, such as aluminium or iron. In this work the Johnson Cook model was used to simulate the aluminium projectiles in Chapters 4 and 5, and the iron targets in Chapter 6. Further discussion on the strain rate dependency in impact cratering simulations into iron targets can be found in Chapter 6.

Drucker-Prager

The Drucker-Prager model is a linear pressure-dependent strength model, mainly used for modelling granular materials.

$$Y = min(Y_0 + fP, Y_m) \tag{3.25}$$

where f is the coefficient of internal friction of the material, P is the pressure, Y_0 is the cohesion (yield strength at zero pressure) and Y_m is the limiting strength at high pressure. In this work, the Drucker-Prager model is used to model impacts into sand, later in this chapter.

LUND

The LUND model in iSALE is a simple pressure-dependent strength model typical of geologic materials (Lundborg, 1967; Collins et al., 2004), which asymptotes to a certain strength at high pressure and is not dependent on strain or damage. The Lundborg strength model defines the yield strength as

$$Y = Y_{d0} + \frac{fP}{1 + fP/(Y_{dm} - Y_{d0})}, \tag{3.26}$$

where P is pressure, f is the coefficient of internal friction and Y_{dm} is the limiting strength for damaged material, at high pressure. Figure 3.8a) shows the pressure as a function of shear strength as described by the Drucker-Prager and LUND models. The LUND model was used here to model regolith-like materials.

ROCK

The ROCK model in iSALE (Collins et al., 2004) is a pressure and damage dependent strength model that describes the behaviour of rock like materials. ROCK is a more complex model than Drucker-Prager or LUND, in which strength is reduced as strain accumulates. The ROCK strength model defines the yield strength as

$$Y = Y_d D + Y_i(1 - D), \tag{3.27}$$

where D is a scalar measure of damage, which is itself a function of accumulated plastic strain.

The behaviour of strength in rocks and soils is more complex than the strength in metals. In iSALE, a damage parameter, D, is used to define the extent of rock fracturing (Collins et al., 2004). This parameter varies between 0 for an intact, undamaged rock, to 1, for a completely fractured, damaged rock. Damaged rock has a much lower strength the intact rock. The work in this thesis used the Ivanov damage model, which prescribes the damage, D, as a function of plastic strain:

$$D = min\left(\frac{\epsilon_p}{\epsilon_f}, 1\right), \tag{3.28}$$

where ϵ_p is the invariant measure of the accumulated plastic strain and ϵ_f is the plastic strain at failure. In this model ϵ_f is defined as a function of pressure as:

$$\epsilon_f = max\left(\epsilon_{fb}, B(P - p_c)\right) \tag{3.29}$$

where ϵ_{fb} is a low minimum failure strain for low pressure states and B and p_c are constants. In iSALE the damage can also be modelled using the Collins model (Collins et al., 2004). The Collins damage model is more complex and accounts for both tensile and shear failure, while the Ivanov damage model only accounts for the shear failure. In this work the Ivanov damage model was preferred over the Collins damage model due to its simpler form.

The damaged material strength, Y_d, is defined by a Drucker-Prager relationship:

$$Y_d = min(Y_{d0} + fP, Y_{dm}). \tag{3.30}$$

The intact material strength, Y_i, is defined by smooth approximation to experimental data first defined by Lundborg (1967):

$$Y_i = Y_{i0} + \frac{f_i p}{1 + f_i P/(Y_{im} - Y_{i0})}, \tag{3.31}$$

where f_i is the coefficient of internal friction for intact material, Y_{im} is the limiting strength at high pressure for intact material, f is the coefficient of internal friction for damaged material and Y_{dm} is the limiting strength for damaged material at high pressure (Fig. 3.8b).

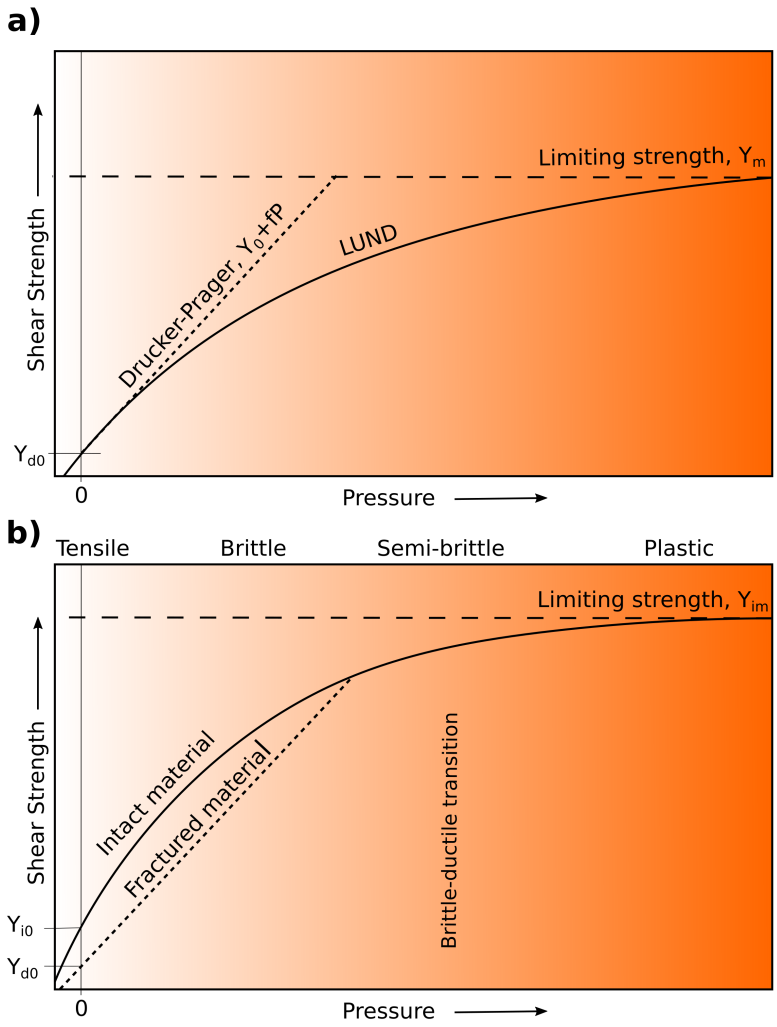

Figure 3.8: Strength of a geologic material as a function of pressure. a) Strength models for fractured malsterials: In the Drucker-Prager strength model, strength of the material increases linearly with pressure up to a limiting strength, Y_m, after which the strength remains constant at $Y = Y_m$. In the LUND strength model, the strength of the damaged material increases smoothly with pressure, approaching a limiting strength, Y_{dm} (here $Y_{dm} = Y_m$). b) Strength model for intact rock-like materials. In ROCK, the intact material follows a smooth LUND relation and the damaged material follows a Drucker-Prager linear relation, up to a limiting strength Y_{im}. The top row represents the different regimes of deformation:tensile, brittle, semi-brittle, and plastic. Adapted from Collins et al. (2004).

3.7 The $\epsilon - \alpha$ porous-compaction model

Asteroids in the Solar System range from almost non-porous (e.g. Ceres, Vesta) to high porosity rubble-piles (e.g Mathilde, Bennu, Ryugu). As discussed in Section 2, depending on the scale, the porosity can be either macroscopic (macroporosity) or small scale (microporosity). In an impact event, the target porosity can greatly influence the

propagation of the shock wave and crater ejecta formation (Housen et al., 2018).

Macroporosity can be included in a numerical model by considering a mixed material with macroscopic voids (e.g. SPH) (Jutzi and Michel, 2014). In shock physics codes such as iSALE, the material is represented as a continuum and therefore the microporosity is modelled as a subresolution material model. The behaviour of porous media is described using a relative measure of the volume of pore space, called distension, rather than the porosity. The distension, α, relates to the material density or porosity ϕ by:

$$\alpha = \frac{1}{1-\phi} = \frac{V_s + V_v}{V_s} = \frac{\rho_s}{\rho}, \tag{3.32}$$

where V_s is the volume of the solid matrix, V_v is the volume of void space, ρ_s is the density of the solid matrix and ρ is the bulk density. A non-porous material, $\phi = 0$, has $\alpha = 1$, while a porous material ($0< \phi <1$) has $\alpha >1$.

To incorporate the porosity into a material model, a porosity model is implemented through the EoS. iSALE uses the equation of state of the solid component to relate the pressure, P, to distension, α and energy, E, by using the thermodynamically consistent relationship (Carroll and Holt, 1972; Holsapple, 2008):

$$P = \frac{1}{\alpha} P_s\left(\rho_s, E_s\right) = \frac{1}{\alpha} P_s\left(\alpha\rho, E\right), \tag{3.33}$$

where P_s, ρ_s and E_s are the pressure, density and energy of a solid material of the same composition.

Eq. 3.33 offers the advantage that the pressure in the matrix can be computed directly from the EoS for non-porous materials, as long as the distension is known. One way to determine α is to relate it to pressure, P, $\alpha(P)$, by means of the P-alpha model. However in this case there is a interdependency between the pressure and distension, and problems occur in the code iteration. For example, at the end of a given time step, t, the distension at the next time step, α_{t+1}, must be known in order to derive the pressure, P_{t+1}, but the distension is itself a function of pressure, $\alpha_{t+1} = f(P_{t+1})$. This problem is usually solved by deriving the distension and the pressure at time $t+1$ simultaneously, but this can be computationally expensive and can become numerically unstable (Wünnemann et al., 2006). To overcome this problem, in iSALE the distension is defined using a strain-

based approach, the $\epsilon - \alpha$ porous-compaction model (Wünnemann et al., 2006; Collins et al., 2011). In the $\epsilon - \alpha$ model, the distension, α, is defined as a function of volume strain, ϵ_V,

$$\alpha = f(\epsilon_V). \tag{3.34}$$

The volumetric strain, ϵ_V, is the ratio between the change in volume in a computational cell, dV, and the initial volume in that cell, V_0. The accumulated volumetric strain can then be expressed as an integral

$$\epsilon_V = \int_{V_0}^{V'} \frac{dV}{V} = \ln\left(\frac{V'}{V_0}\right), \tag{3.35}$$

where V' is the updated volume, $V_0 + dV$. A negative volume strain means compression.

In an idealised porous material, all pore space becomes compacted before any compression of the matrix occurs (Wünnemann et al., 2006), for which case the volumetric strain can be related to distension by

$$\epsilon_V = \ln\left(\frac{V'}{V_0}\right) = \ln\left(\frac{V'}{V_s}\frac{V_s}{V_0}\right) = \ln\left(\frac{\alpha}{\alpha_0}\right), \tag{3.36}$$

where α_0 is the material distension before compaction. Therefore, the distension can be expressed in terms of volumetric strain and initial distension

$$\alpha = \alpha_0 e^{\epsilon_V}. \tag{3.37}$$

In real geological materials, however, compression and compaction will occur at the same time. To account for the compaction rate, the $\epsilon - \alpha$ model contains an additional parameter, κ, which controls how rapidly the pore space becomes compacted during compression. A value of $\kappa = 1$ represents the idealised case in which compression starts only after all the pore space has been compacted, while $\kappa < 1$ represents cases in which compaction and compression occur simultaneously. Previous work has shown that for most geological materials κ takes values between 0.9 and 1. The $\epsilon - \alpha$ model distinguishes between four

regimes that describe the compression of an initially porous material:

$$\text{Elastic compaction:} \quad 0 > \epsilon_V > \epsilon_e \quad \alpha = \alpha_0 \tag{3.38}$$

$$\text{Exponential compaction:} \quad \epsilon_e > \epsilon_V > \epsilon_X \quad \alpha = \alpha_0 e^{\kappa(\epsilon_V - \epsilon_e)} \tag{3.39}$$

$$\text{Power-law compaction:} \quad \epsilon_X > \epsilon_V > \epsilon_c \quad \alpha = 1 + (\alpha_X - 1)\left(\frac{\epsilon_c - \epsilon_V}{\epsilon_c - \epsilon_X}\right)^2 \tag{3.40}$$

$$\text{Compression:} \quad \epsilon_c > \epsilon_V \quad \alpha = 1 \tag{3.41}$$

where ϵ_e is the critical volume strain, ϵ_X is the volumetric strain at the transition between the exponential and the power-law regimes and ϵ_c is the volumetric strain at which all the pore space is crushed out.

For volumetric strains higher than a critical volume strain, $\epsilon_V > \epsilon_e$, the pore compaction is reversible and the cell distension takes the value of the initial distension, α_0 (elastic compaction, Eq. (3.38)). For volumetric strains higher than ϵ_e, pore spaces are crushed and any changes are irreversible. In the 'exponential compaction' regime the pores compaction is primarily achieved by the rearrangement of the material grains (Eq. (3.39)). Above a certain strain ϵ_X, it becomes harder to rearrange grains and the compaction is achieved by crushing the individual grains. Therefore this regime is less rapid than the exponential compaction regime and is represented by a power-law that asymptotes towards $\alpha = 1$ (Eq. (3.40)). Once all the pore space is crushed, at a volumetric strain of ϵ_c, the distension reaches its minimum value, $\alpha = 1$, where the porosity is zero (Eq. (3.41)).

In iSALE, α is not computed directly from Eqs. 3.38–3.41, but rather from the compaction rate, $\frac{d\alpha}{d\epsilon}$ in each regime. The updated distension is calculated from:

$$\alpha_{n+1} = \alpha_n + \frac{d\alpha}{d\epsilon}\frac{d\epsilon}{dt}\Delta t. \tag{3.42}$$

The initial $\epsilon - \alpha$ model (Wünnemann et al., 2006) assumed that in the elastic regime the distension is equal to the initial distension ($\alpha = \alpha_0$), however in reality porosity decreases slightly with increasing volume strain (pressure). An important effect of this assumption is that the elastic wave speed of the porous material can be much smaller than the elastic wave speed in the solid material. To account for the change in

porosity during elastic loading, Collins et al. (2011) defined the elastic compaction rate as

$$\frac{d\alpha}{d\epsilon_V} = \alpha \left[1 - \left(\frac{c(\alpha)}{c_{s0}} \right)^2 \right], \tag{3.43}$$

where c_s is the bulk sound speed of the solid material at zero pressure and $c(\alpha)$ is the bulk sound speed of the porous material at zero pressure, which varies linearly with α:

$$c(\alpha) = c_{s0} + \frac{\alpha - 1}{\alpha_0 - 1}(c_0 - c_{s0}) = 1 + \frac{\alpha - 1}{\alpha_0 - 1}(\chi - 1), \tag{3.44}$$

where $\chi = c_0/c_{s0}$. $\chi = 1$ reverts the $\epsilon - \alpha$ model to its original assumption.

The rate of compaction in the different regimes is calculated from

$$\text{Exponential compaction: } \epsilon_e > \epsilon_V > \epsilon_X \qquad \frac{d\alpha}{d\epsilon_V} = \kappa \alpha_e e^{\kappa(\epsilon_V - \epsilon_e)}, \tag{3.45}$$

$$\text{Power-law compaction: } \epsilon_X > \epsilon_V > \epsilon_c \qquad \frac{d\alpha}{d\epsilon_V} = 2(1 - \alpha_x)\frac{\epsilon_c - \epsilon_V}{(\epsilon_c - \epsilon_X)^2}. \tag{3.46}$$

The iSALE input parameters are summarised in Table 3.2.

Table 3.2: iSALE input parameters for the $\epsilon - \alpha$ compaction model.

Parameter	Description
α_0	Initial distension of porous material
ϵ_e	Elastic volumetric strain threshold
α_X	Distension at transtion from exponential to power-law compaction
κ	Compaction rate parameter in exponential compaction regime
χ	Ratio of porous to solid material sound speed at zero pressure

3.7.1 Deriving the material crush curve from the $\epsilon - \alpha$ input parameters

At sufficiently high pressures, the material compacts by fracture or crushing of the constituent grains, causing the pore space volume to decrease. In laboratory experiments, the crushing of the material grains is often represented by a "crush curve", which is obtained by measuring the volume (density) as a function of applied stress in a uniaxial compressive loading (Housen et al., 2018). The $P - \alpha$ model directly relates the applied stress (pressure) to the distension of the material (Eq. (3.33)). By contrast, the $\epsilon - \alpha$ model relates the distension to volumetric strain. In order to compare iSALE input parameters with experimentally derived crush curves, several approximations and substitutions have to be made.

Firstly, the stiffened gas equation of state (Melosh, 1989; Collins et al., 2011) is used to approximate the pressure in the solid matrix component of a porous material, P_s, at low pressures typical of crush curves:

$$P_s(\rho_s, E) = c_{s0}^2(\rho_s - \rho_{s0}) + \rho_s\Gamma(\rho_s)(E - E_0), \tag{3.47}$$

where c_{s0} is the bulk sound speed, ρ_s is the solid density, ρ_{s0} is the initial, uncompressed density, Γ is the Gruneisen gamma parameter, E and E_0 are the specific internal energy of the solid and the compressed material, respectivelly. $\Gamma(\rho_s)$ is difficult to measure during shock wave experiments and it is often crudely approximated by (Melosh, 1989)

$$\Gamma(\rho_s) \approx \rho_0\Gamma(\rho_0). \tag{3.48}$$

At zero pressure, the Gruneisen gamma parameter is equal to (a+b), where a and b are Tillotson EoS parameters. For the compaction of low-porosity materials, it is sufficient to ignore the thermal pressure component of the equation of state (Eq. (3.47)). The pressure in the solid matrix is then

$$P_s = c_{s0}^2\left(\rho_s - \rho_{s0}\right). \tag{3.49}$$

Eq. (3.33) then gives us the relationship for the pressure in the bulk material, P:

$$P = \frac{P_s}{\alpha} = \frac{\rho_{s0}c_{s0}^2}{\alpha}\left(\frac{\alpha\rho}{\rho_{s0}} - 1\right). \tag{3.50}$$

Using the definitions of the density, ρ, and distension α,

$$\rho = \rho_0 e^{-\epsilon_v}, \tag{3.51}$$

$$\alpha = \alpha_0 e^{\kappa\epsilon_e}, \tag{3.52}$$

we get a relationship between density and distension

$$\rho = \rho_0\left(\frac{\alpha_0}{\alpha}\right)^{1/\kappa}. \tag{3.53}$$

Substituting into the equation for the pressure of the bulk material, Eq. (3.50), gives:

$$P = \frac{\rho_{s0}c_{s0}^2}{\alpha}\left[\frac{\alpha\rho_0}{\rho_{s0}}\left(\frac{\alpha_0}{\alpha}\right)^{1/\kappa} - 1\right], \tag{3.54}$$

$$P = \frac{\rho_{s0} c_{s0}^2}{\alpha} \left[\frac{\alpha \alpha_0 \rho_0}{\alpha \rho_{s0}} \left(\frac{\alpha_0}{\alpha} \right)^{1/\kappa - 1} - 1 \right], \tag{3.55}$$

$$P = \frac{\rho_{s0} c_{s0}^2}{\alpha} \left[\left(\frac{\alpha_0}{\alpha} \right)^{(1-\kappa)/\kappa} - 1 \right]. \tag{3.56}$$

Using the Newton-Laplace equation ($c_{s0} = \sqrt{\frac{K_{s0}}{\rho_{s0}}}$), we can write Eq. (3.56) in terms of the material bulk modulus, K_{s0}, which is an iSALE input parameter, within the Tillotson EoS:

$$P = \frac{K_{s0}}{\alpha} \left[\left(\frac{\alpha}{\alpha_0} \right)^{1 - 1/\kappa} - 1 \right]. \tag{3.57}$$

For a given K_{s0} and α_0, this allows κ to be tuned to best fit experimentally derived $P - \alpha$ data.

3.8 Ejecta measurements

To track ejecta in the impact simulations, iSALE's Lagrangian tracers were placed across the high-resolution domain. A simple and widely-used approach for identifying those tracers that comprise the crater ejecta is to flag the tracer as ejected during the simulation if its trajectory crosses a horizontal line a fixed altitude above the preimpact surface (Fig. 3.9). The mass, velocity vector, and launch position of each ejected tracer can then be recorded at the moment the tracer reaches this altitude. If this "ejecta line" happens to be placed at the height of the transient crater rim, the approach correctly distinguishes ejected material from that which remains in the crater or forms part of the uplifted rim. However, as the transient crater rim height is not known a priori, this work adopted an ejecta line altitude equal to one impactor diameter.

To identify tracers that cross the ejecta line but should not be considered as part of the ejecta, because their final location was inside the crater or within the uplifted crater rim, the ejected tracers were also required to have a maximum speed exceeding that needed to overcome the cohesive strength of the target. In all cases simulated in Chapters 4 and 5 an ejection velocity threshold of 10 cm/s was used, which was larger than

the escape velocity of the asteroid, so that the momentum of the all ejecta contributed to momentum transfer.

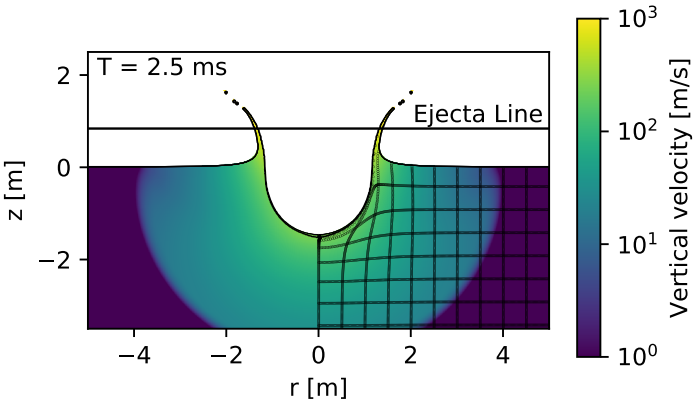

Figure 3.9: Crater profile showing the ejecta measurement method. Properties of the ejecta are recorded at the time the Lagrangian tracers cross the ejecta line, which was set at a height equal to one projectile diameter.

To calculate the speed, angle and launch position of each ejecta tracer, the tracer was projected back from the location it crossed the ejecta line to the target surface. In zero- or very low-gravity scenarios it is sufficient to project back along a straight line trajectory, with a slope given by the ejecta velocity vector. However, in higher-gravity scenarios, such as those considered in the impact simulations replicating lab-scale experiments, it is important to project the ejected material back along a parabolic, ballistic trajectory.

Defining the radius, horizontal and vertical velocity components of the ejecta at the surface and at the ejecta line as (x, u, v) and (x_h, u_h, v_h), respectively. The ballistic motion equations for two dimensional trajectories at height h, can be written as:

$$x - x_h = v_{hx} t, \tag{3.58}$$

$$y - y_h = v_{hy} t + \frac{g t^2}{2}, \tag{3.59}$$

where t is the time and g is the gravitational acceleration (negative down). Substituting t from Eq. (3.58) into Eq. (3.59), and assuming $\tan\alpha = v_{hy}/v_{hx}$, gives:

$$y - y_h = -\frac{g x_h^2}{v_{hx}^2}(x - x)h)^2 + \tan\alpha(x - x_h) \tag{3.60}$$

This equation is a second order polynomial, the standard form of a parabola, which can be written in the form $y = ax^2 + bx + c$, with $a = -2vg^2$, $b = \tan\alpha$ and $c = y_h$. The ejecta launch position, x and the ejection angle, α, can then be determined from the a, b and c coefficients:

$$x = x_h - \frac{b + \sqrt{b^2 - 4ac}}{2a}, \tag{3.61}$$

$$\alpha = \tan^{-1}(2\alpha(x - x_h) + b), \tag{3.62}$$

Assuming that the trajectory of the tracer particles above height h is influenced by gravity alone, the velocity components at the target surface v_x and v_y, can be deduced from the conservation of energy:

$$v_x = v_{hx}, \tag{3.63}$$

$$v_y^2 = v_{hy}^2 - 2gh. \tag{3.64}$$

Then the magnitude of the velocity at the target surface, v, is

$$v = \sqrt{v_x^2 + v_y^2}. \tag{3.65}$$

The surface-projected, ejected tracer data were processed to measure the mass/velocity/launch-position distributions of ejecta resulting from each impact cratering event as well as the cumulative ejected momentum as a function of ejection speed.

3.8.1 Limitations of ejecta measurements in iSALE

In iSALE the material is described as a continuum. This approximation holds in the case of completely damaged or granular material, and material movement and crater formation are generally well resolved. However, a limitation of the continuum approach arises when the material is ejected. The spatial resolution is insufficient to describe the movement of the ejected material, as the ejecta curtain is normally resolved by only a limited number of cells.

3.9 Regridding and resolution tests

For an accurate description of the impact ejecta process, the simulations must record the whole distribution of the ejecta. This is particularly problematic for the very high velocity particles ejected in the early phases of the simulations, which require high spatial resolution to capture accurately (Johnson et al., 2014). Also, due to the low strength of the target materials investigated, the craters grow many times larger than the projectile and over a long time-scale. To use a high spatial resolution for the entire duration of the simulation can be highly computationally expensive. To overcome this, iSALE's regridding option was used. This option allows the computational grid to be coarsened by a factor of two after a predetermined amount of time.

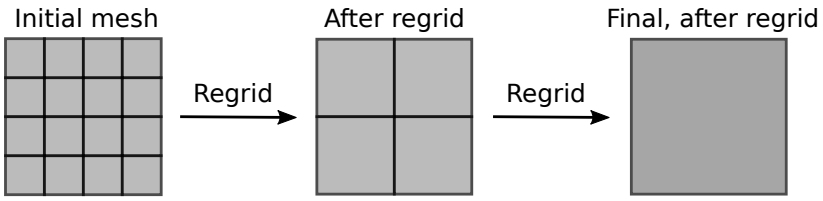

Figure 3.10: Schematic representation of the regridding process.

When restarting a calculation, iSALE's regridding functionality can be used to define a new grid and interpolate the data onto the new grid. The option allows for high-resolution and extension cells to be added to the original grid, as well as coarsening the initial high-resolution domain by a factor of two. For example, for an initial mesh of 16 cells, the mesh coarsening is achieved by deleting the nodes every four cells (Fig. 3.10). The mass within the computational domain is conserved, therefore, if one of the four merged cells contains void, then the new cell will contain the same mass, but the width will increase.

To test iSALE's regridding option, four regrids were performed: the initial resolution was 80 cells per projectile radius (cppr) so that the final effective resolution was 5 cppr.

Resolution tests (Fig. 3.11) showed that this method produces results (e.g., crater volume as a function of time and cumulative ejecta momentum as a function of time)

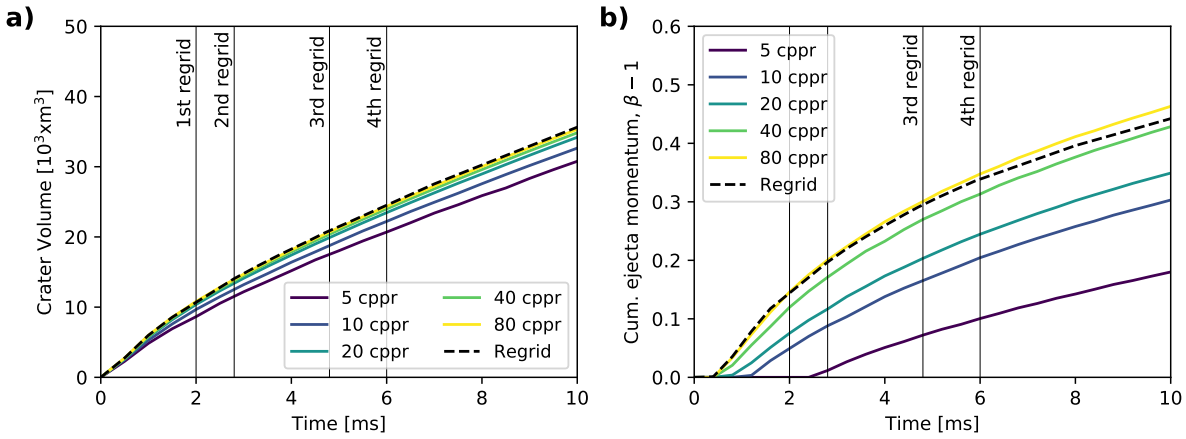

Figure 3.11: Resolution test showing the (a) crater volume growth and (b) ejecta momentum against time, for a 1 m in diameter aluminium projectile, impacting a basalt target at 6.5 km/s simulation, with spatial resolutions between 5 and 80 cppr. Coarsening the domain by a factor of two at the times marked by the vertical lines (regrid) yields an accuracy comparable with the 80 cppr for crater volume and 40 cppr for ejecta momentum.

that are comparable to those obtained by a fixed, 80 cppr or 40 cppr resolution but at an approximately equivalent cost to a fixed 5 cppr resolution run. At 10 ms, the fixed-resolution, 80 cppr produces a crater volume of about 35.3 m^3, 40 cppr produces a crater volume of about 34.8 m^3, the fixed-resolution 5 cppr run, a crater volume of 30.1 m^3, while the simulation with regridding produces a crater volume of 35.0 m^3.

Similarly, at 10 ms, a fixed 80 cppr produces a cumulative ejecta momentum, $p_{ej(z)}/mU$, of about 0.46, the fixed-resolution 40 cppr, an ejecta momentum of 0.43, while a 5 cppr run, an ejecta momentum of 0.18. The regrd allows for most of the fast ejecta to be recorded and the run produces a cumulative ejecta momentum of about 0.44, which is comparable to the 40 cppr run.

3.10 Model validation

Before investigating impacts into asteroid surfaces, iSALE's ability to accurately reproduce impact ejecta data for laboratory experiments were investigated.

3.10.1 Validation against laboratory experiments of impacts into sand

Experiments aimed at studying the ejecta properties from impact cratering events have been performed by various research groups, summarised in Housen and Holsapple (2011). In this work the data collected by Cintala et al. (1999), Anderson et al. (2003), Housen (2011, unpublished) and Hermalyn and Schultz (2011) (Table 3.3) was used as validation data.

Table 3.3: Impact experiments summary.

	Target			Impactor	
Reference	Material	Grain size (mm)	Porosity (%)	Velocity (km/s)	Radius (mm)
Cintala et al. (1999)	Coarse sand	1-3	43	1.9	2.4
Anderson et al. (2003)	Loose sand	0.5	39	1.1	3.2
Housen (2011, unpublished)	Ottawa sand	1.0	32	1.4	6.1
Hermalyn and Schultz (2011)	Ottawa sand	<1.0	35	5.6	3.2

Cintala et al. (1999) conducted a series of laboratory experiments in which they impacted 4.76 mm aluminium spheres into coarse-grained (1-3mm) sand targets, at velocities between 0.8 and 1.9 km/s. A laser-based system captured photographs of individual grains in their ballistic flight, that enabled them to fit parabolas through each ejecta particle's trajectory and infer the ejection angle, α, and ejection velocity, v, as a function of launch position, x.

In the Anderson et al. (2003) experiments, 6.35 mm aluminium spheres were impacted into finer-grained sand (0.5 mm), at velocities of about 1 km/s and various impact angles. The ejection angle, α, and the ejection velocity, v, of the ejected particles were recorded using three-dimensional particle image velocimetry (3D PIV). This technique uses a system of lasers and digital cameras to illuminate a ring of particles, measuring the three-dimensional velocity vectors of the moving ejecta particles, at two slightly different positions. Numerical algorithms were then used to determine the instantaneous velocity vector from each pair of images. However, the digital camera only recorded one pair of images per impact experiment, so several shots of the same impact experiment were required to capture the ejecta curtain at different times in the crater growth evolution and to determine ejection velocity as a function of launch position.

Housen (unpublished work), which we refer to as Housen (2011), performed quarter-space experiments of cylindrical polyethylene, magnesium and aluminium projectiles impacting dense sand targets, at speeds between 1.4 and 1.9 km/s. Results from these experiments were included in the synthesis of experimental impact ejecta studies by (Housen and Holsapple, 2011). The vertical impacts were performed in a vacuum chamber. Coloured markers were placed into the target before the impact, and their trajectory was then measured by analysing footage of the impact recorded by a high-speed digital video camera (Housen and Holsapple, 2011).

Hermalyn and Schultz (2011) used a variety of projectiles to impact median grained Ottawa sand (1 mm) targets, at velocities of approximately 5 km/s. The experiment used a set of high-speed cameras and an imaging technique called Particle Tracing Velocimetry (PTV) to measure ejecta properties. Individual particles were tracked in their ballistic flight, in the plane of the ejecta curtain, which allowed the velocity of the ejecta particles to be derived as a function of time and launch position. The high frame rate allowed very fast ejecta to be recorded. However, the camera had a narrow field of view and did not record the slow ejecta near the final crater rim.

Numerical model set-up

We simulated three impact experiments: the Cintala et al. (1999) experiment of a 4.76-mm diameter spherical projectile at 1.9 km/s (shot 4207 as defined in the Cintala et al. (1999) study), the Housen (2011) impact of an 12.20-mm aluminum cylinder at 1.4 km/s and the Hermalyn and Schultz (2011) impact of an 6.35 mm aluminium spherical projectile at 5.6 km/s.

To simulate the sand targets, we used an ANEOS-derived equation-of-state (EOS) table for SiO_2 (Melosh, 2007) coupled with the $\epsilon-\alpha$ porosity compaction model to describe the thermodynamic and volumetric response and the Drucker-Prager strength model to describe the shear response. This material model has been successfully used previously in validation work by Wünnemann et al. (2016). The Drucker-Prager strength model is a good description of the shear strength of granular materials. To note that the coefficient

of internal friction, f, in the Drucker-Prager model is different from the coefficient of friction used in rock mechanics and in the Mohr-Coulomb model (Elbeshausen et al., 2009), and can be approximately related to the angle of internal friction, θ, as $f \approx \sin(\theta)$.

The angle of internal friction θ was not measured for the coarse sand used in the experiments by Cintala et al. (1999), so we ran several test cases with f between 0.55 and 0.70. The best match of the ejecta distribution was achieved for $f = 0.60$. For the Housen (2011) impact experiment we used $f = \sin(35°) \approx 0.55$ (Housen and Holsapple, 2012) and for the Hermalyn and Schultz (2011), we used $f = \sin(30°) = 0.50$ (Lee and Seed, 1967).

The target densities in the experiments were measured at 1.51 g/cm^3 (Cintala et al., 1999), 1.75 g/cm^3 (Housen, 2011) and 1.70 g/cm^3 (Hermalyn and Schultz, 2011), which corresponds to porosities of: $\phi_0 = 0.42\%$, $\phi_0 = 0.32\%$ and $\phi_0 = 0.35\%$, respectively. In the numerical simulations, these porosities were achieved by using the $\epsilon - \alpha$ model (Wünnemann et al., 2006). The $\epsilon - \alpha$ model takes in five input parameters, which are summarised in Table 3.4. The projectiles were modelled using the Tillotson EoS (Tillotson, 1962) and the Johnson-Cook strength model for aluminium 1100-0 (Johnson and Cook, 1983), with A = 49 MPa; B = 157 MPa; C = 0.016; m = 1.7; n = 0.167; T_{ref} = 800 K (Benck et al., 1976; Pierazzo et al., 2008).

The iSALE simulations were run until the transient crater was formed and all the ejected particles were recorded. As dry sand is cohesionless ($Y_0 = 0$ Pa), the final crater diameter was much larger than the impactor diameter and the process occurred over a long simulation time, making the simulations computationally expensive. To reduce the time needed to run the simulations, the regridding option was used (see Section 3.9. The simulation had an initial resolution of 40 cppr and spatial resolution was coarsened three times by a factor of two, so that the latter stages of crater growth had an effective resolution of 5 cppr.

Table 3.4: Input target material model parameters used in the iSALE simulations.

Description	Symbol	
Equation of state		ANEOS (quartzite)[a]
Strength model		Drucker-Prager
Poisson ratio	ν	0.30[b]
Strength at zero pressure (MPa)	Y_0	0
Strength at inf. pressure (MPa)	Y_∞	1000
Internal friction coefficient	f	0.60/0.55/0.50
Porosity model parameters $(\epsilon - \alpha)$[b,c]		
Initial porosity	ϕ_0	0.43/0.32/0.35
Initial distension	α_0	1.75/1.47/1.54
Elastic volumetric strain threshold	ϵ_{e0}	-0.0013
Distension at transition to power-law	α_x	1.29[d]
Exponential compaction rate	κ	0.99[d]
Ratio of porous/nonporous sound speed	χ	1.00

[a] Melosh (2007);
[b] Wünnemann et al. (2006);
[c] Collins et al. (2011);
[d] Wünnemann et al. (2016).

Results and Discussion

We first compared the results of the iSALE validation test with the Cintala et al. (1999) experiment. The ejection angle, α, and the ejection speed, v, produced by the iSALE simulation are presented as a function of normalised launch position, x/R_r, in Figure 3.12. We note that the crater radius used in the normalisation, R_r, was measured at the rim height in both the experiment and in the numerical simulation. Our numerical simulation produced a crater rim radius of about 11 cm, slightly larger than the experimental value of 9.1 cm. This difference may be attributed to combined effects of coarse resolution after the final regrid (5 cppr), as well as the coarse grains not being accurately represented by a continuous material model.

The angle of ejection was found to vary with launch position, x, in good agreement with the experimental results (Fig. 3.12a). The fast ejecta launched close to the impact site exhibits a steep ejection angle $\approx 50°$; α then decreases with increasing launch position, until it reaches a minimum of $\approx 35°$, after which α increases again as the launch position approaches the final crater rim. A similar trend was observed by Cintala et al. (1999). The measured ejection speed, v, follows a power-law distribution, as predicted by the

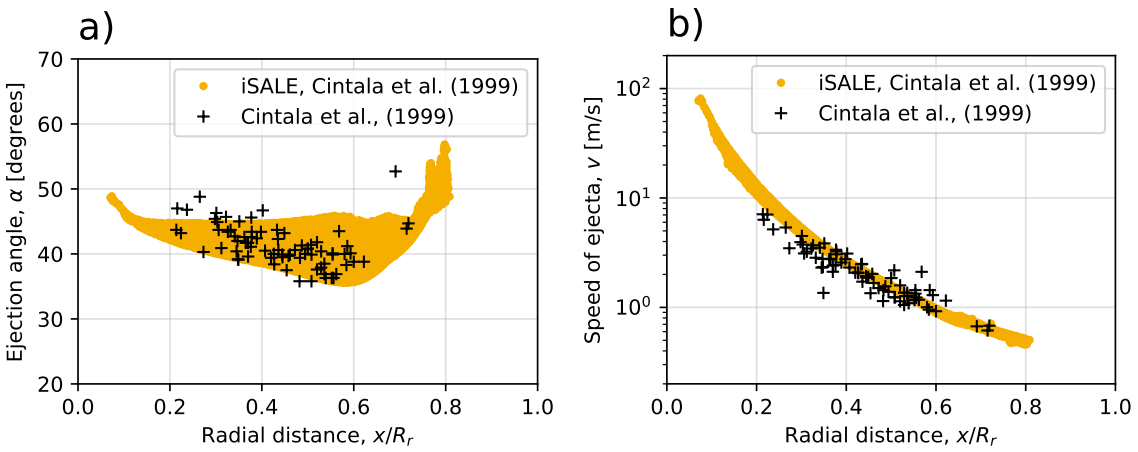

Figure 3.12: Ejecta distribution produced by iSALE, represented by yellow points, compared to the ejecta distribution measured from shot 4207, in the Cintala et al. (1999) experimental study (black crosses). The iSALE simulation used a 2.4 mm aluminium sphere, at 1.9 km/s, impacting a half-space quartzite target, with 43% porosity and a coefficient of friction of f=0.6. a) Ejection angle, in degrees, as a function of radial distance, x normalised by the crater radius, R. b) Speed of the ejecta, in m/s, as a function of normalised radial distance. The crater radius, R_r, was measured at rim height in both the simulation and in the experiment.

dimensional analysis of Housen et al. (1983) and the simulation results closely resemble the Cintala et al. (1999) experiment data.

Data from several studies similar to the Cintala et al. (1999) was then compared with the iSALE validation tests described above. Figure 3.13 shows the normalised ejection speed as a function of normalised radial distance, as measured in the Cintala et al. (1999), Anderson et al. (2003), Housen (2011) and Hermalyn and Schultz (2011) experiments. The ejection speed is normalised by the gravity scaling term $\sqrt{gR}$ (Housen et al., 1983), and the launch position x is normalised by the crater radius, R, which this time is measured at pre-impact level.

The two experiments reproduced here, Housen (2011, unpublished) and Hermalyn and Schultz (2011) differ slightly in impact velocity and target properties from the (Cintala et al., 1999) study. The two iSALE simulations are both in good agreement with the experimental data and as before, the ejection speed decreases with ejection distance following a power-law distribution. However the Hermalyn and Schultz (2010) data is shifted higher, probably due to the higher impact velocity, trend which is well replicated by our numerical simulations.

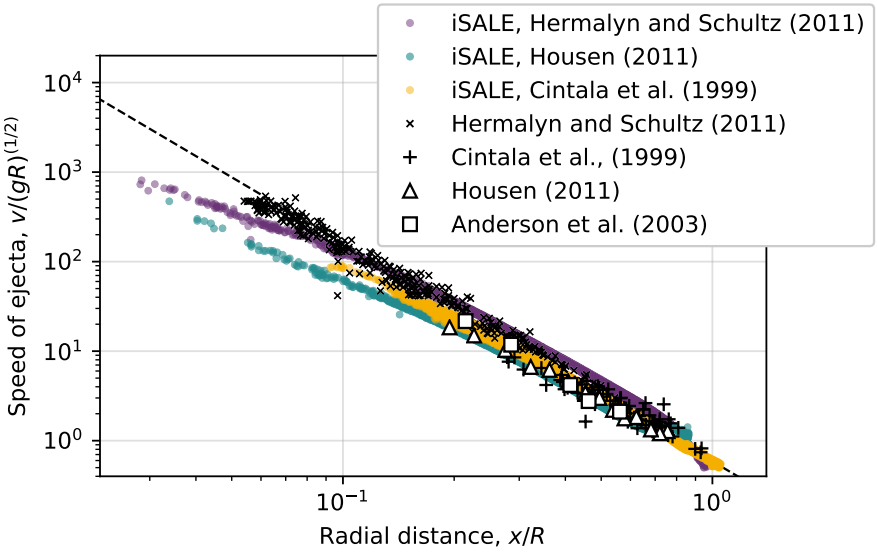

Figure 3.13: Ejecta velocity distribution for iSALE impact simulations into sand targets, compared to the ejecta measurements from laboratory experiments, from Cintala et al. (1999), Anderson et al. (2003), Housen (2011) and Hermalyn and Schultz (2011). For all data, the speed of the ejecta, v, is normalised by the gravity scaling term $\sqrt{gR}$, while the radial distance is normalised by the crater radius measured at the pre-impact level, R. The Cintala et al. (1999) crater radius data is converted from rim-height radius, R_r to pre-impact level radius, R, using the relation $R_r = 1.3R$, as noted by Housen and Holsapple (2011). The Housen et al. (1983) power-law of $\mu = 0.41$ (dashed line) is plotted for comparison.

3.11 Conclusions

iSALE is a shock physics code, based on the SALE hydrocode and similar to the older SALEB code. iSALE was specifically designed for simulating impact processes and it includes strength models suitable for impacts into geologic targets and a porosity compaction model, the $\epsilon - \alpha$ model. In this thesis iSALE was used to simulate impacts on porous asteroid surfaces, which made use of these code capabilities. The targets used for the simulations in this work were modelled using both the Tillotson and ANEOS EoS. While the Tillotson EoS does not accurately represent some rock (e.g. basalt) material at high pressures, it was shown that this deficiency does not represent a problem for the impact scenarios considered here. However, modelling a basalt target using Tillotson EoS reduces the simulation run time by about 10%, compared to the run time for the same impact scenario but modelled using the ANEOS EoS.

Resolution tests have shown that using iSALE's regridding option produced results comparable to a high-resolution 40 cppr run, but at equivalent run times to a low resolution, 5 cppr run. As a result, iSALE's regridding option was used throughout this thesis to record the impact ejecta accurately while achieving a practical run time.

Furthermore, validation tests of impacts into different types of sand have proved that iSALE is an adequate tool to model crater and ejecta formation.

The material models implemented in iSALE, its capability to measure ejecta from impact craters and its accuracy in reproducing impact experiments, make iSALE an ideal tool to construct the simulations presented in the following chapters.

Chapter 4

The role of asteroid target properties in impact momentum transfer

"An asteroid collision would be something against which we have no defence. The last big such collision with us was about sixty-six million years ago and that is thought to have killed the dinosaurs, and it will happen again. This is not science fiction; it is guaranteed by the laws of physics and probability." — Stephen Hawking, *Brief Answers to the Big Questions*

Earth is continually impacted by very small asteroids and debris, and a larger object, though uncommon, could produce a severe natural hazard. During impact crater formation the ballistic ejection of material out of the crater is a major process and can have significant implications for asteroid deflection. This chapter describes numerical simulations of impacts into low-gravity, strength dominated asteroid surfaces using the iSALE shock physics code, and considers the Double Asteroid Redirection Test (DART) mission as a case study. It is found that target cohesion, initial porosity, and internal friction coefficient greatly influence ejecta mass/velocity/launch-position distributions and hence the amount by which an asteroid can be deflected. The results show that as the cohesion is decreased the ratio of ejected momentum to impactor momentum, $\beta - 1$, increases; $\beta - 1$ also increases as the initial porosity and internal friction coefficient of

the asteroid surface decrease. Using nominal impactor parameters and reasonable estimates for the material properties of the Didymos binary asteroid, the DART target, the simulations show that the ejecta produced from the impact can enhance the deflection by a factor of 2 to 4. The self-consistency between the crater size and ejection speed scaling relationships previously derived from the point-source approximation for impacts into the same target material is then investigated. Finally, numerical simulations at vertical, 60°, 45° and 30° impact angles are used to derive an empirical model for the ejecta distribution and momentum transfer from oblique impacts.

4.1 Introduction

Impacts and collisions at high velocity play an important role in planetary formation and have shaped the surfaces of all solid bodies in the Solar System (Fassett and Minton, 2013). A major process during impact crater formation is the ballistic ejection of material out of the crater (Melosh, 1989). Quantifying how target properties such as strength, porosity and internal friction affect the mass-velocity distribution of ejected debris (ejecta) is important for many areas of planetary science and can help explain the evolutionary history of planetary embryos (Housen et al., 1983), the origin of interplanetary space debris (Su, 1990) and meteorites (Greenberg and Chapman, 1983) and the distribution of regolith and secondary impact craters on a planetary surface (Oberbeck, 1975; Schultz and Mendenhall, 1979). One of the most straightforward applications of ejecta studies is in the deflection of asteroids (Belton et al., 2004). To avoid a collision between an asteroid and Earth, the course of the asteroid can be changed by impacting its surface (Ahrens and Harris, 1992; Melosh et al., 1994). The ejecta resulting from the impact can produce additional thrust which enhances the asteroid deflection (Shafer et al., 1994), but this effect has been found to vary significantly depending on the target asteroid's properties and composition (Housen and Holsapple, 2012).

An extensive number of laboratory impact experiments have been performed into various target materials (Gault et al., 1963; Shoemaker et al., 1963; Hartmann, 1985; Housen, 1992; Housen and Holsapple, 2003; Housen and Holsapple, 2011) to illuminate the ejection process and provide a quantitative measure of the mass-velocity distribution of ejected debris material. Such experiments have shown that ejecta properties are highly dependent on the target properties, in particular strength, porosity and internal friction (Housen and Holsapple, 2011; Michel, 2013; Jutzi and Michel, 2014). However, as these experiments typically do not directly replicate the low gravity, low target cohesion or large impactor sizes often involved in impacts on asteroid surfaces, their results must be extrapolated to the relevant regime using scaling theory.

Scaling relations based on the point-source approximation (Housen et al., 1983)

provide a theoretical description of the mass/velocity/launch-position distributions of ejecta. Ejection velocity decreases with increasing launch position, following an inverse power law that breaks down close to the impact point and as it approaches the final crater rim. Recently proposed scaling relations augment the power-law relations with an empirical function to account for the reduction to zero of ejecta launch speeds near the rim (Housen and Holsapple, 2011). The current scaling relations are still not well constrained for very fast ejecta, which are also very difficult to measure in laboratory experiments. The exponent of the power-law was found to be strongly influenced by target properties (Housen et al., 1983), but these properties are interlinked and their individual influence on the ejecta needs further study.

Numerical studies using a range of initial conditions provide an alternative method to systematically determine the reaction of different types of target asteroid surfaces to a possible impact. For example, Luther et al. (2018) used numerical simulations to constrain the influence of impact velocity and target properties on ejection velocity and angles in gravity-dominated impacts. Here, numerical simulations of strength-dominated impacts on small, low-gravity asteroids are used to investigate and quantify the effects of individual asteroid surface material properties, specifically strength, porosity and internal friction, on crater ejecta properties. This chapter uses the NASA's DART mission (Cheng et al., 2016; Michel et al., 2016) as a motivating case study. It first presents the results of simulations of impacts into asteroid surfaces with different cohesions, porosities and internal friction coefficients and records the final crater dimensions and the mass/velocity/launch-position distribution of the resulting ejecta. These results are then used to verify ejecta scaling relationships, to determine the empirical constants that define these relationships for specific material properties, and to determine the momentum transferred from the impactor to the target, which is the important metric for potential asteroid deflection.

4.2 DART mission

If a large asteroid were detected in advance to be on an Earth impacting trajectory, an appropriate action could be taken. Asteroid deflection techniques have been described in Chapter 2. The kinetic impactor (Melosh et al., 1994) seems to be the most straightforward solution, however a technology demonstration has yet to be performed. This work uses the DART mission as a case study.

4.3 Simulation set-up for DART scenario

To simulate vertical impacts on small asteroid surfaces, this work used the iSALE shock physics code (Collins et al., 2004; Wünnemann et al., 2006), which has been described in Chapter 3.

To provide a practical reference point, the simulations were set up to resemble the DART scenario. The impactor was modelled as an aluminium sphere, while the target asteroid surface was modelled using a basaltic rock/regolith-like material model, with a fixed surface gravity of $5{\times}10^{-5}$ m/s^2.

4.3.1 Impactor

The impactor was modelled as a porous 0.84 m diameter sphere of mass 310 kg, using the Tillotson equation of state (EOS) and the Johnson-Cook strength model for aluminium (Johnson and Cook, 1983). The characteristics of the impactor were chosen to resemble a simplified spacecraft, with a bulk density of 1000 kg/m^3, accounting for the voids in the structure. The required porosity of 63% was represented using the $\epsilon - \alpha$ porosity compaction model (Wünnemann et al., 2016). The $\epsilon - \alpha$ model parameters are not known for aluminium, so this work used the nominal parameters: $\alpha_0 = 2.7$, $\alpha_x = 1.0$, $\kappa = 0.9$, $\chi = 1.0$. The impactor properties and impact velocity (7 km/s) were kept constant for all simulations in the following sections.

4.3.2 Target asteroid

Didymoon, the target of the DART spacecraft, is too small and distant from Earth to be individually resolved and no spacecraft has visited it yet, so the material properties and the internal structure are unknown. Being a near-Earth double system asteroid (Durda et al., 2004; Walsh et al., 2008), affected by the YORP effect (Jacobson and Scheeres, 2011; Walsh et al., 2012), it is most likely that the asteroid is a rubble-pile covered by a thin layer of regolith (Murdoch et al., 2017). Moreover, observational studies (Michel et al., 2016; Michel et al., 2018) suggest that Didymos is an S-type asteroid system, and therefore the target asteroid material was considered to be made of weak porous basalt, which is a good approximation of the compositional structure of most asteroids.

Didymoon is approximately 160 m in diameter (Michel et al., 2016), with extremely low surface gravity, which means that the impact crater will most likely form in the so-called strength regime. This is because at such low gravity the resistance to crater growth from the weight of the displaced target is small, while the resistance from the strength of the target material is very important even if the material is weak. Therefore, the accuracy of the strength model used to describe the response of the asteroid surface is paramount. The strength model describes the limiting shear stress that the material can support, which can be a function of pressure, temperature and strain. Here the basaltic target was modelled using the Tillotson EOS and the LUND strength model (see Chapter 3 for details).

Coefficient of friction

The coefficient of internal friction, f, cannot be measured remotely and, in asteroids, can take a range of values. The numerical simulations used coefficients f between 0.2 and 1.2. However, values lower than 0.5 and higher than 1.0 are very unlikely, based on geological analogues, while the most common value for geological materials is around 0.6 (Goodman, 1989).

Porosity

The asteroids in the Solar System have been observed to have a large range of porosities, ϕ_0, even up to 50% porosity in the case of asteroid 253 Mathilde (Yeomans et al., 1997). In the simulations presented here, the porosity of the asteroid was modelled using the $\epsilon - \alpha$ model (Wünnemann et al., 2006) and its value was varied between 10% and 50%.

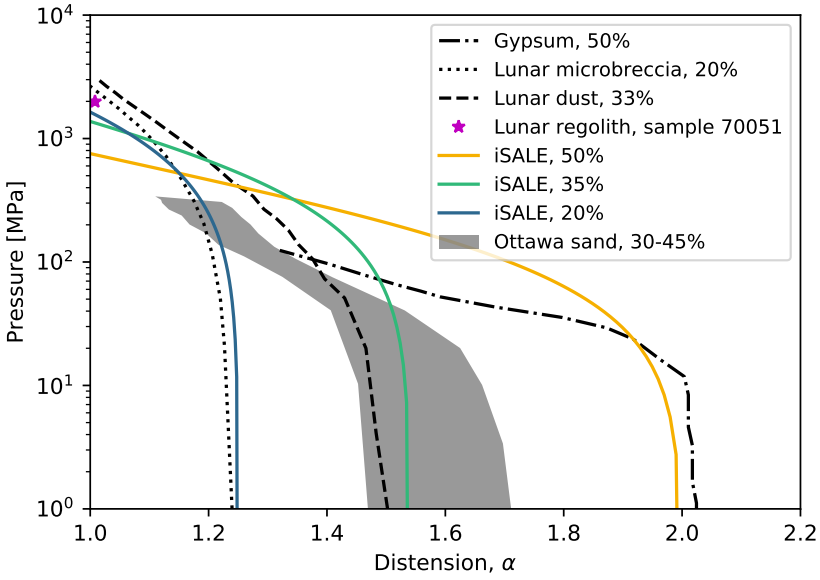

Figure 4.1: Crush curves used in iSALE for homogeneous targets with 20%, 35% and 50% porosity, compared with experimentally derived, quasi-static crush curves for 50% porous gypsum (Nakamura et al., 2009), 30–45% porous Ottawa sand (shaded area) (Hagerty et al., 1993; Housen et al., 2018), lunar dust and lunar microbreccia (Stephens and Lilley, 1970). Also shown is the result of one shock compaction experiment for lunar regolith (sample 70051) (Ahrens and Cole, 1974). To convert bulk density to distension, α is estimated as the ratio of reference grain density to compressed bulk density, ρ_{s0}/ρ.

The input parameters for the $\epsilon - \alpha$ model (Table 4.1) were derived from mesoscale modelling studies of dynamic compaction of chondritic material (Davison et al., 2016) and informed by comparison with measured crush curves (distension as a function of pressure) of analogue materials (Fig. 4.1). Synthetic dynamic crush curves were favoured because they provide a systematic framework for varying all of the compaction model parameters over the range of target porosities considered here. Moreover, without crush-curve measurements of a direct sample of asteroid surface material it is difficult to determine the best analogue for the compaction behaviour of asteroidal materials. Proposed asteroid regolith analogues, including gypsum (Nakamura et al., 2009), sand (Hagerty et al.,

1993; Housen et al., 2018) and lunar regolith (Stephens and Lilley, 1970; Ahrens and Cole, 1974), show a range of compaction behaviour. One way to characterise the compaction response is by a "crushing strength" defined as the pressure required to compact the material by one-half towards its solid density (Housen et al., 2018). For an initial porosity of 20% and 35% the crush curves used in this work are broadly consistent with the quasi-static crush curves of lunar microbreccia and lunar regolith (Fig. 4.1), and have similar crushing strengths (Stephens and Lilley, 1970; Ahrens and Cole, 1974). The crushing strengths in the iSALE simulations included in this work were 450–650 MPa for 35%–20% initial porosity, while the lunar regolith and the lunar microbreccia have crushing strengths of 420 MPa and 800 MPa, respectively. For an initial porosity of 35% and 50% the crush curves at low pressures are also broadly consistent with the crush curves of sand (Hagerty et al., 1993; Housen et al., 2018) and gypsum (Nakamura et al., 2009), respectively (Fig. 4.1). However, both of these earth-sourced analogues have crushing strengths that are somewhat lower than those of the lunar analogous, perhaps because lunar regolith grains are more angular with a higher internal friction angle than their terrestrial counter parts. Nevertheless, in the simulations presented here only a very small fraction of the (high velocity) ejecta experiences pressures above 100 MPa, so the results are not expected to be very sensitive to uncertainty in the high-pressure portion of the regolith crush curve. A small number of test simulations showed that adopting a lower crushing strength for a uniform regolith target changes the value by less than 4%. The simulation parameters are summarised in Table 4.1.

Table 4.1: Material model parameters for simulations of the DART impact. In addition, thermal parameters from Ivanov et al. (2010) were used.

Description	**Symbol**	**Target**
Equation of state		Tillotson[a]
Strength model		ROCK/LUND
Poisson ratio	ν	0.25[b]
Damage strength at zero pressure (kPa)	Y_{d0}	0.1–100
Strength at infinite pressure (MPa)	$Y_{\inf}$	10^3
Internal friction coefficient	f	0.2–1.2
Porosity model parameters $(\epsilon - \alpha)^c$		
Initial porosity	ϕ_0	10–50%
Initial distension	α_0	1.1–2.0
Elastic volumetric strain threshold	ϵ_{e0}	$-2\text{x}10^{-6}$– $-2\text{x}10^{-9}$
Distension at transition to power-law	α_x	1.00
Exponential compaction rate	κ	0.80–0.98
Ratio of porous/nonporous sound speed	χ	1.00

[a]Tillotson (1962); [b]Ivanov et al. (2010); [c]Wünnemann et al. (2006).

4.4 Results for DART scenario

The numerical simulations in this chapter are divided into three distinct systematic parameter studies, aimed at investigating the isolated effects of cohesion (shear strength at zero pressure), Y_{d0}, initial porosity, ϕ_0, and the internal friction coefficient, f. Final crater dimensions, mass/velocity/launch-position distributions of the ejecta and, subsequently, the momentum carried away by the ejecta, $\beta - 1$, were calculated using results from simulations with different combinations of these numerical parameters.

4.4.1 The effect of target properties on crater diameter

As discussed before, the crater size is strongly linked with the amount of ejecta produced, and hence with the amount of momentum transferred. Furthermore, the scaled crater diameters provide a method for determining the scaling exponent, μ.

In this section,the effects of target properties on crater dimensions are investigated and the widely-used strength-regime crater scaling relationship Eq. (6.2) (see Chapter 2) are compared to the simulations results presented here. For all models, the derived scaling exponent, μ, ranges between the momentum scaling limit, $\mu = 1/3$, and the energy scaling limit, $\mu = 2/3$.

The strength-scaled crater diameters for target porosities $\phi_0 = 10\%$, 20% and 50%, and an internal friction coefficient $f = 0.6$, are plotted in Figure 4.2. These results have been plotted alongside experimental results from materials which seem to be appropriate analogs for porous rocky asteroid surfaces: weakly cemented basalt (WCB) (Housen, 1992), and sand/fly ash (SFA) (Housen and Holsapple, 2003).

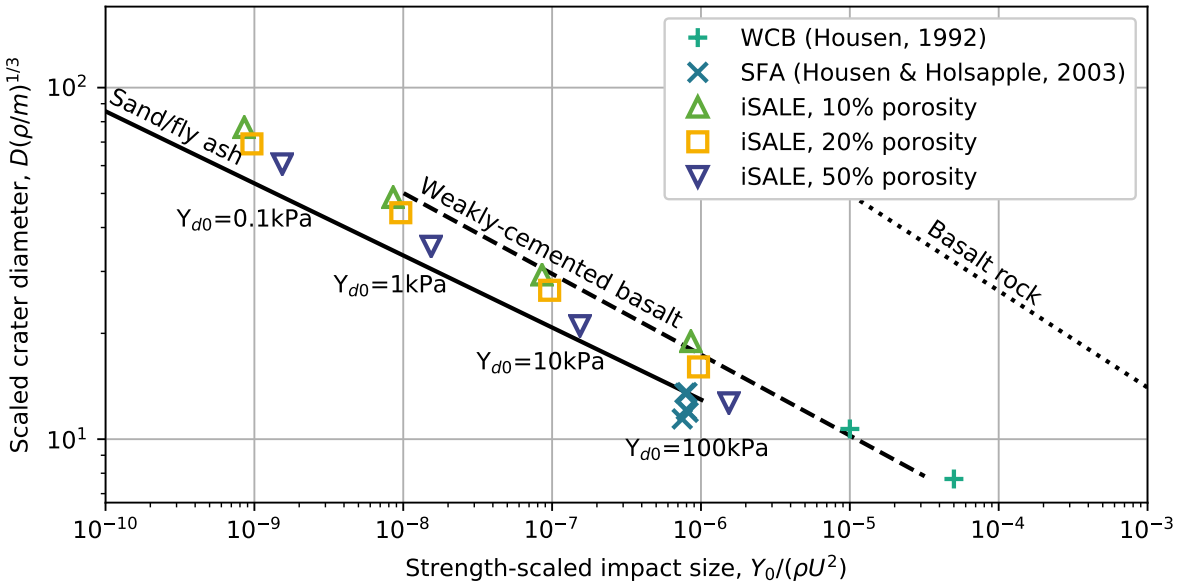

Figure 4.2: Scaled crater diameter as a function of strength-scaled impact size for iSALE simulations at 10%, 20% and 50% porosity, compared with the extrapolations of the experimental results for weakly-cemented basalt (WCB) ($Y = 0.09/0.45$ MPa) (Housen, 1992) and sand/fly ash (SFA) ($Y = 4$ kPa) (Housen and Holsapple, 2003). Note that the scaled crater diameter is the diameter of the formed crater, D, multiplied by the cube root of the target density, ρ, divided by the impactor mass, m, and is plotted against the strength-scaled impact size (the surface strength, Y_0) divided by the target density, ρ, and the square of the impactor velocity, U.

The numerical simulation results lie between the scaling law extrapolations of experimental data, and follow a power-law trend with a slope between $\mu = 0.40$ and $\mu = 0.43$, which is similar to the slope of the expected trend for WCB ($\mu = 0.40$) and SFA ($\mu = 0.46$). These results suggest that the crater diameters predicted by the numerical simulations are consistent with the existing scaling laws for analogous materials, from lab-scale impact experiments, when the lower cohesion of the targets are taken into account. The target material strength used in the numerical simulations was closer to the estimate of the asteroid's regolith strength (Heiken, 1991).

To isolate the effect of target cohesion, this work considered simulation results with different Y_{d0}, between 0.1 and 100 kPa, but with a fixed initial target porosity of 20% and a coefficient of internal friction of 0.6. As all simulated impact craters form in the strength regime, the crater dimensions are very sensitive to Y_{d0}. Crater excavation becomes more efficient as the target material strength exhibits less resistance to the crater growth. The crater diameters were found to vary from about 36 m at 0.1 kPa to about 9 m at 100 kPa. By least-square fitting the point-source scaling relationship in the strength regime, Eq. (6.2), to the scaled crater diameter, $D(\rho/m)^{(1/3)}$, as a function of strength-scaled impact size, $Y_{d0}/(\rho U^2)$, the velocity exponent, μ was derived. For this scenario, μ holds a value of 0.42 ± 0.01.

To measure the additional effect of porosity on the crater dimensions, this work considers the results of four series of simulations with initial target porosity between $\phi_0 = 10\%$ and $\phi_0 = 50\%$, and with a fixed coefficient of internal friction constant of $f = 0.6$. For each target porosity, the series of simulations included four different target cohesions, $Y_{d0} = 0.1$, 1, 10 and 100 kPa.

Consistent with previous work (e.g., Luther et al., 2018), as the porosity of the target material is increased the cratering efficiency decreases slightly. The presence of porosity leads to more energy being used in pore compaction, which leaves less energy available to displace material. On the other hand, with increasing porosity the material becomes less dense and easier to excavate. The results suggest that the former effect dominates slightly over the latter as an increase in target porosity from 10% to 50% leads to a decrease in crater diameter and crater volume of only 20%, while the crater depth remains almost the same.

Least-square fits of Eq. (6.3) through resulting crater dimensions at different porosities and different cohesive strengths, as illustrated in Figure 4.3a, determined the scaling exponent, μ, for each set of simulations. The μ parameter was found to slightly increase with target porosity, from $\mu = 0.40$ at 10% porosity to $\mu = 0.43$ at 50% porosity. This is contrary to expectation from some laboratory scale cratering experiments, but is consistent with recent numerical simulations of simple crater formation on the Moon

(Prieur et al., 2017).

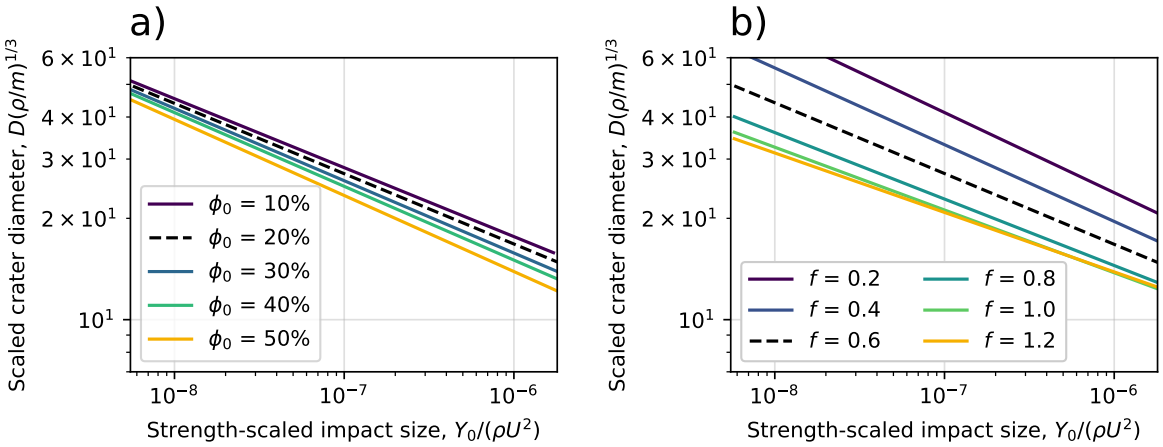

Figure 4.3: Least-square power-law fitting through normalised crater diameter, π_D as a function of strength-scaled impact size, π_3, in logarithmic scale, for asteroid targets with a) different initial porosities, ϕ_0 ($f = 0.6$ for all simulations) and b) different internal friction coefficients, f ($\phi_0 = 20\%$ for all simulations). In both plots, the dashed line represents the results for $\phi_0 = 20\%$ and $f = 0.6$.

To quantify the effect of the internal friction coefficient on crater dimensions, here are considered the results of six series of simulations with different coefficients of friction, f, between 0.2 and 1.2, and with a fixed initial porosity $\phi_0 = 20\%$.

Each simulations series included the same set of target cohesions $Y_{d0} = 1$, 10 and 100 kPa. An increase in f has the effect of significantly reducing the cratering efficiency. A larger coefficient of internal friction in the target material causes more energy to be used in deforming the target and leaves less to excavate the material out of the crater. The crater radius when $f = 0.2$ is more than twice the crater radius formed for $f = 1.2$ (Fig. 4.3b).

The μ exponent was found to decrease with increasing internal friction coefficient, from approximately $\mu = 0.48$ at $f = 0.2$, to approximately $\mu = 0.35$ at $f = 1.2$, which is close to the lower (momentum) theoretical limit for μ.

4.4.2 The effect of target properties on ejecta distribution

In addition to crater diameters, ejecta mass/velocity/launch-position distributions for each simulation was also quantified. This section describes the effect of cohesion, porosity

and internal friction coefficient on the ejecta distributions.

Cohesion

Figure 4.4a shows the cumulative normalised ejecta mass at speeds larger than v, $M(>v)/m$, as a function of normalised ejection velocity, v/U, for four impacts simulations into targets with $\phi_0 = 20\%$, $f = 0.6$ and Y_{d0} between 0.1 kPa and 100 kPa. The results show that the fast ejecta ($v/U > 10^{-2}$) follow the same mass-velocity distribution, regardless of the cohesion; the effects of varying Y_{d0} being negligible. However, towards the end of crater growth when material is ejected at slower speeds, Y_{d0} becomes increasingly important. In the strength regime, the cohesion is the dominant stress that stops the crater from growing and as Y_{d0} is decreased, crater growth continues longer, leading to a greater total ejected mass and more material ejected at a given velocity in the latter portion of crater growth.

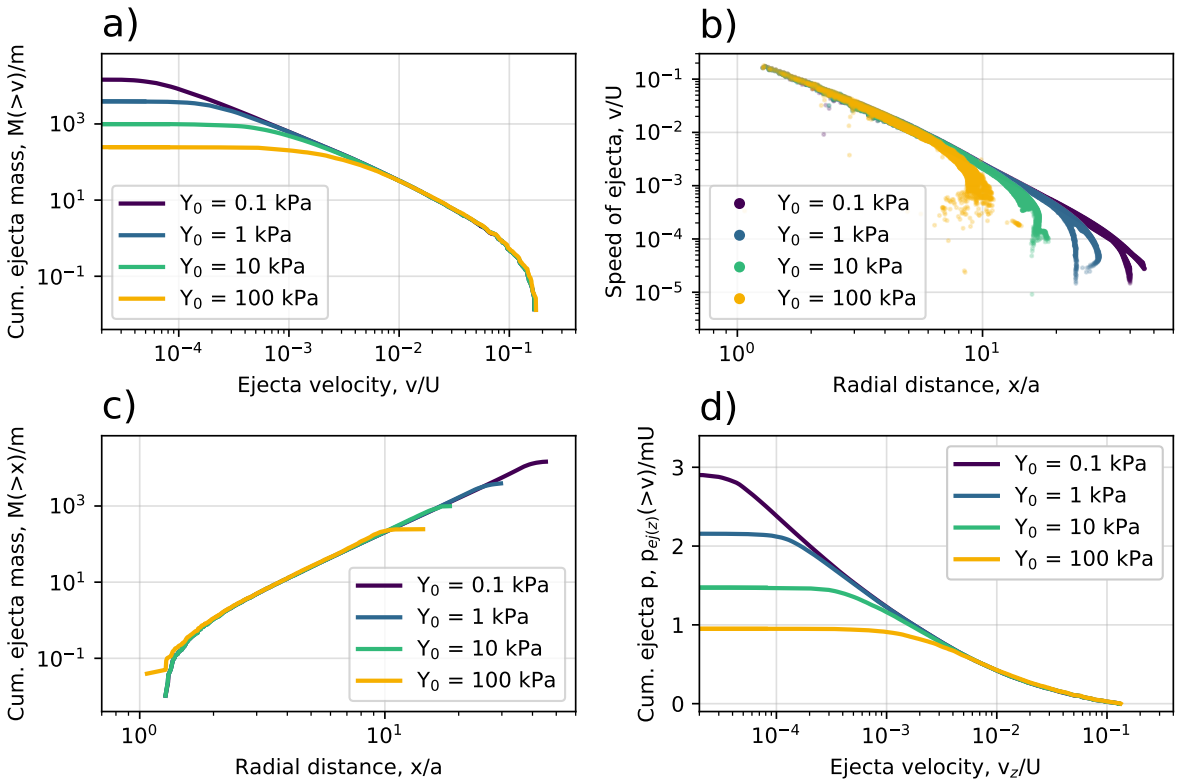

Figure 4.4: Mass-velocity-launch position distribution of ejecta for four different strengths: 0.1, 1, 10 and 100 kPa, for a target with $\phi_0 = 20\%$ and $f = 0.6$.

Ejecta measurements of normalised ejecta speed, v/U, as a function of normalised

launch position, x/a, from the same simulations are plotted in Figure 4.4b. Again, the fast ejecta from the four simulations, launched at similar distances from the impact point, x/a, have the same speed, following the same power-law distribution. An increase in the target cohesion stops the crater from growing, and the launch of ejecta, at a smaller radius. The relatively large scatter in radial distance (launch position) among the slowest ejecta is because this is material ejected from the uplifted rim region with sufficient speed to overcome the cohesive strength of the target.

Figure 4.4c shows the normalised mass of ejecta launched within a radius x, $M(< x)/m$, as a function of normalised launch position, x/a. In this case, the ejecta distributions from the four simulations are very similar. While the cohesion does not influence the amount of ejected mass at a given launch position, it does dictate the maximum radial distance at which particles are ejected, for a given crater.

The ejecta mass-velocity distributions were integrated to determine the cumulative, vertically ejected momentum, $p_{ej(z)}/mU = (\beta - 1)$, as a function of ejection speed in the vertical direction v_z (Fig. 4.4d). Most of the ejecta momentum resides in the slowest ejecta, which is last to leave the crater. The total ejected momentum depends strongly on the total ejected mass (and crater size) and, hence, Y_{d0}. This leads to $\beta - 1$ values between $\approx$1.0 and $\approx$3.0.

Porosity

An increase in target porosity causes the tracer particles close to the impact point to be ejected at lower speeds compared to the less porous cases, as illustrated in Figure 4.5a. For porous targets, more of the energy imparted from the impactor is used to compact the pores, making less available to set the target material in motion and eject material. In addition, as the target is made more porous, the ejected material becomes less dense and so less total mass is ejected from the same radial distance, compared to the denser lower porosity targets. As a consequence, the total momentum transferred by the ejecta, normalised by the impactor momentum, $\beta - 1$ decreases with increasing porosity, as shown in Figure 4.5b. $\beta - 1$ was found to vary between 1.1 at $\phi_0 = 50\%$ and 2.7 at $\phi_0 = 10\%$.

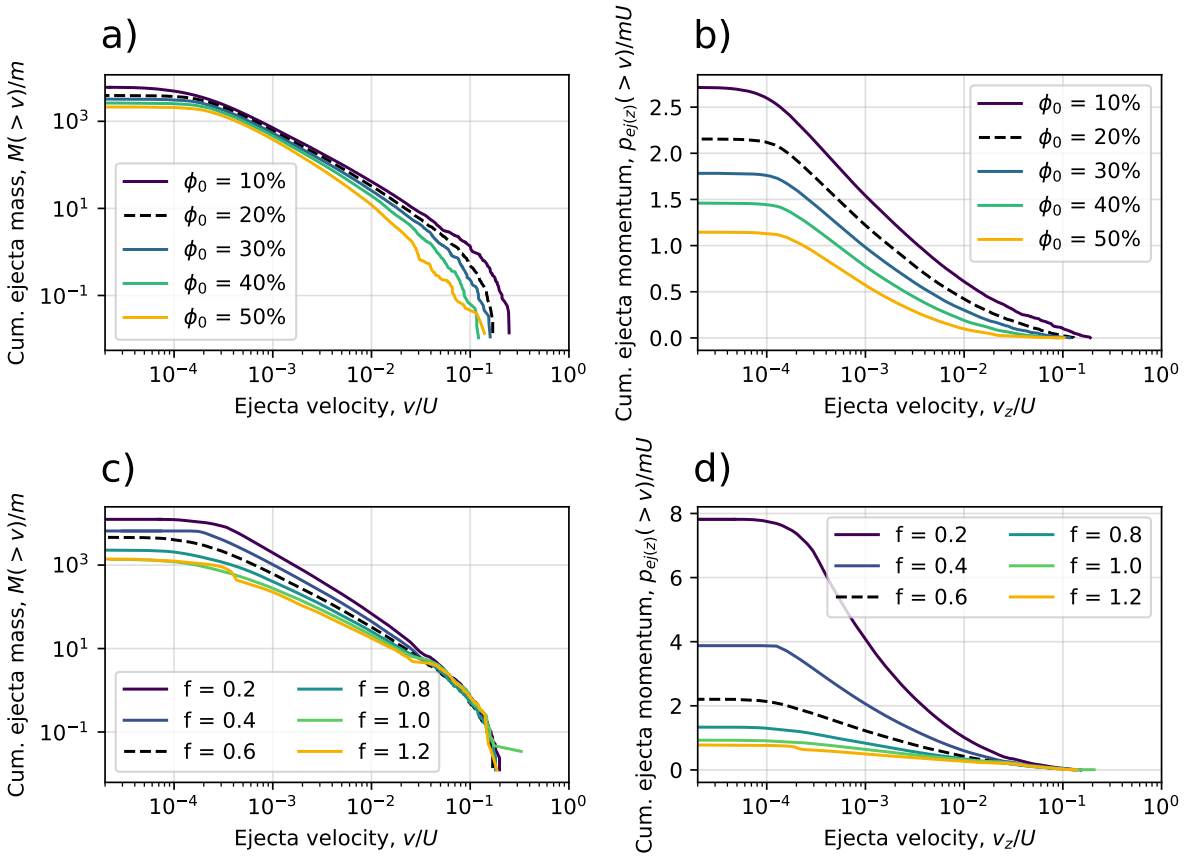

Figure 4.5: Normalised ejected mass at speeds greater than v, as a function of normalised ejection speed, v/U, and total ejected momentum $(\beta - 1)$ as a function of normalised ejection velocity. a) and b) represent the ejecta distributions for impacts into targets with $Y_{d0} = 10$ kPa, $f = 0.6$ and ϕ_0, between 10% and 50%. c) and d) represent ejecta distributions for impacts into targets with $Y_{d0} = 10$ kPa, $\phi_0 = 20\%$ and f, between 0.2 and 1.2.

Internal friction coefficient

Near the impact site, the friction coefficient has little or no influence on the ejecta distribution. The normalised ejected mass $M(> v)/m$, plotted against the normalised ejection speed, v/U, in Figure 4.5c, shows that the effects of coefficient of friction are only visible for $v/U < 5 \times 10^{-2}$. With increasing f, more energy is needed to deform the target and this has the effect of slowing down the ejection speed of the tracers ejected at the same radial distance.

In terms of total momentum transfer, because increasing the coefficient of friction has the effect of slowing down the ejecta, less momentum is carried away by the ejected particles. The difference between $\beta - 1$ at high f (0.6 to 1.2) is very large compared with

the cumulative ejecta momentum at low f (0.2 to 0.4) as seen in Figure 4.5d.

The behaviour of the ejecta in the numerical simulations is consistent with impact experiments. Housen and Holsapple (2011) compared the ejection velocity from impacts into dry sands ($\phi_0 \approx 30$–40%), with ejection velocities from impacts into porous silicates and sand mixtures ($\phi_0 \approx 55$–83%), and noted that the highly porous materials had much lower ejecta velocity compared to the less porous sands. Luther et al. (2018) also observed a similar trend in their numerical impact simulations in the gravity regime.

When comparing the ejection velocity from impact experiments into materials of different internal friction coefficients, no clear trend was determined (Housen and Holsapple, 2011). They note that impact experiments into glass micro-spheres ($f \approx 0.35$) (Yamamoto et al., 2005) produced a much higher ejection velocity compared to impacts into sand ($f \approx 0.50$–0.60). However, the results were not reproduced by Housen (2011, unpublished) so Housen and Holsapple (2011) concluded that the higher velocity might be produced by other material properties. The observed trend for the ejection velocity is again consistent with numerical impact simulations in the gravity regime (Luther et al., 2018).

4.4.3 The effect of target properties on ejection angle

Figure 4.6a shows the ejection angle as a function of radial distance for impact simulations into targets with $Y_{d0} = 10$ kPa, $f = 0.6$ and varying porosity, ϕ_0. The fast ejecta exhibits steeper ejection angles at lower porosities, compared to the higher porosity targets. However, the ejection angle is converging at radial distances larger than $4a$.

Figure 4.6b shows the ejection angle from impacts into targets with $Y_{d0} = 10$ kPa, $\phi_0 = 20\%$ and varying internal friction coefficient, f. The ejection angle decreases with launch position, by up to 20°. At the same time, the average ejection angle decreases with increasing coefficient of internal friction, between about 60° for $f = 0.2$, to about 30° for $f = 1.2$ Similar trends have been observed for impact into gravity regime (Luther et al., 2018).

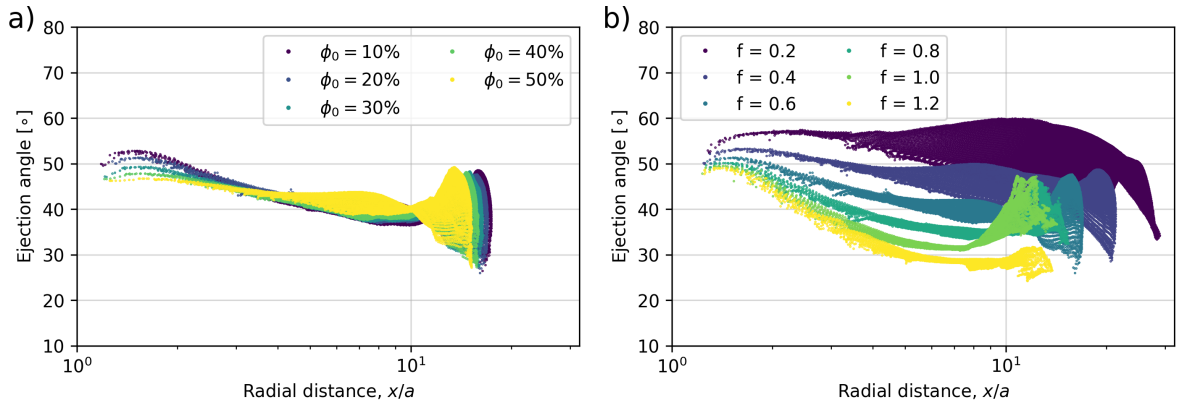

Figure 4.6: Ejection angle as a function of launch position from impacts into 10 kPa targets and (a) varying porosity between 10% and 50% and (b) varying coefficient of internal friction between 0.2 and 1.2.

4.5 The DART impact simulated in three dimensions

The numerical simulations presented in Section 4.4 provide insight to inform future impact deflection missions. However, an important limitation of these numerical simulations is the use of a two-dimensional domain geometry, which restricted the study to vertical impacts, with axially-symmetric ejecta distributions. In such scenarios, the net ejecta momentum is antiparallel to the impact direction, resulting in maximum efficiency of momentum enhancement by ejecta. In reality, the DART spacecraft will likely impact Didymoon's surface at an oblique angle (Cheng et al., 2018), which will produce an asymmetric distribution of ejecta with a net momentum vector that points in a different direction to the impact trajectory. Simplified, 2D impact simulations were used here for computational expediency to allow for a wide range of target properties to be investigated.

4.5.1 The DART impact in 2D vs 3D

To quantify whether model geometry and impact angle play a significant role in momentum transfer, the same vertical impact scenario in iSALE-2D and in iSALE-3D was simulated. The scenario considered was a DART impact into a homogeneous half-space, with the cohesional strength of the damaged material, $Y_{d0} = 10$ kPa, coefficient of internal friction, $f = 0.6$, and initial porosity, $\phi_0 = 20\%$.

Figure 4.7 shows the mass-velocity-launch position ejecta distributions from iSALE-

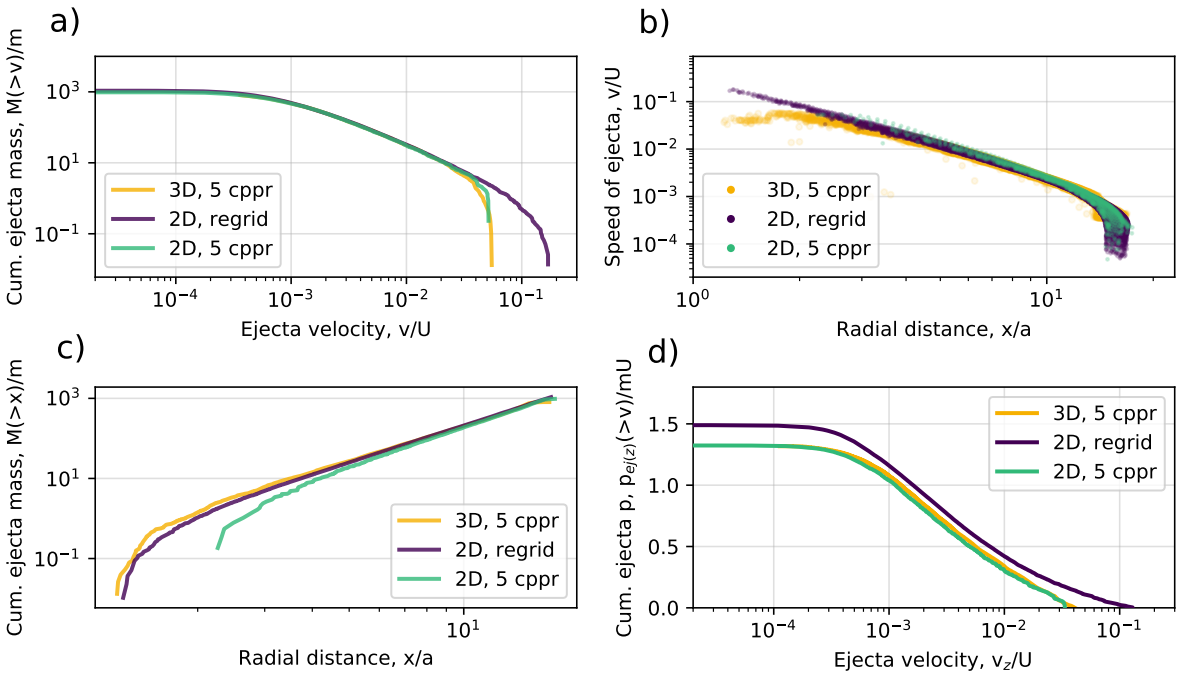

Figure 4.7: Mass-velocity-launch position distribution of ejecta from iSALE-2D simulations at 40 cppr and 5 cppr, compared with ejecta distribution from iSALE-3D at 5 cppr.

2D and iSALE-3D. The three-dimensional (3D) simulation was limited to a spatial resolution of 5 cppr (3D, 5 cppr). Comparison with a 2D simulation of the same resolution (2D, 5 cppr) demonstrates consistency between iSALE2D and iSALE3D results (Fig. 4.7). The cumulative ejecta mass converges to $\approx 10^3 \times m$ in all three impact simulations, where m is the impactor mass. Compared to the results of the equivalent high-resolution 2D simulation where regridding was used (2D, regrid), however, the 3D simulation results under-predict the cumulative ejected momentum, principally because of a failure to capture the fastest ejecta—known to require high spatial resolution at early times (Johnson et al., 2014). These fast particles, although of low mass, add ≈10% to the normalised cumulative ejected momentum (Fig. 4.7d). One aspect of note is that in the 3D simulation the ejecta with the same launch speed appears to originate from a wider range of radial distances (Fig. 4.7b), which is an effect of azimuthal averaging.

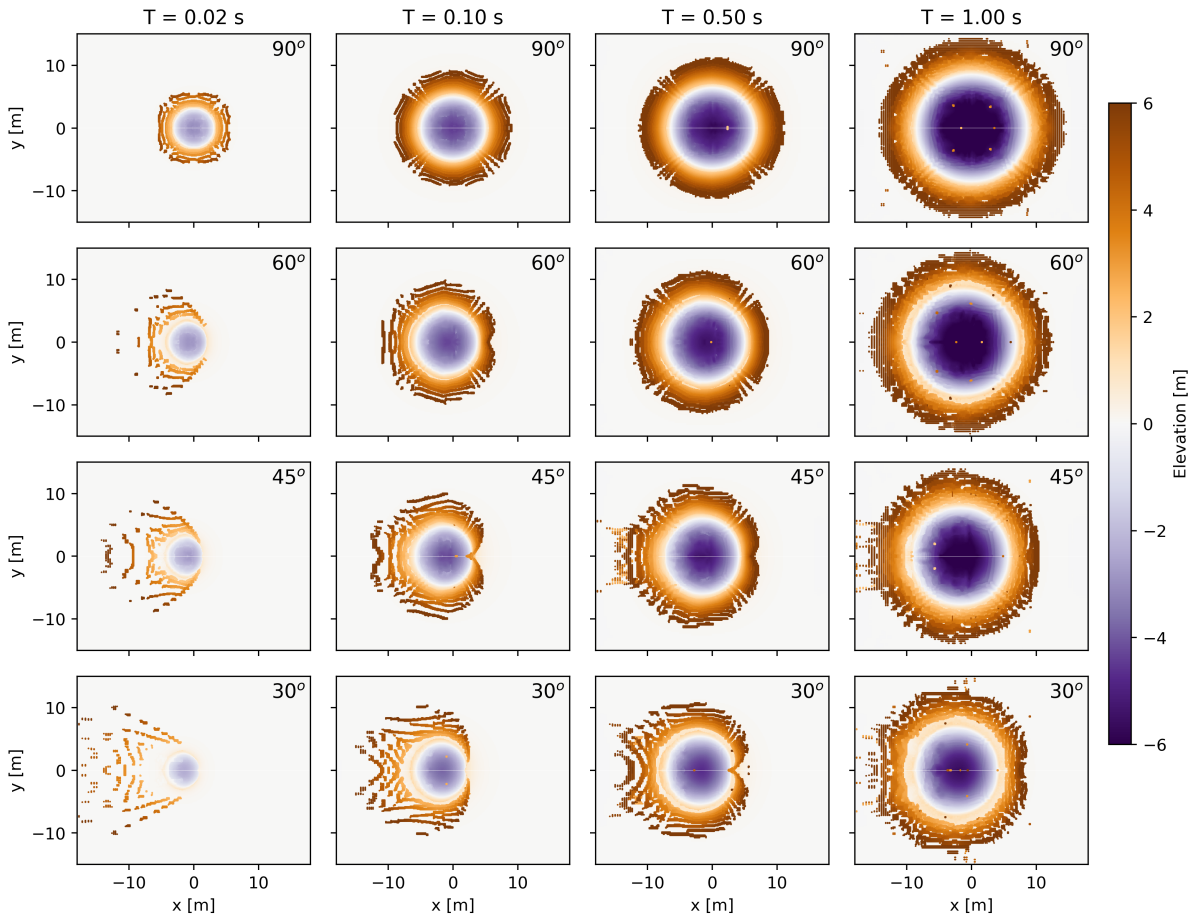

Figure 4.8: Surface topography of the DART impact at 90, 60, 45 and 30 degrees angles, captured at four different times: 0.02 s, 0.10 s, 0.40 s and 1.00 s. The impact direction is right to left.

4.5.2 Influence of the impact angle on the net momentum

Figure 4.8 shows the surface topography of a vertical DART impact, at 90° angle of incidence, and oblique DART impacts, at 60°, 45° and 30° angle. The impact speed is the same in all simulations; all other impactor and target properties are the same. The time-frames of the oblique impact (Figure 4.8b) show a highly asymmetric ejecta distribution at early times of the cratering process < 0.10 s, compared to the same times in the vertical impact (Figure 4.8a). The asymmetric ejecta flow becomes more symmetric as the crater grows towards its final size.

The asymmetry in the ejecta flow is also illustrated by the velocity-launch position distribution of the ejected particles from the oblique impacts at 60, 45 and 30 degrees angle of incidence (Fig. 4.9). In all cases, the speed of the ejecta, v, was normalised

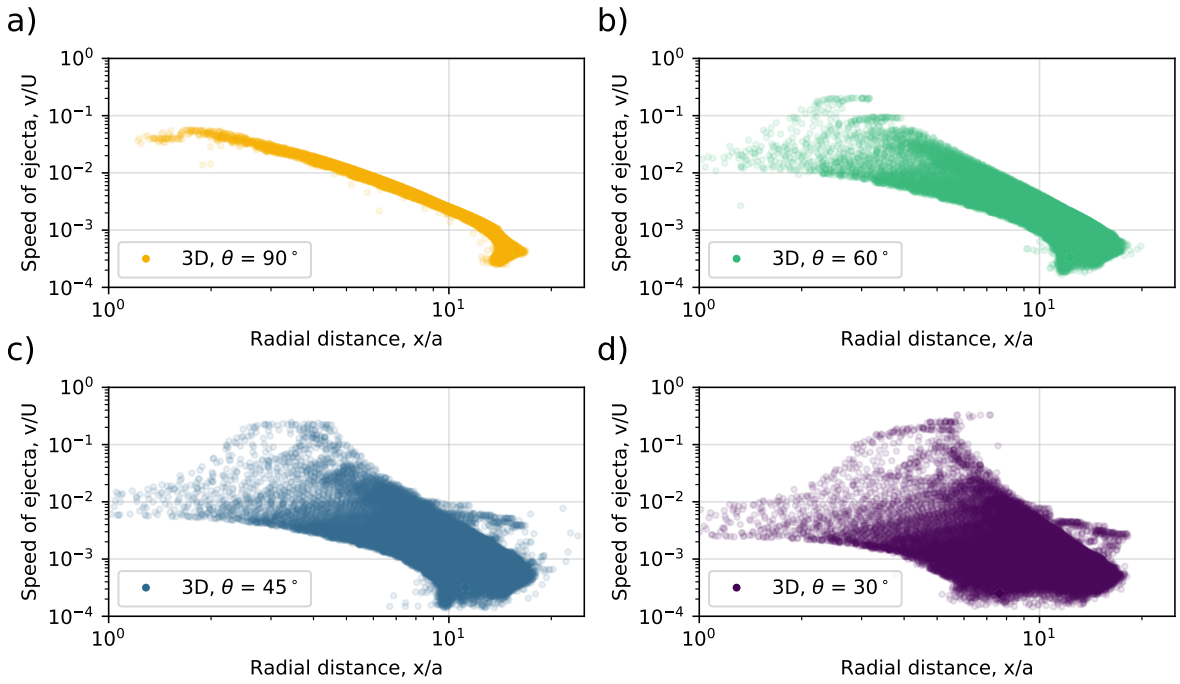

Figure 4.9: Velocity launch position distribution of the ejecta from impacts at 90, 60, 45 and 30 degrees angle of incidence.

by the impact speed, U, and plotted as a function of launch position, x, normalised by the impactor radius, a. The origin was chosen as the impact point. The ejecta from the oblique impacts displays higher speeds and lower ejection angles in the downrange direction, and lower speeds and higher ejection angles in the uprange direction of the impact. This is consistent with previous laboratory-scale oblique impact experiments (Schultz, 1999; Anderson et al., 2003) and DART impact models (Stickle et al., 2015).

The asymmetry of the ejecta can have important implications for momentum transfer. The net momentum of the target after the impact is the vector sum of the impactor momentum and the momentum enhancement vectors. Figure 4.10 shows the direction of the momentum vectors for the vertical ($\theta = 90°$) and oblique impacts ($\theta = 60°$, $45°$ and $30°$). The projectile imparts an initial momentum along the impact direction. As most of the ejecta momentum is carried away in the downrange direction, the momentum imparted to the target is mostly in the uprange direction. The sum between the impactor momentum and the momentum enhancement vectors is therefore between the vertical and the downrange direction.

Figure 4.11 shows the direction of the ejecta momentum (Fig. 4.11a) and the

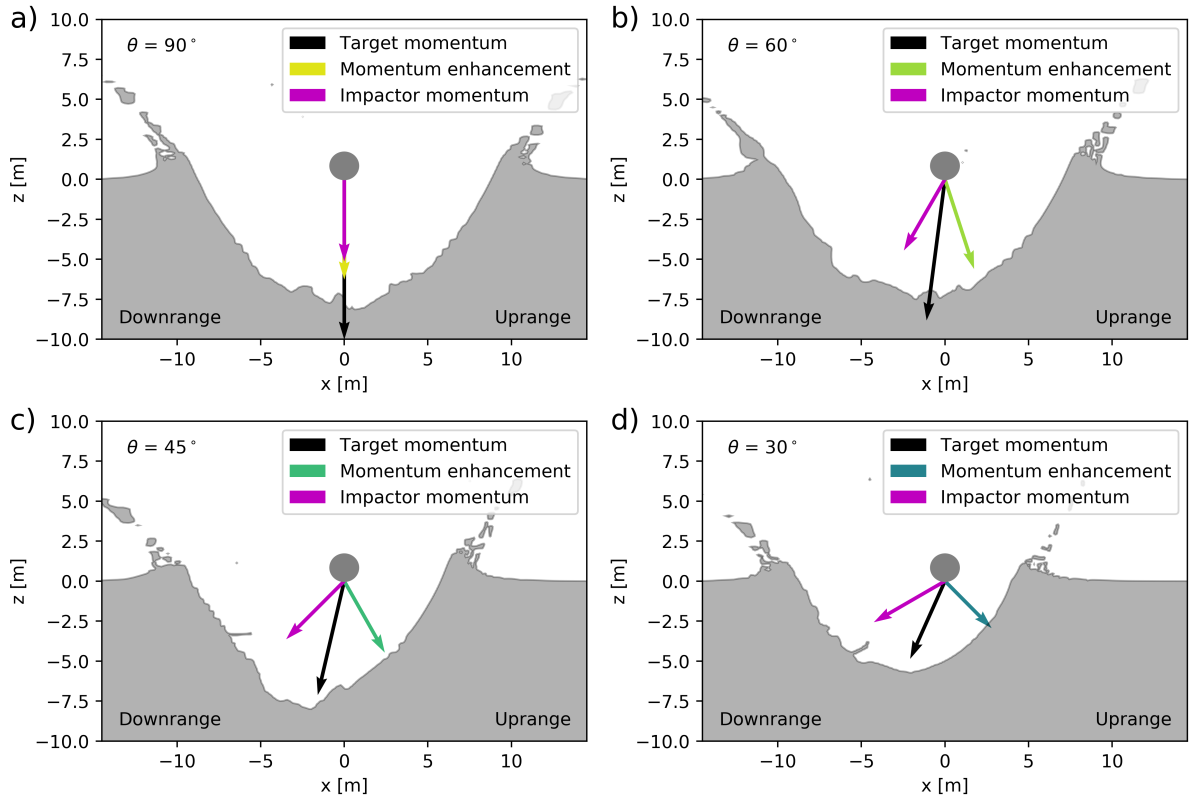

Figure 4.10: Crater profiles showing the direction of the momentum vectors. The impactor momentum is the momentum imparted directly from the impactor, the momentum enhancement is imparted by the ejected particles and the target momentum is the net momentum of the target, after the impact. The impact direction is right to left.

direction of the total momentum (Fig. 4.11b), as a function of time, for the different impact angles. As the crater grows towards its final diameter, the uprange direction of the ejecta momentum becomes more perpendicular to the surface. The direction of the net momentum imparted on the target also changes, from the downrange direction, towards the vertical direction. In the scenarios simulated here, for impacts into a 10 kPa target, the direction of the net momentum at the end of the crater growth is about 83° for the 60° impact, ≈ 77° for the 45° impact and ≈ 66° for the 30° impact.

Here, the crater growth is halted by the target strength before the total momentum direction becomes vertical. However, it is expected that with increasing cratering efficiency (e.g. decreasing strength), the ejecta momentum will have a larger contribution towards the total momentum vector, which will tend to 90°. To test this, more numerical simulations of oblique impacts into targets with lower strength are needed, however due to the increased cratering efficiency, such simulations are very computationally expensive.

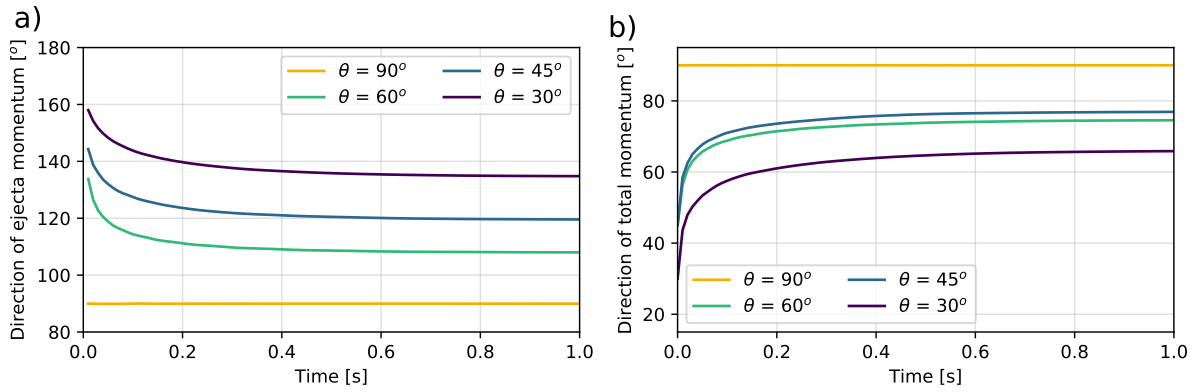

Figure 4.11: Direction of the (a) ejecta momentum and (b) total momentum from vertical, 90°, and oblique, 60°, 45° and 30°, angle of incidence. The direction is measured anticlockwise from the negative x-axis (downrange, 0°) to the positive x-axis (uprange, 180°).

Figure 4.12 shows the cumulative ejecta momentum, normalised by the vertical component of the impactor momentum, as a function of ejecta velocity, normalised by the vertical component of the impact velocity. In the oblique impacts scenarios, the vertical component of the fast ejecta adds up to 40% more momentum to the momentum of the ejecta, compared to a vertical impact. However, the total normalised ejecta momentum is within 10% of the ejecta momentum from an equivalent vertical impact.

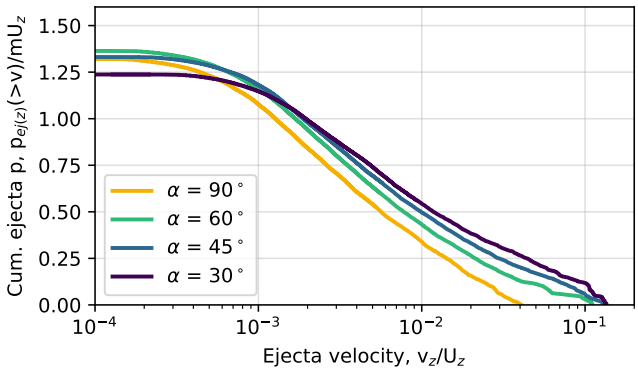

Figure 4.12: Cumulative ejecta momentum normalised by the vertical component of the impactor momentum, as a function of ejecta velocity, normalised by the vertical component of the impact velocity, for vertical and oblique impacts.

4.6 Discussion

4.6.1 Implications for the DART mission

The simulations presented in this thesis deliberately considered impactor and target parameters appropriate for the DART mission and the Didymos asteroid system, allowing to directly relate the numerical results to the DART impact and infer possible deflection outcomes.

In all of the numerical simulations, the asteroid deflection was amplified by the impact ejecta, i.e. $\beta - 1 > 0$. However, the amount by which the deflection was amplified depended strongly on the target properties. Figure 4.13 shows the momentum carried away by the ejecta, $\beta - 1$, for different impact scenarios, as a function of target porosity and at different target strengths. It was found that $\beta - 1$ can vary between 0.5 and 3.5.

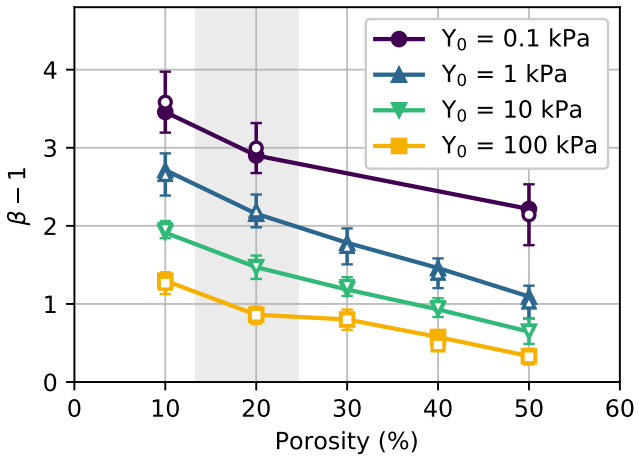

Figure 4.13: Total ejected momentum in the z direction $\beta - 1$ for four different cohesions and different porosities of the target. The numerical value of the ejected momentum (filled symbols) is compared with the analytical approximation of $\beta - 1$ (hollow symbols). The grey shaded region is the current estimate of the ϕ_0 of Didymos (Scheirich and Pravec, 2009).

Impacts into porous targets at Y_d0 between 0.1 and 100 kPa were investigated and it was found that the amount of momentum transferred from the impactor is mainly dictated by the cohesive strength of the target. The weaker the target, the more deflection should be expected. Unfortunately, for DART, it is not possible to measure the cohesive

strength of the target before the impact or to select the impact site. DART could hit anything from a smooth, very weak terrain, with Y_{d0} even lower than the investigated range, which would provide a very large deflection of the asteroid, or it could hit a strong boulder, which could result in almost no momentum enhancement.

The porosity of the surface material can also influence the deflection, but not as considerably as the cohesive strength. An increase in porosity of 10% can decrease $\beta - 1$ by up to 0.5, for a given target material. However, assuming the primary and secondary objects of the Didymos system have the same density, one can approximate the porosity of Didymoon before the impact (Scheirich and Pravec, 2009), and the current estimate is highlighted in Figure 4.13. The coefficient of internal friction can also have a large effect on the momentum transfer, but given the current knowledge of asteroid materials, the most probable range for f is between 0.4 and 0.8.

Taking into account these predictions for the Didymos asteroid system, the expected enhancement resulting from the DART impact is $\beta - 1$ between about 1 and 3, implying a momentum multiplication factor of between 2 and 4. These values are consistent with previous work, where similar targets were used. For example, Syal et al. (2016) found $\beta \approx 4$ for a 20% porous target with a cohesion of 1 kPa. On the other hand, Cheng et al. (2016), Housen and Holsapple (2012), Jutzi and Michel (2014), and Stickle et al. (2015), found β values between about 1 and 2 for experiments and simulations in which much stronger targets (cohesions of a few MPa) were used. These results reinforce the conclusion that for impacts on small asteroid surfaces β is most sensitive to the cohesion of the target.

4.6.2 Ejecta scaling relations for vertical impacts

The simulation results presented here also prompt a closer inspection of the ejecta mass-velocity-launch position distributions and comparison with the recently refined ejecta scaling relationships of Housen and Holsapple (2011). In particular, an ongoing controversy is whether impact crater dimensions and ejecta distributions from impacts in the same material produce consistent values of the velocity exponent μ and what, if anything,

this means for the suitability of the point-source approximation. This work also seeks to verify the analytical estimate of the ejecta momentum transfer, $\beta - 1$, presented by Cheng et al. (2016).

Examining the velocity distribution of ejecta as a function of launch position, three regimes of ejection velocity behaviour are apparent (Housen and Holsapple, 2011), as illustrated in Figure 4.14. The mid-ranged ejecta follows a power-law distribution, which is well described by the Housen et al. (1983) ejection model. This power-law behaviour breaks down close to the crater rim, where the ejection velocity rapidly decreases. An empirical correction to account for this behaviour was introduced by Housen and Holsapple (2011) in their revised ejection model. However, close to the impact point there is the coupling zone, where the projectile is still transferring its energy and momentum to the target. In the simulations, the ejection velocity in this zone is slower than the extrapolated power-law distribution identified for the mid-range ejecta and neither analytical model accounts for this behaviour. The transition between the regimes is gradual and the radial range of each stage is dependent on the projectile and target properties (Hermalyn and Schultz, 2010). For impacts with low cratering efficiency, the coupling stage becomes more important and covers a larger portion of the crater growth time (Schultz, 1988), transitioning directly into the near-rim regime and causing the power-law regime to be almost or entirely non-existent.

In most previous studies of ejection velocity behaviour, both experimental and numerical data were interpreted in the context of the Housen et al. (1983) or Housen and Holsapple (2011) ejection models. However, in several cases this has resulted in μ-values being determined from ejecta data that are inconsistent with the μ-value determined from crater size measurements for the same target material (Cintala et al., 1999; Luther et al., 2018; Tsujido et al., 2015; Yamamoto et al., 2017). This has raised doubts about the applicability of the ejecta scaling relationships and questions regarding how to best determine μ for a particular target material. The work in this chapter investigates the circumstances under which consistency can be achieved between μ values determined from both crater scaling and ejecta scaling.

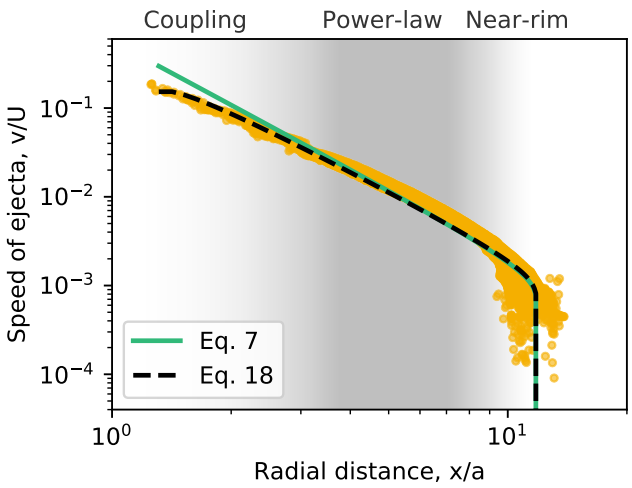

Figure 4.14: Normalised ejection speed, v/U, as a function of normalised launch position, x/R for an impact into a target with 1 kPa cohesion and 20% porosity. The ejecta distribution has three distinct regions: coupling zone, power-law region and near-rim region, denoted by the background shading.

To study this problem further, this work compared values of the velocity exponent, μ, determined by fitting the Housen et al. (1983) power-law (Eq. (2.15)) to ejecta data; by fitting the Housen and Holsapple (2011) ejecta scaling relationship (Eq. (2.16)) to ejecta data; and by fitting the strength-regime crater scaling relationship (Eq. (6.3)) to crater size data. According to the point-source theory, the scaling exponent μ determined from ejecta should be consistent with that determined from the crater scaling.

To fit the Housen et al. (1983) ejecta scaling relationship, Eq. (2.15), to the ejecta data a least-squares fitting algorithm was used, applied only to the power-law regime of velocity-launch position distribution; in other words, the fast and the slow ejecta in the coupling zone, and near-rim zone, respectively, were excluded from the analysis. However, due to the gradual transition between the ejection zones, it is difficult to choose the appropriate limits on the launch distance x for fitting. To account for the coupling zone (fast ejecta), the ejecta with a radial distance $x < 4a$, where a is the impactor radius, was excluded. To exclude the slow ejecta, only the ejected particles from within $x < 0.74R$, where R is the crater radius was considered. These choices of threshold radii were chosen based on the range of ejecta behaviour observed in the simulations and have proven to give good results, as discussed below. To note, however, that together they

place a lower limit of ≈ 6 on the cratering efficiency of impacts that can be used to derive a power-law ejecta trend, because of the requirement that $4a < 0.74R$. The fitting algorithm was set to return values for the scaling exponent μ and the constant C_1, while the other constants were fixed: $n_1 = 1.2$, $n_2 = 1$ and $\nu = 0.4$ (Housen and Holsapple, 2011).

When fitting Eq. (2.16) to the ejecta data, the entire range of the ejecta velocity-launch position distribution was considered. In this case, the fitting algorithm set C_1 and μ as free parameters, while the other constants were fixed. The p constant was also fixed, at $p = 0.2$, in order to reduce errors in the fitting algorithm. Previous studies used larger p values, 0.5 for basalt rock, 0.3 for WCB and 0.2 only for perlite/sand mixture (Housen and Holsapple, 2011).

Figure 4.15 shows the scaling exponent μ returned by the fitting algorithm for ejecta data from each simulation, as a function of cohesion, Y_{d0}, porosity, ϕ_0, and coefficient of internal friction, f. The scaling exponent, μ, obtained from the power-law (Eq. (2.15)) fitting is represented by filled markers, while the μ obtained from fitting Eq. (2.16) is represented by hollow markers. The two sets of scaling exponents are compared to the μ-value determined from crater scaling (see Section 4.4.1), which are represented by the shaded grey region. The results presented here show that the scaling exponent μ determined using a simple power-law (for $4a < x < 0.74R$) is in good agreement with the μ-value obtained from crater size scaling, while using (Eq. (2.16)) produces μ-values that are systematically larger.

4.6.3 A revised ejecta scaling relationship

To avoid the need for somewhat arbitrary exclusion of some ejecta data to determine the velocity exponent μ by a simple power-law fit, this work also considered a modified version of the Housen and Holsapple (2011) ejection model Eq. (4.1) that attempts to account for the coupling zone of the ejecta distribution. The revised expression includes an additional term dependent on the n_1 cut-off constant, the impactor radius, a, and a

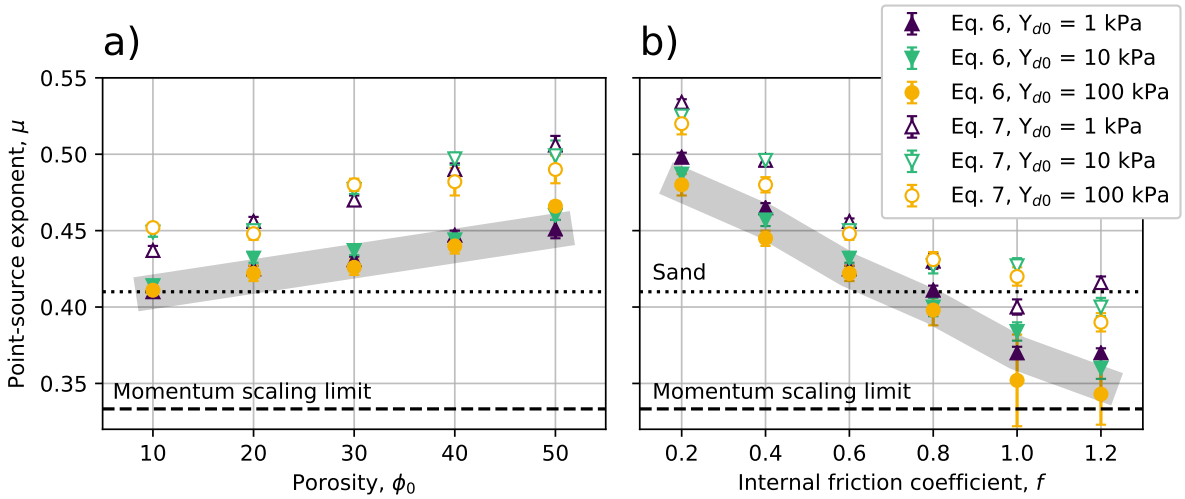

Figure 4.15: Ejecta velocity-launch position distribution fitting results. Filled markers represent the results from fitting Eq. (2.15) (Housen et al., 1983), hollow markers denote results from fitting Eq. (2.16). a) the scaling exponent μ is presented as a function of porosity, for fixed coefficient of internal friction, $f = 0.6$; b) the scaling exponent μ is presented as a function of internal friction coefficient, for fixed porosity, $\phi_0 = 20\%$. The shaded area represents the crater scaling results.

new fitting constant, q

$$\frac{v(x)}{U} = C_1 \left[\frac{x}{a}\left(\frac{\rho}{\delta}\right)^{\nu}\right]^{-\frac{1}{\mu}} \left(1 - \frac{x}{n_2 R}\right)^{p} \left(1 - \frac{n_1 a}{x}\right)^{q}. \tag{4.1}$$

Preliminary studies showed that q holds a value between 0.1 and 0.2. It is also important to note that this equation only holds for $x > n_1 a$ and $x \leq n_2 R$.

To test this new approach, this work used a least-squares method to fit Eq. (4.1) to the simulation model data, and determine the scaling exponent μ. Figure 4.14 shows the best fits of Eq. (2.16) and of Eq. (4.1) (dashed line), to the velocity-launch position distribution of the ejecta from an impact simulation with $Y_{d0} = 10$ kPa, $f = 0.6$, and an initial porosity of 20%. Eq. (4.1) was fitted to the entire range of the data, while Eq. (2.16) was only fitted through the power-law and the near-rim regions. Even though the two equations appear quite similar graphically, they return different values for the fitting constants. Figure 4.16 shows the velocity exponent μ as a function of porosity and internal friction coefficient, obtained by fitting Eq. (4.1) to the ejecta data. In almost all cases, fitting Eq. (4.1) to the model data results in μ-values that are consistent between ejecta scaling and crater scaling, and this is achieved without any exclusion of ejecta data

or choice regarding the radial range over which power-law behaviour is present.

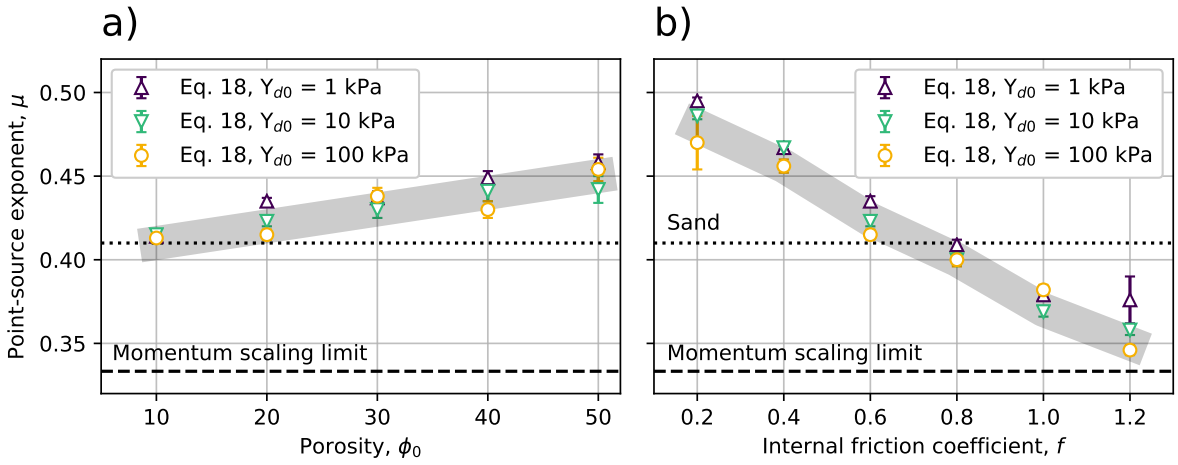

Figure 4.16: Results for the point-source exponent, μ, obtained by least-square fitting Eq. (4.1)) to the model data. μ is determined for three different target cohesions (Y_{d0} = 1, 10, 100 kPa) and plotted as a function of (a) porosity and (b) coefficient of internal friction.

4.6.4 Practical application of ejecta scaling

When comparing the fitting constants found from the numerical simulations presented here with the ones found from laboratory experiments, there are several discrepancies: Extrapolating from impact experiments, it was expected that μ decreases with increasing initial target porosity. The numerical results presented here show however that an increase in the target porosity, from 10% to 50%, leads to a an increase in μ, from ≈ 0.40 to ≈ 0.46 (Fig. 4.16a). These values are also consistent with the μ found from the crater scaling (Section 4.4.1). Note however that this trend cannot be extrapolated to the no porosity case, where significantly larger μ values were found by Prieur et al. (2017).

Also from experiments, it was noted that targets with lower μ generally also have a lower C_1, but the studies presented here showed that C_1 decreases as μ increases (Cheng et al., 2016). The k parameter value fluctuates as a function of porosity, between 0.37 and 0.45, but there is no clear trend that can be inferred.

Impact experiments into basalt rock ($\phi_0 \approx$ few %), found $\mu = 0.55$ and $C_1 = 1.5$ (Gault et al., 1963; Housen and Holsapple, 2011), impacts into weakly-cemented basalt (WCB) ($\phi_0 \approx 20\%$) found $\mu = 0.46$ and $C_1 = 0.18$ (Housen, 1992; Housen and Holsapple,

2011), while impacts into sand fly-ash (SFA) ($\phi_0 \approx 45\%$) found $\mu = 0.40$ and $C_1 = 0.55$. This trend is in contradiction with the results of this work and suggests that it is not straightforward to compare values of μ and C_1 determined from experiments for a specific target material with numerical simulations using idealised material models, as other material properties might be involved and play an important role in the response of real materials (Table 4.2).

Table 4.2: Impact ejecta scaling parameters for Basalt, WCB, SFA and numerical simulations from this work ($\phi_0 = 10\%$–50% and $f = 0.6$). For all cases ν=0.4, n_1=1.2, n_2=1.0.

Target	$\boldsymbol{\phi_0}$	$\boldsymbol{\mu}$	$\mathbf{C_1}$	**k**
Basalt[a]	few%	0.55	1.50	0.3
WCB[b]	20%	0.46	0.18	0.3
SFA[c]	45%	0.40	0.55	0.3
iSALE	10%	0.41	1.58	0.4
iSALE	20%	0.42	1.06	0.4
iSALE	30%	0.43	0.80	0.4
iSALE	40%	0.44	0.58	0.4
iSALE	50%	0.45	0.41	0.4

[a]Housen and Holsapple (2011); [b]Housen (1992); [c]Housen and Holsapple (2003).

When increasing the coefficient of internal friction, the point source exponent, μ, decreases from 0.48 to 0.35 (Fig. 4.16b). This behaviour of the ejecta and the determined μ are again consistent with the crater scaling constants determined in Section 6.1. With increasing f, C_1 also increases from 1 to 1.8. While the k constant remained almost constant when varying the porosity of the target, when increasing coefficient of internal friction, k slowly decreases from 0.5 for $f = 0.2$, to 0.3 for $f = 1.2$.

The fitting constants determined in this section (μ, C_1, k) can be directly used to infer an analytical value for the amount of momentum transferred from an impact. Inputting the values into Eq. (2.16), determined $\beta - 1$ values that are comparable to the simulation data. The analytical values of $\beta - 1$ are represented by hollow symbols in Figure 4.13 and they plot very close to the $\beta - 1$ values obtained from the numerical simulations, represented by filled symbols. The relative error between the numerical and

analytical results is principally derived from uncertainties in the least-squares fitting of Eq. (4.1) to the numerical data, and ranges between about 5% and 40%.

4.6.5 Advances towards an ejecta scaling relationship for oblique impacts

The ejecta scaling laws are useful relationships when determining the ejecta distribution and momentum transfer from vertical impacts. However, most planetary impacts are oblique and the single point source scaling becomes inadequate.

Previous attempts at determining the ejecta distribution from oblique impacts empirically include the studies by Anderson et al. (2004) and Richardson et al. (2007). Anderson et al. (2003) conducted impact experiments of $\approx$ 6 mm diameter aluminium spheres into medium-grained sand, at 90 and 30 degrees impact angles and an impact velocity of 1 km/s. From each impact experiment they recorded the ejection velocities, angles, and positions of the ejecta expelled at one moment during the first half of the crater growth. They observed that in the oblique impact cases, the velocity distribution of the ejected particles varies around the impact point. They defined the ratio between the downrange and the uprange ejection velocities (DR/UR) as a measure of the asymmetries in the ejecta curtain. At early times, they recorded a 40% increase in the ejection velocity from the uprange to the downrange sides of the crater. At later times, about when the crater radius reaches about half of the final radius, the difference between the velocities in the uprange and in the downrange sides of the craters decreased to about 20%. Anderson et al. (2004) ran additional impact experiments at 45° impact angles and tried to use the Maxwell Z-Model to predict the ejection velocities and ejection angles. One major difficulty with deriving a scaling law using this approach was the assumption that there is a single, stationary point source.

The work in this section attempts to develop an ejecta scaling relationship for oblique impacts, based on numerical simulation data. Three-dimensional simulations of the DART impact into a 10 kPa, 20% porous target, at vertical, 60°, 45° and 30° impact angles provide information about the ejecta distribution as a function of impact angle. The momentum carried away by the ejecta from a vertical impact, $\beta - 1$, can be found

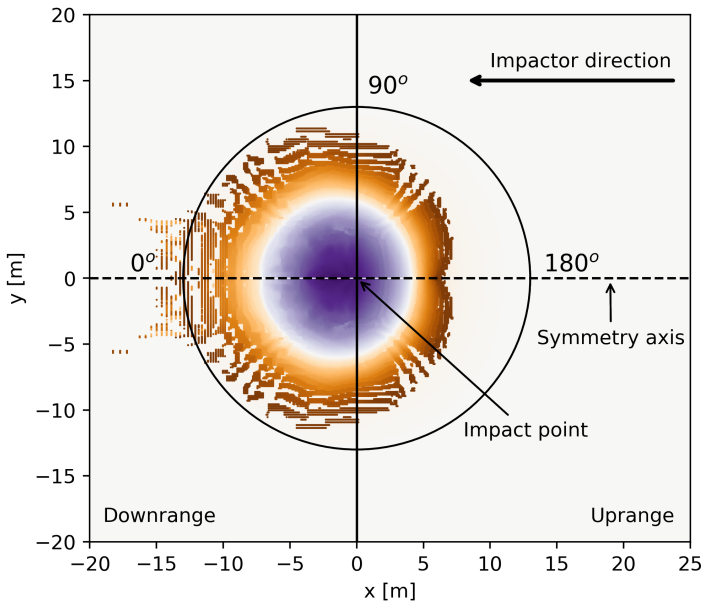

Figure 4.17: Surface topography of the DART impact at 30 degrees angle of incidence, showing the direction of the impactor and the azimuthal coordinates relative to the impact point.

from integrating the mass, dM, within the radial distance range from n_1 to $n_2 R/a$ (Cheng et al., 2016)

$$P_{ej} = \frac{9km}{4\pi}\frac{\rho}{\delta}\int_{n_1}^{\frac{n_2 R}{a}} w^2 v_z dw, \tag{4.2}$$

where $w = x/a$ and v_z is the ejecta velocity in the z direction. The momentum carried away by the ejecta, $\beta - 1$ is then:

$$\beta - 1 = \frac{P_{ej}}{mU} = \frac{9k}{4\pi}\frac{\rho}{\delta}\int_{n_1}^{\frac{n_2 R}{a}} w^2 \frac{v_z}{U} dw. \tag{4.3}$$

Following the Anderson et al. (2004) approach, the ejecta velocity distribution was split into azimuthal sections, between 0°, which represents the downrange direction and 180°, which represents the uprange direction. Figure 4.17 shows the surface topography of the DART impact at 30° impact angle and a diagram of the locations of the impact point, symmetry axis and the azimuth angles.

Anderson et al. (2004) plotted the ejecta velocity as a function of azimuth, at a fixed point in time. However, because in oblique impacts the ejection velocity varies with both time and azimuth, here the entire ejecta velocity distribution was plotted as a function of normalised radial distance x/a, for 5° azimuthal segments. Unlike in the

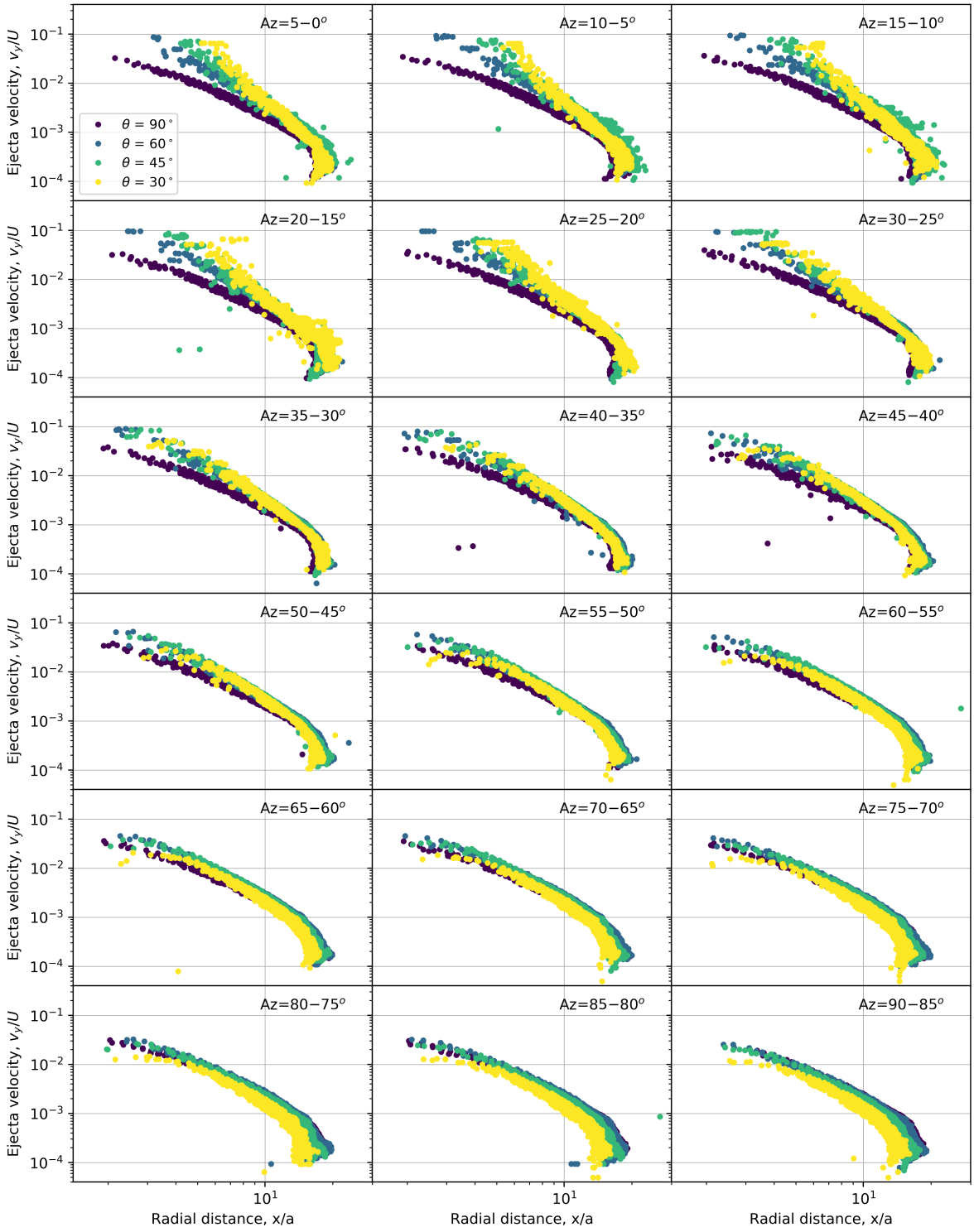

Figure 4.18: Ejecta vertical velocity - launch position distribution from vertical and oblique impacts ($\theta = 90°$, $60°$, $45°$, $30°$) at azimuth between 0 and 90°.

vertical impacts, in oblique impacts the centre of the crater is not stationary, but instead it moves from the impact point towards the downrange direction, with crater growth. When determining the radial distance of the ejecta, the origin was defined as the impact

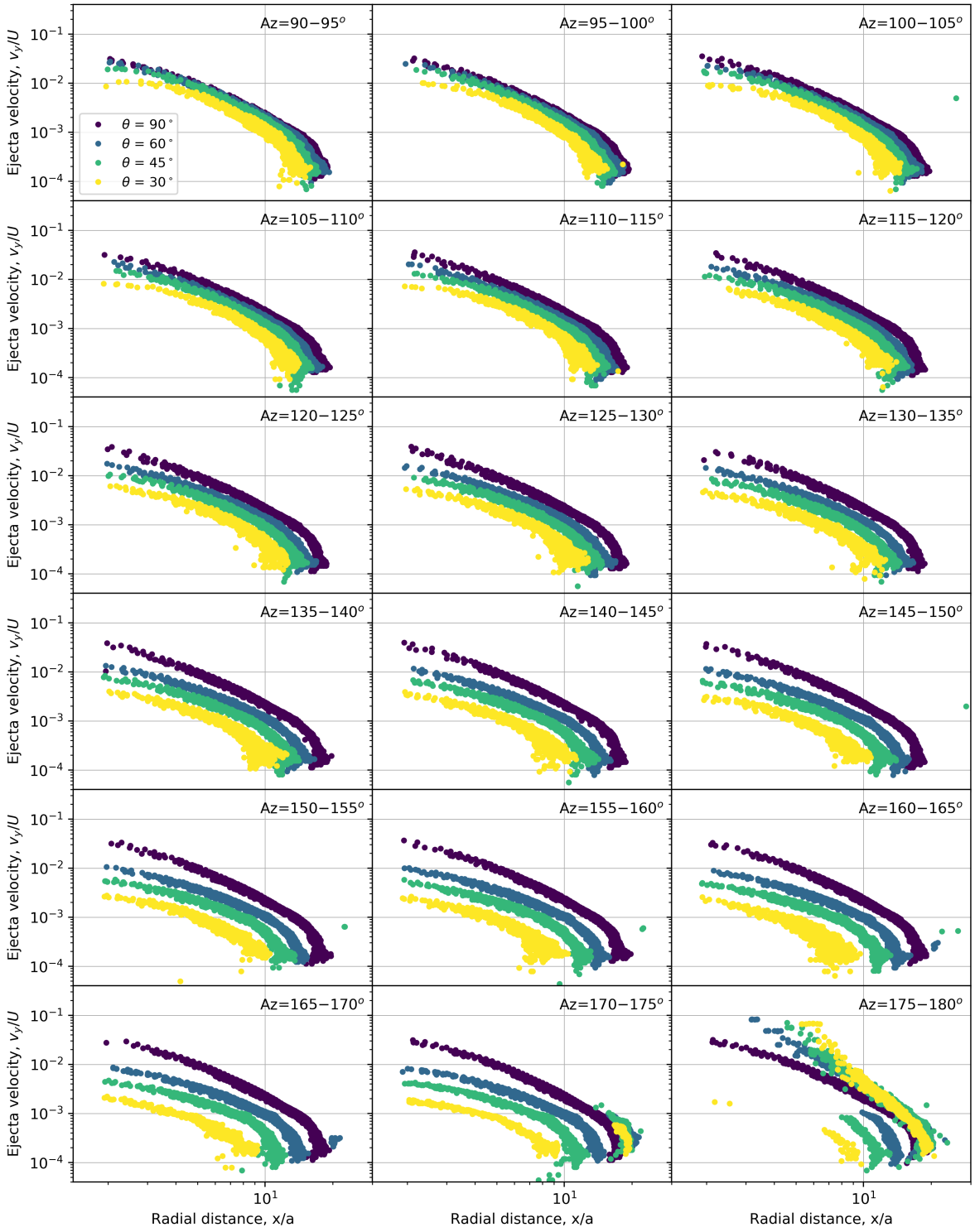

Figure 4.19: Ejecta vertical velocity - launch position distribution from vertical and oblique impacts ($\theta = 90°$, $60°$, $45°$, $30°$) at azimuth between 90 and 180°.

point, rather than the centre of the final crater. This convention caused a larger spread in the launch distance compared to the 90° impact, and must be accounted for in the ejecta analysis.

Figures 4.18 and 4.19 shows the ejecta velocity normalised by the impact velocity, v/U, as a function of radial distance, normalised by the impactor size x/a, for four different impact angles and divided into 5° azimuthal segments. The ejecta distributions from the oblique impacts seems to coincide with the ejecta distribution from the vertical impact case, at azimuths of about 90°, and then varies systematically with azimuth and impact angle. In all cases, the middle part of the ejecta velocity distribution can be fit by a power law.

Using a best fit of Eq. (2.15) through the middle 50% of the ejecta velocity distributions showed in Figures 4.18 and 4.19, the fitting constants μ and C_1 for each azimuth and impact angle investigated here can be determined. The azimuthal radius, R_{Az}, which here is defined as the distance between the impact point and the crater rim for each azimuthal segment can also be determined. Similarly, the constant k can be found by best fitting Eq.(2.17) to the cumulative ejecta mass distribution, as a function of radial distance. In the vertical impact case, the constant k must be divided by the number of azimuthal segments considered.

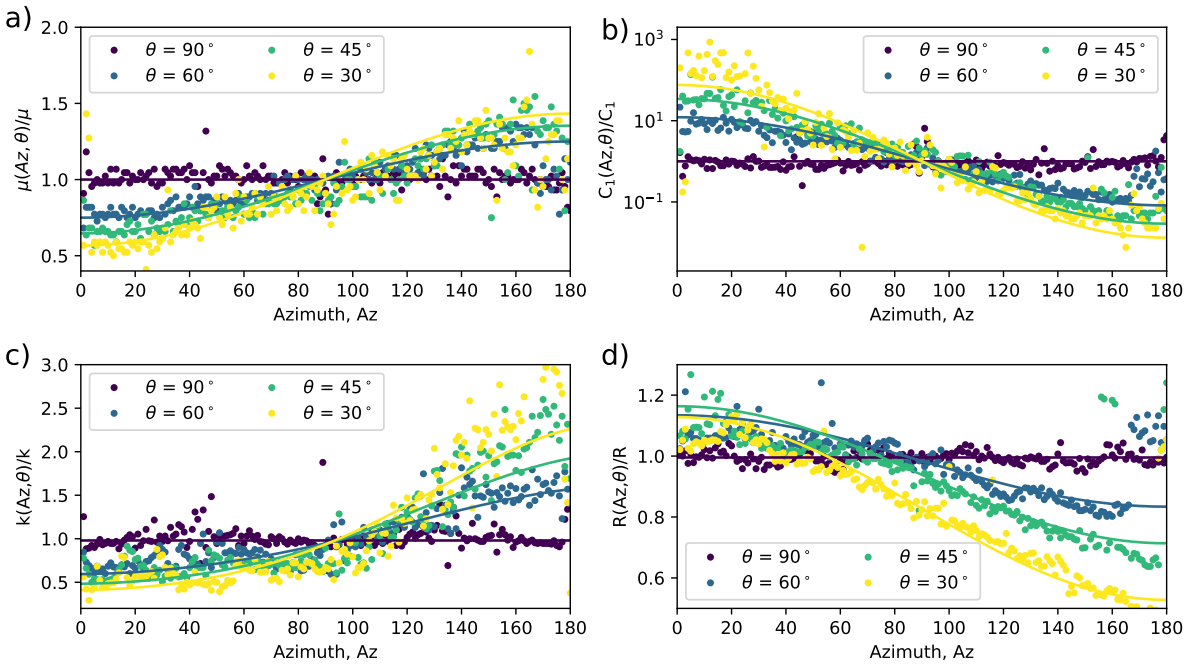

Figure 4.20: Constants μ (a), C_1 (b), k (c) and R_{Az} (d), normalised by the average value in the 90° impact scenario, as a function of azimuth around the crater (centred at the impact point).

Figure 4.20 shows the best fit constants μ (Fig. 4.20a), C_1 (Fig. 4.20b), k (Fig. 4.20c) and R_{Az} (Fig. 4.20d) as a function of azimuth, for the four different impact angles. The constants were normalised by the average μ, C_1, k and R constants found for the $\theta = 90°$ impact scenario. All four constants, μ, C_1, k and R_{Az}, seem to vary as periodic functions of impact angle and azimuth around the impact point. In this work a simple trigonometric functions is fit through the constants distribution, as a function of azimuth and angle.

The point source exponent, $\mu(Az, \theta)$, can be approximated by

$$\mu(Az, \theta) \approx \mu \times \left[1 - \frac{1}{2}\cos(Az)\cos(\theta)\right], \tag{4.4}$$

where μ is the point source exponent in the vertical impact scenario. The constant $C_1(Az, \theta)$ varies as an exponential of cosine

$$C_1(Az, \theta) \approx C_1 \times \exp\left[5\cos(Az)\cos(\theta)\right], \tag{4.5}$$

where C_1 is the constant derived for the vertical impact scenario.

$$k(Az, \theta) \approx \frac{k}{n_{Az}} \times \exp\left[-0.02\cos(Az)\cos(\theta)\right], \tag{4.6}$$

where k is the constant derived for the vertical impact scenario and n_{Az} is the number of azimuthal segments considered.

$$R(Az, \theta) \approx R \times \left[1 + \frac{90 - \theta}{100}\frac{\cos(Az)}{2}\right], \tag{4.7}$$

where R is the crater radius in the vertical impact scenario.

The ejecta momentum, $\beta - 1$, can then be found from the sum of the momentum calculated for each azimuth wedge.

$$\beta - 1 \approx 2 \times \sum_{Az=0}^{180} \frac{9k_{Az}}{4\pi}\frac{\rho}{\delta}\int_{R_{Az}}^{n_1 a} \frac{v_z(x)}{U} w^2 dw \tag{4.8}$$

where $w = x/a$ and $k_{Az} = k/n_a z$.

Substituting Eq. (2.15) into Eq. (4.8), the momentum enhancement can be approximated by

$$\beta - 1 \approx 2 \times \sum_{Az=0}^{180} \frac{9k(Az, \theta)}{4\pi}\frac{\rho}{\delta}\int_{n_1}^{\frac{n_2 R(Az,\theta)}{a}} \left[C_1(Az, \theta)\left[(w)\left(\frac{\rho}{\delta}\right)^{\nu}\right]^{-1/\mu(Az,\theta)}\right] w^2 dw. \tag{4.9}$$

The best-fit through ejecta velocity-radial distance distribution from a vertical impact into a 1 kPa, 20% porous target gives the fitting constants $\mu \approx 0.42$, $C_1 \approx 1.1$ and $k \approx 0.4$. Table 4.3 shows the $\beta - 1$ values from the vertical, 60°, 45° and 30° impacts. The first column contains the $\beta - 1$ values as measured from the Lagrangian tracer particles. The second column contains the $\beta - 1$ determined using Eq. (4.9) and the best-fit constants μ, C_1, k and R_{Az} (Fig. 4.20). The last column contains the $\beta - 1$ values obtained using Eq. (4.9) and the analytical expressions for: μ as a function of azimuth and impact angle (Eq. (4.4)), C_1 as a function of azimuth and impact angle (Eq. (4.5)), k as a function of azimuth and impact angle (Eq. (4.6)) and R_{Az} as a function of azimuth and impact angle (Eq. (4.7)). The $\beta - 1$ values found using the best-fit constants are within 3% for a 90° impact, and 18% for a 30° impact. Using the analytical approach, $\beta - 1$ is found within 1.5% of the simulation value for a 90° impact, and withing 25% for a 30° impact.

Table 4.3: Ejecta momentum in the vertical direction, $\beta - 1$, measured from the Lagrangian tracers, compared with $\beta - 1$ calculated from the best-fit constants and calculated using the newly derived analytical approximations (Eq. (4.9)).

Impact angle $\boldsymbol{\theta}$	**Measured** $\boldsymbol{\beta - 1}$	**Best-fit** $\boldsymbol{\beta - 1}$	**Analytical** $\boldsymbol{\beta - 1}$
90°	1.28	1.24	1.30
60°	1.16	1.17	1.17
45°	0.93	0.97	0.96
30°	0.61	0.72	0.76

Having proven that the analytical expressions derived here give reasonable $\beta - 1$ approximations, that are within 25% of the numerical data, these expressions can then be used to extrapolate the $\beta - 1$ values for impacts into target cohesions and porosities not simulated here. Substituting the μ, C_1 and k constant derived from the two-dimensional simulations (Table 4.2) into Eq. (4.9), $\beta - 1$ can be calculated for a range of cohesions and fixed porosity. Figure shows the analytical $\beta - 1$ results for impacts at vertical, 60°, 45° and 30°, into targets with cohesions between 1 Pa and 1 MPa and a fixed porosity of 20% (Fig. 4.21a) and 50% (Fig. 4.21b).

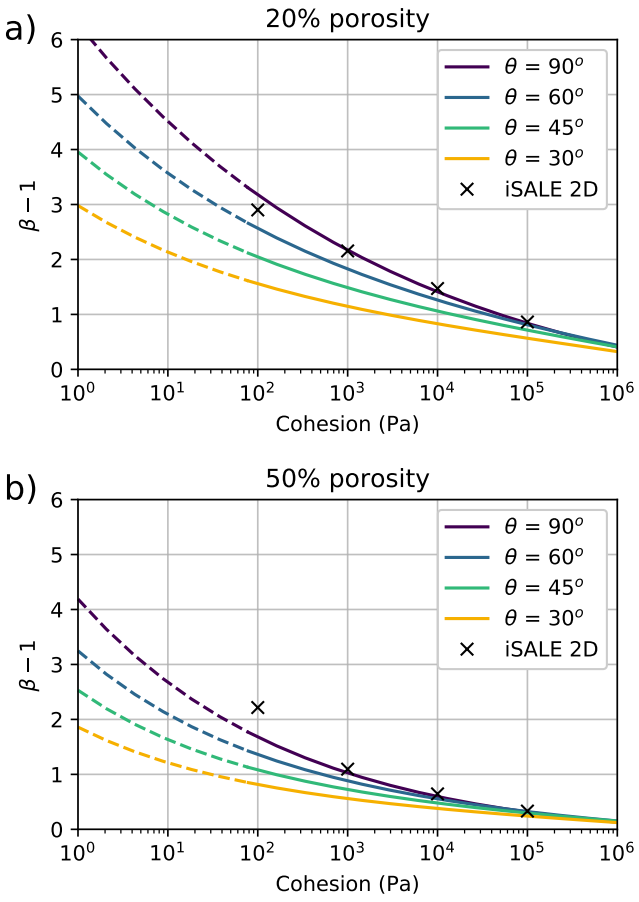

Figure 4.21: $\beta - 1$ trends found using Eq. 4.9, for oblique impacts into a 20% porous and a 50% porous target.

The $\beta - 1$ values found using the analytical approximation of vertical impacts shows good agreement to the $\beta - 1$ found from numerical simulations in two-dimensions (see Section 4.6.1). However not sufficient simulation data is available for impacts at oblique angles and a larger collection of numerical simulations is needed to fully understand the limits of applicability of these scaling relationships and to quantify any associated errors.

4.7 Conclusions

This chapter used the iSALE shock physics code to numerically simulate impacts into low-gravity, strength-dominated asteroid surfaces, to quantify the sensitivity of ejecta properties and momentum transfer to variations in asteroid properties. It was found that key target material properties, cohesion (of the post-shock target), initial porosity and internal friction coefficient, greatly influence ejecta mass/velocity/launch-position

distributions. It was also found that an increase in porosity or in internal friction leads to lower ejection velocities, while an increase in target cohesion only slows down the last ejecta to leave the crater. This is consistent with the results of recent numerical simulations of ejecta behaviour in gravity-dominated impacts (Luther et al., 2018). As a result, the momentum transferred to the target and carried away by the ejecta is also very sensitive to these material properties.

NASA's DART mission aims to be the first to test a controlled deflection of an asteroid by impact momentum transfer. The simulation results presented here suggest the cohesion of the target asteroid's surface after passage of the shock wave has the greatest influence on momentum transfer. As the cohesion is decreased the ratio of ejected momentum to impactor momentum $\beta - 1$ increases; $\beta - 1$ also increases as the initial porosity and internal friction coefficient of the asteroid surface decrease. Using nominal impactor parameters and reasonable estimates for the material properties of the Didymos binary asteroid, the DART target, the β factor ranged from approximately 2.4 for a cohesion of 10 kPa to approximately 4 for a cohesion of 0.1 kPa. For a tighter constraint on the β value, a more accurate characterisation of the target asteroid is needed and as such, it would be advantageous to survey the target before or after impact. An accurate measurement of the DART impact crater diameter would help constrain the cohesion of the target surface. It was also found that the analytical expression for estimating β for a given impact scenario derived by Cheng et al. (2016) is consistent with the numerical simulation results presented in this chapter to within $\approx$10%.

The final crater sizes predicted by the numerical simulations are consistent with strength-regime crater scaling relationships based on laboratory impact experiments in two asteroid analogous materials: weakly-cemented basalt (WCB) (Housen, 1992) and the Sand Fly/ash (SFA) (Housen and Holsapple, 2003). Widely-used, power-law scaling relationships for estimating both crater size and ejecta behaviour are linked by a target-material-specific parameter, μ, known as the velocity exponent. For the same impactor parameters, the numerical simulation results suggest that μ is independent of target cohesion and decreases slightly as the initial target porosity increases from 10% to 50%. On

the other hand μ decreases rapidly with increasing target coefficient of internal friction. This dependence of μ on target properties is slightly different to that inferred from impact experiments, but it is consistent with other recent numerical impact simulations (Luther et al., 2018; Prieur et al., 2017; Wünnemann et al., 2016).

Finally, it was investigated the self-consistency between the crater size and ejection speed scaling relationships derived from point-source approximation of impacts in the same target material (Housen et al., 1983; Holsapple, 1993; Housen and Holsapple, 2011). Contrary to some previous ejecta studies, it was found that for the strength-regime impacts presented in this chapter, the two relationships do give consistent values of the velocity exponent μ, so long as a simple power-law function is used to fit the ejecta data over the radial range $4a < x < 0.74R$, where a is the impactor radius and R is the final crater rim radius. Alternatively, a revision to the Housen and Holsapple (2011) ejecta scaling relationship that accounts for the non-power-law behaviour in the coupling zone close to the impact point and provides a good fit to the numerical simulation results over the full radial range of ejecta data $a < x < R$ was proposed. This relationship also leads to consistent μ values obtained from ejecta and crater size data in the same target material, but allows a much greater range of ejecta data to be included. The consistency in μ values between crater size and ejecta scaling data provides support for applicability of the point-source approximation in impact ejecta scaling.

The two-dimensional numerical study presented in this chapter is consistent with three-dimensional geometry studies. In the specific cases simulated here, it was found that the vertical momentum enhancement normalised by the vertical component of the impact velocity is comparable to the momentum enhancement from a vertical impact. The oblique impact simulations included here were then used to derive an analytical model for the ejecta distribution from oblique impacts. While the derived model is in good agreement with the numerical simulations included in this chapter, further studies are needed to determine its limits of applicability.

Chapter 5

The effects of asteroid layering on crater formation and ejecta distribution

"Asteroid impacts, by any reasonable reckoning, are the only preventable natural disasters. So my fellow Earthlings, let's get busy and see to it that we never take this kind of hit." — Bill Nye, *Undeniable: Evolution and the Science of Creation*

Most bodies in the Solar System do not have a homogeneous structure. Understanding the outcome of an impact into regolith layers of different properties is especially important for NASA's Double Asteroid Redirection Test (DART) and ESA's Hera missions. Here the iSALE shock physics code was used to simulate the DART impact into three different target scenarios in the strength regime: a homogeneous porous half-space; layered targets with a porous weak layer overlying a stronger bedrock; and targets with exponentially decreasing porosity with depth. For each scenario this work determined the sensitivity of crater morphology, ejecta mass-velocity distribution and momentum transferred from the ejecta for deflection, $\beta - 1$, to target properties and structure. It was found that for a homogeneous porous half-space, cohesion and porosity play a significant role and the DART impact is expected to produce a $\beta - 1$ between 1 and 3. In a two-layer

target scenario, the presence of a less porous, stronger lower layer close to the surface can cause both amplification and reduction of ejected mass and momentum relative to the homogeneous upper-layer case. For the case of DART, the momentum enhancement can change by up to 90%. Impacts into targets with an exponentially decreasing porosity with depth only produced an enhancement in the ejected mass and momentum for sharp decreases in porosity that occur within 6 m of the asteroid surface. Together with measurements of the DART crater by the Hera mission, these results can be used to test the predictive capabilities of numerical models of asteroid deflection.

5.1 Introduction

Impact cratering is a fundamental process involved in planetary formation. During the excavation stage of crater formation, a large amount of material is ejected ballistically out of the crater as ejecta (Oberbeck, 1975; Housen et al., 1983). Previous laboratory (Housen and Holsapple, 2011) and numerical studies (Jutzi and Michel, 2014; Luther et al., 2018; Raducan et al., 2019) of impact events into homogeneous targets have shown that the speed and mass of ejecta depends sensitively on target material properties, such as cohesive strength, porosity and the coefficient of internal friction. However, most bodies in the Solar System are not homogeneous, as shown by past missions to asteroids, such as the NEAR-Shoemaker (Veverka et al., 2001), the OSIRIS-REx (Lauretta et al., 2019; Walsh et al., 2012) or the Hayabusa missions (Yano et al., 2006; Watanabe et al., 2019), as well as Earth-based thermal infrared observations (Delbo et al., 2014).

The surface material and the substructure varies from one asteroid to another. While the recent flybys to Ryugu and Bennu revealed a very rocky surface, a large sample of the visited asteroids have been observed to be covered by a layer of fine particles, termed regolith, which overlies a much stronger bedrock substrate (Gundlach and Blum, 2013). Examples of such asteroids include 21 Lutetia (Coradini et al., 2011), 243 Ida, 433 Eros, 951 Gaspra (Sullivan et al., 2002) or 25143 Itokawa (Miyamoto et al., 2007).

The effects of target layering on impact cratering were studied extensively through laboratory experiments conducted by Quaide and Oberbeck (1968). They investigated cratering in analogue lunar regolith of different thicknesses, covering a denser, stronger substrate. The study concluded that for a certain size-range of craters, the depth of the regolith has a large influence on the crater morphology and on the cratering efficiency. For the same impact parameters, a deeper regolith resulted in larger craters (Quaide and Oberbeck, 1968).

The presence of a substrate has also been shown to change the mass-velocity distribution and evolution of ejecta (Schultz, 1992; Senft and Stewart, 2007), which could have important implications for planetary defence, e.g. asteroid deflection by a kinetic

impactor (Ahrens and Harris, 1992; Melosh et al., 1994; Shafer et al., 1994). The outcome of an impact into regolith layers of different properties and depths is especially important to understand in the context of space missions such as NASA's Double Asteroid Redirection Test (DART) (Cheng et al., 2016; Cheng et al., 2018) and ESA's Hera (Michel et al., 2018).

The previous chapter presented numerical simulations of strength-dominated impacts on a homogeneous, small-asteroid surface. It quantified the influence of target cohesion, porosity and internal friction coefficient on the mass-velocity ejecta distribution produced by an example artificial impact and used the DART mission (Cheng et al., 2016; Michel et al., 2016) as a motivating case study.

In this chapter, the work from the previous chapter is extended to include impacts into asteroid surfaces with different internal structures. The chapter begins with a brief summary of current understanding of asteroid surfaces, followed by a summary of past research of impacts into homogeneous and layered targets. Then the effects of the target structure on crater morphology, the mass-velocity distribution of the ejected material and the amount of momentum transferred from the impactor to the asteroid for deflection are quantified. As a layered structure has been proposed for a number of asteroids observed by spacecraft, this work considered three possible impact scenarios: a) a homogeneous half-space target, with constant porosity, b) a layered target with a dense interior, covered by a homogeneously porous regolith layer and c) a target with a porosity that decreases exponentially with depth.

5.1.1 Kinetic impactor test

To avoid a collision between an asteroid and Earth, the course of the asteroid could be changed by impacting its surface (Ahrens and Harris, 1992; Melosh et al., 1994). The Double Asteroid Redirection Test (DART), set to launch in 2021 (Cheng et al., 2018), aims to demonstrate a controlled deflection of a Near-Earth binary asteroid, nicknamed 'Didymoon'. In a high velocity impact event, the change in momentum of the asteroid can be amplified by the momentum of crater ejecta that exceeds the escape velocity, enhancing

the asteroid deflection (Housen and Holsapple, 2011). A more detailed description of the kinetic impact asteroid deflection method can be found in Chapter 2.

The efficiency of momentum transfer has been found to vary significantly depending on the target asteroid's properties and its composition (Housen and Holsapple, 2012; Jutzi and Michel, 2014; Stickle et al., 2015; Syal et al., 2016). Based on the results of experimental impacts in layered targets (Quaide and Oberbeck, 1968), it is likely that target layering will also affect the mass and velocity of the ejecta, and therefore, β.

5.1.2 Lunar regolith

Regolith is defined as a layer of weak of unconsolidated material overlying a stronger substrate (Shoemaker et al., 1963). Most of the lunar regolith is of impact origin (McKay et al., 1991) and consists of particles smaller than 1 cm in size; however, larger fragments or boulders can also be found on the surface. The regolith on the Moon was well characterised in many previous studies (McKay et al., 1991; Wilcox et al., 2005) thanks to the samples returned to Earth from the Apollo missions. The cohesion was measured to be between 0.1 and a few kPa and the porosity was measured to be 50% (Mitchell, 1974; Colwell et al., 2007), dropping to 40% in just a few meters. The regolith covers the entire lunar surface and was estimated to be 4–5 m in depth in the mare areas and 10–15 m in the older highland regions (McKay et al., 1991).

5.1.3 Regolith on Didymoon

The DART mission's target, Didymoon, has a diameter of about 160 m (Michel et al., 2016) and a fast spinning primary close to the critical limit of stability (Walsh et al., 2012). Moreover, like many near-Earth asteroids, the double asteroid system is affected by the YORP effect (Jacobson and Scheeres, 2011).

Asteroids of about 200 m and up to 10 km in size are likely to be rubble-pile objects (Michel et al., 2001; Scheirich and Pravec, 2009), aggregates held together only by self-gravity or cohesive forces (Richardson et al., 2002), while fast-spinning asteroids smaller than 150 m can be competent bodies (Sánchez and Scheeres, 2014). Regardless

of the deep internal structure, the surface of many asteroids is expected to be covered by a layer of regolith (Sullivan et al., 2002), but its properties can differ from those of the lunar regolith, as well as from one asteroid to another. The thickness of the regolith layer and the particle size distribution can depend on the size of the asteroid or the internal structure (e.g. a porous asteroid would retain more regolith than a competent body of the same mass).

For example, the high escape velocity on asteroid 21 Lutetia, 99 km in diameter, has allowed a significant amount of the crater ejecta to be retained on the surface (Murdoch et al., 2015), creating an extensive regolith layer, similar to the lunar regolith, of up to 600 m in depth (Vincent et al., 2012). Asteroid 433 Eros, 17 km in diameter, has a regolith with particle sizes ranging from dust grains to large boulders, which extend to depths of up to several tens of meters (Veverka et al., 2001; Cheng et al., 2002). Most interesting of all is the 300 m asteroid NEA (25143) Itokawa. Itokawa is believed to be a rubble-pile asteroid (Fujiwara et al., 2006), and has two types of surface terrains: a boulder-rich terrain, with particles larger than 1 cm, and a smooth terrain, with a 2.5 m thick layer of fine regolith particles covering a boulder rich substrate (Barnouin-Jha et al., 2008).

On the other hand, more recent space missions to top-shaped asteroids—e.g., JAXA's Hayabusa2 to the 435 m Ryugu (Watanabe et al., 2019) and NASA's OSIRIS-REx to the 268 m Bennu (Lauretta et al., 2019; Walsh et al., 2019)–have revealed boulder rich, almost regolith-free surfaces. However, until the arrival of DART at the Didymos system, the surface and internal structure of Didymoon will not be known. Depending on the formation mechanisms involved (Durda et al., 2004; Walsh et al., 2008), Didymoon could be a highly porous fractured body or a regolith-free rubble-pile (like Ryugu and Bennu); it could have a solid intact interior (e.g. a "competent" or "monolithic" body), or it could have a layered structure (like Lutetia, Eros or Itokawa) (Scheeres et al., 2010; Sánchez and Scheeres, 2014; Murdoch et al., 2017). The work presented in this chapter investigates impacts into a variety of simple internal structures, where the target properties vary only with depth, as possible near-surface structures for Didymoon.

5.1.4 Impact studies on layered targets

Several previous studies have investigated impacts into layered targets and the resulting crater formation. Oberbeck and Quaide (1967) studied fresh craters, with diameters less than 250 m, on the lunar maria and found four distinct crater morphologies: concentric, flat-bottomed, with a central mound and bowl shaped. They used laboratory impact experiments to determine the impact conditions responsible for each crater morphology occurrence. In their experiments, they set up a simple two-layer target model, consisting of a loose quartz sand upper layer, overlying a substrate of denser cohesive quartz sand cemented with epoxy resin. The layered target was then impacted by various projectiles at velocities between 1 and 7 km/s. Oberbeck and Quaide (1967) were able to reproduce each of the observed crater morphologies by varying the thickness of the upper target layer. The pre-impact layer thickness that produced each crater type was shown to be influenced by the strength ratio of the target layers (Quaide and Oberbeck, 1968), but did not seem to change with variations in the impact velocity, the angle of impact or projectile type.

Senft and Stewart (2007) performed numerical simulations of vertical impacts into basalt two-layer targets on the Moon, where the impact velocity was 17 km/s and the upper layer was 10 m thick. They varied the projectile radius to produce different crater sizes and replicated the Quaide and Oberbeck (1968) crater types. The layered targets had different strength parameter configurations (e.g. cohesion, coefficient of internal friction), which were found to strongly influence the ejecta curtain.

Prieur et al. (2018) also conducted numerical studies of impact crater formation in two-layer targets under lunar conditions and investigated the conditions under which the crater morphologies defined by Quaide and Oberbeck (1968) were produced. In agreement with Quaide and Oberbeck (1968) and Senft and Stewart (2007), they found that the different types of crater morphology are the result of the variations between the properties in the two layers. However, they also found that the transitions between the different crater morphologies depend on the mass and velocity of the impactor, as well as layer-strength variations, which was not observed by Quaide and Oberbeck (1968).

5.2 Numerical Model

This work used the iSALE2D shock physics code (Collins, 2014; Wünnemann et al., 2006) to numerically simulate impacts into asteroid targets with different internal structures. To mimic the material response of an asteroid surface, this work used strength models suitable for impacts into geologic targets (Collins et al., 2004) and a porosity compaction model, the model (Wünnemann et al., 2006; Collins et al., 2011), both of which are included in iSALE2D. A detailed description of the numerical methods used here can be found in Chapter 3.

Craters and ejecta distributions produced by impacts simulated with iSALE have been validated previously against laboratory impact experiments (Wünnemann et al., 2016; Luther et al., 2018) and in this thesis, in Chapter 3. iSALE has also been benchmarked against other hydrocodes (Pierazzo et al., 2008), with crater size typically agreeing to within 10%.

5.2.1 Impactor

The impactor parameters were chosen to approximate the DART spacecraft. This work assumed a 310 kg porous sphere, with a diameter of 0.84 m, modelled using the Tillotson equation of state (EoS) and the Johnson-Cook strength model for aluminium (Johnson and Cook, 1983). The internal structure of the spacecraft was heavily simplified and the $\epsilon - \alpha$ porosity model (Wünnemann et al., 2006) was used to account for the voids in the spacecraft structure and achieve a bulk density of 1000 kg/m^3 (63% bulk porosity). The $\epsilon - \alpha$ model took the nominal input parameters: $\alpha_0 = 2.7$, $\alpha_x = 1.0$, $\kappa = 0.9$, $\chi = 1.0$. To isolate the influence of target properties, this work used used the same impactor properties and an impact velocity of 7 km/s for all simulations.

5.2.2 Target asteroid

As discussed in the previous section, Didymoon's surface properties or internal structure are not well understood. To study the target material response to a possible impact, this

work contains numerical simulations of impacts into three distinct target scenarios: (a) a homogeneous porous half-space (Fig. 5.1a); (b) a layered target with a porous weak upper layer overlying a stronger bedrock layer (Fig. 5.1b); and (c) a target with a porosity that decreased exponentially with depth (Fig. 5.1c). For each of these target scenarios, the target material properties (e.g. cohesive strength, initial porosity – including crush curve, layer thickness or porosity e-folding depth) were systematically varied and the crater morphology, the amount of ejected mass and the normalised momentum carried away by the ejecta, $\beta - 1$ were determined.

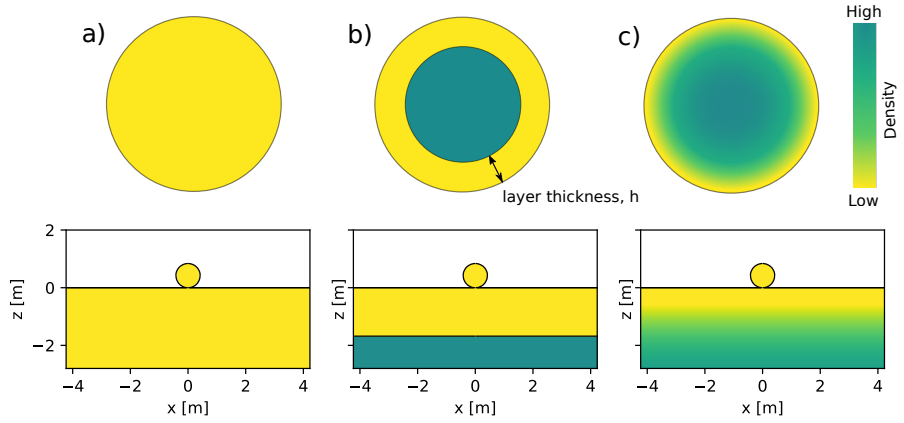

Figure 5.1: Schematic representation of the asteroid structure (upper row) and the equivalent numerical simulation set-up (lower row), for: a) homogeneous porous half-space; b) layered target consisting of a weak, porous upper layer covering a stronger, less porous substrate; c) target with a continuous porosity gradient.

As an S-type silicaceous asteroid system (Michel et al., 2016; Michel et al., 2018), the target asteroid material was considered to be made of weak porous basalt, which is a reasonable approximation of the compositional structure of most asteroids. Therefore, for all impact scenarios, the target was modelled using the Tillotson EOS for basalt (Tillotson, 1962; Benz and Asphaug, 1999). The surface gravity was kept constant at 5 cm/s^2.

Homogeneous porous half-space

The first scenario investigated DART impacts into a homogeneous porous half-space. This scenario is similar to the impact simulations presented in the previous chapter. The shear strength of the target was modelled using a simple pressure-dependent strength

model typical of rock-like materials, referred in this paper as LUND (Lundborg, 1967). The cohesive strength of the damaged target (at zero pressure), Y_{d0}, was varied between 0.1 and 100 kPa. The coefficient of internal friction, f, which can take a range of values on asteroid surfaces, was set to 0.6. This value was based on geological analogues and is the most common for geological materials (Goodman, 1989). The initial porosity of the target, ϕ_0, was varied between 0% and 50%, and was modelled using the model (Wünnemann et al., 2006). The input parameters are summarised in Table 6.1. A justification of the choice of input parameters for the porosity model can be found in the previous chapter.

Table 5.1: Material model parameters for simulations of the DART impact. In addition, thermal parameters from Ivanov et al. (2010) were used.

Description	Symbol	Half-space	Regolith	Substrate
Equation of state		Tillotson[a]	Tillotson[a]	Tillotson[a]
Strength model		LUND	LUND	ROCK
Poisson ratio[b]	ν	0.25	0.25	0.25
Intact strength at zero pressure (MPa)	Y_{i0}	–	–	1
Damage strength at zero pressure (kPa)	Y_{d0}	0.1–100	1	100
Strength at infinite pressure (MPa)	Y_{inf}	10^3	10^3	10^3
Coefficient of internal friction (intact)	f_i	–	–	1.0
Coefficient of internal friction (damaged)	f	0.6	0.6	0.6
Porosity model parameters $(\epsilon - \alpha)$[c]				
Initial porosity	ϕ_0	0–50%	35%/50%	0%/10%
Initial distension**	α_0	1.0–2.0	1.54/2.0	1.0/1.11
Distension at transition to power-law	α_x	1.0	1.0/1.0	– /1.0
Elastic volumetric strain threshold*	ϵ_{e0}	$-2(10^{-9}\text{to}-10^{-6})$	-2×10^{-8}	$-/-2 \times 10^{-6}$
Exponential compaction rate**	κ	0.80–0.98	0.94/0.98	– /0.80
Ratio of porous/nonporous elastic wave speed	χ	1.0	1.00/1.00	– /1.00

[a]Tillotson (1962); [b]Ivanov et al. (2010); [c]Wünnemann et al. (2006).
* ϵ_{e0} varies proportionally with Y_{d0}.
** $\alpha_0 = 1/(1 - \phi_0)$ and κ vary with ϕ_0.

Two-layer targets

The second impact scenario considered a simple two-layer target structure, consisting of a weak, porous upper layer covering a stronger, less porous substrate. This target scenario is similar to what is observed on the lunar mare. To quantify the effects of target layering on the crater morphology and ejecta, this work considered four sets of simulations, with different layer porosity configurations.

For all simulation sets, both the upper and the lower target materials were modelled using the Tillotson EOS for basalt. The upper layer had a cohesive strength of 1 kPa and was modelled using the LUND strength model (Lundborg, 1967), while the lower layer had a cohesive strength of 100 kPa and was modelled using a more complex strength model, in which the strength is reduced as strain accumulates (Collins et al., 2004), referred in this paper as the ROCK model. (Senft and Stewart, 2007) showed that at least a two-orders-of-magnitude difference between the strength in the upper layer and the substrate is required in order to produce different crater morphologies. Both layers had a coefficient of internal friction of the damaged material $f = 0.6$, while the coefficient of internal friction of the intact material (only in the ROCK model) was set to $f_i = 1.0$.

This work contains four sets of simulations. For each set of simulations the porosity in the upper and lower layers were varies. In the first two sets, the upper layer (the regolith) had a nominal porosity of 35% and 50%, respectively, while the lower layer (the substrate) was non-porous (0% porosity). These two simulations will be referred to as R35-S0 and R50-S0 (Table 5.3). The next two sets considered less extreme variation in porosity between the regolith and substrate. In these two cases the regolith was 35% and 50% porous, respectively, while the substrate had a porosity of 10%. These simulation sets were labelled R35-S10 and R50-S10. The full range of input parameters can be found in Table 6.1 and a summary of the simulation sets can be found in Table 5.3.

Table 5.2: iSALE input parameters for the layered target.

Parameter	R35-S0	R50-S0	R35-S10	R50-S10
Regolith porosity, ϕ_{r0}	35%	50%	35%	50%
Substrate porosity, ϕ_{s0}	0%	0%	10%	10%

To investigate the influence of the regolith layer on the crater morphology and the ejecta produced, for each set of simulations the regolith layer thickness, h, was varied between 1 and 20 impactor radii.

Targets with exponentially decreasing porosity

As noted by (Sullivan et al., 2002), the transition between regolith and megaregolith on asteroids might not be as sharp as on the lunar mare, but instead might be more gradual. The third target scenario considered a target in which porosity decreased exponentially with depth. In all cases, strength was assumed to be independent of porosity and modelled using the LUND strength model with a fixed cohesive strength and coefficient of friction ($Y_0 = 1$ kPa and $f = 0.6$). In iSALE, the distension, α, is defined as the ratio of solid density to bulk density, ρ_s/ρ, which is equivalent to $1/(1-\phi)$, where ϕ is the porosity (Collins et al., 2011). To achieve an exponential decrease in porosity with depth, the distension as a function of depth, $\alpha(h)$, is defined as

$$\alpha(h) = (\alpha_0 - \alpha_k) \times \exp(h/h_\star) + \alpha_k \tag{5.1}$$

where α_0 is the distension at the surface (maximum distension), α_k is the minimum distension (asymptotic limit), h is the depth and $h_\star$ is the e-folding depth. For this impact scenario, the $\epsilon - \alpha$ parameters were kept constant for all initial distensions, including the critical volume strain for the onset of plastic compaction, ϵ_{e0}.

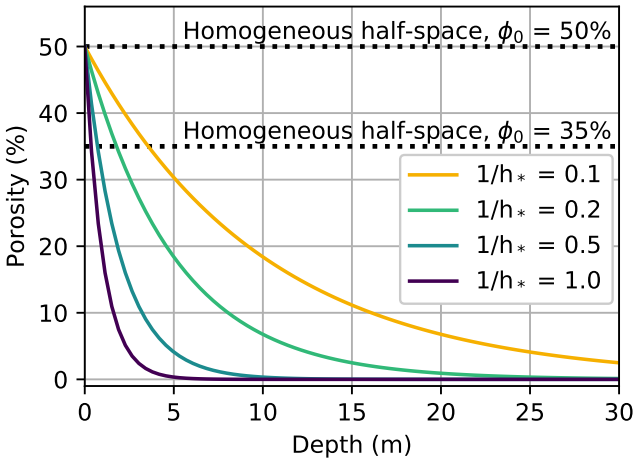

Figure 5.2: Target porosity as a function of depth for a range of values $1/h_*$, between 0.12 and 1.2. The surface porosity is 50% and the minimum porosity is 0%. The porosity in homogeneous half-space cases, at 35% and 50% porosity, are plotted for comparison.

To investigate impacts into targets with exponentially decreasing porosity, this work considered two simulation sets. The first set had a surface porosity, ϕ_0, of 50% and

a minimum porosity, ϕ_k, of 0%, while the second set had $\phi_0 = 35\%$ and $\phi_k = 10\%$. For each set, the e-folding depth, $1/h_\star$ was varied between 0.12 and 1.2.

Table 5.3: iSALE input parameters for the porosity gradient target.

Parameter	S50-K0	S35-K10
Surface porosity, ϕ_0	50%	35%
Minimum porosity, ϕ_k	0%	10%

5.2.3 Regridding and resolution tests

High spatial resolution is required to capture the particles ejected at very high velocities in the early stages of impact. At the same time, in all of the simulations included in this chapter, the crater grows to become many times larger than the projectile and cratering occurs over a long time-scale, due to the low gravity and low strength of the targets investigated. To achieve high spatial resolution at early times, whilst limiting the computational expense of simulations, this work used the iSALE's regridding option. Regridding allowed the simulation domain to be coarsened by a factor of two after predetermined amounts of time. This method was described in Chapter 3.

Lagrangian tracer particles were placed across the computational domain and their mass and velocity were recorded if they crossed a fixed altitude, equal to one impactor diameter. Tracers that crossed this line were identified as ejecta in post-processing if their maximum speed exceeded both the escape velocity (≈ 6 cm/s) and the velocity required to overcome the cohesive strength of the target. In all cases considered here, the velocity threshold was 10cm/s. Due to the very small size of the simulated asteroid, the ejecta analysis presented here ignored the effect of gravity on the absolute value of the ejecta velocity at infinity (Housen and Holsapple, 2003). The gravity of Didymoon, albeit small, would affect the slower ejecta, which introduces an uncertainty in β of 2–4%.

The numerical simulations were run until all the ejecta was measured, however it is important to note that the end of the simulation was not necessarily the end of the cratering process. Further crater collapse, which due to the very low surface gravity occurs over a much longer time-scale than crater excavation, was not simulated.

5.3 Results of the DART impact

To understand and quantify the effects of target structure on the crater morphology, amount of ejected mass and ejecta momentum, the numerical studies were divided into three different impact scenarios.

5.3.1 DART impact into a homogeneous porous half-space

To investigate the individual effects of target cohesion and porosity on crater excavation and ejection processes, a series of simulations of impacts into homogeneous half-space targets were first performed. These simulations extend results presented in the previous chapter, by providing additional numerical runs that cover a larger range of target porosities.

To investigate the effects of target cohesion, Y_{d0} was varied between 0.1 and 100 kPa, while keeping the porosity set at 20% and all the other impact parameters constant. It was found that the target cohesion had a large influence on the crater diameter at the preimpact surface level, which varied from 36 m for a 0.1 kPa target, to 9 m at 100 kPa.

To investigate the effects of porosity at constant cohesion, the porosity was varied between 0% and 50%, for cohesions of 1, 10 and 100 kPa. For all cohesions, the crater diameter decreased by about one third between the non-porous and 50% porosity target scenarios. However, the relative change in crater diameter between the 20% and the 50% porosity targets was less than 2 m (8–14%), which might be difficult to resolve from images taken by a potential post-impact fly-by. This relatively modest change in crater diameter with porosity is consistent with previous experiments (Housen and Holsapple, 2003) and numerical simulations (Wünnemann et al., 2006; Prieur et al., 2017) of impacts in low-to-moderate porosities (up to 50%). A greater dependence of crater diameter and depth on crater size is expected for higher porosity targets not considered here (Housen and Holsapple, 2003).

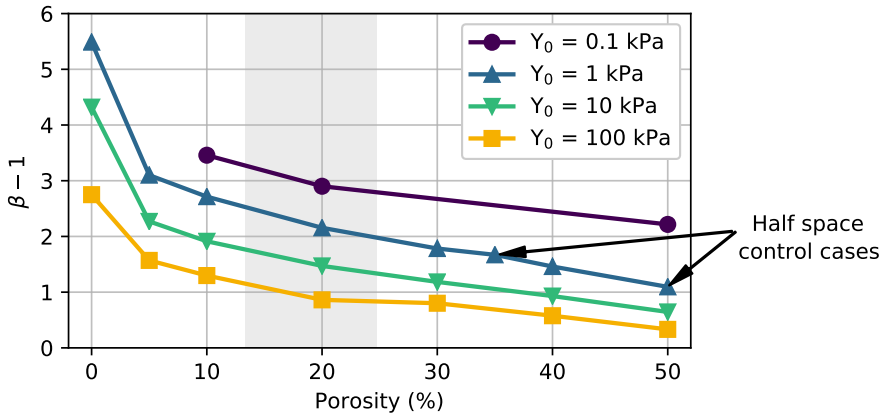

Figure 5.3: Total ejected momentum in the z direction ($\beta - 1$) for four different cohesions and different porosities of the target.

By analysing the impact ejecta,it was found that an increase in target porosity led to lower ejection velocities, while an increase in target cohesion resulted in lower ejection speeds only for the last ejecta to leave the crater. This is consistent with the results of recent numerical simulations of ejecta behaviour in gravity-dominated impacts (Luther et al., 2018).

By integrating the mass-velocity ejecta distribution, this work determined the momentum transferred to the target and carried away by the ejecta, $\beta-1$. The simulation results suggest that $\beta - 1$ is also very sensitive to the material properties investigated, with the target cohesion having the greatest influence. Figure 5.3 shows the ratio of ejected momentum to impactor momentum $\beta - 1$, as a function of target porosity, for four different cohesions. As the cohesion is decreased, $\beta - 1$ increases; $\beta - 1$ also increases as the initial porosity of the asteroid surface decreases. For a target with 20% porosity, which is the current best estimate for the Didymos asteroid system (Michel et al., 2016), $\beta - 1$ was determined to range between 1 for a cohesion of 100 kPa and approximately 3 for a cohesion of 0.1 kPa.

The results presented here are broadly consistent with previous impact simulations where targets with similar cohesive strengths were used. For example, simulations by (Syal et al., 2016) suggested a 10 km/s impact into a 1 kPa, 20% porous target would produce a $\beta - 1 \approx 3$, while impacts into much stronger targets, of a few MPa, have been shown to produce $\beta - 1$ between 0.1 and 1 (Jutzi and Michel, 2014; Stickle et al., 2015;

Cheng et al., 2016). As discussed in the previous chapter, these results emphasise the importance of cohesion in determining the β value and the outcome of asteroid deflection.

5.3.2 DART impact into a two-layer target

This work contains four sets of numerical simulations of impacts into layered Didymoon-like targets, where each set had a different porosity configuration in the upper and lower layers, as summarised in Table 5.3. For each simulation set the thickness of the regolith, h, was varied from 0.5 to 20 times the impactor radius, a.

Crater morphology

Varying the upper-layer thickness resulted in craters with different morphologies. The same four types of crater morphologies as reported by (Quaide and Oberbeck, 1968) were identified here: concentric craters, flat-floor craters, central-mound craters and bowl shaped craters. Examples of crater profiles of these morphologies, from iSALE simulations, are illustrated in Figure 5.4. The crater profiles are recorded at the end of the crater growth process (10 s); however, the material velocity in the rim area is non-zero and directed inwards at this time. This suggests that further collapse of rim material might occur, but over a long timescale due to the low gravity of the body. In Figure 5.4, the material with a particle velocity pointing downwards and that might collapse is highlighted in red.

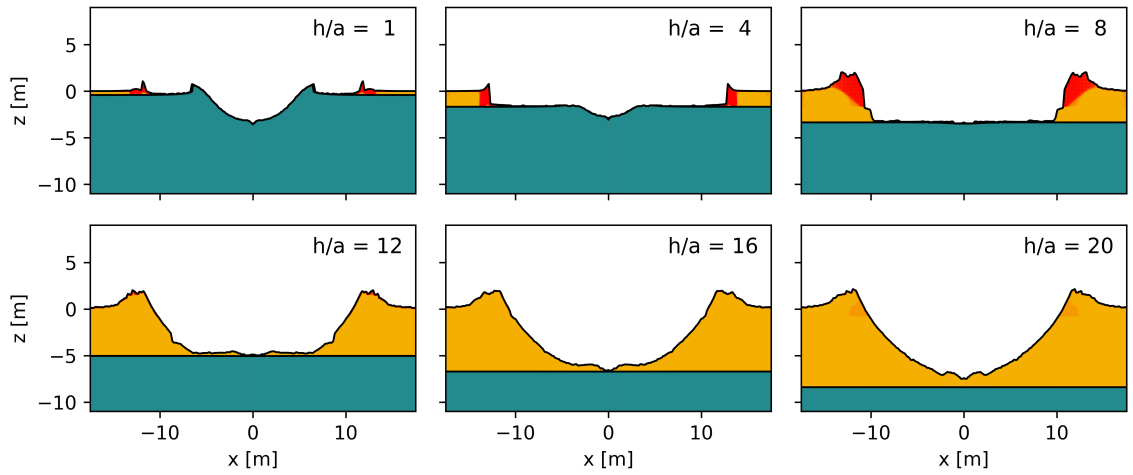

Figure 5.4: Example of crater profiles with distinct morphologies: concentric crater (h/a = 1), flat-bottomed (h/a = 8), central-mound (h/a = 12) and bowl shaped (h/a = 20). The upper layer had a pre-impact porosity of 35%, while the substrate was non-porous. Crater rim material highlighted in red is expected to undergo late-stage collapse.

For very thin regolith layers, $h/a < 4$, cratering deformed both the upper and the lower layers, to produce concentric craters with both an inner and outer crater rim. As the regolith layer was increased, in the range $4 < h/a < 10$, the same impact conditions produced a crater that only formed into the upper layer and exhibited a flat floor. For regolith layer thicknesses h/a between 10 and 16, the impact produced central-mound craters, while for very thick regolith layers, h/a >16, the substrate had no influence on the cratering process. In this case, the crater took the form of a simple bowl shaped crater, similar to the craters formed in the equivalent homogeneous target simulation.

In this study, the transition threshold between these crater morphologies did not appear to be influenced by the range of porosities investigated. However, Prieur et al. (2018) noted the transition threshold between crater morphologies, for a given impact into a layered target, depended on the impactor's mass and velocity.

Crater size

For the impacts into layered targets simulated here, the crater radius only varies for $h/a < 6$, while the crater depth varies for layer thicknesses $h/a < 6$. Figure 5.5 shows the normalised crater dimensions (radius, R and depth, d), as a function of regolith thickness, h/a. The crater radius was measured at the pre-impact level, while the crater depth was

measured from the pre-impact level, downwards. In the non-porous substrate layered cases, the crater radius increased with increasing regolith thickness, until it reached a peak value of just over $30a$, at around $h/a \approx 6$. Then, as the regolith thickness was increased further, the crater radius slightly decreased to a constant value of about $25a$. By contrast, the crater depth remained constant with increasing regolith thickness, until $h/a \approx 6$, then increased as the stronger substrate became submerged deeper beneath the regolith layer.

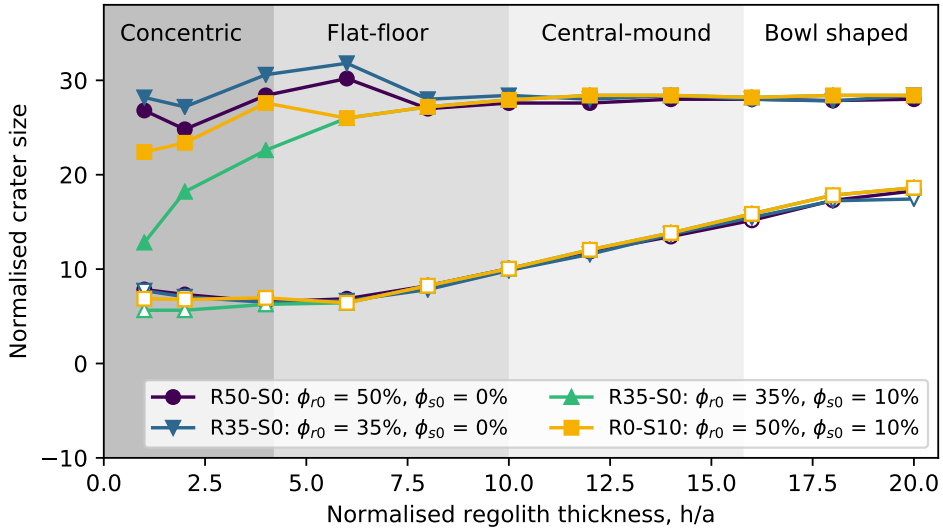

Figure 5.5: Normalised crater size for impacts into layered targets. Crater radius (filled symbols) and crater depth (hollow symbols) normalised by the impactor radius, a, as a function of normalised regolith thickness, h/a, for four different layering configurations. The shaded areas denote the corresponding cratering morphology from each impact.

Ejected mass

It was shown in the previous section that DART impacts into two-layer targets produce different crater morphologies, each of which had a different cratering efficiency. For impacts into homogeneous targets, the crater size is strongly correlated with the amount of ejecta produced, and a similar behaviour is expected for impacts into layered targets.

Figure 5.6 shows the total ejected mass, M, as a function of the upper layer thickness, normalised by the impactor radius, h/a. The ejected mass for each simulation is normalised by the amount of ejected mass from an equivalent impact into a half-space regolith target, with no lower layer, M_{hs}. R35-S0 and R35-S10 results are normalised

by the total mass ejected from an impact into a 35% porosity homogeneous half-space target, while R50-S0 and R50-S10 results are normalised by the mass ejected from an impact into 50% porosity half-space target.

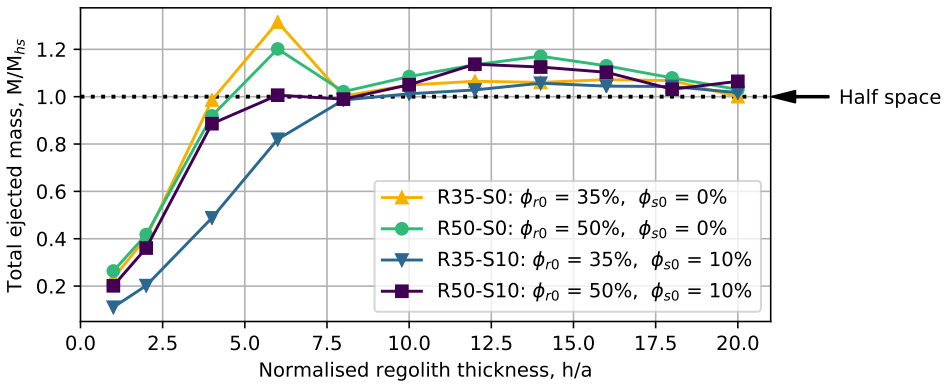

Figure 5.6: Total ejected mass, M, normalised by the mass ejected in the half-space case, M_{hs}, for impacts into layered targets with different regolith-substrate porosities configurations: R35-S0, R50-S0, R35-S10 and R50-S1 (see Table 5.3 for details). The total mass is plotted as a function of regolith thickness h normalised by the impactor radius, a.

For impacts into regolith layers with a thickness greater than $\approx 18h/a$, the total ejected mass converged to the mass ejected in the equivalent homogeneous regolith scenario. As the crater only formed in the upper layer, the influence of the substrate on the excavation flow was not significant. However, as the substrate got closer to the surface, up to 20% more mass was ejected than in the porous homogeneous regolith cases. This amplification in ejected mass is a consequence of the difference in the mechanical impedance (the product of density and wave speed) between the upper and lower layers. The impedance contrast results in a strong reflection of the shock wave at the boundary, and only partial transmission of energy into the substrate. As a result, less of the impactor kinetic energy was transmitted into the substrate and more was retained within the shallow subsurface, which amplified the ejection speeds in the upper layer.

On the other hand, for thin regolith layers (h/a less than 4; concentric craters) the ejected mass is less than in the homogeneous upper-layer case, despite the greater density of the material in the lower layer. At these regolith thicknesses, the excavation flow is strongly impeded at depth by the higher strength in the lower layer, but less im-

peded in the weaker regolith. The large strength difference between the layers more than compensates for the higher density of the substrate material and results in a reduction in total ejected mass relative to the homogeneous upper-layer case.

For intermediate regolith layer thicknesses of about $4< h/a <10$, the total ejected mass can be higher or lower than in the homogeneous upper-layer case, depending on the size of the porosity contrast between the layers. In this regime, both effects— increased resistance to flow in the substrate, and reflection of kinetic energy back into the regolith—are in competition. For the scenarios with a nonporous substrate, maximum ejecta mass amplification (20–30%) occurs at a regolith thickness of $h/a \approx 6$. A small amount (10%) of porosity in the substrate material is sufficient to negate most of the amplification of ejection from shock wave reflection.

Ejected momentum

Figure 5.7a shows the cumulative mass ejected at speeds higher than velocity v, $M(> v)$, normalised by the mass of the impactor, m, as a function of ejection velocity, v, normalised by the impactor velocity, U. The cases illustrated are for a 35% porosity upper layer and a nonporous substrate (R35-S0). The ejecta mass-velocity distributions were integrated to determine the cumulative, vertically ejected momentum, $p_{ej(z)}/mU = (\beta - 1)$, as a function of ejection speed in the vertical direction (Fig. 5.7b).

An impact into a 35% porous homogeneous regolith target produced a normalised total ejecta momentum, $\beta - 1$, of about 1.75 (y-intercept of the dotted line in Fig. 5.7b). The effects of layer thickness on ejected momentum are more complex than on the ejected mass, as layering influences both the velocity and the mass of ejecta. For a regolith layer thickness $h/a = 14$, $\beta - 1$ is 10% greater than in the regolith half-space case. At this regolith thickness, the top of the substrate is sufficiently close to the surface for the reflected shock wave to significantly increase ejection speeds towards the end of crater growth. This results in the amplification of ejection speeds and momentum of the slowest ejecta that is last to leave the crater.

For regolith thicknesses $4< h/a <10$, where the impact formed flat-floored craters,

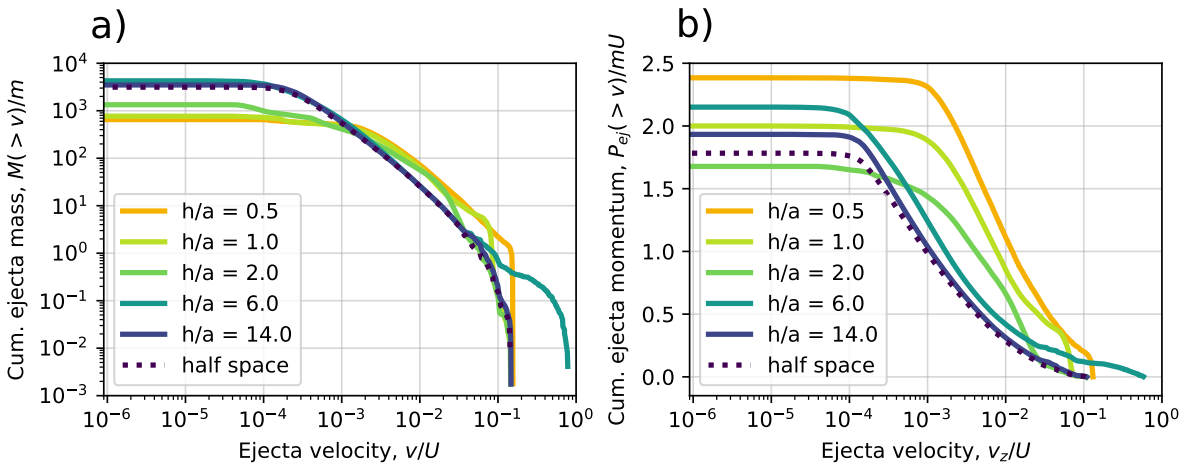

Figure 5.7: Ejecta distribution from impacts into layered targets with a 35% porosity regolith of varying thicknesses ($0.5< h/a <14$), overlying a non-porous substrate. a) Cumulative ejected mass, $M(> v)$, normalised by the mass of the impactor, m, as a function of normalised ejection velocity, v/U. b) Total ejected momentum, $\beta - 1$, as a function of the normalised vertical component of the velocity, v_z/U.

the shock wave reflects off the regolith-substrate boundary earlier in the cratering process, because the boundary is closer to the surface. Earlier shock wave reflection likewise results in amplification of ejection speeds earlier in the cratering process, such that even the fastest ejecta are given an extra acceleration from the reflected shock wave. For $h/a \approx 6$, $\beta - 1$ is increased to over 2.

For thin regolith layers, $h/a < 6$, a number of competing effects are observed. On the one hand, as regolith thickness is decreased the reflected shock wave occurs earlier and earlier, tending to produce an even larger amplification of ejection speeds. On the other hand, the high strength of the substrate also acts to retard the excavation flow at depth, which reduces ejection speeds. Finally, as the regolith layer becomes very thin, $h/a <1$, dense, lower layer material becomes part of the ejecta mass. Both the mass and the speed of the fastest ejecta, relative to the porous half-space case, were increased by the high density and the low shock wave attenuation of the lower layer. The highest $\beta-1$ value was observed in the thinnest regolith layer case simulated, with $h/a = 0.5$.

Fig. 5.8 shows the momentum carried away by the ejecta, $\beta - 1$, as a function of regolith thickness, h/a, for the four layering scenarios investigated here: R35-S0, R50-S0, R35-S10 and R50-S10. For thick regolith layers, the trend in all cases is well behaved,

while for thinner regolith layers, h/a <10, the behaviour is more complex. In this range, $\beta - 1$ is very sensitive to the material properties of the two layers. The figure also shows that when the substrate has a small porosity, any amplification in ejected momentum is reduced or even negated for thin-layer scenarios.

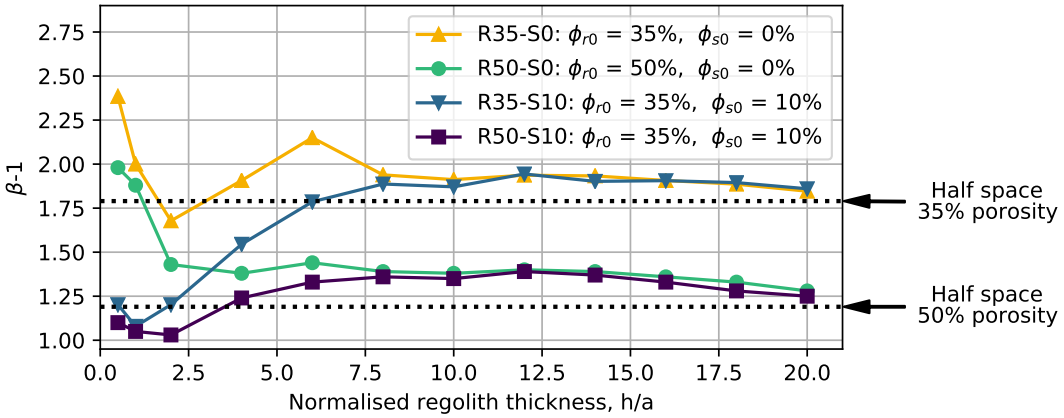

Figure 5.8: Normalised ejected momentum, $\beta - 1$, from impact simulations into four different configurations of layered targets, R35-S0, R50-S0, R35-S10 and R50-S10 (Table 3). $\beta - 1$ is plotted as a function of target regolith thickness, h, normalised by the impactor radius, a. $\beta - 1$ from impacts into 35% and 50% porous half-space are plotted for comparison (dotted horizontal lines).

Compared with the uniform half-space cases, it was found that the optimum layer thickness that produces the maximum ejected momentum depends on the strength and density ratios of the two layers, and it can be different to the layer thickness that results in the greatest total ejected mass.

In the R35-S0 impact scenario, the most mass was ejected at $h/a = 6$, and the largest $\beta - 1$ amplification was at $h/a < 0.5$, with a 30% amplification, and at $h/a = 6$, with a 20% amplification. On the other hand, in the R50-S0 impact scenario, the most mass was ejected at $h/a = 6$, while was only 10% larger than in the regolith half-space case. This suggests that the additional mass is ejected at very low velocities and it does not add significantly to the total momentum of the ejecta. The greatest ejected momentum occurred at $h/a = 0.5$, even though the ejected mass in this case was 70% lower than the homogeneous regolith case.

5.3.3 DART impact into targets with an exponentially decreasing porosity with depth

The last simulated scenario considered DART impacts into asteroid targets with a porosity that decreased exponentially with depth. Impacts into two target configurations were numerically simulated, one with a surface porosity of $\phi_0 = 50\%$ and a minimum porosity of $\phi_k = 0\%$ (S50–K0), and one with surface porosity of $\phi_0 = 35\%$ and a minimum porosity of $\phi_k = 10\%$ (S35–K10). For each target configuration the porosity e-folding depth $1/h_*$ was varies between 0.1 and 1.0.

All the impacts simulated in this case formed simple bowl-shaped craters, with radii that remained almost constant with varying e-folding depth, h_*. The crater radius was 10 m in the S50–K0 case and $\approx$ 10.5 m in the S35–K10 case, which is comparable to the radius of craters formed in the equivalent half-space targets, with 50% and 35% porosity, respectively.

Figure 5.9a shows the total ejected mass for the two simulated scenarios, S50–K0 and S35–K10, as a function of normalised porosity e-folding depth, h_*/a. A smaller e-folding depth implies a more rapid decrease in porosity with depth below the surface (Fig. 5.9). In both cases, the ejected mass is normalised by the total ejected mass in their corresponding minimum porosity half-space scenario. Figure 5.9b shows the total momentum carried away by the ejecta in the z-direction, normalised by the impactor momentum, $\beta - 1$, as a function of normalised porosity e-folding depth, h_*/a.

Both the ejected mass and the ejected momentum graphs follow the same trend. For large porosity e-folding depths, h_*/a >12, there was no significant increase in the ejected mass or the ejected momentum, compared to the equivalent half-space scenario. On the other hand, as porosity e-folding depth decreased, h_*/a <12, more mass was ejected as the density of the ejected subsurface material increased. Similarly, the denser ejected mass also added to the amount of ejected momentum, $\beta - 1$, causing an amplification of up to 25%.

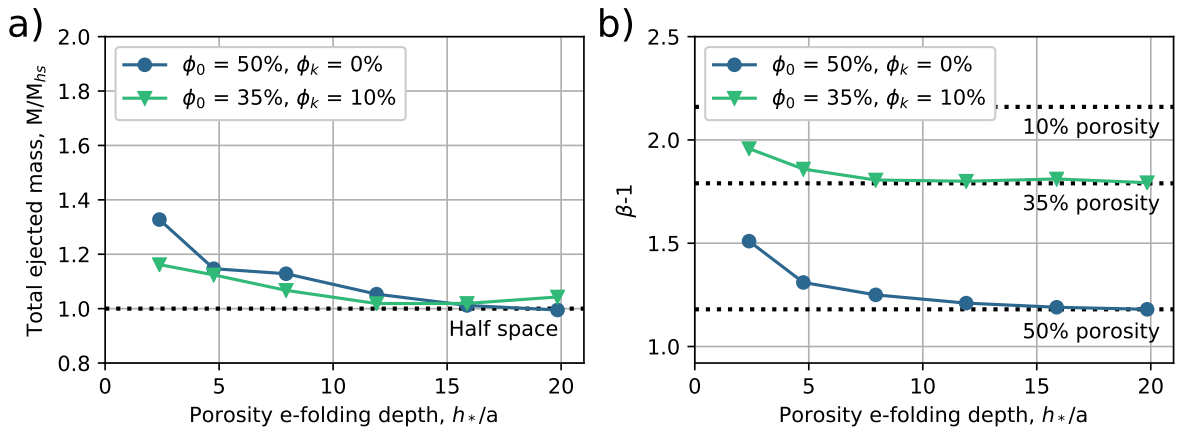

Figure 5.9: Numerical simulations results for impacts into targets with a continuous porosity gradient. a) Total ejected mass, as a function of normalised porosity e-folding depth, h_*/a. The mass ejected from the $\phi_0 = 50\%$, $\phi_k = 0\%$ case was normalised by the 50% half-space scenario and the mass from $\phi_0 = 35\%$, $\phi_k = 10\%$ was normalised by the 35% half-space scenario. b) Normalised ejected momentum, $\beta - 1$ as a function of normalised porosity e-folding depth. The dotted horizontal lines represent the $\beta - 1$ in the 10%, 35% and 50% porosity half-space.

5.4 Discussion

5.4.1 Comparing ejecta from impacts into layered targets with impacts into targets with a porosity gradient

To allow for a meaningful comparison between two impacts, where one is in a layered target and one is in a homogeneous target with exponentially increasing density, this work compared the ejecta mass and momentum transfer from impacts into targets with equivalent mass per unit area. The porosity-target depth function for each simulated target was integrated and it was found that a layered target of thickness h/a has the same mass per unit area as a target with a porosity e-folding gradient of h_*/a. For example, a target with a surface porosity $\phi_0 = 50\%$, minimum porosity $\phi_k = 0\%$ and an e-folding depth of $h_*/a = 20$ had the same integrated area as a target with a $20a$ thick 50% porous regolith layer overlying a non-porous substrate (Fig. 5.10).

Figure 5.11a shows the total ejected mass from the R50-S0 layering scenario (50% porosity upper layer over a non-porous substrate), compared with the S50–K0 porosity gradient scenario (50% surface porosity and 0% minimum porosity). The ejected mass

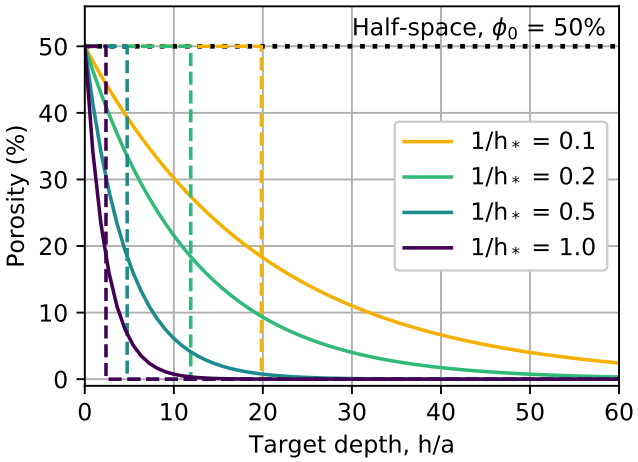

Figure 5.10: Target porosity as a function of depth for a range of e-folding depths, $0.1 < 1/h_* < 1.0$. The surface porosity is 50% and the minimum porosity is 0%. The equivalent integrated area from a layered target porosity-depth function is shown in same colour and dashed lines. The homogeneous half-space case at 50% porosity is plotted for comparison (dotted line).

in the layered targets is plotted as a function of regolith layer thickness, h/a, while the ejected mass from the exponentially-decreasing porosity targets is plotted as a function of porosity e-folding depth, h_*/a. Similarly, Figure 5.11c shows the normalised ejected momentum, $\beta - 1$ for the R50-S0 layering scenario, compared with the S50–K0 exponentially-decreasing porosity scenario.

Impacts into both the layered target and the exponentially-decreasing porosity target scenarios display an amplification in the amount of ejected momentum, $\beta - 1$, compared to the homogeneous 50% half-space case. In both cases, $\beta - 1$ has an ascending trend with decreasing regolith thickness, and with values of up to 60% larger than in the half-space case (Fig. 5.11c). However, the mechanism responsible for the amplification differs between the two scenarios. For the exponentially-decreasing porosity scenarios, the amplification in $\beta - 1$ is caused by the ejection of denser subsurface material. In the layered scenario, the amount of ejected mass is limited by the high strength of the substrate, which impedes the excavation flow (Fig. 5.11a). The amplification in $\beta - 1$ is instead caused by the ejecta acceleration due to the reflection of the shock wave.

Fig. 5.11b and d shows the normalised total ejected mass and the normalised ejected momentum from the R35-S10 layering scenario (35% porosity upper layer over

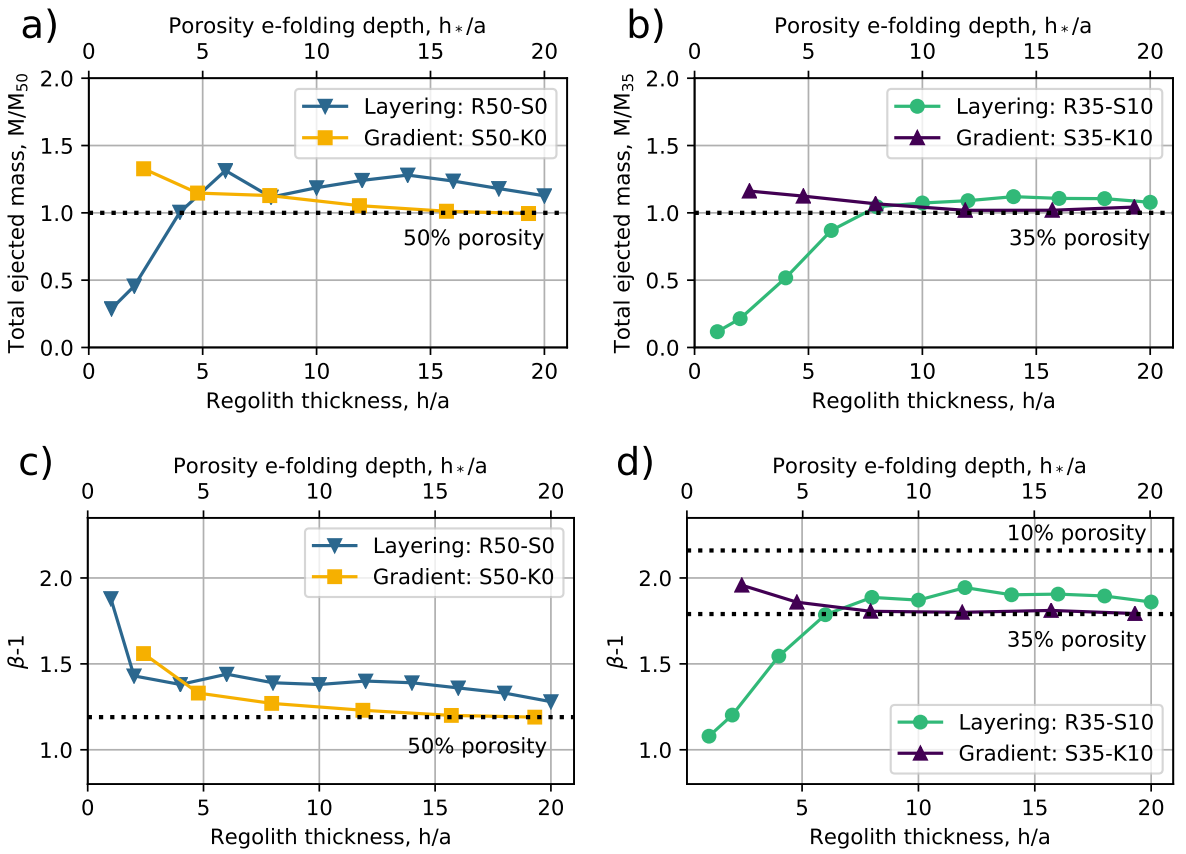

Figure 5.11: a) Total ejected mass, M, normalised by the ejected mass in the 50% porosity half-space scenario, M_50, as a function of regolith layer thickness, h/a, for R50-S0 and S50–K0 target scenarios. b) Total ejected mass normalised by the mass ejected in the 35% half-space scenario, M/M_{35}, as a function of regolith layer thickness, h/a, for R35-S10 and S35–K10 target scenarios. c) Normalised ejected momentum, $\beta - 1$, as a function of regolith thickness, h/a, for R50-S0 and S50–K0 target scenarios. d) $\beta - 1$, as a function of regolith thickness, for R35-S10 and S35–K10 target scenarios. In all figures, the upper label shows the equivalent porosity e-folding depth, h_*/a. The equivalent ejected mass and $\beta - 1$ for the porous half-space scenarios are plotted for comparison (dotted lines).

a 10% porous substrate), compared with the S35–K10 porosity gradient scenario (35% surface porosity and 10% minimum porosity).

For $h/a < 10$, impacts into the S35–K10 target scenario produced similar trends for $\beta - 1$ as in the S50–K0 target scenario, with an increased amplification in the amount of ejected momentum towards sharper porosity gradients, compared to an impact into a 35% porous half-space. At the same time, for the same h/a, impacts into R35-S10 produced smaller $\beta - 1$. This is caused by the difference in strength: in the layered case, the lower layer is denser, but also stronger; in the porosity gradient case, the deeper material is denser, but not stronger.

The work presented here is just a first step in understanding the effects of layering on small-body crater formation. Future work is needed to examine the effect of a continuous increase in strength with depth commensurate with the decrease in porosity. Impact angle is also expected to play a significant role in the ejecta distribution and momentum transfer. While numerical simulations presented were restricted to vertical impact only, future studies should also investigate and quantify the role of the impact angle on the ejecta distribution of impacts into homogeneous and layered asteroid targets.

5.4.2 Implications for the DART mission

The DART mission will be the first to produce a controlled deflection of a near-Earth asteroid. DART will provide a useful opportunity to test human's capability to deflect a potentially hazardous asteroid and to calibrate numerical simulations of m-scale impacts on asteroids. As mentioned previously, an approximate measure of the deflection (β) will be determined from astronomical observations of the double system, before and after impact.

The numerical simulations presented here used impactor properties appropriate for the DART spacecraft and target scenarios consistent with the current understanding of DART's target, Didymoon. In all of the target scenarios simulated, the deflection caused by the DART impact was amplified by the escaping crater ejecta; i.e., $\beta - 1 > 0$.

This work shows that $\beta - 1$ can vary significantly depending on the target asteroid's properties and structure. If the DART spacecraft impacts a homogeneous porous target, $\beta - 1$ can have values between 0.5 and 3.5, depending on the target cohesion and porosity. On the other hand, if the DART spacecraft impacts a layered target, the deflection can be both amplified by up to 30% or reduced by up to 60%, compared with the equivalent homogeneous upper layer case. If the transition between the surface material and the substrate is gradual, then $\beta - 1$ can be amplified by up to 30% compared with the case of a homogeneous high-porosity subsurface.

However the simulations presented here also suggest that similar deflection (i.e., similar β values) can be achieved by impacting targets with very different material prop-

erties or structures. In a homogeneous target scenario, the same deflection amplification were found for a series of targets with different cohesion-porosity combinations, while in the layered and the porosity gradient target scenarios, the same $\beta - 1$ was found for different layering/porosity configurations.

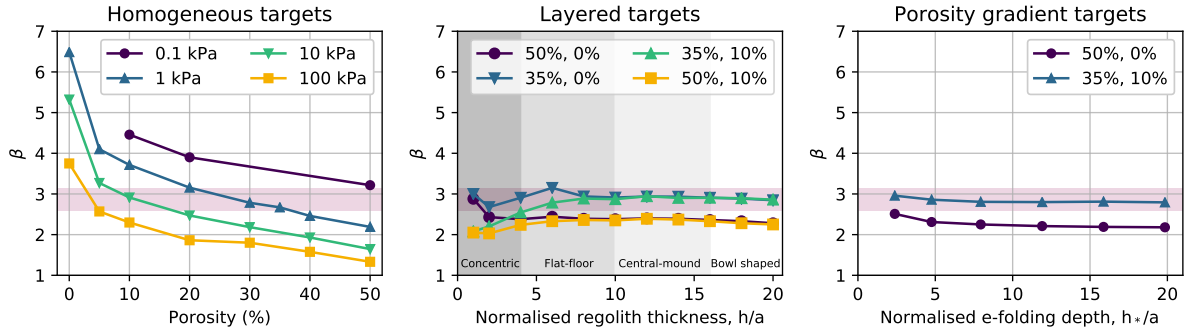

Figure 5.12: Total ejected momentum in the z direction ($\beta - 1$) for: a) Impacts into homogeneous half-space with four different cohesions and different porosities. b)$\beta - 1$ from impacts into layered targets, as a function of normalised regolith thickness, h/a, for four different layering configurations. The shaded areas represent the corresponding cratering morphology formed by each impact. c) $\beta - 1$ from impacts into targets with exponentially decreasing porosity with depth, as a function of normalised e-folding depth, $h_{/a}$, for two different porosity configurations.

For example, $\beta - 1 \approx 1.9$ was found for impacts into a homogeneous targets with cohesion and porosity of: 100 kPa and few percent porosity, 10 kPa and 20% porosity, 1 kPa and $\approx$ 30% porosity or 0.1 kPa and 50% porosity. These results suggests that a measurement of the momentum transfer alone is not sufficient to validate numerical models and to turn the DART experiment into a well understood and reproducible asteroid deflection method.

5.4.3 Ejecta plume measurements by LICIACube

In addition to the momentum transfer, information about the ejecta plume will be provided by the LICIACube. LICIACube was described in detail in Section 2.8.

LICIACube, will be able to monitor the ejecta plume behaviour and a similar exercise was achieved by the NASA's Deep Impact mission, which released a 366 kg impactor into the nucleus of Comet 9P/Tempel 1, at approximately 10 km/s. The evolution of the ejecta plume was captured in a sequence of images taken by the flyby spacecraft.

The material ejected from the crater reflected back the sunlight, with different opacities as a function of time and distance from the ejecta source. Subsequent studies of these measurements (Richardson et al., 2009; Holsapple and Housen, 2007) showed that the optical thickness, e.g. how opaque the cone-shaped cloud formed by the ejected particles is at various times and positions, can be estimated from the particle size distribution and the mass in the plume (Holsapple and Housen, 2007). LICIACube therefore plans to capture similar images of the DART ejecta plume, at 136–163 seconds after the DART impact.

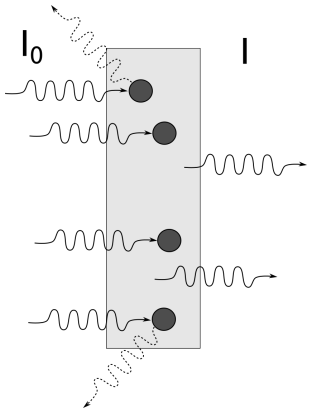

Figure 5.13: Schematic representation of the optical depth. Incident radiance of intensity I_0 gets scattered or absorbed by the component particles in a material. The radiance that gets transmitted through the material has an intensity I.

From observations, the opacity of the ejecta plume can be determined in terms of the optical thickness of the plume, τ, which is the natural logarithm of the ratio between the incident and transmitted radiance intensity,

$$\tau = \ln\left(\frac{I_0}{I}\right). \tag{5.2}$$

Figure 5.13 shows a schematic representation of the optical depth calculation. Incoming parallel light rays of intensity I_0, get scattered or absorbed by if colliding with particles inside a rectangular section of material. The light going through the material has an intensity I. If τ is smaller than 1, then the material is optically thin. For τ larger than 1, the transmitted radiance intensity is much smaller than the incident intensity, $I_0 >> I$, and the material is optically thick (opaque).

From numerical calculations, the opacity of the ejecta plume at various times and

positions can be estimated from the size distribution of the ejecta particles and the mass in the plume.

The particle size distribution is not known on Didymoon, however it is expected to be a coarse regolith, similar to the one on Itokawa (Nakamura et al., 2012; Mazrouei et al., 2014; Tancredi et al., 2015), Bennu (Walsh et al., 2019) or Ryugu (Michikami et al., 2019). Therefore, assuming the same size-particle distribution as on Itokawa, $n(s) = 2.746 \times 10^5 s^{-3.98}$, the cross sectional area in the in the size range from $d_1 = 1$ mm to $d_2 = 1$ m can be calculated from:

$$A = \int_{1mm}^{1m} \frac{\pi s^2 n(s)}{4} ds, \tag{5.3}$$

where s is the particle radius. The cross-sectional area per unit mass is then $\frac{A_d}{\rho V_d}$, where ρ is the particle density and V_d is the volume occupied by the same size-particle distribution:

$$V = \int_{1mm}^{1m} \frac{\pi s^3 n(s)}{6} ds. \tag{5.4}$$

The total cross sectional area per unit mass of ejecta is then

$$\frac{A_d}{\rho V_d} = 0.1962 \mathrm{m}^3/\mathrm{kg}. \tag{5.5}$$

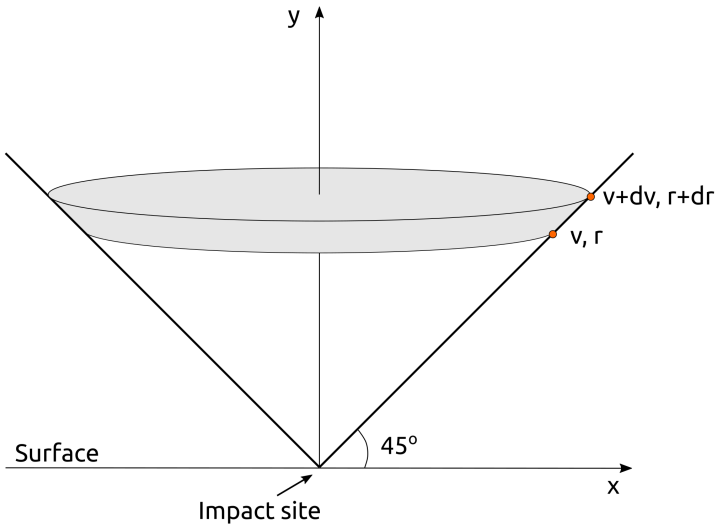

Figure 5.14: Schematic representation of the ejecta cone.

Considering two particles, with velocity v and $v + dv$, their position as a function

of time can be calculated from the ballistic equations:

$$x_1 = v_x t \tag{5.6}$$

$$y_1 = v_y t - \frac{1}{2} g t^2 \tag{5.7}$$

$$x_2 = (v_x + dv_x)t \tag{5.8}$$

$$y_2 = (v_y + dv_y)t - \frac{1}{2} g t^2 \tag{5.9}$$

where v_x and v_y are the horizontal and vertical components of the velocity, respectively, t is time and g is the acceleration due to gravity on Didymoon. For a vertical impact, $M(> v)$ gives the mass of ejecta launched at velocities higher than v and dM/dv gives the total mass in the velocity increment (Fig. 5.14). At time t after the impact, the mass of ejecta within a distance $r = vt$ from the impact point, $M(> r)$ can be calculated from $M(> v)$ (Housen and Holsapple, 2011). Then the ejecta mass within dr is dM/dr.

It is then assumed that the ejecta plume forms an inverted cone that makes 45° angle with the surface, which remains fixed in time, and and that the ejecta cone is much larger than the crater size, which here is ignored. Then the area occupied by the ejecta in the velocity increment dv can be calculated from the lateral surface of a truncated cone (Fig. 5.14). The optical depth, τ, of the ejecta cone resulted from an impact can then be approximated as the ratio of the total cross sectional area of the ejected particles to the spatial area they occupy (Holsapple and Housen, 2007):

$$\tau = \frac{\frac{dM}{dr}\frac{A}{\rho V}}{\sqrt{2}\pi r}. \tag{5.10}$$

τ also depends on the obliquity of the intersection of LICIACube's line of sight through the ejecta cone and the scattering or extinction efficiency (Cheng et al. 2019), but for simplicity these effects are ignored here.

Using the analytical approximation of the optical thickness, τ (Eq. 5.10), opacity of the ejecta plume from the DART impact can be calculated as function of ejecta height, at different times after the DART impact.

As discussed previously, one of the biggest unknown about Didymoon is the surface cohesion. Fig. 5.15 shows the plume thickness as a function of height for a vertical DART impact into a 20% porous homogeneous target, with assumed cohesion between $Y_0 = 100$

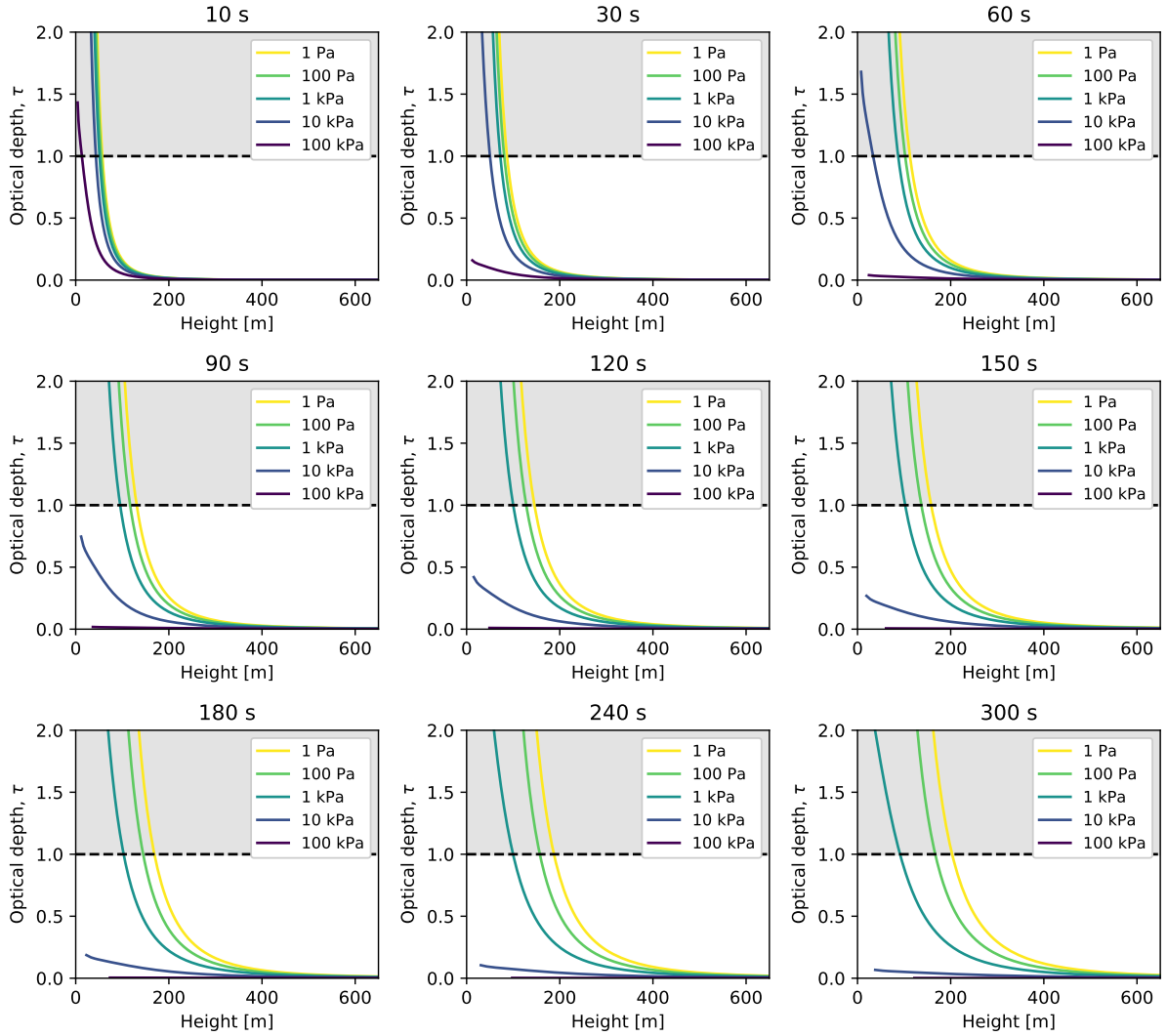

Figure 5.15: Ejecta plume opacity as a function of height, at different times after the impact and for different target cohesions.

Pa and $Y_0 = 1$ MPa. It can be seen that for a target stronger than 100 kPa, most of the ejecta plume would have dissipated beyond the point it is no longer visible in the first 10 seconds after the impact. At the time LICIACube will take the images (t = 136-166 seconds after the DART impact), the ejecta plume from a target stronger than 1 kPa would have mostly cleared out, allowing the cubesat to photograph the asteroid surface and the impact crater. However, it is likely that the surface strength will be lower than 1 kPa, in which case a significant amount of the ejected mass will still obscure the crater. In this case, the height at which the ejecta plume becomes opaque could be interpreted as an approximate measure of the target strength.

This analytical approach of estimating the opacity of the ejecta plume as a function

of height, is only valid for a vertical impact into a homogeneous target of a given surface cohesion. The ejecta plume distribution can also vary depending on the target subsurface structure and impact angle.

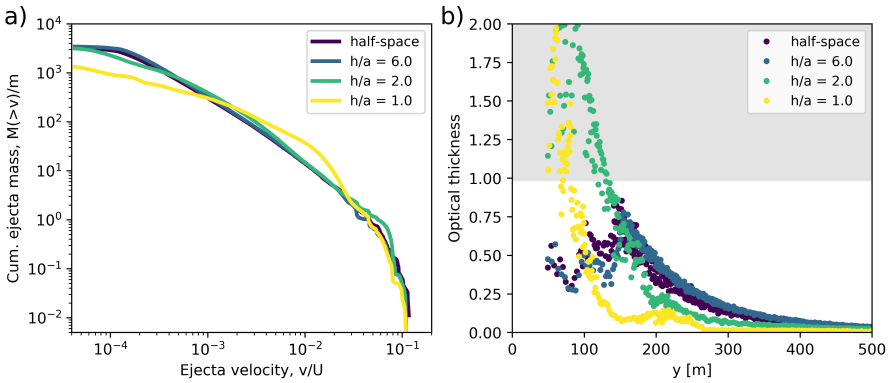

Figure 5.16: Mass-velocity distribution (a) and ejecta plume opacity as a function of height (b), at $T = 165$ s after the DART impact into a 35%, 1 kPa half-space and layered targets (R35-S0: $\phi_{r0} = 35\%$, $\phi_{s0} = 0\%$) with $h/a = 1$, 2 and 6.

For example, Figure 5.16a and b show the mass velocity distribution and the ejecta plume opacity as a function of height for impacts into a 35% porous, 1 kPa half-space and layered targets with a 35% porous regolith overlying a non-porous substrate (R35-S0: $\phi_{r0} = 35\%$, $\phi_{s0} = 0\%$), and several layer thicknesses: $h/a = 1$, $h/a = 2$ and $h/a = 6$. While at large h/a the ejecta plume thickness as a function of height is indistinguishable from the half-space scenario, at $h/a < 3.0$, the height at which the ejecta plume becomes opaque is lower and depends on h/a. Therefore, the optical thickness as a function of height can not be used as a diagnostic of the asteroid surface cohesion, unless the asteroid has a homogeneous internal structure or the layer is thick enough to not influence the ejecta distribution (e.g. $h/a > 6$).

5.4.4 Validation of numerical models using the Hera missions measurements

The results presented in this chapter show that some simulated impacts into different targets produced very similar $\beta - 1$ values and that the measurements taken by the LICIACube might not give us enough additional information about the target composition and structure. However, the impact craters simulated here produced very different crater sizes and morphologies. For example, the same deflection amplification ($\beta - 1 \approx 1.9$) was

found when impacting homogeneous targets with cohesions and porosities of: 100 kPa and few percent porosity, 10 kPa and 20% porosity, 1 kPa and ≈30% porosity or 0.1 kPa and 50% porosity. Meanwhile, the same impacts produced craters that had radii of 5 m, 15 m, 23 m and 37 m, respectively.

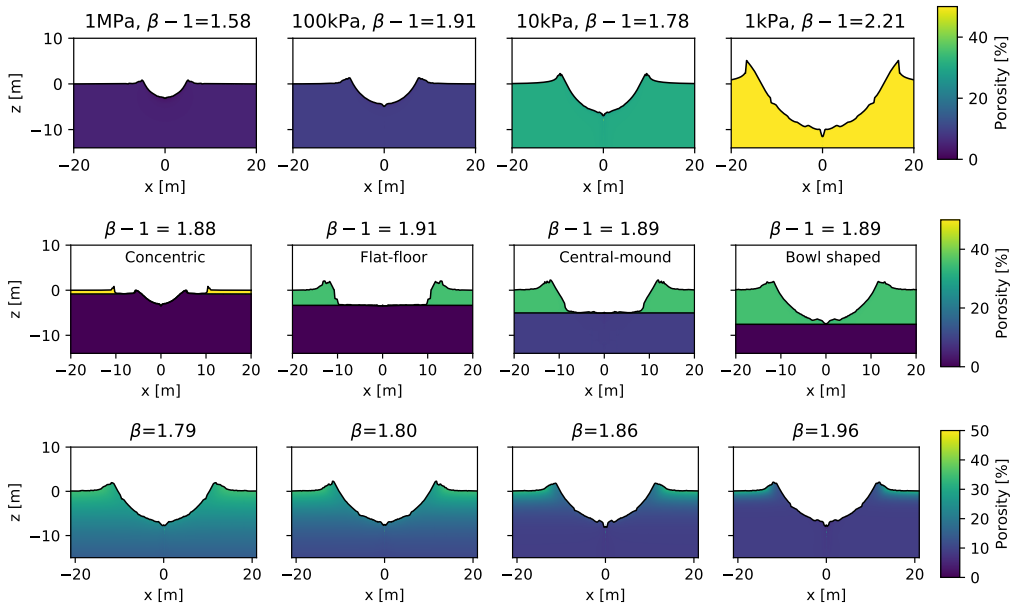

Figure 5.17: Crater morphologies for impacts into targets with different properties that produce a similar total ejected momentum ($1.3 < \beta - 1 < 1.9$). a) Impacts into homogeneous half-space; b)impacts into layered targets; c) Impacts into targets with exponentially decreasing porosity withdepth.

The same amplification, $\beta - 1 \approx 1.9$, was also produced in different layered-target scenarios: An impact into a 50% porous regolith layer, one impactor radius thick, overlying a non-porous substrate produced a concentric crater with a radius of 4 m, while an impact into a regolith layer eight impactor radii thick, overlying a non-porous or few percent (<10%) porous substrate, produced a flat-floor crater, with a radius of ≈ 10 m. $\beta - 1 \approx 1.9$ was also observed in the simulations of impacts into targets in which porosity decreased exponentially with depth from a porosity of 35% at the surface to a minimum subsurface porosity of 10% at a depth of ≈ 1–2 m, which produced bowl shaped craters with radii of about 10 m.

To further study the outcome of the DART impact, ESA is sending a rendezvous mission, Hera, which will arrive at the asteroid system several years after DART (Cheng et al., 2018; Michel et al., 2018). Hera will take high-resolution images of the surface

and accurate measurements of the deflection. Therefore, before the arrival of Hera at Didymoon, which will be able to evaluate the outcome of the DART impact in great detail, measurements of $\beta - 1$ alone will not be sufficient for the purpose of numerical model validation. Data collected by the Hera spacecraft will be used to construct a shape model of Didymoon and constrain its bulk density, as well as setting approximate limits on the surface cohesion by surveying the asteroid surface roughness and performing a CubeSat bouncing experiment (Küppers et al., 2019). In addition, high-resolution images of the DART impact crater will determine the crater size and morphology.

Validation of numerical models of impact deflection against a controlled impact scenario with a measured $\beta - 1$ value is not only important for planetary defence, but also for inferring the subsurface structure of small asteroids. The DART crater morphology can provide insight into the surface and subsurface properties of Didymoon, whilst helping our understanding of the origin and formation processes of small near-Earth binary asteroids.

5.5 Conclusions

The work presented in this chapter contains numerical simulations of the DART impact using the iSALE shock physics code. Various different impact scenarios in the strength regime were investigated to determine the sensitivity of crater morphology, ejecta mass-velocity distribution and momentum enhancement, β, to target properties and structure. Targets with three different structures were investigated: homogeneous porous half-space, layered targets with a porous weak upper layer overlying a stronger bedrock layer and targets with porosity that decreased exponentially with depth.

For impacts into homogeneous porous half-space, it was found that cohesion has the greatest influence on crater diameter, while both cohesion and porosity have a major influence on the ejected mass and subsequently, the amount of momentum transferred from the impact for deflection. For the DART impact, the expected deflection was calculated as $\beta - 1$ between 1 and 3, implying a momentum multiplication factor of between

2 and 4.

For impacts into layered targets, it was found that the presence of a less porous, stronger lower layer within six impactor diameters of the surface can influence the crater morphology and the mass velocity distribution of ejecta. This chapter showed that there is an amplification in the amount of ejected mass, caused by the proximity of the stronger substrate to the surface and that the change in mass and velocity of the material ejected is dependent on the thickness of the upper layer. However, this amplification does not always result in an enhancement of ejected momentum relative to the homogeneous upper-layer case. Both amplification and reduction of ejected mass and momentum relative to the homogeneous upper-layer case can occur in two-layer targets. This result has important implications for asteroid deflection. For the case of DART, momentum enhancement can change by up to 90%.

Impacts into targets with an exponentially decreasing porosity with depth produced an enhancement in the ejected mass and ejected momentum, but the effects were only considerable for relatively sharp decreases in porosity that occur within 6 m of the asteroid surface.

By measuring the DART crater, the Hera mission will provide vital data to test the predictive capabilities of numerical simulations of asteroid deflection.

Chapter 6

Morphological diversity of impact craters on asteroid (16) Psyche

The asteroid (16) Psyche, target of NASA's 'Psyche' mission, is thought to be one of the most massive exposed iron cores in the Solar System. Earth-based observations suggest that Psyche has a metal rich surface, however its internal structure cannot be determined from ground-based observations. This chapter presents simulations of impacts into a variety of possible target structures on Psyche, and shows the possible diversity in crater morphologies that the 'Psyche' mission could encounter. If Psyche's interior is homogeneous, then the mission will find simple bowl-shaped craters, with a depth-diameter ratio diagnostic of rock or iron. Craters will be much deeper than those on other visited asteroids and possess much more spectacular rims if the surface is dominated by metallic iron. On the other hand, if Psyche has a layered structure, the spacecraft could find craters with more complex morphologies, such as concentric or flat-floored craters. Furthermore, if ferrovolcanism occurred on Psyche, then the morphology of craters less than 2 km in diameter could be even more exotic. Based on 3-4 proposed large craters on Psyche's surface, model size-frequency distributions suggest that if Psyche is indeed an exposed iron core, then the spacecraft will encounter a very old and evolved surface, that would be more than 4 billion years old. For a rocky surface, then Psyche could be at least 3 billion years old.

6.1 Introduction

Asteroid (16) Psyche is one of the most intriguing Main-belt asteroids. Classified as an M-type asteroid (Tholen, 1984), early spectroscopic measurements showed consistency with iron-nickel meteorites observed in laboratory, making Psyche a possible candidate parent body for iron meteorites (Bell et al., 1989; Cloutis et al., 1990; Britt et al., 1992). Measuring approximately 223 km in diameter (Shepard et al., 2017; Viikinkoski et al., 2018), Psyche was long believed to be a massive exposed core of a differentiated planetesimal, which had its mantle stripped off by hit-and-run collisions in the early solar system (Asphaug et al., 2006).

The metal-rich composition of Psyche is supported by radar observations, which have reported unusually high radar albedos, almost three times higher than the albedos observed for S-type or C-type asteroids (Shepard et al., 2017). The radar observations also suggest a high mean bulk density (3600+600/-400 kg/m^3) of the upper 1 m (Shepard et al., 2017), and a uniform metal content across Psyche's surface (Sanchez et al., 2017). The asteroid's thermal inertia measurements are some of the highest recorded, which also suggests a metal-rich surface (Matter et al., 2013).

Despite the compelling evidence for a metal-rich surface and interior composition, more recent density estimates (Shepard et al., 2017; Hanuš et al., 2017; Drummond et al., 2018; Viikinkoski et al., 2018) and ground-based visible and near-infrared spectroscopic observations, have challenged the interpretation that Psyche is an intact iron core remnant. Estimates of Psyche's bulk density range between 3.8 and 4.6 g/cm^3 (Shepard et al., 2017; Hanuš et al., 2017; Drummond et al., 2018; Viikinkoski et al., 2018), which although much higher than the measured bulk densities of siliceous or chondritic asteroids (Britt et al., 2002; Carry, 2012), are lower than the density of iron meteorites (Henderson and Perry, 1954). Moreover, high-resolution spectroscopic observations have revealed weak absorption features in the 0.9 μm, 0.43 μm (Hardersen et al., 2005; Fornasier et al., 2010) and 3 μm spectral regions (Takir et al., 2016), which indicate the presence of silicates and hydrated silicates on Psyche's surface. Water or hydroxyl is not expected to be found

on a primarily Fe–Ni body, and is inconsistent with a bare metallic core (Rivkin et al., 2000).

Several formation mechanisms, and therefore possible internal structures, have been proposed that could explain Psyche's metallic composition and relatively low bulk density (Shepard et al., 2017; Viikinkoski et al., 2018). If Psyche is the product of a series of disruptive collisions that also stripped away the silicate mantle, then the asteroid could have a predominantly Fe-Ni composition, with a bulk porosity of 40-50% generated by fragmentation and reaccumulation of core material (Shepard et al., 2017). Alternatively, Davis et al. (1999) argued that because there are no asteroid families associated with Psyche's missing mantle material, the proto-asteroid could have been shattered by impacts, with material from both core and mantle re-accumulating into a rubble pile body. The surface would then contain a mixture of metal and silicate material, similar to mesosiderites (Viikinkoski et al., 2018). On the other hand, if Psyche formed closer to the Sun (Bottke et al., 2006), it could be composed of highly reduced material that never melted (Elkins-Tanton et al., 2016). One of the most interesting formation scenarios attributes the elevated metal content at the surface to ferrovolcanism (Abrahams and Nimmo, 2019; Johnson et al., 2019), which would have exhumed metal-rich material to the surface, covering the mantle.

Asteroid (16) Psyche will be visited by the Discovery-class mission 'Psyche' (Elkins-Tanton et al., 2016; Elkins-Tanton et al., 2017), due to be launched in 2022 and arrive at the asteroid in 2026. Along with a gamma-ray and neutron spectrometer, a magnetometer and an X-band radio telecommunications system, the spacecraft will be equipped with a multispectral imager that will take high-resolution images of Psyche's surface (Bell et al., 2016). The instrument intends to map the entire surface at a spatial resolution of approximately 500 m/px, with $\geq$ 50% of the surface at 200 m/px or better and $\geq$ 30% at 20 m/px or better.

Asteroids like Psyche have a long collisional history that has reshaped their surface and even modified their internal structure. The size and morphology of a crater on an asteroid's surface are determined by both the projectile's properties (e.g. mass,

velocity), and the target's properties (e.g. strength, porosity, structure) (Melosh, 1989). The mapping and subsequent study of the impact craters on Psyche will help estimate the age of the asteroid surface (Neukum et al., 1975; Ivanov et al., 2002), as well as determine the near subsurface structure and composition. However, due to the unknown and possibly unusual geological history of Psyche, the spacecraft may find a much more complex asteroid topography than expected, with impact crater morphologies that are very different from those observed on other visited asteroids.

This chapter presents numerical simulations of impacts on asteroid Psyche analogues that include several possible internal asteroid structures. The chapter first summarises current observations of Psyche's surface, before describing the numerical approach and the different target scenarios considered. These included a homogeneous dunite mantle material, intact and porous exposed iron cores, and different mantle-core/iron-rock layering configurations. For each impact scenario this work investigated the resulting crater size and morphology, and used these results to derive scaling relationships and model crater size-frequency distributions.

6.1.1 Observations of possible craters on Psyche

Numerous observational studies, using different techniques, have characterised Psyche's surface topography. Thermal inertia measurements suggest that Psyche has a smooth surface (Matter et al., 2013), consistent with a fine-grained silicate regolith mixed with coarse iron grains on the surface; this interpretation is also consistent with emissivity spectrum measurements (Landsman et al., 2018). Radar (Shepard et al., 2017) and near-IR (Hardersen et al., 2005) observations indicate that the metal and silicates are spread homogeneously on Psyche's surface, however the metal/silicate ratio of the regolith seems to vary with rotation (Ockert-Bell et al., 2010).

Reconstructed 3D shape models (Shepard et al., 2017; Viikinkoski et al., 2018) have revealed several large quasi-circular depressions. Shepard et al. (2017) studied the southern hemisphere of the asteroid and identified two distinct depressions that they interpreted as impact craters: a wider and shallower depression (D1), $\approx$ 70 km in diameter,

and a smaller but deeper depression (D2), ≈ 50 km in diameter. Viikinkoski et al. (2018) studied the northern hemisphere of the asteroid, identifying two further units: a quasi-circular depression 80-100 km in diameter, referred to as D3, and an irregularly shaped depression, 90 km wide and 10 km deep. This chapter examined impacts into different target structures and asses whether any of them could reproduce these observed features.

6.1.2 Hydrated minerals on Psyche

For a long time Psyche was catalogued as an anhydrous M-class asteroid (Rivkin et al., 2000); however, the recent detection of a weak 3 μm band in the mid-IR spectra (Takir et al., 2016) suggests the presence of hydrated minerals on the surface. The 3 μm band spectra has been detected in four different rotation phases (Takir et al., 2016), and it appears to be non-uniformly distributed across Psyche's surface. An indigenous origin of minerals containing H_2O and/or HO bearing phases is not consistent with an exposed metallic core hypothesis.

A possible explanation is that the hydrated minerals could have an exogenous origin, delivered by impacts with asteroid families that exhibit 3 μm spectra features (Sanchez et al., 2017; Avdellidou et al., 2018). Volatile-rich exogenous material has already been detected on asteroids Vesta and Ceres. On Vesta, the Dawn mission revealed prominent low albedo terrains, named 'dark materials', distributed globally in a non-uniform manner (McCord et al., 2012; Reddy et al., 2012). The dark material is spectrally similar to carbonaceous chondrites (Reddy et al., 2012) and has absorption features attributed to the mineral serpentine, a typical component of CM meteorites (Nathues et al., 2014). Similarly, at least some of the hydrated material on Ceres is believed to have been delivered by impacts (Vernazza et al., 2017). This work examines the fate of hydrated minerals, namely serpentine, during impact events on three possible Psyche-like asteroid surfaces: non-porous dunite, non-porous iron and 40% porous, damaged iron.

6.1.3 Simple to complex crater transition

Impact craters are widely distributed on asteroids, and most of them are simple craters; however, above a critical crater diameter, D_{sc}, impact craters transition from a bowl-shaped internal structure, to a 'complex' one, as they undergo late-stage gravity-driven modification. Complex craters generally have a smaller depth-to-diameter ratio, compared with simple craters in the same target material, and can exhibit features such as central peaks, flat floors or terraced walls.

The simple-to-complex crater transition is usually relatively abrupt (occurs over a narrow range in diameter) and it is relatively well defined for impacts into large planetary bodies, occurring at approximately 5 km on Mars (Pike, 1980) and approximately 15 km on the Moon. D_{sc} appears to scale approximately as the inverse power of the surface gravity and is also substantially smaller on icy bodies compared with rocky bodies (Hiesinger et al., 2016). On asteroid Vesta, craters larger than 30 km are in a transitional simple-to-complex regime, exhibiting both simple and complex features, with only the biggest crater, Rheasilvia being considered completely complex (Schenk et al., 2012). On Ceres, which has an icy surface, the transition takes place at much smaller diameters than on silicate bodies (Hiesinger et al., 2016), probably due to the ice-rich surface being weaker than silicate.

A very simple model of the simple-to-complex transition equates the approximate gravitational stress beneath a crater at the transition diameter $\rho g D_{sc}$ with a constant measure of the effective strength Y of the target surface (Melosh, 1989). Such a model allows the simple-to-complex transition diameter to be compared on two worlds with different surface gravity, density and strength (Pike, 1980; Holsapple, 1993; Davison et al., 2013):

$$D_{sc} = D_M \left(\frac{g_M}{g}\right) \left(\frac{\rho_M}{\rho}\right) \left(\frac{Y}{Y_M}\right) \tag{6.1}$$

where g_M, ρ_M, Y_M and D_M are the surface gravity, surface density, surface cohesion and the simple-to-complex transition diameter on the Moon, respectively, and g, ρ and Y are the surface gravity, surface density and surface cohesion of the body of interest.

According to this equation, if Psyche's near surface is predominantly rocky silicate

($\rho \approx \rho_M$, $Y \approx Y_M$), and we assume an acceleration due to gravity, g, of 0.06 m/s (Shepard et al., 2017), then we would expect a transition diameter near 150 km. On the other hand, if Psyche's near surface is predominantly metal, with an effective strength much higher than a silicate surface $Y >> Y_M$, then the transition diameter on Psyche could be even higher than 150 km. However, complex craters have not yet been observed on metal-rich surfaces and other material specific properties, not included in Eq. 6.1, might also influence the simple-to-complex transition diameter.

Regardless, given that the current best estimate of Psyche's diameter is approximately 225 km, and the bulk density is estimated to be between 3.8 and 4.6 g/cm^3 (Shepard et al., 2017), it is very unlikely that any craters found on the asteroid's surface will exhibit a classical complex morphology.

As the proposed craters in this study are well below the simple-to-complex transition, here we neglected the acoustic fluidization effects. However, the acoustic fluidization effects for iron targets are not known and our omission might produce discrepancies between the simulated and observed craters.

6.2 Numerical model

To determine the size and morphology of impact craters on Psyche, the iSALE2D shock physics code (Collins et al., 2004; Wünnemann et al., 2006) was used to numerically simulate typical asteroid impacts into a variety of possible analog surfaces. iSALE2D is a multi-material, multi-rheology extension of the SALE hydrocode (Amsden et al., 1980), specifically developed for simulating impact processes and similar to the older SALEB hydrocode (Ivanov et al., 1997; Ivanov and Artemieva, 2002). iSALE includes a strength model suitable for impacts into geologic targets (Collins et al., 2004) and a porosity compaction model: the $\epsilon - \alpha$ model (Wünnemann et al., 2006; Collins et al., 2011). iSALE has been extensively validated against laboratory impact experiments (Wünnemann et al., 2016; Raducan et al., 2019), as well as benchmarked against other hydrocodes (Pierazzo et al., 2008; Davison et al., 2011) for simulating crater size and

morphology.

6.2.1 Resolution and regridding

Each numerical impact simulation ran until the crater was completely formed and the ejecta in close proximity to the crater had landed. Some simulations required a high spatial resolution to numerically resolve the near-surface target structure. However, due to the low gravitational acceleration on Psyche (≈ 0.06 m/s^2), ejecta traveling below the escape velocity takes a long time to fall back on to the target. To reduce the computational expense of such simulations, the simulation domain had an initial spatial resolution of 40 cells per impactor radius (cppr) that was coarsened by a factor of two after predetermined amounts of time, ending up with a 10 cppr resolution, using the regridding method described in Chapter 3.

6.2.2 Material models

The impacts simulated here considered a nonporous dunite impactor, modelled using the ANEOS equation of state and strength model described by Collins et al. (2004), with input parameters summarised in Table 6.1. The impact velocity was kept at 5 km/s, which represents the average impact velocity in the Main Asteroid Belt (Farinella and Davis, 1992). Craters on Psyche will have been formed by impacts at a range of oblique angles to the target surface, with the most likely angle of 45°. However, due to the axially-symmetric mesh geometry, our study was limited to vertical impacts only.

Table 6.1: Material model parameters for impact simulations into Psyche analogues. For all simulated materials we used the thermal parameters from Ivanov et al. (2010).

Description	Symbol	Dunite	Solid iron	Porous iron
Equation of state		Aneos[a,b]	Aneos[d]	Aneos[d]
Strength model		Rock	Johnson-Cook[e]	Johnson-Cook[f]
Poisson ratio[c]	ν	0.25	0.30	0.30
Thermal parameters				
Melting temperature (K)	T_m	1436	1811	1811
T_{frac}		1.2	1.2	1.2
A_{simon} (GPa)		1.40	24.25	24.25
C_{simon}	cs	5.00	2.11	2.11
ROCK strength parameters				
Intact strength at zero pressure (MPa)	Y_i	10	–	–
Damage strength at zero pressure (kPa)	Y_d	10	–	–
Strength at infinite pressure (GPa)	Y_{inf}	3.5	–	–
Internal friction coefficient (intact)	f_i	1.2	–	–
Internal friction coefficient (damaged)	f_d	0.6	–	–
Johnson-Cook strength parameters[e]				
Strain coefficient A (MPa)	A	–	175	175/35
Strain coefficient B (MPa)	B	–	380	380/76
Strain exponent	n	–	0.32	0.32
Strain rate coefficient	C	–	0.06	0.06
Thermal softening	m	–	0.55	0.55
Reference temperature (K)	T_{ref}	–	293	293
Porosity model parameters $(\epsilon - \alpha)^g$				
Initial porosity	ϕ_0	–	–	40%
Initial distension	α_0	–	–	1.67
Distension at transition to power-law	α_x	–	–	1.15[h]
Elastic volumetric strain threshold	ϵ_{e0}	–	–	0[h]
Exponential compaction rate	κ	–	–	0.97[h]

[a]Thompson and Lauson (1972); [b]Benz et al. (1989); [c]Ivanov et al. (2010); [d]Ivanov et al. (2010); [e]Johnson and Cook (1983); [f]Johnson and Cook (1985); [g]Wünnemann et al. (2006); [h]Collins et al. (2011).

6.2.3 Possible target structures

To develop a target model for the modern asteroid Psyche, this work considered a scenario that assumes that Psyche's parent body started out as a Vesta-like asteroid (Ivanov et al., 2010; Ivanov and Melosh, 2013), approximately 500 km in diameter, that underwent a long history of collisions before becoming the asteroid observed today. The structure of a typical once molten, differentiated body has a layered configuration in which a thin basaltic crust and a thick, dense olivine-rich mantle covers an iron core (Bell et al., 1989; Gaffey et al., 1993; McCoy et al., 2006). It was assumed that all of the basaltic crust and the majority of the silicate mantle was eroded by hit-and-run collisions in Psyche's early history (Asphaug, 2018). Therefore this work considered Psyche analogues that are made entirely of iron or retained a small volume of remnant mantle. In all scenarios

that include mantle materials, the same dunite material model was used to represent the mantle as that used to represent the impactor. The dunite material model uses an ANEOS-derived equation of state table (Thompson and Lauson, 1972; Benz et al., 1989) and the pressure dependent Rock strength model from Collins et al. (2004). In the Rock model, the pressure-dependent shear strength reduces with the accumulation of plastic strain from an intact curve to a damaged one (Collins et al., 2004). A full description of the ANEOS-derived equation of state table and the Rock strength model can be found in Chapter 3. The Rock strength model is appropriate for geological materials, and in the simulations presented in this chapter, the intact strength at zero pressure was set to $Y_{i0} = 10$ MPa, the damaged strength at zero pressure was set to $Y_{d0} = 10$ kPa and the internal friction coefficient of the damaged material was set to $f = 0.6$.

The iron material was modelled using an ANEOS-derived equation of state table (Thompson and Lauson, 1972; Ivanov et al., 2010) and the Johnson-Cook strength model for iron (Johnson and Cook, 1983), with the input parameters of Armco iron (Johnson and Cook, 1985). The ANEOS-derived equation of state table for iron we use was constructed by Boris Ivanov (pers. comm.) based on parameters by (Thompson and Lauson, 1972). It is distributed with the iSALE shock physics code (Collins et al., 2016) and has been used in several previous works (Ivanov et al., 2010; Potter et al., 2012; Lyons et al., 2019) to represent the metallic core of asteroids and planets. The equation of state includes an approximation of the solid-solid phase transition at ≈ 11 GPa, but does not include a melt transition and is restricted to a maximum pressure and temperature of 2300 GPa and 86700 K, respectively. While this tabular equation of state is unsuitable for investigating the thermodynamic consequences of high-speed impacts (> 20 km/s) it is adequate for the present work, which considers predominantly low-speed (5 km/s) impacts, with a maximum shock pressure of ≈ 10 GPa, and focuses on strength-dominated crater formation. More information about the ANEOS-derived equation of state is included in Chapter 3.

While ground-based observations of Psyche provide us with some constraints on the near-surface composition (e.g., iron and silicates), the exact structure is still unknown,

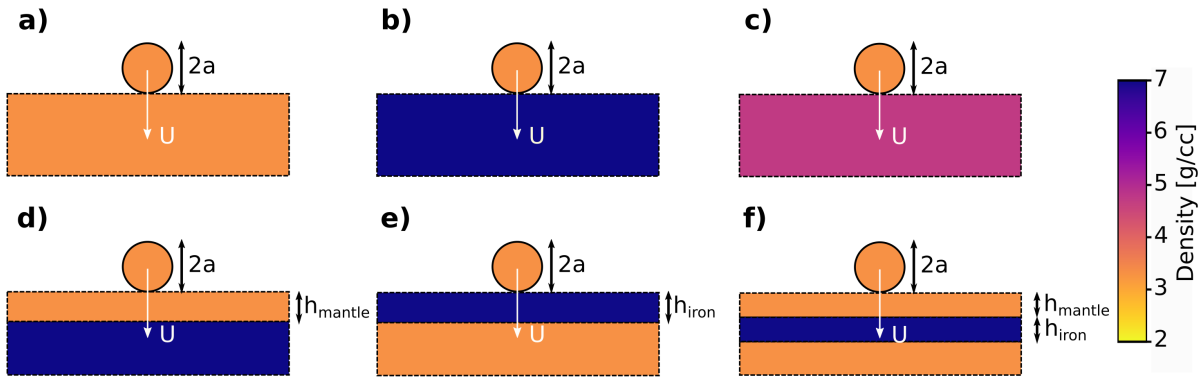

Figure 6.1: Schematic representation of the initial set-up for impacts into: a) dunite targets; b) non-porous intact iron targets; c) damaged, porous iron targets; d) dunite-iron layered targets; c) iron-dunite layered targets; and dunite-iron-dunite layered targets.

and will remain so until the arrival of the Psyche spacecraft. To investigate the diversity of possible crater morphologies that might be encountered by the space mission, six different target scenarios were modelled (Fig. 6.1), that are described below. In all of the simulations included in this chapter, the surface gravity was kept constant, at 0.06 m/s^2.

a) Impacts into a homogeneous dunite half-space (Fig. 6.1a).

This scenario considers impacts on Psyche in localised regions of residual thick mantle or before its silicate mantle was stripped off.

b) Impacts into a nonporous intact iron half-space (Fig. 6.1b).

This scenario considers impacts on an exposed dense and intact core, after a long series of hit-and-run collisions (Asphaug et al., 2006) and subsequent impacts removed the entirety of the silicate mantle.

c) Impacts into a shattered, porous iron half-space.

If Psyche's composition is almost exclusively Fe-Ni, the asteroid today is most probably not a pristine iron core, but rather a highly fractured body, with a bulk porosity of $\approx$ 40% (Shepard et al., 2017). For this reason, in this impact scenario we assume that the entirety of the mantle was removed by hit-and-run collisions, which also shattered the core, leaving behind a highly porous iron aggregate. Several theoretical (Danninger et al., 1993; German, 1994) and experimental (Kutsch et al., 1997) studies reported a reduction in strength due to porosity in stainless steel and iron rich materials. Data from Kubicki (1995) for porous iron estimates that a 40% porosity causes an 80% reduction

in strength (Klar and Samal, 2007). In iSALE, the shear strength, as determined by the Johnson-Cook strength model (Johnson and Cook, 1983), can be reduced by a damage parameter D, which varies between intact ($D = 0$) and fully damaged with no strength ($D = 1$). To achieve a strength reduction of 80%, the target was assigned an initial damage of $D = 0.8$. This had the effect of reducing the Johnson-Cook parameters A and B by 80% and reducing the strain and the strain rate used in the strength model by the same amount. The 40% bulk porosity was modelled using the $\epsilon - \alpha$ porosity model (Wünnemann et al., 2006). The $\epsilon - \alpha$ porosity model parameters for iron were determined by fits to Hugoniot data for porous iron (Collins et al., 2011), and took the following values: $\alpha_0 = 1.7$, $\epsilon_e = 0$, $\alpha_x = 1.15$, $\kappa = 0.97$ and $\chi = 1.0$.

d) Impacts into an iron core covered by a layer of silicate regolith.

Spectroscopic studies (Ockert-Bell et al., 2010; Neeley et al., 2014; Sanchez et al., 2017; Landsman et al., 2018) and radar observations (Shepard et al., 2017) found evidence of fine grained silicate regolith overlaying a metallic bedrock. These measurements suggest that Psyche might have retained some of its mantle, however an estimate of this layer thickness is not known. Therefore two scenarios that consider either a 5 or a 10 km dunite layer overlaying an iron substrate were chosen arbitrarily. The dunite layer was modelled as in scenario a), while the iron core was modelled as either an intact core (scenario b) or a shattered, porous core (scenario c).

e) Impacts into a dunite mantle covered by a thin iron layer.

One hypothesis that may explain the observed elevated metal content on Psyche's surface is the presence of a thin iron layer covering the mantle as a result of ferrovolcanism (Abrahams and Nimmo, 2019; Johnson et al., 2019). During the cooling period of proto-Psyche, compressional stresses produced in the cooling crust were relieved by faults, allowing Fe-Ni rich material from the core to propagate to the surface in dikes. Abrahams and Nimmo (2019) showed that repeated ferrovolcanic eruptions on a fully metallic asteroid would be able to raise enough molten iron material to the surface to cover a more dense iron shell. Johnson et al. (2019) showed that ferrovolcanic eruptions are also possible on iron asteroids covered by a thin mantle, however an estimate of the amount of molten iron

erupted was not given. Therefore, here we assumed that the impacts occurred after the iron melt cooled and formed a 50-m layer covering the mantle. The thickness of the iron layer was chosen based on a plausible estimate of the volume of iron that could be erupted in the absence of a mantle (Abrahams and Nimmo, 2019). The iron layer was modelled as non-porous iron (see scenario b), while the mantle substrate was modelled as in scenario a.

f) Impacts into dunite-iron layered targets

This impact scenario assumed that the thin iron layer from scenario e) was submerged under a 50-m thick layer of mantle material, possibly due to ejecta from impacts after the emplacement of the iron lava by ferrovolcanism. The mantle layer was modelled in the same way as the mantle substrate material in a).

6.2.4 Quantifying the amount of surviving hydrated material in a vertical impact

To quantify the surviving hydrated impactor material, this work considered a 1 km serpentine sphere, impacting three different homogeneous targets: a dunite mantle, an iron core and a porous, damaged iron core. The projectile was modelled using the ANEOS table for serpentine (Brookshaw, 1998) and the strength model input parameters from Davison et al. (2016). Serpentine is a hydrated ultramafic mineral, with an average $\approx$ 13 wt% H_2O content (Ulmer and Trommsdorff, 1995), found in carbonaceous chondrites (Krot et al., 2014), and a good analog of possible hydrated impactors. In this case, the impact velocity was varied between 1 km/s and 5 km/s. The targets were modelled in the same way as the homogeneous targets described above.

In any impact scenario, the impactor material experiences the most extreme shock pressures and temperatures involved in the collision, which often result in the large fractions of the impactor material being melted or vaporised (Potter and Collins, 2013), and in the case of hydrated minerals, before they dehydrate. Based on laboratory experiments (Tyburczy et al., 2001), impact induced devolatisation begins at 5 GPa initial shock pressure for porous serpentine and 10 GPa for non-porous serpentine; full dehydration occurs

at 30 GPa. Lange and Ahrens (1982) reported somewhat higher shock pressures for serpentine dehydration, with the dehydration process beginning at shock pressures of ≈ 20 GPa, and complete dehydration occurring at ≈ 60 GPa. This work used the Tyburczy et al. (2001) values as a more conservative threshold for hydrated material survival.

As well as peak pressures, the peak temperatures experienced by the impactor material was also considered. Due to the significant contribution to overall heating from shear heating compared with shock heating in low velocity impacts, it is also important to consider peak temperatures when determining the amount of surviving hydrated material in asteroidal collisions (Kurosawa and Genda, 2018). The dehydration reaction in serpentine begins at about 400°C (673.15 K), being fully dehydrated at about 600°C (873.15 K).

Lagrangian tracer particles were used to record the thermodynamic history of the impactor material, which were placed in every cell across the impactor, at the beginning of the simulation. This allowed for the peak pressures and temperatures to be recorded and analysed in post-processing. Even though the peak values occur early in the crater formation, each of the numerical simulations was ran until the crater was fully formed. In the analysis included here, only the impactor material that did not escape Psyche's gravity was considered. The impactor had an initial resolution of 40 cppr, and the regridding method described above was used.

6.3 Diverse crater morphologies in rock/iron targets

6.3.1 Large craters into homogeneous targets

The first distinguishable surface features the 'Psyche' mission will encounter will probably be the largest impact craters on the asteroid's surface, which may be a few tens of km in diameter. To determine the likely morphology of these large craters on Psyche, as well as the relationship between crater size and impactor size, impacts into homogeneous asteroid surfaces were simulated considering three scenarios: (a) a non-porous dunite target; (b) a non-porous iron target and (c) a 40% porous iron target. For each of these scenarios,

the dunite impactor radius was varied between 500 m and 15 km and the vertical impact speed was held constant at 5 km/s.

All the simulated impacts in these three scenarios formed craters that were circular, bowl-shaped depressions with raised rims, commonly known as 'simple' craters. Impacts into a non-porous dunite target formed wide and shallow craters, with very smooth rims. The crater radius varied with impactor size between 5.5 km, for a 1 km impactor, up to 98 km, for a 30 km impactor, while the crater depth varied between 2.8 and 53 km. The average crater depth to diameter ratio was 0.26, slightly larger than the average ratio on Vesta (Vincent et al., 2014). Fig. 6.2a shows the crater profile resulting from an impact of a 10 km dunite projectile into a nonporous dunite target, which produced a 80-km wide and 21-km deep crater.

The much higher strength and density of iron compared to dunite implied that the craters formed by impacts into non-porous iron (scenario b) were much narrower and shallower than their scenario a counterparts. All simulated craters in scenario b displayed curled, overturned rims characteristic of laboratory impacts in metal targets (e.g., Pierazzo et al., 2008; Libourel et al., 2019), and their shape appeared to be independent of the crater size. The simulated craters in nonporous iron varied in radius between 1.7 km for a 1 km impactor, to 50 km, for a 15 km impactor, while the crater depth varied between 1.5 and 43 km. The average crater depth to diameter ratio was ≈ 0.41. Similar depth-to-diameter ratios were measured in craters formed by recent laboratory impact experiments into metallic iron-rich targets (Marchi et al., 2019). In the simulations presented here, a 10 km dunite projectile produced a crater 34 km wide and 13 km deep (Fig. 6.2b).

For the same impact conditions, impacts into damaged, porous iron targets (scenario c) resulted in craters with sharp but not curled rims, slightly wider and deeper than the craters formed in the non-porous targets. In this scenario, the crater radius was comparable with the crater depth, resulting in an average depth-to-diameter ratio of 0.65. Fig. 6.2c shows the crater formed by a 10 km dunite projectile, which was 42 km wide and 27 km deep.

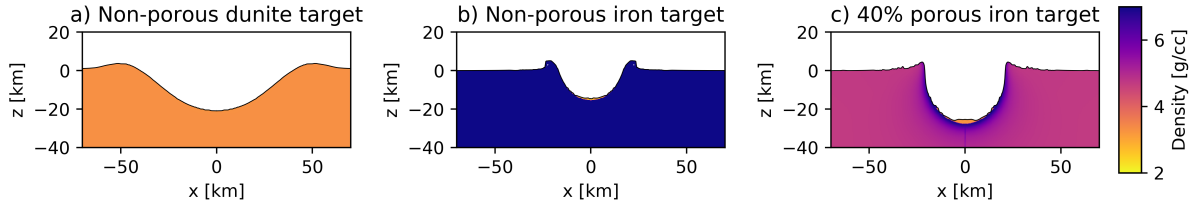

Figure 6.2: Crater profiles for a 10 km dunite sphere impacting a a) Dunite target, b) Non-porous iron target and c) 40% porous iron target.

6.3.2 Large craters in layered targets

Observations of Psyche suggest that the surface of the asteroid is covered by a fine grained silicate regolith, mixed with coarse iron grains (Landsman et al., 2018). These observations are consistent with a layered structure scenario, where an iron substrate is covered by a thin, remnant silicate mantle.

To determine the morphology of craters formed on layered Psyche analogues, as well as the relationship between impactor size and crater dimensions, this work includes iSALE simulations for impacts into a 5 km and a 10 km dunite mantle, covering both a solid iron core and a porous iron core (scenario d). The simulated impactors varied in radius between 500 m and 15 km; again the vertical impact speed was held constant at 5 km/s.

Previous experimental and numerical studies of impacts on layered targets showed that the greatest diversity in crater morphology caused by layering occurs when the ratio between the crater diameter, D, to the upper layer thickness, h, is in the range $0.08 < h/D < 0.3$ (Quaide and Oberbeck, 1968; Senft and Stewart, 2007; Raducan et al., 2020). In these studies, which examined crater formation in weak regolith-like targets, underlain by a rocky substrate, the craters exhibited four distinct morphologies depending on the h/D ratio. For large ratios, $h/D > 0.3$, the upper layer is thick enough that the substrate does not influence the cratering process and the resulting crater is bowl-shaped. For $0.2 < h/D < 0.3$, the crater forms mainly in the upper layer, but growth is influenced by the shallowly submerged lower layer, creating flat-bottomed and central-mound craters. For $h/D < 0.2$, the impactor penetrates the upper layer and the crater forms in both the upper and the lower layers. The result is a concentric crater,

which can have both an inner and an outer crater rim. Although the nature of the layering in this work is very different, being a rocky layer over a denser, stronger metallic layer, it was found that the range in crater morphologies is approximately the same. Therefore, using the previous studies as a guide, a mantle thickness that would illustrate the full diversity of possible crater morphologies was selected, given the range in impactor size.

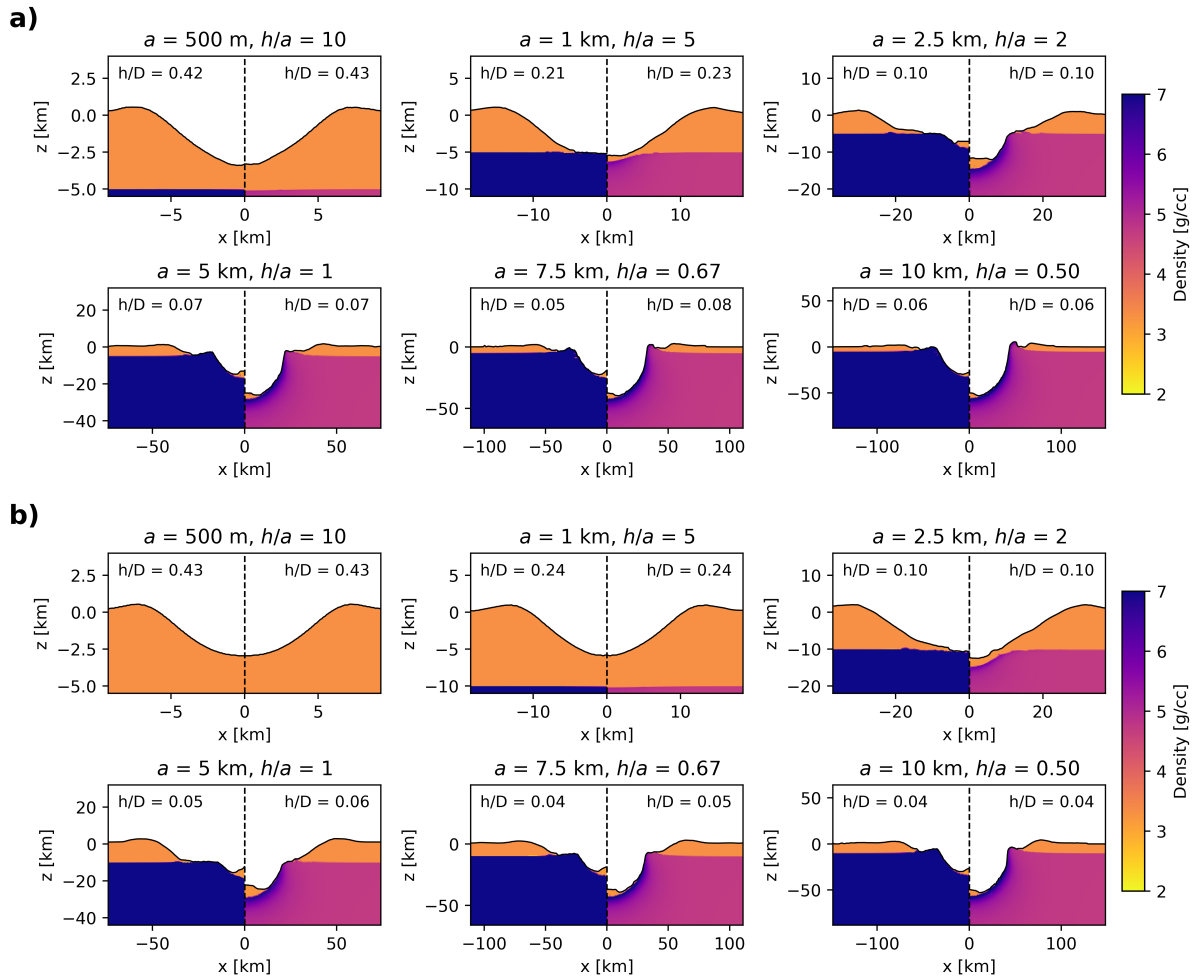

Figure 6.3: Crater profiles from impacts into a a) $h = 5$ km dunite mantle and b) $h = 10$ km dunite mantle covering an intact iron target (left) or pre-damaged, 40% porous iron target (right). The impactor radius, a, was varied between 500 m and 10 km.

Figure 6.3 shows the crater profiles for impacts of varying projectile radius into a 5 km dunite mantle (Fig. 6.3a) and a 10 km dunite mantle (Fig. 6.3b) covering a solid iron substrate (left side of each panel) and a porous iron substrate (right side of each panel). In all cases, for large layer thickness to crater diameter ratios, $h/D > 0.2$, the crater forms into the dunite mantle alone and no core material is excavated. For smaller

ratios, $h/D < 0.2$, the impactor's kinetic energy is largely dissipated in the dunite mantle layer, forming a wide crater in the dunite mantle and only a small shallow crater in the core. This is known as a concentric crater morphology (Quaide and Oberbeck, 1968).

Craters formed in a target of dunite covering a non-porous iron substrate (scenario d) exhibit the full suite of two-layered target crater morphologies (e.g. bowl-shaped, flat-floor and concentric craters), similar to craters formed in the regolith on the Moon (Quaide and Oberbeck, 1968). However, craters on dunite covering a porous iron substrate seem to only create bowl-shaped and concentric craters. This result could reflect the limited number of impactor sizes considered here, however it could also be due to the less extreme transition in material properties between the dunite and the porous iron layers. In their simulations of impacts in lunar layered targets, Prieur et al. (2018) found crater morphology transitioned directly from bowl-shaped to concentric if the impact velocity was higher than about 12 km/s or when the two layers did not have a high strength difference.

6.3.3 Crater sizes on Psyche

For the 5 km/s vertical impacts considered here, the crater radius and crater depth for a given impactor radius a can differ dramatically depending on the target material (Fig. 6.4). An additional complication in determining crater size arises from the ambiguity in defining the crater rim. For the homogeneous targets a single rim is produced and the only ambiguity is the altitude at which to measure the crater diameter. In this work, crater radius and depth were measured at pre-impact level. The difference between the rim-to-rim diameter and the pre-impact level diameter was ≈ 1.1 for impacts into iron and porous iron and ≈ 1.3 for impacts into dunite. However, the large craters formed in layered targets have concentric morphologies, which exhibit characteristic double rims. In these cases, it is ambiguous which rim should be interpreted as the topographic crater rim (for comparison with observations): the outer crater rim, formed in the rocky layer, or the inner crater rim, formed in the iron substrate. For example, for $h/D > 0.1$, the outer crater rim is much more prominent than the inner crater rim (Fig. 6.3), while for

$h/a < 0.1$ the inner crater rim becomes more prominent than the outer crater rim. For this reason, Fig. 6.4 shows both the outer and the inner rim diameters (dashed lines) and emphasise the highest crater rim out of the two (solid line).

Figure 6.4 shows the crater radius as a function of impactor radius for 5 km/s vertical impacts into each of the Psyche target models considered in this work. Three of the quasi-circular depressions identified by Shepard et al. (2017) and and Viikinkoski et al. (2018), which are denoted by D1, D2 and D3 are plotted for comparison. While the radius of the impactor responsible for each of the observed craters will depend on the unknown, unique combination of impactor density, shape, angle and speed, the results for one possible combination (vertical impact of a dunite sphere at 5 km/s) provide an indication of the sensitivity of impactor size to the nature of the cratered target material. For example, if Psyche's surface is rocky, the vertical impact simulations that correspond best to the observed crater diameters are those with impactor radii between 2 km and 7 km (Fig. 6.4a). For a solid iron surface and the same impactor parameters, impactor radii between 8 and 15 km produce the same range in crater diameter (Fig. 6.4a). For a layered structure of rock above solid iron, and assuming that the most prominent crater rim is measured, then the three craters could have been formed by impactors with radii between 2 and 15 km, depending in part on the thickness of the rocky mantle (Fig. 6.4a, d). Similarly, if Psyche is a porous, damaged iron core, then the three craters could have been created by impactors with radii between 5 and 12 km (Fig. 6.4b). And for a layered structure of rock above porous iron, the implied impactor radii range between 2 and 12 km (Fig. 6.4b, e).

Fig. 6.4c and Fig. 6.4f show crater depth to diameter ratios, d/D, from the simulated craters. The impacts into dunite had a $d/D \approx 0.28$, similar to the craters observed on Vesta (Vincent et al., 2014). The craters into iron and porous iron have a much higher d/D ratios, of about 0.4 and 0.65, respectively.

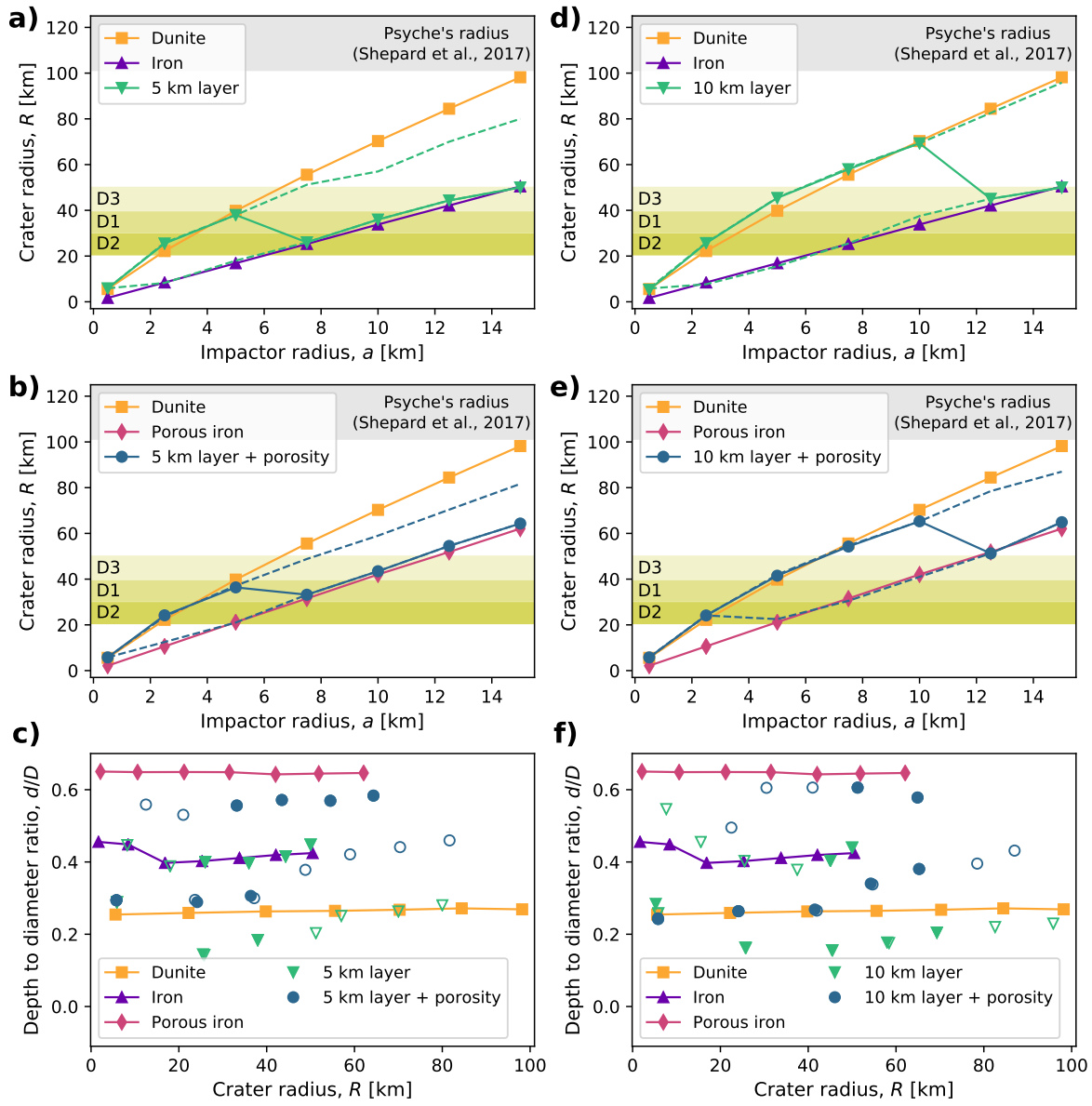

Figure 6.4: Crater radius, R, as a function of impactor radius, for impacts into homogeneous targets (Dunite, Iron, Porous iron) and different layering configurations: a) into a 5 km mantle covering a solid iron substrate (5 km layer); b) into a 5 km mantle covering a porous iron substrate (5 km layer + porosity); d) into a 10 km mantle covering a solid iron substrate (10 km layer) and e) into a 10 km mantle covering a porous iron substrate (10 km layer + porosity). The dashed lines show the inner and the outer crater radii for the craters formed on layered targets. The radii and depths of the crater like depressions identified by Shepard et al. (2017), $D1$ and $D2$, and the radius of the *Meroe* unit (Viikinkoski et al., 2018), denoted by $D3$, are plotted for comparison. c) and f) show the crater depth to diameter ratios. For the craters into layered targets, the hollow symbols show the ratio for both the inner and outer crater rims, while the filled symbols show the ratios for the topographic rim.

6.3.4 Morphology of the small craters on Psyche

The morphology of a small impact crater is more susceptible to small-scale variations in the surface and sub-surface properties of an asteroid than to the large scale variation. As a result the morphology of small craters might differ substantially from those of large craters. Ferrovolcanism has the potential to cause substantial small-scale variations in near-surface strength, density and surface topography on Psyche (Abrahams and Nimmo, 2019; Johnson et al., 2019). As discussed previously, Abrahams and Nimmo (2019) showed that repeated ferrovolcanic eruptions can produce a global iron layer of up to 50 m in thickness for a Psyche-sized asteroid. To determine the effect of such a layer on small-crater morphology, iSALE simulations of vertical impacts of 10- to 100-m radius dunite spheres impacting at 5 km/s into a 50-m thick iron layer over a dunite substrate were conducted. If ferrovolcanic eruptions occurred early in Psyche's evolution it is likely that ejecta blankets produced by subsequent large impacts redistributed rocky material on top of the iron layer. Hence, this work also considered a target scenario with a 50-m thick dunite layer over a 50-m thick iron layer covering a dunite substrate.

Fig. 6.5 shows the simulated transient and the final crater profiles for all scenarios considered. The left hand side each panel in the figure shows the crater profiles for impacts into a 50-m thick iron layer covering a dunite mantle. Small, $a < 10$ m impactors create a bowl-shaped crater when impacting directly in the iron layer. In addition, the strong shock wave transmitted from the iron layer to the rock beneath is sufficient to generate excavation flow and a transient subsurface cavity in the rock beneath it, even though the impactor does not penetrate the iron layer. For $a \geq 25$ m impactors, the transient crater exhibits hanging iron rims, that then collapse, causing dunite and iron material to be intimately mixed at the bottom. Similarly, for the $a = 50$ m and $a = 100$ impactors, if the impact occurs directly on the iron layer then the resulting crater undergoes major rim collapse owing to the extra weight of the iron in the uplifted rim.

On the other hand, if the iron layer is covered by a rocky layer that is thicker than about one impactor diameter (right hand side of each panel in Fig. 6.5), then target deformation is restricted to the upper layer and no iron material gets excavated, resulting

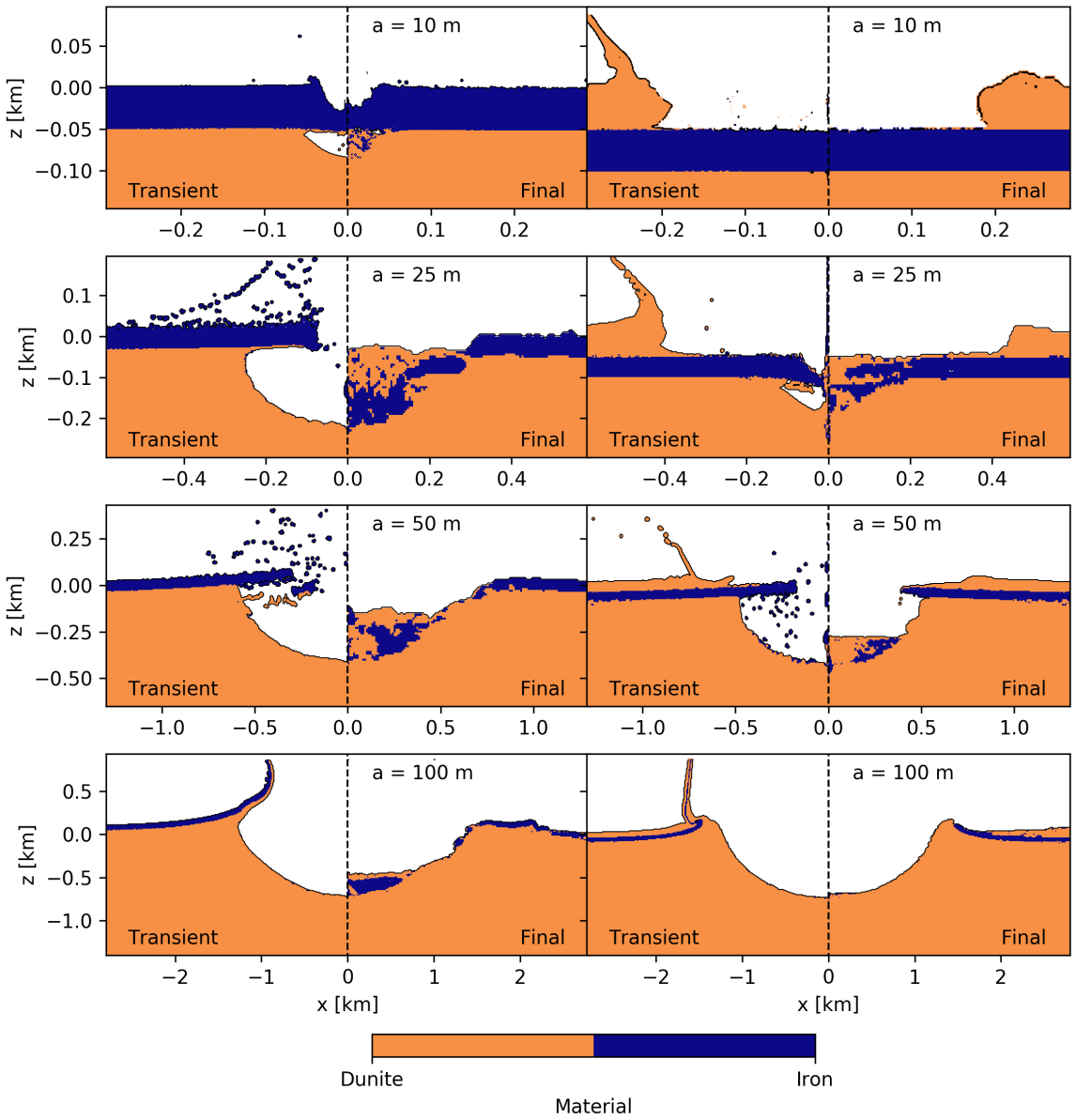

Figure 6.5: Crater density profiles for impacts into a 50 m iron layer covering a dunite mantle (left) and a 50 m dunite layer, over a 50 m iron layer, covering a dunite mantle (right).

in a shallow, flat-floored crater. For the $a = 25$ m impactor, the hanging crater rim mixes with the substrate rocky material. Interestingly, for the $a = 50$ m impactor, if the impact occurs over a rocky layer rather than directly directly on the iron layer, then the uplifted iron layer in the transient crater rim remains largely intact and is strong enough to resist complete subsequent collapse. For impacts > 100 m, in this particular dunite layer over iron layer scenario, the iron is excavated and repositioned outside the crater, leaving the inside of the crater iron-free.

6.4 Discussion

6.4.1 Crater scaling on Psyche

The simulation results presented here demonstrate that depending on the target material and structure, the crater radius produced by a given set of impactor parameters can vary considerably. To predict the radius of the crater formed by an impact into a homogeneous target, other than the scenarios considered here, the simulation results were interpreted in the framework of the widely used π-group scaling relationships (e.g., Holsapple, 1993).

The most general form of the scaling relationship for crater radius, R, as a function of impactor properties (assuming vertical impact of a spherical impactor): velocity, U; radius, a; density, δ; mass, m and target properties: density, ρ; strength, Y and gravitational acceleration, g, is given by (e.g., Holsapple, 1993):

$$R\left(\frac{\rho}{m}\right)^{1/3} = K_{R1}\left\{\frac{ga}{U^2}\left(\frac{\rho}{\delta}\right)^{\frac{(6\nu-2-\mu)}{3\mu}} + \left[K_{R2}\left(\frac{Y}{\rho U^2}\right)\left(\frac{\rho}{\delta}\right)^{\frac{(6\nu-2)}{3\mu}}\right]^{\frac{2+\mu}{2}}\right\}^{\frac{-\mu}{2+\mu}} \tag{6.2}$$

where μ, ν, K_{R1} and K_{R2} are empirically determined constants.

Previous experimental studies (Schmidt, 1980; Housen and Holsapple, 2003) suggest that the density scaling parameter, ν, holds a value of ≈ 0.4, which was also adopted here. On the other hand, the so-called velocity scaling exponent, μ, varies with target material between theoretical limits of $\mu = 1/3$ if the crater size scales with the momentum of the impactor, and $\mu = 2/3$ if the crater size scales with the impact energy (Holsapple and Schmidt, 1987).

To apply Eq. 6.2 to a planetary surface, values for the constants μ, ν, K_{R1} and K_{R2} as well as the target properties ρ, g and Y must be determined. A particular challenge is the selection of the appropriate measure of target strength Y, as this is poorly defined and unlikely to be well characterised by a single value (Holsapple, 2009). For this reason, it is common to eliminate one of the material-specific constants K_{R2} by subsuming it into the definition of Y to define an effective "cratering" strength $\bar{Y}$ (e.g., Holsapple, 1993; Prieur et al., 2017; Marchi et al., 2019). In principle, this allows $\bar{Y}$ to be determined empirically for a given target material (e.g., Marchi et al., 2019); however, in practice

this approach requires an independent method to determine K_{R1}, which is typically only possible with numerical simulations (e.g., Prieur et al., 2017).

The relationship described by Eq. 6.2 is dominated by different terms depending on whether target strength Y or the gravitational stress $\sim \rho g a$ dominates the resistance to crater growth. For small craters or materials with very high strength, the dominant resisting force to crater growth is the strength, and the crater formation is said to occur in the 'strength' regime. In this case, the term $\pi_2 = \frac{ga}{U^2}$, can be neglected, and crater radius can be expressed as a function of the strength-scale size, $\pi_3 = \frac{Y}{\rho U^2}$.

$$R\left(\frac{\rho}{m}\right)^{1/3} = H_{R2}\left(\frac{Y}{\rho U^2}\right)^{-\mu/2}\left(\frac{\rho}{\delta}\right)^{(1-3\nu)/3} \quad \text{(strength)}. \tag{6.3}$$

where $H_{R2} = K_{R1}K_{R2}^{-\mu/2}$.

For large craters or weak target materials, the gravitational stress dominates over strength and the crater is said to form in the 'gravity' regime. In such cases, π_3 can be neglected and crater radius can be expressed in terms of the gravity-scaled size, $\pi_2 = \frac{ga}{U^2}$:

$$R\left(\frac{\rho}{m}\right)^{1/3} = K_{R1}\left(\frac{\rho}{\delta}\right)^{(2+\mu-6\nu)/[3(2+\mu)]}\left(\frac{ga}{U^2}\right)^{-\mu/(2+\mu)} \quad \text{(gravity)}, \tag{6.4}$$

To determine suitable constants for a rocky, nonporous-iron or porous-iron Psyche surface, additional impact simulations were performed, of a 10 km impactor at impact velocities varying between 1 and 25 km/s, to span a large range of π_2 and π_3. For impacts into a dunite target the simulations spanned both the gravity and the strength regimes, thus the scaling parameters were determined by fitting Eq. 6.2 to the simulation data (Fig. 6.6a). As the impactor-target density ratio was not varied, a fixed value of $\nu = 0.4$ was adopted, as suggested by previous experimental studies (Schmidt, 1980; Housen and Holsapple, 2003) and only μ, K_{R1} and K_{R2} were varied. To define the target strength Y, this work used the zero-pressure shear strength (cohesion) from the dunite shear strength model $Y_d = 10$ kPa. The best fit gave $K_{R1} = 0.78$, $K_{R2} = 0.60$ and $\mu = 0.39$.

For the nonporous and porous iron targets the simulations did not reach the gravity regime and were mostly in the strength regime (rather than the transition regime). In this case, it was only possible to determine the constants H_{R2} and μ by fitting Eq. 6.3

to the simulation results (Fig. 6.6a and b). For these fits $\nu = 0.4$ was assumed. For the porous iron targets, the cohesion of the target material accounting for a damaged of 0.8 was used to define the strength parameter $Y = 0.2A = 35$ MPa. The best-fit parameters for porous iron were $H_{R2} = 0.44$ and $\mu = 0.48$.

As the Johnson-Cook strength model was used to describe the non-porous iron target materials, Y was defined in Eq. 6.3 in terms of the Johnson-Cook input parameters. The complete Johnson-Cook strength model defines the shear strength as:

$$Y_{JC} = \left(A + B\varepsilon^N\right)\left(1 + C\ln\dot{\epsilon}\right)\left[1 - \left(\frac{T - T_{ref}}{T_m - T_{ref}}\right)^M\right], \tag{6.5}$$

where ϵ is the equivalent plastic strain, $\dot{\varepsilon}$ is the strain rate, T is temperature, T_{ref} is a reference temperature and T_m is the melt temperature. A, B, C, N and M are constants (see Chapter 3). Although both temperature and strain can be high near the impact point neither of these terms is likely to vary significantly with impactor size. On the other hand, it is well documented that iron's yield strength rises significantly at high strain rates and recent laboratory experiments into iron targets (Marchi et al., 2019) have noted the importance of accounting for the effect of strain rate when extrapolating from laboratory-scale crater measurements to planetary scales, or vice-versa. For example, laboratory measurements of the quasistatic yield strength of iron meteorites give values between 200 and 400 MPa (Petrovic, 2001), however at high strain rates, e.g. $\dot{\epsilon} >> 10^3 s^{-1}$, the equivalent strength can almost double (Marchi et al., 2019). This effect was only considered for the solid iron targets and not for the pre-damaged porous iron targets. Therefore, for the purpose of fitting crater scaling relationship, Y was defined using a simplified version of the Johnson-Cook strength model that includes both the reference shear strength A and the influence of strain rate:

$$Y = A(1 + C\ln\dot{\epsilon}). \tag{6.6}$$

The simulations presented here adopted a value of $A = 175$ MPa for iron (Johnson and Cook, 1983). C is a material specific constant determined from lab experiments (Johnson and Cook, 1983) and here $C = 0.06$. To define the strain rate $\dot{\epsilon}$ for a given impact scenario, here it was approximated as the reciprocal of the crater growth time, T_g

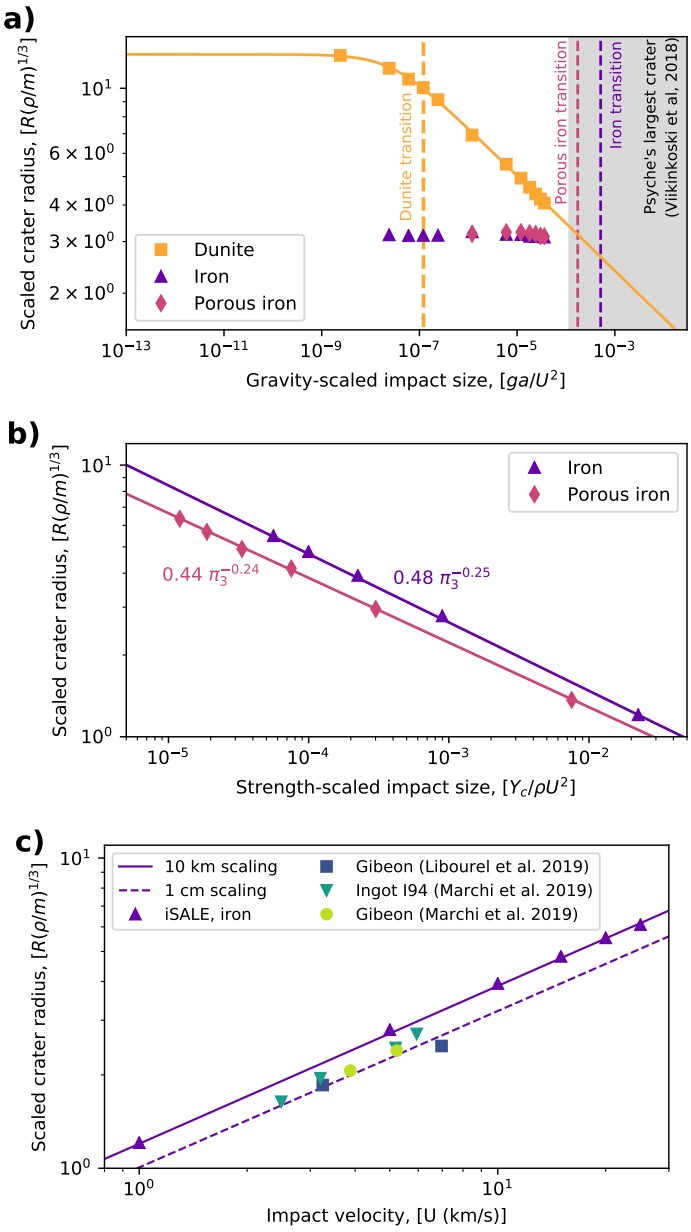

Figure 6.6: a) Scaled crater radius as a function of gravity scaled impact size for impacts into dunite, iron and porous iron, at 5 km/s. The transition between the strength the gravity regime is plotted with dashed lines for each target material. The shaded area shows crater observed on Psyche (Viikinkoski et al., 2018), normalised by a range of possible impact speeds. b) Scaled crater radius as a function of strength-scaled impact size for iSALE simulations of 10 km impacts into iron and porous iron targets, at velocities between 1 km/s and 25 km/s. c) Scaled crater radius for iSALE simulations of 10 km impacts into iron targets, compared to scaled crater radius for lab scale impacts, from Libourel et al. (2019) and Marchi et al. (2019). The continuous line represents the corresponding scaling law for 10 km impacts and the dashed line represents the scaling law for cm sized impacts.

$$\dot{\epsilon} = \frac{1}{T_g(Y)} \tag{6.7}$$

Based on the average strain in the deformed target material, a strain of 1 was adopted to define the strain rate.

The crater growth time in the strength regime can be expressed as a function of crater radius and target properties using another π-group scaling relationship (Holsapple and Housen, 2007)

$$T_g(Y) = C_2 \frac{R}{\sqrt{\frac{Y}{\rho}}}, \tag{6.8}$$

which can be rewritten in terms of impactor and target properties by substitution of Eq. 6.3 in Eq. 6.8 to give:

$$T_g(Y) = C_3 m^{1/3} Y^{\frac{1-\mu}{2}} U^{\mu} \delta^{\frac{3\nu-1}{3}} \rho^{\frac{\mu-2\nu+1}{2}} \tag{6.9}$$

where C_3 is a constant. By fitting Eq. 6.9 to the simulation data in this work, it was found that $C_3 \approx 0.14$.

To determine the scaled crater size for a given impact scenario in iron the procedure is therefore: (a) estimate the crater growth time T_g using Eq. 6.9 with $Y = A$; (b) define the rate-dependent effective strength of the target using Eq. 6.6 with $\dot{\epsilon} = 1/T_g$; and finally (c) use this rate-dependent strength in Eq. 6.3 to determine the scaled-crater size. It is noted that, strictly speaking, steps (a) and (b) should be solved iteratively as $T_g(Y)$ and $Y(T_g)$; however, in practice it was found that using $Y = A$ in Eq. 6.9 is sufficient to determine the rate-dependent Y to within a few percent, which avoids the need for iteration. This procedure was used to determine Y when fitting Eq. 6.3 to the simulation results for nonporous and porous iron. The best fit parameters for iron were $H_{R2} = 0.48$ and $\mu = 0.50$.

To test the scale-dependence of the strength-regime scaling relationship for nonporous iron, the relationship was also applied to data from recent laboratory-scale impact experiments in metallic iron-rich target materials (Libourel et al., 2019; Marchi et al., 2019). Figure 6.6c shows the scaled crater radius as a function of impact velocity for iSALE simulations of 10 km dunite impacts into iron targets at 1, 5, 10, 15, 20 and 25 km/s, together with the best-fit scaling relationship (Eq. 6.3) to the simulation data. The dotted line on Fig. 6.6c) shows the same scaling relationship adjusted to the higher

strain rates of laboratory-scale (1-cm diameter) impacts. In other words, the dotted line represents Eq. 6.3 with $Y(\dot{\epsilon})$ defined using Eq. 6.6, but with the crater growth timescale (Eq. 6.9) calculated for an impactor mass, m, appropriate for a cm-scale, laboratory impactor rather than a 10-km wide asteroid. The excellent agreement between the scaling relationship and the experimental data from impacts into Gibeon and iron ingot targets from Libourel et al. (2019) and Marchi et al. (2019) suggests that the scaling relationship is broadly applicable for impacts on an exposed iron target over a large range in impactor size.

6.4.2 Oblique impacts

The numerical simulations of impacts on Psyche presented here considered only vertical impacts and the crater scaling relationships above do not account for impact angle. However, impacts on Psyche, as on any planetary body, will occur at a range of impact angles, with a most probable angle of 45° to the target plane (Pierazzo and Melosh, 2000). Previous simulations and experiments of oblique impacts on metallic targets suggest that the crater volume and diameter are expected to decrease with impact angle and suggest that a good approach to include the effect of impact angle in crater scaling relationships is to replace the impact velocity in Eq. 6.2 and 6.3 with the vertical component of the impact velocity ($U \sin\theta$; Chapman and McKinnon, 1986; Elbeshausen et al., 2009; Davison et al., 2011).

It is also worth noting that while most craters are expected to be circular in planform, in very oblique angle impacts the crater planform is expected to be elliptical, with elongation in the along-trajectory direction. Collins et al. (2011) showed that the transition from a circular to an elliptical crater occurs at a threshold impact angle, θ_c, which depends on the vertical-impact cratering efficiency (the ratio of crater diameter to impactor diameter in a vertical impact scenario). For craters on Psyche, this cratering efficiency is mainly determined by the target strength. The elliptical crater transition angle, and hence the proportion of craters that show significant ellipticity, is therefore likely to be substantially larger for an iron Psyche than for a rocky Psyche. Based on the

cratering efficiency in the vertical impact simulations conducted in this work, elliptical craters are expected to occur at impact angles lower than $\theta_c \approx 23°$ for impacts into iron, while for porous iron the expected threshold angle is $\theta_c \approx 20°$. These threshold angles correspond to elliptical crater populations of 15% and 12% of all craters, respectively. Similar critical impact angles ($\theta_c \approx 20°$) have been observed for oblique impacts into aluminium (Burchell and Mackay, 1998; Davison et al., 2011). For the 5 km/s impacts into dunite considered here, which span the transition from the strength to the gravity regime, the elliptical crater threshold impact angle is expected to vary with the size of the impactor, between $\theta_c \approx 13°$ for 500-m impactors and 17° for 10-km impactors. In this case, elliptical craters would constitute less than 5-9% of all craters.

6.4.3 Size-frequency distribution of craters on Psyche

To determine an estimate of the size-frequency distribution of craters on Psyche, this work used the `CHESS` (Collisional Histories in the Early Solar System) Monte Carlo model[a] (Davison et al., 2013). `CHESS` uses the results from collisional and dynamical evolution models, coupled with the π-group scaling relationships (Housen et al., 1983; Housen and Holsapple, 2011) to predict the impact history of a given body. The impacting population was taken from time-varying impactor size-frequency distributions derived from collisional evolution models (O'Brien et al., 2006,0; O'Brien, 2009), and the intrinsic collision probability was taken from those models for the first 100 Myr and then set to a fixed value of 2.86×10^{-18} km^{-2} yr^{-1} (Bottke et al., 1994). The impact velocity was randomly selected from a Maxwellian distribution with a mean of 5.3 kms^{-1}. The impact angle was chosen randomly, with $P(> \theta) = \cos^2\theta$ (Gilbert, 1893; Shoemaker, 1962), where $P(> \theta)$ is the probability of the impact angle being greater than θ.

To apply the `CHESS` model to Psyche, the target asteroid diameter was set to 225 km and the model was run for several different Psyche surface ages between 1 billion years and 4.5 billion years. In each case, 10^5 target asteroids were considered to produce a statistically meaningful result. `CHESS` incorporates the π-group scaling relationships

[a]The CHESS model runs included in this chapter were generated by Thomas Davison.

defined above (Eqs. 6.2-6.4), modified to include the effect of impact angle to the horizontal by replacing the velocity term with the vertical component of the velocity ($U \sin\theta$; Chapman and McKinnon, 1986). To determine how the size of the craters produced by the impacting population might differ depending on the target material on Psyche's surface, the derived scaling exponents for dunite, iron and porous iron were applied. For impacts into iron and porous iron this work employed the procedure described above for determining the appropriate strain-rate dependent strength for use in the π-group scaling relationships.

Because almost no data exists on the cratering record on Psyche, the aim of this analysis was not to determine a specific age for Psyche, but rather to determine age constrains for different target scenarios and determine whether the possible few observed craters are consistent with the expected crater population on a rocky or an iron-rich surface.

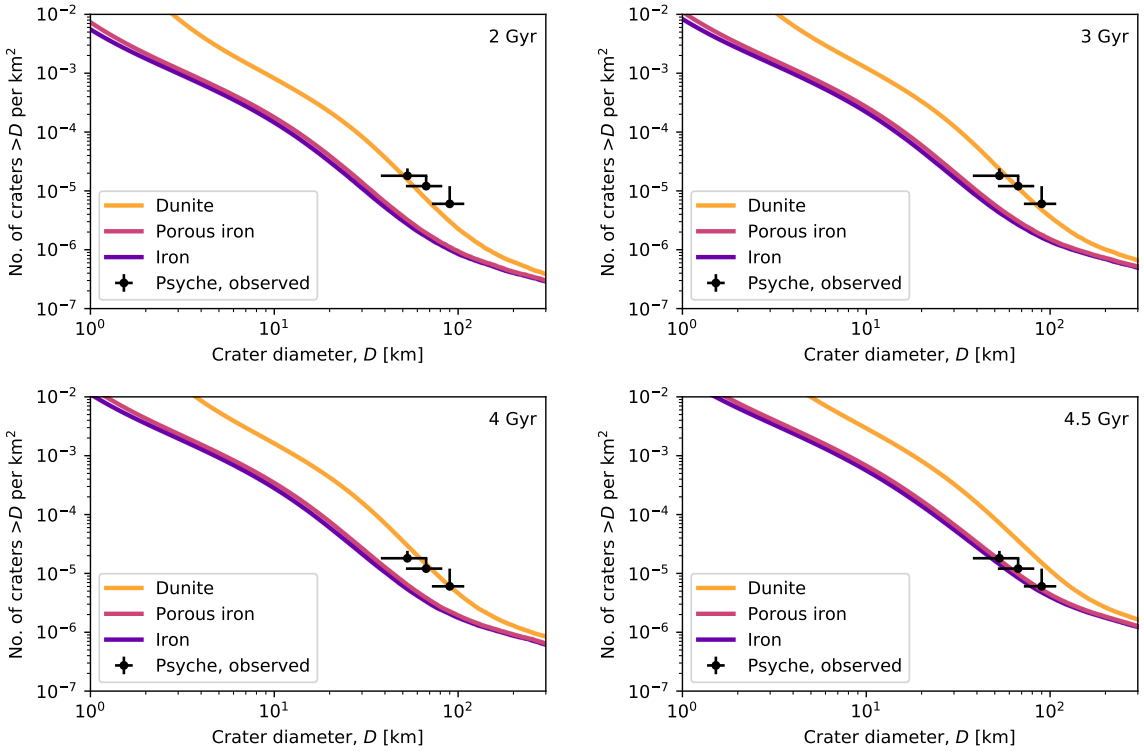

Figure 6.7: Crater size-frequency distribution on a Psyche-sized asteroid, based on three different asteroid surface materials (dunite, porous iron and iron) and for four surface ages: (a) 2 Gyr, (b) 3 Gyr and (c) 4 Gyr and d) 4.5 Gyr. The observed crater-shaped depressions (Shepard et al., 2017; Viikinkoski et al., 2018) are plotted on top of the size frequency distribution. The vertical error bars account for the uncertainty in the number of $\approx$ 90 km craters on Psyche, as observed by Viikinkoski et al. (2018).

Fig. 6.7 shows the crater size-frequency distribution (SFD) for a Psyche-sized asteroid that experienced the same impact history as the main belt population, over the last two billion years (Fig. 6.7a), the last three billion years (Fig. 6.7b), the last four billion years (Fig. 6.7c) and 4.5 billion years (Fig. 6.7d). The three observed crater-like depressions, D1, D2 and D3 (Shepard et al., 2017; Viikinkoski et al., 2018) are plotted on top of the SFDs. Horizontal error bars represent the uncertainty in the size of those craters. A fourth depression identified by (Viikinkoski et al., 2018), which could also be an impact crater, is represented by the vertical error bar associated with the plotted craters.

The π-group scaling relationships predict the crater diameter for a given impact measured at the pre-impact surface, while from observations crater diameter is usually measured from rim to rim. The ratio between the rim-diameter and the preimpact level diameter $D_r/D \approx$ for the Psyche impact simulations in rock was 1.3, which is consistent with the ratio for experimental craters in sand and weak soils (Housen and Holsapple, 2011). This ratio was used to convert from pre-impact level diameter to rim-to-rim diameter for impacts into rocky mantle. For impacts into iron and porous iron this work adopted $D_r/D \approx$1.1, based on the Psyche impact simulation results, to convert from the pre-impact level to rim-height crater diameters (Fig. 6.7).

For a dunite target scenario, if the proposed large craters on Psyche are confirmed they would suggest a surface age that is at least $\approx$ 2-3 billion years old, and up to about 4 billion years. If, on the other hand, Psyche's surface is dominated by iron or porous iron, the same size craters are consistent with model crater SFDs of a surface that is at least 4 billion years old. This suggests that the any mantle stripping events and large impacts on Psyche must have occurred very early in Solar System formation.

These results suggest that for a very old Psyche, having an iron-rich surface is not only possible, but even likely. However, these results have very large associated errors caused by the uncertainties in the observed crater sizes. More precise measurements of the craters, together with a better understanding of the surface composition on Psyche will yield a much more accurate estimation of surface age.

6.5 Exogeneous origin of the hydrated minerals on Psyche

Recent observations of Psyche detected a weak, 3 μm spectral absorption band, suggesting the presence of hydrated materials on the surface. Due to the variations in spectra detection with rotation and the incompatibility of these observations with a metallic surface scenario, the hydrated material was proposed to have been delivered by impacts.

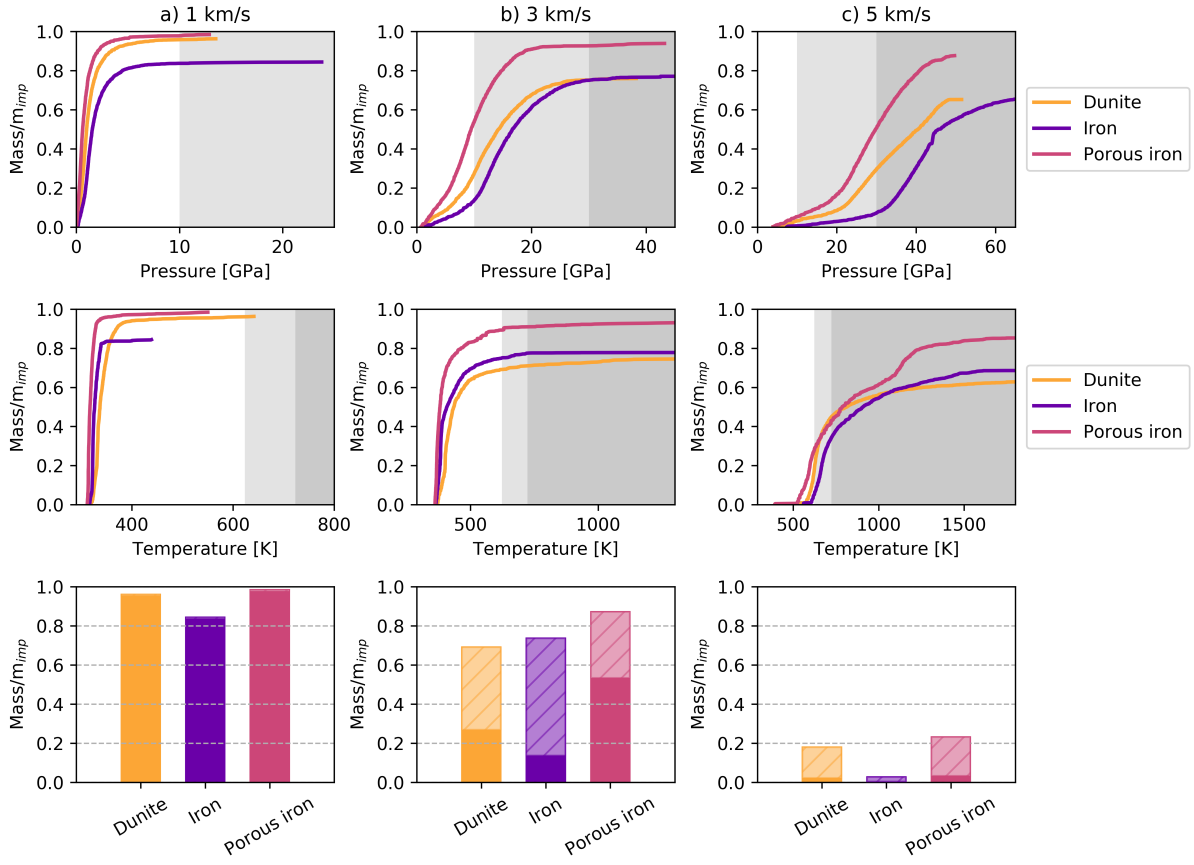

Figure 6.8: Cumulative mass fraction of impactor material with $v_{ej} < v_{esc}$ (i.e., retained on Psyche), and that experiences a shock pressure less than a given pressure (top row) and a peak shock temperature less than a given temperature (middle row), for vertical impacts at a) 1 km/s, b) 3 km/s and c) 5 km/s, into dunite, iron and porous iron targets. The grey shaded areas represent the pressure and temperature thresholds for partial and complete serpentine dehydration. The bottom row shows the mass fraction of impactor material that remains fully hydrated (solid colour) and partially hydrated (hatched colour), and remains on Psyche.

Fig. 6.8 and Fig. 6.9 show the fate of a 1-km diameter impactor after impacting vertically onto a dunite, iron and porous iron target at 1 km/s, 3 km/s and 5 km/s.

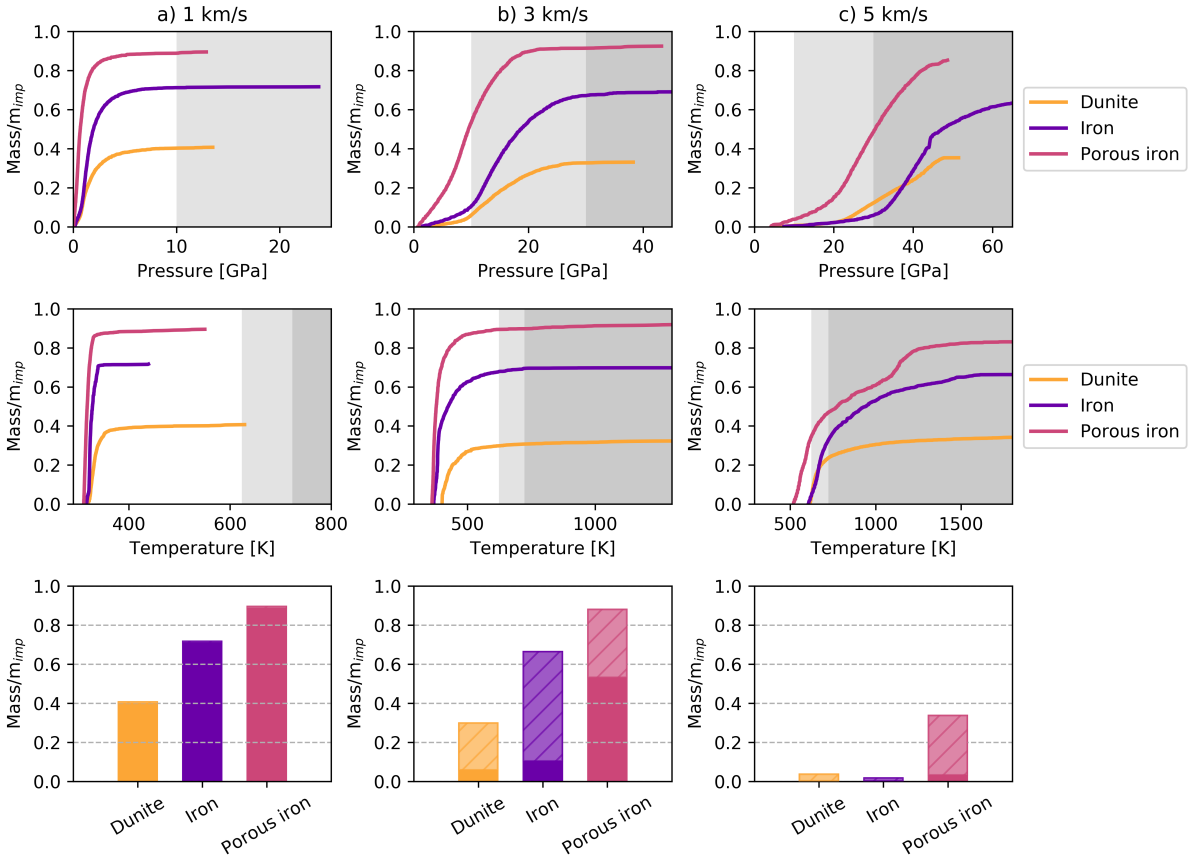

Figure 6.9: Cumulative mass fraction of impactor material that remained inside the crater and that experiences a shock pressure less than a given pressure (top row) and a peak shock temperature less than a given temperature (middle row), for vertical impacts at a) 1 km/s, b) 3 km/s and c) 5 km/s, into dunite, iron and porous iron targets. The grey shaded areas represent the pressure and temperature thresholds for partial and complete serpentine dehydration. The bottom row shows the mass fraction of impactor material that remains fully hydrated (solid colour) and partially hydrated (hatched colour), and remains inside the crater.

The fate of the impactor material can be divided as follows: material that is ejected at velocities above Psyche's escape velocity; material that is ejected below the escape velocity and therefore is scattered on Psyche's surface, including within the crater (Fig. 6.8); and material that remains inside the crater (Fig. 6.9). For further analysis, only the impactor material that remains on Psyche is considered.

This work conservatively assumes that the impactor material remains hydrated if it experienced peak pressures less than 10 GPa and peak temperatures of less than 673 K. As discussed previously, this is a lower limit as partially hydrated material has been recovered experimentally for pressures of up to ≈20 GPa and temperatures of up to ≈773 K. Moreover, the 3 μm absorption spectra might still be detectable for hydrated material

being shocked and heated up above those thresholds (Libourel et al., 2019).

It is important to note that hydrated material that remains trapped by Psyche's gravitational field but not inside the crater can undergo further shock and heating as it lands back on the surface, effects that are not modelled here. It is therefore safer to consider the hydrated material trapped on the asteroid's surface as an upper limit and the hydrated material that remains within the crater as a lower limit for the total amount of impactor hydrated material that should be expected on Psyche.

At low vertical impact velocities, of about 1 km/s, more than 95% of the impactor mass remains hydrated and trapped on Psyche, regardless of the target material (Fig. 6.8a). Of this material, about 40% will remain inside the crater in a dunite target scenario, about 20% in an iron target scenario and almost 75% in a porous iron scenario (Fig. 6.9a). At 3 km/s, the amount of hydrated impactor material on Psyche's surface decreases to 65% (Fig. 6.8b), with 25% inside the crater for a dunite target (Fig. 6.9b). For an iron target, 63% of the hydrated material should be found on the surface, with 38% inside the crater. This amount increases by about 20% for a porous iron target (Fig. 6.8b). At 5 km/s, however, the amount of surviving hydrated impactor material decreases to less than 5%, for all three target scenarios, with almost no hydrated material found within the crater boundaries (Fig. 6.9c).

This study shows that for vertical impacts at low impact velocities, of $\approx$ 3 km/s or less, the impactor material is very likely to remain hydrated, and therefore could represent the source of the observed 3 μm spectral signature (Takir et al., 2016). The maximum impact velocity below which hydrated impactor material is still expected, is smaller than the average impact speed in the main belt. However, there are still a number of carbonaceous chondrite hydrated asteroid families that can have lower impact velocities – e.g. the Themis impactors family has an average impact speed of $\approx$3 km/s (Farinella and Davis, 1992).

A large proportion of the surviving impactor material will not be found withing the crater boundaries, but is instead scattered across Psyche's surface. This study of impactor material survivability limited itself to vertical impacts only. However, as shown

by previous numerical studies of impacts into the Moon (Bland et al., 2008), the amount of material found within the crater decreases with impact angle, reaching only few percent at 15° impact angles.

6.6 Conclusions

The asteroid Psyche is one of the most intriguing Main-belt asteroids. Earth-based observations suggest that the asteroid has an iron-rich surface, however, the low bulk density estimates and the detection of hydrated minerals on the surface have questioned the interpretation that Psyche has a predominantly metallic composition. Proposed formation mechanisms suggest several possible internal structures that could reconcile the iron-rich surface composition and the low bulk density estimates.

NASA's 'Psyche' mission, which will arrive at Psyche in 2026, will be able to take the necessary measurements to determine Psyche's surface composition. The study of impact craters on Psyche will inform that analysis, but due to the possibly unusual history of Psyche, the spacecraft might find a much more complex asteroid topography than expected, with impact crater morphologies that are very different from those observed on other visited asteroids.

This chapter contains numerical simulations of impacts into Psyche analogues that considered several possible target surface materials and structures: a homogeneous rocky (dunite) target; an exposed, dense iron core; a porous, fractured exposed iron core; as well as layered structures with a rocky mantle covering a dense or porous iron core, and a thin near-surface iron layer within or atop the rocky mantle.

The simulations presented here reveal a wide diversity of potential crater morphologies. The classical "complex" craters observed on large planets, moons and even large asteroids are not expected owing to the high strength and low gravity of Psyche's surface. However, because of the large difference in strength between rock and iron, the presence of near-surface iron-rock layering or other forms of heterogeneity is likely to result in a range of crater morphologies, many of which may be unique or witnessed for

the first time. If Psyche's near-surface structure is homogeneous, then the spacecraft is expected to find simple, bowl-shaped craters, although they will be much deeper than those on other visited asteroids and possess much more spectacular rims if the surface is dominated by metallic iron. On the other hand, if Psyche has a layered structure, the mission could also find shallow craters with flat floors or concentric craters with at least two prominent rims. If the surface strength is more representative of iron than rock, then the cratering efficiency on Psyche will be substantially lower than on more familiar rocky asteroids. Consequently, the threshold impact angle (relative the horizontal) to produce elliptical craters will be greater, resulting in a higher proportion of elliptical craters on Psyche compared with other asteroids.

Small craters, which are more susceptible to small-scale variations in the target structure, have the potential to exhibit even more exotic morphologies. If ferrovolcanism occurred on Psyche and produced thin surficial or near-surface lenses of iron, then craters less than about 1 km in diameter in such areas might display a range of complex morphologies, including central mounds of iron or over-hanging metallic rims covering a larger cavity in the rocky mantle below. Ferrovolcanism could have also brought iron-rich material to the surface, and iron mixed with rock would reside on the surface around small craters. Moreover, as ferrovolcanism requires a relatively thin mantle, direct excavation of the iron core by large impacts offers another mechanism for iron exhumation, in addition to volcanism.

Three quasi-circular depressions with diameters larger than 50 km have been identified in 3D reconstructions of Psyche and interpreted as possible impact craters. Using crater scaling relationships constrained by the impact simulations, together with models of the collisional history of the asteroid belt, this work determined a number of model crater size-frequency distributions for Psyche that differ in the age and composition of its surface. If the observed depressions on Psyche are impact craters, then the model crater size-frequency distributions suggest that the Psyche spacecraft will most likely find an old asteroid surface that is at least 3 billion years old. Moreover, the presence of three large $D > 50$ km craters on Psyche seems to be most compatible with a surface material that

is either rocky or made of porous iron. If Psyche's surface was predominantly nonporous iron then fewer than three $D > 50$ km craters would be expected, even if the asteroid's surface was as old as the solar system. However, more accurate measurements of the large craters on Psyche are needed in order to better estimate the surface age or to infer the surface material, which might not be available until the arrival of the spacecraft at Psyche.

The presence of hydrated materials on Psyche's surface has been attributed to delivery by impacts. Here it was shown that the hydrated material could have been delivered by low-velocity vertical impacts at speeds below the current main belt average. During low velocity impacts, of less than 3 km/s, a large fraction of impactor material could have survived and spread across Psyche's surface. For a porous iron target scenario, most of the impactor material would be found within the crater boundaries. Further studies of oblique impacts are needed to quantify the amount of hydrated material that could be found on Psyche's surface.

The numerical simulations and the results presented here represent a first step towards understanding the exotic impact craters on metallic or metal-rich asteroids such as Psyche and provide an insight into the intriguing possible discoveries when the spacecraft arrives at its destination.

Chapter 7

Conclusion

7.1 Motivation

Asteroids represent a unique opportunity to study the building blocks and mechanisms that led to the formation of planets in the Solar System, including Earth. They are abundant in the Solar System, and diverse, including carbonaceous chondrites asteroids to metal asteroids. In addition, their surface material properties, such as cohesion, porosity or internal friction coefficient can vary significantly from one body to another. Besides providing an insight into the Solar System formation and composition, asteroids may pose a future threat of colliding with Earth, with severe or even catastrophic consequences. A better understanding of asteroids can help us prevent such events.

Past laboratory and numerical simulations have shown that the crater size, morphology and ejecta from an impact is highly dependant on target properties and structures. Numerical simulations can help predict impact cratering effects given a range of impact conditions. While there have been several numerical studies in which target parameters were systematically varied to quantify the effects of target properties on crater size and crater ejecta, these have focused on gravity dominated targets (Prieur et al., 2017; Luther et al., 2018) or very strong targets (Jutzi and Michel, 2014; Stickle et al., 2015; Syal et al., 2016), which are not appropriate to small asteroids.

The work presented in this thesis set out to investigate the influence of typical

asteroid surface and subsurface properties and structure on the crater size, morphology and ejecta formation, and to expand the current scaling laws into more regimes of applicability (e.g. close to the crater rim for vertical impacts an for oblique impacts). This work used the DART and the Psyche space missions as motivating case studies, and the main findings are summarised below.

7.2 Summary of results

Chapter 4 presented a systematic study of iSALE numerical simulations of the reaction of different types of target asteroid surfaces to a possible impact. The aim was to investigate impacts into strength dominated, low-gravity asteroids and to quantify the effects of asteroid surface material properties, namely strength, porosity and internal coefficient, on crater ejecta properties. The study used reasonable estimates for the material properties of the Double Asteroid Redirection Test (DART) asteroid target. The main findings of the study were:

- Target cohesion, porosity and internal friction coefficient were found to have a great influence on the ejecta mass-velocity-launch position distribution and thus on the ratio of ejected momentum to impactor momentum, $\beta - 1$. The target cohesion was found to be the main driver for the momentum transfer. An increase in target cohesion lead to a significant decrease in $\beta - 1$. An increase in target porosity or the target coefficient of friction also lead to a decrease in $\beta - 1$.

- Using parameters appropriate to the DART mission, $\beta - 1$ was estimated between approximately 1.4 for a cohesion of 10 kPa and approximately 3 for a cohesion of 0.1 kPa.

- The work also presented a revision to widely used ejecta scaling laws to account for the non-power law behaviour of the ejecta in the coupling zone. The scaling constant μ was found to be independent of the target cohesion, but to decrease slightly with porosity and to decrease rapidly with coefficient of internal friction.

- Numerical simulations at vertical and oblique impact angles were used to derive an empirical model for the ejecta distribution and momentum transfer from oblique impacts.

Chapter 5 extended the study presented in Chapter 4 to include the effects of target subsurface structure on crater morphology and ejecta properties. The work compared results from numerical simulations of impacts into three target structures: a homogeneous half-space target, with constant porosity; a layered target with a dense interior, covered by a homogeneously porous regolith layer and a target with a porosity that decreases exponentially with depth. The main conclusions of this chapter were:

- The crater morphology is dependant on the upper layer thickness. The craters can be concentric, with a central mound, with a flat-floor or bowl shaped. This is consistent with previous studies (Quaide and Oberbeck, 1968; Prieur et al., 2018).

- Impacts into layered targets can produce amplification or reduction of ejected mass and momentum relative to homogeneous upper-layer, depending on the upper layer thickness to impactor size ratio.

- Impacts into targets with exponentially decreasing porosity produce an amplification in $\beta - 1$ only for sharp gradients, while the crater size remains unchanged.

- The same amplification $\beta - 1$ was found for impacts into target with properties and structures configurations, however these impacts produced different crater sizes or morphologies.

The work presented in chapter 6 used iSALE to numerically simulate impacts into asteroid (16) Psyche analogues. The aim of this study was to determine how different target structures influence the crater morphology. Asteroid Psyche is one of the most intriguing Main-belt asteroids due to its iron rich surface, yet relatively low bulk density. The work considered several possible target scenarios: a homogeneous rocky target; an exposed, dense iron core; a porous, fractured exposed iron core; as well as layered structures with a rocky mantle covering a dense or porous iron core, and a thin near-surface iron layer within or atop the rocky mantle. The main findings were:

- Depending on the abundance of iron and its proximity to the surface, a wide diversity of crater morphologies are possible. For large craters, if the asteroid surface is homogeneous, the craters are expected to be bowl shaped. On the other hand, if the asteroid surface is layered, the craters are expected to be shallow, with flat floors or concentric, with at least two prominent rims. If ferrovolcanism occured on Psyche, then small craters are expected to have even more exotic morphologies.

- Models of collisional history of the Main belt, which used scaling relationships constrained by the numerical simulations of impacts into possible Psyche target scenarios suggest that Psyche probably has a very old surface, of at least 2-3 billion years if rocky and at least 4 billion years if metal-rich.

- It was shown that the hydrated material detected on Psyche could have been delivered by low-velocity impacts with hydrated impactors. In the case of a non-porous surface (either rocky or metal), the impactor material could have spread across the asteroid surface, while in the case of a porous surface, most of the impactor material would remain localised inside the crater boundaries.

7.3 Limitations and future work

Chapter 4 presented revisions to the existing ejecta scaling laws, however further validation work of Eq. (4.1) is required to determine the limits of theorised equation's applicability. Firstly, it is important to note that the equation should only be used when the entire range of the ejecta is measured (e.g. in impact numerical simulations or in very high resolution experiments) and it does not require parts of the data to be cut off. For impact experiments that do not capture the inner and outer regimes, the best approach is to use the simple power-law form, Eq. (2.15). Moreover, the numerical studies used to derive these equations employed the same impactor and a constant velocity of 7 km/s. Hermalyn and Schultz (2010) found that the fast ejecta is influenced by the impactor properties so future work is needed to determine the effects of target-impactor density ratio or impactor velocity on the equation fit.

The results included in Chapter 4 showed that the ejecta momentum from oblique impacts 'straightens up' with crater growth, however it is not yet understood how this effect varies with target properties, especially with target strength. It is also not yet understood at what point in the crater growth does the ejecta become symmetric, as a function of impactor and target properties.

Chapter 4 also presented a first attempt to develop an ejecta scaling relationship for oblique impacts, based on numerical simulation data. The analytical expressions were based on a set of four 3D numerical simulations of impacts in the strength regime and using low-strength targets. Such models are very computationally expensive, which led to several shortcomings. Firstly, the 3D numerical simulations used a low spatial resolution, of only 5 cppr. As shown in this work, low resolution models do not capture the early high-speed ejecta, which can lead to an underestimate of the ejecta momentum of 10% compared to a similar high-resolution models. Secondly, the high computational costs meant that only four 3D impact scenarios have been simulated, which only considered a very specific set of impact scenarios. Therefore insufficient simulation data was available for impacts at oblique angles. A larger collection of experimental data and numerical simulations is needed to test and refine these scaling relationships, to fully understand the limits of applicability and to quantify any associated errors. Furthermore, future work needs to consider scaling for the horizontal component of the momentum transfer, not just the vertical component.

Chapter 5 presented numerical simulations into simple asteroid target structures. However this work is just a first step in understanding the effects of complex target structures on small-body crater formation. Future work is also needed to examine the effect of a continuous increase in strength with depth commensurate with the decrease in porosity. Then more laboratory experiments and numerical simulations are needed to study the effects of more complex target inhomogeneities on ejecta formation and final crater morphology.

Impact angle is also expected to play a significant role in the ejecta distribution and momentum transfer. While numerical simulations presented in Chapter 5 were restricted

to vertical impact only, future studies should also investigate and quantify the role of the impact angle on the ejecta distribution of impacts into layered asteroid targets.

The work presented in both Chapter 4 and Chapter 5 used porous targets simulated using the $\epsilon - \alpha$ compaction model with parameters derived to match the crush curve of lunar regolith. While a small number of test simulations showed that adopting a lower crush strength for the uniform regolith targets changes the momentum transfer by less than 4%, more studies into the influence of the target crush curve are needed.

In Chapter 4 and Chapter 5 the minimum target cohesion was set to 100 Pa and 1 kPa, respectively. While scaling laws provide an efficient way to extrapolate the result presented here to lower target cohesions, these extrapolations have not been validated yet and may not apply to very low strength, especially in the strength-gravity transition regime. While there have been many validation works which proved iSALE's capabilities in reproducing impact crater sizes, ejecta velocity and angle distributions (e.g. this work, Wünnemann et al., 2016; Luther et al., 2018), more impact experiments, that are specially designed to measure the momentum transfer from a high velocity impact, are needed to further validate iSALE's capabilities.

For the impact simulations into asteroid Psyche analogues, presented in Chapter 6, the target scenarios were chosen to illustrate a full range of possible crater morphologies. However not much is known about the asteroid's surface properties and more precise surface measurements, which will be acquired by the Psyche mission, will help determine the most possible target properties and surface configurations. The porous iron target material used in Chapter 6 was described using a simple model approximation, however laboratory experiments are needed to better characterise such a material. Furthermore, the chapter only contains vertical impact simulations, however three-dimensional simulations are needed to determine how the presented crater morphologies vary with impact angle.

7.4 Implications for future missions to asteroids and asteroid deflection capabilities

The work presented in this thesis represents a framework for predicting asteroid deflection efficiency. It also showed that impact craters on asteroids can provide a direct way of surveying an asteroid's surface and subsurface properties.

The work on asteroid deflection included in this thesis used the DART spacecraft and Didymos B as a motivating test case. Measurements of both the momentum transfer, taken by Earth observatories, and the DART crater, taken by the Hera mission, will be vital in validating numerical models and transforming the DART mission into a well understood and reproducible planetary defence technique.

However, if an asteroid was detected coming towards Earth, it is likely that its surface properties will be different from the ones on Didymos B. The numerical simulations presented here included a wide range of target scenarios, providing the necessary information to extrapolate to impact scenarios not covered by the numerical simulations. The improved scaling laws, which have been validated in this work, can be used with the scaling constants also derived in this work to extrapolate to an even larger variety of possible target properties. Once the deflection capabilities are proven by the DART and Hera space missions, a mitigation strategy can be put in place.

The kinetic deflection of a potentially hazardous asteroid is relaying on the incoming asteroid being detected and characterised years or even decades before its trajectory intersects Earth's. However, in the case of an asteroid detected 10-20 years in advance, its trajectory will remain uncertain until repeated observations are possible. In the scenario where an asteroid is on a colliding path with Earth, the probability that the asteroid will impact Earth will remain low and might not increase significantly until it is just a few years away.

Therefore, for an efficient deflection, the decision to act needs to be taken shortly after the asteroid's discovery and before the possible impact is certain. Furthermore, due to the uncertainties in the asteroid target properties, the deflection efficiency will

also not be known until a deflection attempt. A simple solution is to send a rendezvous mission to asses the trajectory, mass and surface of the asteroid before any deflection attempts. Knowledge of the asteroid trajectory will reduce the uncertainties in whether the asteroid is hazardous or not and it might even dismiss it as being one. The mass of the asteroid is vital in determining the effects of a kinetic impactor, while images of the surface will help estimate surface properties. After the initial assessment conducted by the rendezvous mission, a decision can then be taken on whether to send one or multiple kinetic impactors.

For the flow-chart to work in a timely manner, the rendezvous mission needs to be ready to launch soon after the asteroid detection (and confirmation). This might prove challenging as even simple spacecraft can take years to build. The most forward-looking solution would be to have a spacecraft equipped with only a few instruments (e.g. a camera) ready to launch and waiting on stand-by.

Bibliography

Abrahams, J. N. H. and Nimmo, F. (2019). Ferrovolcanism: Iron Volcanism on Metallic Asteroids. *Geophysical Research Letters*, 46(10):5055–5064.

Ahrens, T. J. and Cole, D. M. (1974). Shock compression and adiabatic release of lunar fines from Apollo 17. *Lunar and Planetary Science Conference Proceedings*, 3:2333.

Ahrens, T. J. and Gregson, V. G. (1964). Shock compression of crustal rocks: Data for quartz, calcite, and plagioclase rocks. *Journal of Geophysical Research (1896-1977)*, 69(22):4839–4874.

Ahrens, T. J. and Harris, A. W. (1992). Deflection and fragmentation of near-Earth asteroids. *Nature*, 360(6403):429–433.

Ahrens, T. J. and Okeefe, J. D. (1977). Equations of state and impact-induced shock-wave attenuation on the moon. *Impact and explosion cratering: Planetary and terrestrial implications; Proceedings of the Symposium on Planetary Cratering Mechanics*, pages 639–656.

Amsden, A. A., Ruppel, H. M., and Hirt, C. W. (1980). SALE: a simplified ALE computer program for fluid flow at all speeds. Technical Report LA-8095, 5176006.

Anderson, J. L. B., Schultz, P. H., and Heineck, J. T. (2003). Asymmetry of ejecta flow during oblique impacts using three-dimensional particle image velocimetry. *Journal of Geophysical Research: Planets*, 108(E8).

Anderson, J. L. B., Schultz, P. H., and Heineck, J. T. (2004). Experimental ejection angles for oblique impacts: Implications for the subsurface flow-field. *Meteoritics & Planetary Science*, 39(2):303–320.

Artemieva, N. A. and Shuvalov, V. V. (2016). From Tunguska to Chelyabinsk via Jupiter. *Annual Review of Earth and Planetary Sciences*, 44(1):37–56.

Asphaug, E. (2018). Signatures of hit and run collisions. *Planetesimals: Early Differentiation and Consequences for Planets*, 1810:7–37.

Asphaug, E., Agnor, C. B., and Williams, Q. (2006). Hit-and-run planetary collisions. *Nature*, 439(7073):155–160.

Avdellidou, C., Delbo, M., and Fienga, A. (2018). Exogenous origin of hydration on asteroid (16) Psyche: The role of hydrated asteroid families. *Monthly Notices of the Royal Astronomical Society*, 475(3):3419–3428.

Avramenko, M. I., Glazyrin, I. V., Ionov, G. V., and Karpeev, A. V. (2014). Simulation of the airwave caused by the Chelyabinsk superbolide. *Journal of Geophysical Research: Atmospheres*, 119(12):7035–7050.

Barnouin-Jha, O. S., Cheng, A. F., Mukai, T., Abe, S., Hirata, N., Nakamura, R., Gaskell, R. W., Saito, J., and Clark, B. E. (2008). Small-scale topography of 25143 Itokawa from the Hayabusa laser altimeter. *Icarus*, 198(1):108–124.

Bell, J. F., Davis, D. R., Hartmann, W. K., and Gaffey, M. J. (1989). Asteroids - The big picture. In Binzel, R. P., Gehrels, T., and Matthews, M. S., editors, *Asteroids II*, pages 921–945.

Bell, J. F., Elkins-Tanton, L. T., Polanskey, C., Ravine, M. A., Caplinger, M. A., Asphaug, E., Berkovici, D., Bills, B., Binzel, R. P., Bottke, W., Jaumann, R., Marchi, S., Park, R. S., Raymond, C. A., Wenkert, D., Wieczorek, M., Weiss, B., and Zuber, M. (2016). The Psyche Multispectral Imager Investigation: Characterizing the Geology, Topography, and Compositional Properties of a Metallic World. volume 47, page 1366.

Belton, M. J. S., Belton, M. J. S., Morgan, T. H., Samarasinha, N. H., and Yeomans, D. K. (2004). *Mitigation of Hazardous Comets and Asteroids*. Cambridge University Press.

Benck, R. F., Filbey Jr, G. L., and Murray Jr, E. (1976). Quasi-static compression stress-strain curves–iv, 2024-t3510 and 6061-t6 aluminum alloys. Technical report, Army Ballistic Research Lab Aberdeen Pooving Ground MD.

Benson, D. J. (1992). Computational methods in Lagrangian and Eulerian hydrocodes. *Computer Methods in Applied Mechanics and Engineering*, 99(2):235–394.

Benz, W. and Asphaug, E. (1999). Catastrophic Disruptions Revisited. *Icarus*, 142(1):5–20.

Benz, W., Cameron, A. G. W., and Melosh, H. J. (1989). The origin of the Moon and the single-impact hypothesis III. *Icarus*, 81(1):113–131.

Binzel, R. P., Reddy, V., and Dunn, T. L. (2015). The Near-Earth Object Population: Connections to Comets, Main-Belt Asteroids, and Meteorites. *aste*, pages 243–256.

Bland, P. A. and Artemieva, N. A. (2005). The rate of small impacts on Earth. *Meteoritics & Planetary Science Archives*, 41(4):607–631.

Bland, P. A., Artemieva, N. A., Collins, G. S., Bottke, W. F., Bussey, D. B. J., and Joy, K. H. (2008). Asteroids on the Moon: Projectile Survival During Low Velocity Impact. In *Lunar and Planetary Science Conference*, volume 39, page 2045.

Bottke, W. F., Durda, D. D., Nesvorný, D., Jedicke, R., Morbidelli, A., Vokrouhlický, D., and Levison, H. F. (2005). Linking the collisional history of the main asteroid belt to its dynamical excitation and depletion. *Icarus*, 179(1):63–94.

Bottke, W. F., Nesvorný, D., Grimm, R. E., Morbidelli, A., and O'Brien, D. P. (2006). Iron meteorites as remnants of planetesimals formed in the terrestrial planet region. *Nature*, 439(7078):821.

Bottke, W. F., Nolan, M. C., Greenberg, R., and Kolvoord, R. A. (1994). Velocity Distributions among Colliding Asteroids. *Icarus*, 107(2):255–268.

Bowell, E., Chapman, C. R., Gradie, J. C., Morrison, D., and Zellner, B. (1978). Taxonomy of asteroids. *Icarus*, 35(3):313–335.

Britt, D. T., Tholen, D. J., Bell, J. F., and Pieters, C. M. (1992). Comparison of asteroid and meteorite spectra: Classification by principal component analysis. *Icarus*, 99(1):153–166.

Britt, D. T., Yeomans, D., Housen, K., and Consolmagno, G. (2002). Asteroid Density, Porosity, and Structure. In *Asteroids III*, pages 485–500.

Brookshaw, L. (1998). An equation of state for serpentine. Technical report.

Brown, P., Spalding, R. E., ReVelle, D. O., Tagliaferri, E., and Worden, S. P. (2002). The flux of small near-Earth objects colliding with the Earth. *Nature*, 420(6913):294–296.

Burbine, T. H. and Binzel, R. P. (2002). Small Main-Belt Asteroid Spectroscopic Survey in the Near-Infrared. *Icarus*, 159(2):468–499.

Burchell, M. J. and Mackay, N. G. (1998). Crater ellipticity in hypervelocity impacts on metals. *Journal of Geophysical Research: Planets*, 103(E10):22761–22774.

Bus, S. J. and Binzel, R. P. (2002). Phase II of the Small Main-Belt Asteroid Spectroscopic Survey: A Feature-Based Taxonomy. *Icarus*, 158(1):146–177.

Carroll, M. and Holt, A. C. (1972). Suggested Modification of the P- Model for Porous Materials. *Journal of Applied Physics*, 43(2):759–761.

Carry, B. (2012). Density of asteroids. *Planetary and Space Science*, 73(1):98–118.

Chapman, C. R. and McKinnon, W. B. (1986). Cratering of planetary satellites. In Burns, J. A. and Matthews, M. S., editors, *Satellites*, pages 492–580. University of Arizona Press, Tucson.

Chapman, C. R., Morrison, D., and Zellner, B. (1975). Surface Properties of Asteroids: A Synthesis of Polarimetry, Radiometry, and Spectrophotometry. *Icarus*, 25(1):104–130.

Cheng, A. F., Izenberg, N., Chapman, C. R., and Zuber, M. T. (2002). Ponded deposits on asteroid 433 Eros. *Meteoritics & Planetary Science Archives*, 37(8):1095–1105.

Cheng, A. F., Michel, P., Jutzi, M., Rivkin, A. S., Stickle, A., Barnouin, O., Ernst, C., Atchison, J., Pravec, P., and Richardson, D. C. (2016). Asteroid Impact & Deflection Assessment mission: Kinetic impactor. *Planetary and Space Science*, 121:27–35.

Cheng, A. F., Rivkin, A. S., Michel, P., Atchison, J., Barnouin, O., Benner, L., Chabot, N. L., Ernst, C., Fahnestock, E. G., Kueppers, M., Pravec, P., Rainey, E., Richardson, D. C., Stickle, A. M., and Thomas, C. (2018). AIDA DART asteroid deflection test: Planetary defense and science objectives. *Planetary and Space Science*, 157:104–115.

Cheng, A. F., Weaver, H. A., Conard, S. J., Morgan, M. F., Barnouin-Jha, O., Boldt, J. D., Cooper, K. A., Darlington, E. H., Grey, M. P., Hayes, J. R., Kosakowski, K. E., Magee, T., Rossano, E., Sampath, D., Schlemm, C., and Taylor, H. W. (2008). Long-Range Reconnaissance Imager on New Horizons. *Space Science Reviews*, 140(1):189–215.

Cintala, M. J., Berthoud, L., and Hörz, F. (1999). Ejection-velocity distributions from impacts into coarse-grained sand. *Meteoritics & Planetary Science*, 34(4):605–623.

Cloutis, E. A., Gaffey, M. J., Smith, D. G. W., and Lambert, R. S. J. (1990). Reflectance spectra of glass-bearing mafic silicate mixtures and spectral deconvolution procedures. *Icarus*, 86(2):383–401.

Collins, G. S. (2014). Numerical simulations of impact crater formation with dilatancy. *Journal of Geophysical Research: Planets*, 119(12):2014JE004708.

Collins, G. S., Elbeshausen, D., Davison, T. M., Robbins, S. J., and Hynek, B. M. (2011). The size-frequency distribution of elliptical impact craters. *Earth and Planetary Science Letters*, 310(1):1–8.

Collins, G. S., Elbeshausen, D., Davison, T. M., Wünnemann, K., Ivanov, B., and Melosh, H. J. (2016). isale-dellen manual.

Collins, G. S., Melosh, H. J., and Ivanov, B. A. (2004). Modeling damage and deformation in impact simulations. *Meteoritics & Planetary Science*, 39(2):217–231.

Collins, G. S., Melosh, H. J., Morgan, J. V., and Warner, M. R. (2002). Hydrocode Simulations of Chicxulub Crater Collapse and Peak-Ring Formation. *Icarus*, 157(1):24–33.

Collins, G. S., Melosh, H. J., and Wünnemann, K. (2011). Improvements to the epsilon-alpha porous compaction model for simulating impacts into high-porosity solar system objects. *International Journal of Impact Engineering*, 38(6):434–439.

Collins, G. S., Wünnemann, K., Artemieva, N., and Pierazzo, E. (2012). Numerical Modelling of Impact Processes. In *Impact Cratering*, pages 254–270. John Wiley & Sons, Ltd.

Colwell, J. E., Batiste, S., Horányi, M., Robertson, S., and Sture, S. (2007). Lunar surface: Dust dynamics and regolith mechanics. *Reviews of Geophysics*, 45(2).

Coradini, A., Capaccioni, F., Erard, S., Arnold, G., De Sanctis, M. C., Filacchione, G., Tosi, F., Barucci, M. A., Capria, M. T., Ammannito, E., Grassi, D., Piccioni, G., Giuppi, S., Bellucci, G., Benkhoff, J., Bibring, J. P., Blanco, A., Blecka, M., Bockelee-Morvan, D., Carraro, F., Carlson, R., Carsenty, U., Cerroni, P., Colangeli, L., Combes, M., Combi, M., Crovisier, J., Drossart, P., Encrenaz, E. T., Federico, C., Fink, U., Fonti, S., Giacomini, L., Ip, W. H., Jaumann, R., Kuehrt, E., Langevin, Y., Magni, G., McCord, T., Mennella, V., Mottola, S., Neukum, G., Orofino, V., Palumbo, P., Schade, U., Schmitt, B., Taylor, F., Tiphene, D., and Tozzi, G. (2011). The Surface Composition and Temperature of Asteroid 21 Lutetia As Observed by Rosetta/VIRTIS. *Science*, 334(6055):492–494.

Cuzzi, J. N., Dobrovolskis, A. R., and Champney, J. M. (1993). Particle-Gas Dynamics in the Midplane of a Protoplanetary Nebula. *Icarus*, 106(1):102–134.

Cuzzi, J. N. and Weidenschilling, S. J. (2006). Particle-Gas Dynamics and Primary Accretion. *Meteorites and the Early Solar System II*, 943:353–381.

Danninger, H., Jangg, G., Weiss, B., and Stickler, R. (1993). Microstructure and mechanical properties of sintered iron. pt. 1; basic considerations and review of literature.

Davis, D. R., Farinella, P., and Marzari, F. (1999). The Missing Psyche Family: Collisionally Eroded or Never Formed? *Icarus*, 137(1):140–151.

Davison, T. M., Collins, G. S., and Bland, P. A. (2016). Mesoscale modeling of impact compaction of primitive solar system solids. *The Astrophysical Journal*, 821(1):68.

Davison, T. M., Collins, G. S., Elbeshausen, D., Wünnemann, K., and Kearsley, A. (2011). Numerical modeling of oblique hypervelocity impacts on strong ductile targets. *Meteoritics & Planetary Science*, 46(10):1510–1524.

Davison, T. M., O'Brien, D. P., Ciesla, F. J., and Collins, G. S. (2013). The early impact histories of meteorite parent bodies. *Meteoritics & Planetary Science*, 48(10):1894–1918.

Delbo, M., Libourel, G., Wilkerson, J., Murdoch, N., Michel, P., Ramesh, K. T., Ganino, C., Verati, C., and Marchi, S. (2014). Thermal fatigue as the origin of regolith on small asteroids. *Nature*, 508(7495):233–236.

Denneau, L., Jedicke, R., Grav, T., Granvik, M., Kubica, J., Milani, A., Veres, P., Wainscoat, R., Chang, D., Pierfederici, F., Kaiser, N., Chambers, K. C., Heasley, J. N., Magnier, E. A., Price, P. A., Myers, J., Kleyna, J., Hsieh, H., Farnocchia, D., Waters, C., Sweeney, W. H., Green, D., Bolin, B., Burgett, W. S., Morgan, J. S., Tonry, J. L., Hodapp, K. W., Chastel, S., Chesley, S., Fitzsimmons, A., Holman, M., Spahr, T., Tholen, D., Williams, G. V., Abe, S., Armstrong, J. D., Bressi, T. H., Holmes, R., Lister, T., McMillan, R. S., Micheli, M., Ryan, E. V., Ryan, W. H., and Scotti, J. V. (2013). The Pan-STARRS Moving Object Processing System. *Publications of the Astronomical Society of the Pacific*, 125(926):357–395.

Drummond, J. D., Merline, W. J., Carry, B., Conrad, A., Reddy, V., Tamblyn, P., Chapman, C. R., Enke, B. L., Pater, I. d., Kleer, K. d., Christou, J., and Dumas, C. (2018). The triaxial ellipsoid size, density, and rotational pole of asteroid (16) Psyche from Keck and Gemini AO observations 2004-2015. *Icarus*, 305:174–185.

Durda, D. D., Bottke, W. F., Enke, B. L., Merline, W. J., Asphaug, E., Richardson, D. C., and Leinhardt, Z. M. (2004). The formation of asteroid satellites in large impacts: results from numerical simulations. *Icarus*, 170:243–257.

Elbeshausen, D., Wünnemann, K., and Collins, G. S. (2009). Scaling of oblique impacts in frictional targets: Implications for crater size and formation mechanisms. *Icarus*, 204(2):716–731.

Elkins-Tanton, L., Asphaug, E., Bell, J., Bercovici, D., Bills, B., Binzel, R., Bottke, W., Goldsten, J., Jaumann, R., Jun, I., Lawrence, D., Marchi, S., Oh, D., Park, R., Peplowski, P., C.A., P., Prettyman, T., Raymond, C., Russell, C., Weiss, B., Wenkert, D., Wieczorek, M., and Zuber, M. (2017). Asteroid (16) psyche: Visiting a metal world. *LPSC 48*, page 1718.

Elkins-Tanton, L. T., Asphaug, E., Bell, J., Bercovici, D., Bills, B., Binzel, R., Bottke, W., Goldsten, J., Jaumann, R., Jun, I., Lawrence, D., Marchi, S., Oh, D., Park, R., Peplowski, P., C.A., P., Prettyman, T., Raymond, C., Russell, C., Weiss, B., Wenkert, D., Wieczorek, M., and Zuber, M. (2016). Asteroid (16) psyche: The science of visiting a metal world. *LPSC 47*, page 1631.

Elkins-Tanton, L. T., Weiss, B. P., and Zuber, M. T. (2011). Chondrites as samples of differentiated planetesimals. *Earth and Planetary Science Letters*, 305(1):1–10.

Farinella, P. and Davis, D. R. (1992). Collision rates and impact velocities in the main asteroid belt. *Icarus*, 97(1):111–123.

Fassett, C. I. and Minton, D. A. (2013). Impact bombardment of the terrestrial planets and the early history of the Solar System. *Nature Geoscience*, 6(7):520–524.

Fornasier, S., Clark, B. E., Dotto, E., Migliorini, A., Ockert-Bell, M., and Barucci, M. A. (2010). Spectroscopic survey of M-type asteroids. *Icarus*, 210(2):655–673.

French, B. M. (1998). *Traces of Catastrophe: A Handbook of Shock-Metamorphic Effects in Terrestrial Meteorite Impact Structures*. LPI Contribution No. 954, Lunar and Planetary Institute, Houston.

Fujiwara, A., Kawaguchi, J., Yeomans, D. K., Abe, M., Mukai, T., Okada, T., Saito, J., Yano, H., Yoshikawa, M., Scheeres, D. J., Barnouin-Jha, O., Cheng, A. F., Demura, H., Gaskell, R. W., Hirata, N., Ikeda, H., Kominato, T., Miyamoto, H., Nakamura, A. M., Nakamura, R., Sasaki, S., and Uesugi, K. (2006). The Rubble-Pile Asteroid Itokawa as Observed by Hayabusa. *Science*, 312(5778):1330–1334.

Gaffey, M. J., Burbine, T. H., and Binzel, R. P. (1993). Asteroid spectroscopy: Progress and perspectives. *Meteoritics*, 28(2):161–187.

Gault, D., Shoemaker, E., Moore, H., Aeronautics, U. S. N., Administration, S., and Center", A. R. (1963). *Spray Ejected from the Lunar Surface by Meteoroid Impact*. NASA technical note. National Aeronautics and Space Administration.

Gault, D. E., Guest, J. E., Murray, J. B., Dzurisin, D., and Malin, M. C. (1975). Some comparisons of impact craters on Mercury and the Moon. *Journal of Geophysical Research*, 80(17):2444–2460.

Gault, D. E., Oberbeck, V. R., and Quaide, W. L. (1968). Impact cratering mechanics and structures. pages 87–99.

German, R. M. (1994). *Powder Metallurgy Science*. Metal Powder Industries Federation. Google-Books-ID: eSZvQgAACAAJ.

Gilbert, G. K. (1893). The moon's face. A study of the origin of its features. *Bulletin of the Philosophical Society of Washington*, 12:241–292.

Goldreich, P. and Ward, W. R. (1973). The Formation of Planetesimals. *The Astrophysical Journal*, 183:1051–1062.

Goodman, R. (1989). *Introduction to Rock Mechanics*. Wiley.

Gradie, J. and Tedesco, E. (1982). Compositional Structure of the Asteroid Belt. *Sci*, 216(4553):1405–1407.

Greenberg, R. and Chapman, C. R. (1983). Asteroids and meteorites: Parent bodies and delivered samples. *Icarus*, 55(3):455–481.

Gundlach, B. and Blum, J. (2013). A new method to determine the grain size of planetary regolith. *Icarus*, 223(1):479–492.

Güldemeister, N., Wünnemann, K., and Poelchau, M. (2015). Scaling impact crater dimensions in cohesive rock by numerical modeling and laboratory experiments. In *Geological Society of America Special Papers*, volume 518, pages 17–29. Geological Society of America.

Hagerty, M. M., Hite, D. R., Ullrich, C. R., and J., H. D. (1993). One–Dimensional High–Pressure Compression of Granular Media. *Journal of Geotechnical Engineering*, 119(1):1–18.

Hanuš, J., Viikinkoski, M., Marchis, F., Ďurech, J., Kaasalainen, M., Delbo', M., Herald, D., Frappa, E., Hayamizu, T., Kerr, S., Preston, S., Timerson, B., Dunham, D., and Talbot, J. (2017). Volumes and bulk densities of forty asteroids from ADAM shape modeling. *A&A*, 601:A114.

Hardersen, P. S., Gaffey, M. J., and Abell, P. A. (2005). Near-IR spectral evidence for the presence of iron-poor orthopyroxenes on the surfaces of six M-type asteroids. *Icarus*, 175(1):141–158.

Harris, A. W. (1996). *The Rotation Rates of Very Small Asteroids: Evidence for 'Rubble Pile' Structure*, volume 27 of *Lunar and Planetary Science Conference*.

Harris, A. W., Barucci, M. A., Cano, J. L., Fitzsimmons, A., Fulchignoni, M., Green, S. F., Hestroffer, D., Lappas, V., Lork, W., Michel, P., Morrison, D., Payson, D., and Schäfer, F. (2013). The European Union funded NEOShield project: A global approach to near-Earth object impact threat mitigation. *Acta Astronautica*, 90(1):80–84.

Harris, A. W. and D'Abramo, G. (2015). The population of near-Earth asteroids. *Icarus*, 257:302–312.

Hartmann, W. K. (1985). Impact experiments. *Icarus*, 63(1):69–98.

Heiken, G. H. V. (1991). Lunar sourcebook - A user's guide to the moon. Technical report.

Henderson, E. P. and Perry, S. H. (1954). A discussion of the densities of iron meteorites. *Geochimica et Cosmochimica Acta*, 6(5):221–240.

Hermalyn, B. and Schultz, P. H. (2010). Early-stage ejecta velocity distribution for vertical hypervelocity impacts into sand. *Icarus*, 209(2):866–870.

Hermalyn, B. and Schultz, P. H. (2011). Time-resolved studies of hypervelocity vertical impacts into porous particulate targets: Effects of projectile density on early-time coupling and crater growth. *Icarus*, 216(1):269–279.

Hiesinger, H., Marchi, S., Schmedemann, N., Schenk, P., Pasckert, J. H., Neesemann, A., O'Brien, D. P., Kneissl, T., Ermakov, A. I., Fu, R. R., Bland, M. T., Nathues, A., Platz, T., Williams, D. A., Jaumann, R., Castillo-Rogez, J. C., Ruesch, O., Schmidt, B., Park, R. S., Preusker, F., Buczkowski, D. L., Russell, C. T., and Raymond, C. A. (2016). Cratering on Ceres: Implications for its crust and evolution. *Science*, 353(6303):aaf4759.

Hirabayashi, M. and Scheeres, D. J. (2014). Stress and Failure Analysis of Rapidly Rotating Asteroid (29075) 1950 DA. *The Astrophysical Journal*, 798(1):L8.

Holsapple, K. A. (1993). The Scaling of Impact Processes in Planetary Sciences. *Annual Review of Earth and Planetary Sciences*, 21(1):333–373.

Holsapple, K. A. (2008). Porous material models for impact studies. In *Lunar Planet. Sci. XXXIX*, page 2257. Lunar and Planetary Institute, Houston.

Holsapple, K. A. (2009). On the "strength" of the small bodies of the solar system: A review of strength theories and their implementation for analyses of impact disruptions. *Planetary and Space Science*, 57(2):127–141.

Holsapple, K. A. and Housen, K. R. (2007). A crater and its ejecta: An interpretation of Deep Impact. *Icarus*, 191(2, Supplement):586–597.

Holsapple, K. A. and Housen, K. R. (2012). Momentum transfer in asteroid impacts. I. Theory and scaling. *Icarus*, 221(2):875–887.

Holsapple, K. A. and Schmidt, R. M. (1982). On the scaling of crater dimensions. II - Impact processes. *Journal of Geophysical Research*, 87:1849–1870.

Holsapple, K. A. and Schmidt, R. M. (1987). Point source solutions and coupling parameters in cratering mechanics. *Journal of Geophysical Research: Solid Earth*, 92(B7):6350–6376.

Housen, K. R. (1992). *Crater Ejecta Velocities for Impacts on Rocky Bodies*, volume 23 of *Lunar and Planetary Science Conference*.

Housen, K. R. and Holsapple, K. A. (2003). Impact cratering on porous asteroids. *Icarus*, 163(1):102–119.

Housen, K. R. and Holsapple, K. A. (2011). Ejecta from impact craters. *Icarus*, 211(1):856–875.

Housen, K. R. and Holsapple, K. A. (2012). Deflecting asteroids by impacts: what is beta? page 2.

Housen, K. R., Schmidt, R. M., and Holsapple, K. A. (1983). Crater ejecta scaling laws: Fundamental forms based on dimensional analysis. *Journal of Geophysical Research: Solid Earth*, 88(B3):2485–2499.

Housen, K. R., Sweet, W. J., and Holsapple, K. A. (2018). Impacts into porous asteroids. *Icarus*, 300:72–96.

Ivanov, B. A. (2005). Numerical Modeling of the Largest Terrestrial Meteorite Craters. *Solar System Research*, 39(5):381–409.

Ivanov, B. A. and Artemieva, N. A. (2002). Numerical modeling of the formation of large impact craters. In *Special Paper 356: Catastrophic events and mass extinctions: impacts and beyond*, volume 356, pages 619–630. Geological Society of America.

Ivanov, B. A., Deniem, D., and Neukum, G. (1997). Implementation of dynamic strength models into 2d hydrocodes: Applications for atmospheric breakup and impact cratering. *International Journal of Impact Engineering*, 20(1):411–430.

Ivanov, B. A. and Deutsch, A. (1999). Sudbury impact event: Cratering mechanics and thermal history. In *Large Meteorite Impacts and Planetary Evolution II, Geological Society of America, Special Paper 339*, pages 389–397. Geological Society of America.

Ivanov, B. A. and Melosh, H. J. (2013). Two-dimensional numerical modeling of the Rheasilvia impact formation. *J. Geophys. Res: Planets*, 118(7):1545–1557.

Ivanov, B. A., Melosh, H. J., and Pierazzo, E. (2010). Basin-forming impacts: Reconnaissance modeling. *Geological Society of America Special Papers*, 465:29–49.

Ivanov, B. A., Neukum, G., Bottke, Jr., W. F., and Hartmann, W. K. (2002). The Comparison of Size-Frequency Distributions of Impact Craters and Asteroids and the Planetary Cratering Rate. In *Asteroids III*, pages 89–101.

Jacobson, S. A. and Scheeres, D. J. (2011). Dynamics of rotationally fissioned asteroids: Source of observed small asteroid systems. *Icarus*, 214(1):161–178.

Jewitt, D., Agarwal, J., Li, J., Weaver, H., Mutchler, M., and Larson, S. (2014). Disintegrating Asteroid P/2013 R3. *The Astrophysical Journal*, 784(1).

Johnson, B., Bowling, J. T., and Melosh, J. (2014). Jetting during vertical impacts of spherical projectiles. *Icarus*, 238:13–22.

Johnson, B. C., Sori, M. M., and Evans, A. J. (2019). Ferrovolcanism on metal worlds and the origin of pallasites. *Nature Astronomy*, pages 1–4.

Johnson, G. R. and Cook, W. H. (1983). A constitutive model and data for metals subjected to large strains, high strain rates and high temperatures. *Proceedings of the 7th International Symposium on Ballistics, The Hague*, pages 541–547.

Johnson, G. R. and Cook, W. H. (1985). Fracture characteristics of three metals subjected to various strains, strain rates, temperatures and pressures. *Eng Fract Mech*, 21(1):31–48.

Jones, D. L., Goyer, G. G., and Plooster, M. N. (1968). Shock wave from a lightning discharge. *Journal of Geophysical Research (1896-1977)*, 73(10):3121–3127.

Jutzi, M. and Michel, P. (2014). Hypervelocity impacts on asteroids and momentum transfer I. Numerical simulations using porous targets. *Icarus*, 229:247–253.

Kieffer, S. W. (1977). Sound speed in liquid-gas mixtures: Water-air and water-steam. *Journal of Geophysical Research (1896-1977)*, 82(20):2895–2904.

Klar, E. and Samal, P. K. (2007). *Powder Metallurgy Stainless Steels: Processing, Microstructures, and Properties*. ASM International.

Krot, A., Alexander, C., Nagashima, K., Ciesla, F., and Fujiya, W. (2014). Aqueous activity and sources of water on the chondrite parent asteroids. In Muinonen, K., Penttilä, A., Granvik, M., Virkki, A., Fedorets, G., Wilkman, O., and Kohout, T., editors, *Asteroids, Comets, Meteors 2014*.

Kubicki, B. (1995). *Sintered Machine Elements*. Ellis Horwood.

Küppers, M., Michel, P., Carnelli, I., Ulamec, S., Abell, P. A., and the Hera team (2019). Hera – the european contribution to the first asteroid deflection demonstration. *Lunar and Planetary Science, L*, page 2567.

Kurosawa, K. and Genda, H. (2018). Effects of Friction and Plastic Deformation in Shock-Comminuted Damaged Rocks on Impact Heating. *Geophysical Research Letters*, 45(2).

Kutsch, U., Beiss, P., and Jager, H.-J. (1997). Asteroid (16) psyche: The science of visiting a metal world. *Proc. Euro PM 97 Conference (Munich, Germany)*, pages 174–182.

Landis, R. and Johnson, L. (2018). Advances in planetary defense in the United States. *Acta Astronautica*.

Landsman, Z. A., Emery, J. P., Campins, H., Hanuš, J., Lim, L. F., and Cruikshank, D. P. (2018). Asteroid (16) Psyche: Evidence for a silicate regolith from spitzer space telescope spectroscopy. *Icarus*, 304:58–73.

Lange, M. A. and Ahrens, T. J. (1982). Impact Induced Dehydration of Serpentine and the Evolution of Planetary Atmospheres. *Lunar and Planetary Science Conference Proceedings*, 87:451.

Lauretta, D. S., DellaGiustina, D. N., Bennett, C. A., Golish, D. R., Becker, K. J., Balram-Knutson, S. S., Barnouin, O. S., Becker, T. L., Bottke, W. F., Boynton, W. V., Campins, H., Clark, B. E., Connolly, H. C., d'Aubigny, C. Y. D., Dworkin, J. P., Emery, J. P., Enos, H. L., Hamilton, V. E., Hergenrother, C. W., Howell, E. S., Izawa, M. R. M., Kaplan, H. H., Nolan, M. C., Rizk, B., Roper, H. L., Scheeres, D. J., Smith, P. H., Walsh, K. J., and Wolner, C. W. V. (2019). The unexpected surface of asteroid (101955) Bennu. *Nature*, 568(7750):55.

Lee, K. L. and Seed, H. B. (1967). Drained Strength Characteristics of Sands. *Journal of the Soil Mechanics and Foundations Division*, 93(6):117–141.

Libourel, G., Nakamura, A. M., Beck, P., Potin, S., Ganino, C., Jacomet, S., Ogawa, R., Hasegawa, S., and Michel, P. (2019). Hypervelocity impacts as a source of deceiving surface signatures on iron-rich asteroids. *Science Advances*, 5(8):eaav3971.

Lissauer, J. J. (1993). Planet formation. *Annual Review of Astronomy and Astrophysics*, 31:129–174.

Lu, E. T. and Love, S. G. (2005). Gravitational tractor for towing asteroids. *Nature*, 438(7065):177–178.

Lundborg, N. (1967). The strength-size relation of granite. *International Journal of Rock Mechanics and Mining Sciences & Geomechanics Abstracts*, 4(3):269–272.

Luther, R., Zhu, M.-H., Collins, G., and Wünnemann, K. (2018). Effect of target properties and impact velocity on ejection dynamics and ejecta deposition. *Meteoritics & Planetary Science*, 53(8):1705–1732.

Lyons, R. J., Bowling, T. J., Ciesla, F. J., Davison, T. M., and Collins, G. S. (2019). The effects of impacts on the cooling rates of iron meteorites. *Meteoritics & Planetary Science*, 54(7):1604–1618.

Lyttleton, R. A. (1961). An accretion hypothesis for the origin of the solar system. *Monthly Notices of the Royal Astronomical Society*, 122:399.

Marchi, S., Durda, D. D., Polanskey, C. A., Asphaug, E., Bottke, W. F., Elkins-Tanton, L. T., Garvie, L. a. J., Ray, S., Chocron, S., and Williams, D. A. (2019). Hypervelocity impact experiments in iron-nickel ingots and iron meteorites: Implications for the NASA Psyche mission. *Journal of Geophysical Research: Planets*.

Mason, B. (1963). The Carbonaceous Chondrites. *SSRv*, 1(4):621–646.

Matter, A., Delbo, M., Carry, B., and Ligori, S. (2013). Evidence of a metal-rich surface for the asteroid (16) Psyche from interferometric observations in the thermal infrared. *Icarus*, 226(1):419–427.

Mazrouei, S., Daly, M. G., Barnouin, O. S., Ernst, C. M., and DeSouza, I. (2014). Block distributions on Itokawa. *Icarus*, 229:181–189.

McCord, T. B., Li, J.-Y., Combe, J.-P., McSween, H. Y., Jaumann, R., Reddy, V., Tosi, F., Williams, D. A., Blewett, D. T., Turrini, D., Palomba, E., Pieters, C. M., De Sanctis, M. C., Ammannito, E., Capria, M. T., Le Corre, L., Longobardo, A., Nathues, A., Mittlefehldt, D. W., Schröder, S. E., Hiesinger, H., Beck, A. W., Capaccioni, F., Carsenty, U., Keller, H. U., Denevi, B. W., Sunshine, J. M., Raymond, C. A., and Russell, C. T. (2012). Dark material on Vesta from the infall of carbonaceous volatile-rich material. *Nature*, 491(7422):83–86.

McCoy, T. J., Mittlefehldt, D. W., and Wilson, L. (2006). Asteroid Differentiation. *Meteorites and the Early Solar System II*, pages 733–745.

McCrea, W. (1988). Formation of the solar system: brief review and revised protoplanet theory. *The physics of the planets: Their origin, evolution and structure*, pages 421–439.

McCrea, W. H. (1960). The origin of the solar system. *Proceedings of the Royal Society of London. Series A. Mathematical and Physical Sciences*, 256(1285):245–266.

McKay, D. S., Heiken, G., Basu, A., Blanford, G., Simon, S., Reedy, R., French, B. M., and Papike, J. (1991). *The lunar regolith, in The Lunar Sourcebook*. Cambridge Univ. Press, New York.

Melosh, H. J. (1989). *Impact cratering: a geologic process*. Oxford monographs on geology and geophysics. Oxford University Press.

Melosh, H. J. (2007). A hydrocode equation of state for SiO2. *Meteoritics & Planetary Science Archives*, 42(12):2079–2098.

Melosh, H. J., Nemchinov, I. V., and Zetzer, Y. I. (1994). Non-nuclear strategies for deflecting comets and asteroids. pages 1111–1132.

Melosh, H. J., Ryan, E. V., and Asphaug, E. (1992). Dynamic fragmentation in impacts: hydrocode simulation of laboratory impacts. *Journal of Geophysical Research*, 97(E9). Publisher: Wiley-Blackwell.

Melosh, H. J. and Sonett, C. P. (1986). When worlds collide: jetted vapor plumes and the Moon's origin. *Origin of the moon; Proceedings of the Conference, Kona, HI, October 13-16, 1984*, pages 621–642.

Michel, P. (2013). Physical properties of Near-Earth Objects that inform mitigation. *Acta Astronautica*, 90(1):6–13.

Michel, P., Benz, W., Tanga, P., and Richardson, D. C. (2001). Collisions and Gravitational Reaccumulation: Forming Asteroid Families and Satellites. *Science*, 294(5547):1696–1700.

Michel, P., Cheng, A., Küppers, M., Pravec, P., Blum, J., Delbo, M., Green, S., Rosenblatt, P., Tsiganis, K., Vincent, J., Biele, J., Ciarletti, V., Hérique, A., Ulamec, S., Carnelli, I., Galvez, A., Benner, L., Naidu, S., Barnouin, O., Richardson, D., Rivkin, A., Scheirich, P., Moskovitz, N., Thirouin, A., Schwartz, S., Campo Bagatin, A., and Yu, Y. (2016). Science case for the asteroid impact mission (aim): A component of the asteroid impact & deflection assessment (aida) mission. *Advances in Space Research*, 57(12):2529 – 2547.

Michel, P., Kueppers, M., Sierks, H., Carnelli, I., Cheng, A. F., Mellab, K., Granvik, M., Kestilä, A., Kohout, T., Muinonen, K., Näsilä, A., Penttila, A., Tikka, T., Tortora, P., Ciarletti, V., Hérique, A., Murdoch, N., Asphaug, E., Rivkin, A., Barnouin, O., Bagatin, A. C., Pravec, P., Richardson, D. C., Schwartz, S. R., Tsiganis, K., Ulamec, S., and Karatekin, O. (2018). European component of the AIDA mission to a binary asteroid: Characterization and interpretation of the impact of the DART mission. *Advances in Space Research*, 62(8):2261–2272.

Micheli, M., Wainscoat, R. J., and Denneau, L. (2018). Detectability of Chelyabinsk-like impactors with Pan-STARRS. *Icarus*, 303:265–272.

Michikami, T., Honda, C., Miyamoto, H., Hirabayashi, M., Hagermann, A., Irie, T., Nomura, K., Ernst, C. M., Kawamura, M., Sugimoto, K., Tatsumi, E., Morota, T., Hirata, N., Noguchi, T., Cho, Y., Kameda, S., Kouyama, T., Yokota, Y., Noguchi, R., Hayakawa, M., Hirata, N., Honda, R., Matsuoka, M., Sakatani, N., Suzuki, H., Yamada, M., Yoshioka, K., Sawada, H., Hemmi, R., Kikuchi, H., Ogawa, K., Watanabe, S.-i., Tanaka, S., Yoshikawa, M., Tsuda, Y., and Sugita, S. (2019). Boulder size and shape distributions on asteroid Ryugu. *Icarus*, 331:179–191.

Mitchell, J. K. H. (1974). Apollo soil mechanics experiment S-200, nasa contract nas 9-11266, space sciences laboratory. Technical report.

Miyamoto, H., Yano, H., Scheeres, D. J., Abe, S., Barnouin-Jha, O., Cheng, A. F., Demura, H., Gaskell, R. W., Hirata, N., Ishiguro, M., Michikami, T., Nakamura, A. M., Nakamura, R., Saito, J., and Sasaki, S. (2007). Regolith Migration and Sorting on Asteroid Itokawa. *Science*, 316(5827):1011–1014.

Morbidelli, A., Bottke, W., Nesvorny, D., and Levison, H. F. (2009). Asteroids Were Born Big. *Icarus*, 204:558–573. arXiv: 0907.2512.

Morgan, J., Warner, M., the Chicxulub Working Group, Brittan, J., Buffler, R., Camargo, A., Christeson, G., Denton, P., Hildebrand, A., Hobbs, R., Macintyre, H., Mackenzie, G., Maguire, P., Marin, L., Nakamura, Y., Pilkington, M., Sharpton, V., Snyder, D., Suarez, G., and Trejo, A. (1997). Size and morphology of the Chicxulub impact crater. *Nature*, 390(6659):472–476.

Morgan, J. V., Gulick, S. P. S., Bralower, T., Chenot, E., Christeson, G., Claeys, P., Cockell, C., Collins, G. S., Coolen, M. J. L., Ferrière, L., Gebhardt, C., Goto, K., Jones, H., Kring, D. A., Ber, E. L., Lofi, J., Long, X., Lowery, C., Mellett, C., Ocampo-Torres, R., Osinski, G. R., Perez-Cruz, L., Pickersgill, A., Poelchau, M., Rae, A., Rasmussen, C., Rebolledo-Vieyra, M., Riller, U., Sato, H., Schmitt, D. R., Smit, J., Tikoo, S., Tomioka, N., Urrutia-Fucugauchi, J., Whalen, M., Wittmann, A., Yamaguchi, K. E., and Zylberman, W. (2016). The formation of peak rings in large impact craters. *Science*, 354(6314):878–882.

Murdoch, N., Hempel, S., Pou, L., Cadu, A., Garcia, R. F., Mimoun, D., Margerin, L., and Karatekin, O. (2017). Probing the internal structure of the asteriod Didymoon with a passive seismic investigation. *Planetary and Space Science*, 144:89–105.

Murdoch, N., Sanchez, P., Schwartz, S. R., and Miyamoto, H. (2015). Asteroid Surface Geophysics. *Asteroids IV, Patrick Michel, Francesca E. DeMeo, and William F. Bottke (eds.), University of Arizona Press, Tucson.*

Nakamura, A. M., Hiraoka, K., Yamashita, Y., and Machii, N. (2009). Collisional disruption experiments of porous targets. *Planetary and Space Science*, 57(2):111–118.

Nakamura, E., Makishima, A., Moriguti, T., Kobayashi, K., Tanaka, R., Kunihiro, T., Tsujimori, T., Sakaguchi, C., Kitagawa, H., Ota, T., Yachi, Y., Yada, T., Abe, M., Fujimura, A., Ueno, M., Mukai, T., Yoshikawa, M., and Kawaguchi, J. (2012). Space environment of an asteroid preserved on micrograins returned by the Hayabusa spacecraft. *Proceedings of the National Academy of Sciences*, 109(11):E624–E629.

Nakazawa, S., Watanabe, S., Kato, M., Iijima, Y., Kobayashi, T., and Sekine, T. (1997). Hugoniot equation of state of basalt. *Planetary and Space Science*, 45(11):1489–1492.

Nathues, A., Hoffmann, M., Cloutis, E. A., Schäfer, M., Reddy, V., Christensen, U., Sierks, H., Thangjam, G. S., Le Corre, L., Mengel, K., Vincent, J.-B., Russell, C. T., Prettyman, T., Schmedemann, N., Kneissl, T., Raymond, C., Gutierrez-Marques, P., Hall, I., and Büttner, I. (2014). Detection of serpentine in exogenic carbonaceous chondrite material on Vesta from Dawn FC data. *Icarus*, 239:222–237.

Neeley, J. R., Clark, B. E., Ockert-Bell, M. E., Shepard, M. K., Conklin, J., Cloutis, E. A., Fornasier, S., and Bus, S. J. (2014). The composition of M-type asteroids II: Synthesis of spectroscopic and radar observations. *Icarus*, 238:37–50.

Neukum, G., Koenig, B., Fechtig, H., and Storzer, D. (1975). Cratering in the earth-moon system: consequences for age determination by crater counting. *Lunar and Planetary Science Conference Proceedings*, 3:2597.

Oberbeck, V. R. (1975). The role of ballistic erosion and sedimentation in lunar stratigraphy. *Reviews of Geophysics*, 13(2):337–362.

Oberbeck, V. R. and Quaide, W. L. (1967). Estimated thickness of a fragmental surface layer of Oceanus Procellarum. *Journal of Geophysical Research*, 72(18):4697–4704.

O'Brien, D. P., Morbidelli, A., and Bottke, W. F. (2007). The primordial excitation and clearing of the asteroid belt—Revisited. *Icarus*, 191(2):434–452.

O'Brien, D. P., Morbidelli, A., and Levison, H. F. (2006). Terrestrial planet formation with strong dynamical friction. *Icarus*, 184(1):39–58.

Ockert-Bell, M. E., Clark, B. E., Shepard, M. K., Isaacs, R. A., Cloutis, E. A., Fornasier, S., and Bus, S. J. (2010). The composition of M-type asteroids: Synthesis of spectroscopic and radar observations. *Icarus*, 210(2):674–692.

Osinski, G. R. and Pierazzo, E. (2012). *Impact Cratering: Processes and Products*. Wiley.

O'Brien, D. P. (2009). The Yarkovsky effect is not responsible for small crater depletion on Eros and Itokawa. *Icarus*, 203(1):112–118.

Perna, D., Barucci, M. A., Drube, L., Falke, A., Fulchignoni, M., Harris, A. W., Harris, A. W., and Kanuchova, Z. (2015). A global response roadmap to the asteroid impact threat: The NEOShield perspective. *Planetary and Space Science*, 118:311–317.

Petit, J.-M., Morbidelli, A., and Chambers, J. (2001). The Primordial Excitation and Clearing of the Asteroid Belt. *Icarus*, 153(2):338–347.

Petrovic, J. J. (2001). Review mechanical properties of meteorites and their constituents. *Journal of Materials Science*, 36:1579–1583.

Piekutowski, A. J. (1980). Formation of bowl-shaped craters. *LPSC*, 3:2129–2144.

Pierazzo, E., Artemieva, N., Asphaug, E., Baldwin, E. C., Cazamias, J., Coker, R., Collins, G. S., Crawford, D. A., Davison, T., Elbeshausen, D., Holsapple, K. A., Housen, K. R., Korycansky, D. G., and Wünnemann, K. (2008). Validation of numerical codes for impact and explosion cratering: Impacts on strengthless and metal targets. *Meteoritics & Planetary Science*, 43(12):1917–1938.

Pierazzo, E., Artemieva, N., and Ivanov, B. (2005). Starting conditions for hydrothermal systems underneath Martian craters: Hydrocode modeling. In Kenkmann, T., Hörz, F., and Deutsch, A., editors, *Large Meteorite Impacts III*, volume 384, page 0. Geological Society of America.

Pierazzo, E. and Melosh, H. J. (2000). Melt Production in Oblique Impacts. *Icarus*, 145(1):252–261.

Pierazzo, E., Vickery, A. M., and Melosh, H. J. (1997). A Reevaluation of Impact Melt Production. *Icarus*, 127(2):408–423.

Pike, R. J. (1980). Formation of complex impact craters: Evidence from Mars and other planets. *Icarus*, 43(1):1–19.

Poelchau, M. H., Kenkmann, T., Thoma, K., Hoerth, T., Dufresne, A., and Schäfer, F. (2013). The MEMIN research unit: Scaling impact cratering experiments in porous sandstones. *Meteoritics & Planetary Science*, 48(1):8–22.

Popova, O., Borovička, J., Hartmann, W. K., Spurný, P., Gnos, E., Nemtchinov, I., and Trigo-Rodríguez, J. M. (2011). Very low strengths of interplanetary meteoroids and small asteroids. *Meteoritics & Planetary Science*, 46(10):1525–1550.

Popova, O. P., Jenniskens, P., Emel'yanenko, V., Kartashova, A., Biryukov, E., Khaibrakhmanov, S., Shuvalov, V., Rybnov, Y., Dudorov, A., Grokhovsky, V. I., Badyukov, D. D., Yin, Q.-Z., Gural, P. S., Albers, J., Granvik, M., Evers, L. G., Kuiper, J., Kharlamov, V., Solovyov, A., Rusakov, Y. S., Korotkiy, S., Serdyuk, I., Korochantsev, A. V., Larionov, M. Y., Glazachev, D., Mayer, A. E., Gisler, G., Gladkovsky, S. V., Wimpenny, J., Sanborn, M. E., Yamakawa, A., Verosub, K. L., Rowland, D. J., Roeske, S., Botto, N. W., Friedrich, J. M., Zolensky, M. E., Le, L., Ross, D., Ziegler, K., Nakamura, T., Ahn, I., Lee, J. I., Zhou, Q., Li, X.-H., Li, Q.-L., Liu, Y., Tang, G.-Q., Hiroi, T., Sears, D., Weinstein, I. A., Vokhmintsev, A. S., Ishchenko, A. V., Schmitt-Kopplin, P., Hertkorn, N., Nagao, K., Haba, M. K., Komatsu, M., Mikouchi, T., and Consortium), t. C. A. (2013). Chelyabinsk Airburst, Damage Assessment, Meteorite Recovery, and Characterization. *Science*, 342(6162):1069–1073.

Potter, R. W. K. and Collins, G. S. (2013). Numerical modeling of asteroid survivability and possible scenarios for the Morokweng crater-forming impact. *Meteoritics & Planetary Science*, 48(5):744–757.

Potter, R. W. K., Collins, G. S., Kiefer, W. S., McGovern, P. J., and Kring, D. A. (2012). Constraining the size of the South Pole-Aitken basin impact. *Icarus*, 220(2):730–743.

Pravec, P. and Harris, A. W. (2000). Fast and Slow Rotation of Asteroids. *Icarus*, 148(1):12–20.

Prentice, A. J. R. (1984). Formation of the Saturnian System - a Model Laplacian Theory. *Earth, Moon, and Planets*, 30(3):209–228.

Prieur, N. C., Rolf, T., Luther, R., Wünnemann, K., Xiao, Z., and Werner, S. C. (2017). The effect of target properties on transient crater scaling for simple craters. *Journal of Geophysical Research: Planets*, 122(8):2017JE005283.

Prieur, N. C., Rolf, T., Wünnemann, K., and Werner, S. C. (2018). Formation of Simple Impact Craters in Layered Targets: Implications for Lunar Crater Morphology and Regolith Thickness. *Journal of Geophysical Research: Planets*, 123(6):1555–1578.

Quaide, W. L. and Oberbeck, V. R. (1968). Thickness determinations of the lunar surface layer from lunar impact craters. *Journal of Geophysical Research*, 73(16):5247–5270.

Raducan, S. D., Davison, T. M., and Collins, G. S. (2020). The effects of asteroid layering on ejecta mass-velocity distribution and implications for impact momentum transfer. *Planetary and Space Science*, 180:104756.

Raducan, S. D., Davison, T. M., Luther, R., and Collins, G. S. (2019). The role of asteroid strength, porosity and internal friction in impact momentum transfer. *Icarus*, 329:282–295.

Reddy, V., Le Corre, L., O'Brien, D. P., Nathues, A., Cloutis, E. A., Durda, D. D., Bottke, W. F., Bhatt, M. U., Nesvorny, D., Buczkowski, D., Scully, J. E. C., Palmer, E. M., Sierks, H., Mann, P. J., Becker, K. J., Beck, A. W., Mittlefehldt, D., Li, J.-Y., Gaskell, R., Russell, C. T., Gaffey, M. J., McSween, H. Y., McCord, T. B., Combe, J.-P., and Blewett, D. (2012). Delivery of dark material to Vesta via carbonaceous chondritic impacts. *Icarus*, 221(2):544–559.

Richardson, D. C., Leinhardt, Z. M., Melosh, H. J., Bottke, Jr., W. F., and Asphaug, E. (2002). Gravitational Aggregates: Evidence and Evolution. In *Asteroids III*, pages 501–515.

Richardson, D. C., Michel, P., Walsh, K. J., and Flynn, K. W. (2009). Numerical simulations of asteroids modelled as gravitational aggregates with cohesion. *Planetary and Space Science*, 57(2):183–192.

Richardson, J. E., Melosh, H. J., Lisse, C. M., and Carcich, B. (2007). A ballistics analysis of the Deep Impact ejecta plume: Determining Comet Tempel 1's gravity, mass, and density. *Icarus*, 190(2):357–390.

Rivkin, A. S., Howell, E. S., Lebofsky, L. A., Clark, B. E., and Britt, D. T. (2000). The Nature of M-Class Asteroids from 3-m Observations. *Icarus*, 145(2):351–368.

Safronov, V. S. (1972). Evolution of the protoplanetary cloud and formation of the earth and planets. *Evolution of the protoplanetary cloud and formation of the earth and planets., by Safronov, V. S.. Translated from Russian. Jerusalem (Israel): Israel Program for Scientific Translations, Keter Publishing House*, page 212.

Sanchez, J. A., Reddy, V., Shepard, M. K., Thomas, C., Cloutis, E. A., Takir, D., Albert Conrad, Kiddell, C., and Applin, D. (2017). Detection of Rotational Spectral Variation on the M-type Asteroid (16) Psyche. *AJ*, 153(1):29.

Sánchez, P. and Scheeres, D. J. (2014). The strength of regolith and rubble pile asteroids. *Meteoritics & Planetary Science*, 49(5):788–811.

Scheeres, D. J., Hartzell, C. M., Sanchez, P., and Swift, M. (2010). Scaling forces to asteroid surfaces: The role of cohesion. *Icarus*, 210(2):968–984.

Scheeres, D. J. and Sánchez, P. (2018). Implications of cohesive strength in asteroid interiors and surfaces and its measurement. *Progress in Earth and Planetary Science*, 5(1):25.

Scheirich, P. and Pravec, P. (2009). Modeling of lightcurves of binary asteroids. *Icarus*, 200(2):531–547.

Schenk, P. M., O'brien, D. P., Marchi, S., Gaskell, R. W., Preusker, F., Roatsch, T., Jaumann, R., Buczkowski, D. L., McCord, T. R., McSween, H. Y., Williams, D. N., Yingst, A. R., Raymond, C., and Russell, C. (2012). The geologically recent giant impact basins at Vesta's south pole. *Science*, 336(6082):694–697.

Schmidt, R. M. (1980). Meteor Crater: Energy of formation - Implications of centrifuge scaling. volume 11, pages 2099–2128.

Schmidt, R. M. and Holsapple, K. A. (1982). Estimates of crater size for large-body impact: Gravity-scaling results. *Geological Society of America Special Papers*, 190:93–102.

Schulte, P., Alegret, L., Arenillas, I., Arz, J. A., Barton, P. J., Bown, P. R., Bralower, T. J., Christeson, G. L., Claeys, P., Cockell, C. S., Collins, G. S., Deutsch, A., Goldin, T. J., Goto, K., Grajales-Nishimura, J. M., Grieve, R. A. F., Gulick, S. P. S., Johnson, K. R., Kiessling, W., Koeberl, C., Kring, D. A., MacLeod, K. G., Matsui, T., Melosh, J., Montanari, A., Morgan, J. V., Neal, C. R., Nichols, D. J., Norris, R. D., Pierazzo, E., Ravizza, G., Rebolledo-Vieyra, M., Reimold, W. U., Robin, E., Salge, T., Speijer, R. P., Sweet, A. R., Urrutia-Fucugauchi, J., Vajda, V., Whalen, M. T., and Willumsen, P. S. (2010). The Chicxulub Asteroid Impact and Mass Extinction at the Cretaceous-Paleogene Boundary. *Science*, 327(5970):1214–1218.

Schultz, P. H. (1988). Cratering on Mercury - A relook. In *Mercury, University of Arizona Press*, pages 274–335.

Schultz, P. H. (1992). Atmospheric effects on cratering efficiency. *Journal of Geophysical Research: Planets*, 97(E1):975–1005.

Schultz, P. H. (1999). Ejecta Distribution from Oblique Impacts into Particulate Targets. volume 30.

Schultz, P. H. and Mendenhall, M. H. (1979). On the Formation of Basin Secondary Craters by Ejecta Complexes. In *Lunar and Planetary Science Conference X*, volume 10, pages 1078–1080.

Schultz, R. A. and Frey, H. V. (1990). A new survey of multiring impact basins on Mars. *Journal of Geophysical Research: Solid Earth*, 95(B9):14175–14189.

Schunová-Lilly, E., Jedicke, R., Vereš, P., Denneau, L., and Wainscoat, R. J. (2017). The size-frequency distribution of H > 13 NEOs and ARM target candidates detected by Pan-STARRS1. *Icarus*, 284:114–125.

Senft, L. E. and Stewart, S. T. (2007). Modeling impact cratering in layered surfaces. *Journal of Geophysical Research: Planets*, 112(E11):E11002.

Shafer, P. B., Garcia, D. M., Scammon, J. R., Snell, C., Stellingwerf, F. R., Remo, J., Managan, R., and Rosenkilde, E. C. (1994). The Coupling of Energy to Asteroids and Comets. -1:955.

Sharp, T. G. and de Carli, P. S. (2006). Shock Effects in Meteorites. *Meteorites and the Early Solar System II*, pages 653–677.

Shepard, M. K., Richardson, J., Taylor, P. A., Rodriguez-Ford, L. A., Conrad, A., de Pater, I., Adamkovics, M., de Kleer, K., Males, J. R., Morzinski, K. M., Close, L. M., Kaasalainen, M., Viikinkoski, M., Timerson, B., Reddy, V., Magri, C., Nolan, M. C., Howell, E. S., Benner, L. A. M., Giorgini, J. D., Warner, B. D., and Harris, A. W. (2017). Radar observations and shape model of asteroid 16 Psyche. *Icarus*, 281:388–403.

Shoemaker, E. M. (1962). Interpretation of lunar craters. *Physics and astronomy of the Moon*, pages 283–359.

Shoemaker, E. M., Batson, R. M., Holt, H. E., Morris, E. C., Rennilson, J. J., and Whitaker, E. A. (1969). Observations of the lunar regolith and the Earth from the television camera on Surveyor 7. *Journal of Geophysical Research*, 74(25):6081–6119.

Shoemaker, E. M., Gault, D. E., Moore, H. J., and Lugn, R. V. (1963). Hypervelocity impact of steel into coconino sandstone. *American Journal of Science*, 261(7):668–682.

Stephens, D. R. and Lilley, E. M. (1970). Compressibilities of Lunar Crystalline Rock, Microbreccia, and Fines to 40 Kilobars. *Science*, 167(3918):731–732.

Stickle, A. M., Atchison, J. A., Barnouin, O. S., Cheng, A. F., Crawford, D. A., Ernst, C. M., Fletcher, Z., and Rivkin, A. S. (2015). Modeling Momentum Transfer from Kinetic Impacts: Implications for Redirecting Asteroids. *Procedia Engineering*, 103:577–584.

Su, S.-Y. (1990). The velocity distribution of collisional fragments and its effect on future space debris environment. *Advances in Space Research*, 10(3-4):389–392.

Sullivan, J. R., Thomas, C. P., Murchie, L. S., and Robinson, S. M. (2002). Asteroid Geology from Galileo and NEAR Shoemaker Data. *Asteroids III*.

Syal, M. B., Owen, J. M., and Miller, P. L. (2016). Deflection by kinetic impact: Sensitivity to asteroid properties. *Icarus*, 269:50–61.

Takir, D., Reddy, V., Sanchez, J. A., Shepard, M. K., and Emery, J. P. (2016). Detection of water and/or hydroxyl on asteroid (16) psyche. *The Astronomical Journal*, 153(1):31.

Tancredi, G., Roland, S., and Bruzzone, S. (2015). Distribution of boulders and the gravity potential on asteroid Itokawa. *Icarus*, 247:279–290.

Tholen, D. J. (1984). Asteroid taxonomy from cluster analysis of photometry. *Ph.D. Thesis*.

Tholen, D. J. (1989). Asteroid taxonomic classifications. Tucson, AZ, United States.

Thomas, P. C., Prockter, L., Robinson, M., Joseph, J., and Veverka, J. (2002). Global structure of asteroid 433 Eros. *Geophysical Research Letters*, 29(10):46–1–46–4.

Thompson, S. L. and Lauson, H. S. (1972). Improvements in the CHART D radiation-hydrodynamic code II: A revised program. Technical Report SC-RR-71-0713, Sandia Labs.

Thompson, S. L. and Lauson, H. S. (1974). Improvements in the CHART D radiation-hydrodynamic code III: revised analytic equations of state. Technical Report SC-RR–71-0714, Sandia Labs.

Tillotson, H. J. (1962). Metallic Equations of State for Hypervelocity Impact. *General Atomic Report*, GA-3216:141.

Tonry, J. L. (2011). An Early Warning System for Asteroid Impact. *Publications of the Astronomical Society of the Pacific*, 123(899):58–73.

Tsujido, S., Arakawa, M., Suzuki, A. I., and Yasui, M. (2015). Ejecta velocity distribution of impact craters formed on quartz sand: Effect of projectile density on crater scaling law. *Icarus*, 262:79–92.

Tyburczy, J. A., Xu, X., Ahrens, T. J., and Epstein, S. (2001). Shock-induced devolatilization and isotopic fractionation of H and C from Murchison meteorite: some implications for planetary accretion. *Earth and Planetary Science Letters*, 192(1):23–30.

Ulmer, P. and Trommsdorff, V. (1995). Serpentine Stability to Mantle Depths and Subduction-Related Magmatism. *Science*, 268(5212):858–861.

Vereš, P., Jedicke, R., Wainscoat, R., Granvik, M., Chesley, S., Abe, S., Denneau, L., and Grav, T. (2009). Detection of Earth-impacting asteroids with the next generation all-sky surveys. *Icarus*, 203(2):472–485.

Vernazza, P., Marsset, M., Groussin, O., Lamy, P., Jorda, L., Mousis, O., Delsanti, A., Castillo-Rogez, J., Beck, P., Emery, J., Brunetto, R., Djouadi, Z., Dionnet, Z., Delbo, M., Carry, B., Marchis, F., Zanda, B., and Borondics, F. (2017). Different origins or different evolutions? decoding the spectral diversity among c-type asteroids. *Astronomical Journal (Online)*, 153(2).

Veverka, J., Farquhar, B., Robinson, M., Thomas, P., Murchie, S., Harch, A., Antreasian, P. G., Chesley, S. R., Miller, J. K., Jr, W. M. O., Williams, B. G., Yeomans, D., Dunham, D., Heyler, G., Holdridge, M., Nelson, R. L., Whittenburg, K. E., Ray, J. C., Carcich, B., Cheng, A., Chapman, C., Iii, J. F. B., Bell, M., Bussey, B., Clark, B., Domingue, D., Gaffey, M. J., Hawkins, E., Izenberg, N., Joseph, J., Kirk, R., Lucey, P., Malin, M., McFadden, L., Merline, W. J., Peterson, C., Prockter, L., Warren, J., and Wellnitz, D. (2001). The landing of the NEAR-Shoemaker spacecraft on asteroid 433 Eros. *Nature*, 413(6854):390–393.

Viikinkoski, M., Vernazza, P., Hanus, J., Coroller, H. L., Tazhenova, K., Carry, B., Marsset, M., Drouard, A., Marchis, F., Fetick, R., Fusco, T., Durech, J., Birlan, M., Berthier, J., Bartczak, P., Dumas, C., Castillo-Rogez, J., Cipriani, F., Colas, F., Ferrais, M., Grice, J., Jehin, E., Jorda, L., Kaasalainen, M., Kryszczynska, A., Lamy, P., Marciniak, A., Michalowski, T., Michel, P., Pajuelo, M., Podlewska-Gaca, E., Santana-Ros, T., Tanga, P., Vachier, F., Vigan, A., Warner, B., Witasse, O., and Yang, B. (2018). (16) Psyche: A mesosiderite-like asteroid? *Astronomy & Astrophysics*, 619:L3.

Vincent, J.-B., Besse, S., Marchi, S., Sierks, H., Massironi, M., Osiris Team (A'Hearn, M., Barbieri, C., Barucci, A., Bertaux, J.-L., Cremonese, G., Da Deppo, V., Davidsson, B., Debei, S., De Cecco, M., Fornasier, S., Fulle, M., Groussin, O., Gutierrez, P., Hviid, S., Ip, W.-H., Jorda, L., Keller, H., Koschny, D., Knollenberg, J., Kramm, J., Kuehrt, E., Lamy, P., Lara, L., Lazzarin, M., Lopez-Moreno, J., Marzari, F., Michalik, H., Naletto, G., Rickman, H., Rodrigo, R., Sabau, L., Thomas, N., Wenzel., K.-P., and Angrilli, F. (2012). Physical properties of craters on asteroid (21) Lutetia. *Planetary and Space Science*, 66:79–86.

Vincent, J. B., Schenk, P., Nathues, A., Sierks, H., Hoffmann, M., Gaskell, R. W., Marchi, S., O'Brien, D. P., Sykes, M., Russell, C. T., Fulchignoni, M., Kellerg, H. U., Raymond, C., Palmer, E., and Preusker, F. (2014). Crater depth-to-diameter distribution and surface properties of (4) vesta. *Planetary and Space Science*, 103:57–65.

Walsh, K. J., Jawin, E. R., Ballouz, R.-L., Barnouin, O. S., Bierhaus, E. B., Connolly, H. C., Molaro, J. L., McCoy, T. J., Delbo', M., Hartzell, C. M., Pajola, M., Schwartz, S. R., Trang, D., Asphaug, E., Becker, K. J., Beddingfield, C. B., Bennett, C. A., Bottke, W. F., Burke, K. N., Clark, B. C., Daly, M. G., DellaGiustina, D. N., Dworkin, J. P., Elder, C. M., Golish, D. R., Hildebrand, A. R., Malhotra, R., Marshall, J., Michel, P., Nolan, M. C., Perry, M. E., Rizk, B., Ryan, A., Sandford, S. A., Scheeres, D. J., Susorney, H. C. M., Thuillet, F., and Lauretta, D. S. (2019). Craters, boulders and regolith of (101955) Bennu indicative of an old and dynamic surface. *Nature Geoscience*, 12(4):242.

Walsh, K. J., Morbidelli, A., Raymond, S. N., O'Brien, D. P., and Mandell, A. M. (2011). A low mass for Mars from Jupiter's early gas-driven migration. *Nature*, 475(7355):206–209.

Walsh, K. J., Richardson, D. C., and Michel, P. (2008). Rotational breakup as the origin of small binary asteroids. *Nature*, 454:188.

Walsh, K. J., Richardson, D. C., and Michel, P. (2012). Spin-up of rubble-pile asteroids: Disruption, satellite formation, and equilibrium shapes. *Icarus*, 220(2):514–529.

Watanabe, S., Hirabayashi, M., Hirata, N., Hirata, N., Noguchi, R., Shimaki, Y., Ikeda, H., Tatsumi, E., Yoshikawa, M., Kikuchi, S., Yabuta, H., Nakamura, T., Tachibana, S., Ishihara, Y., Morota, T., Kitazato, K., Sakatani, N., Matsumoto, K., Wada, K., Senshu, H., Honda, C., Michikami, T., Takeuchi, H., Kouyama, T., Honda, R., Kameda, S., Fuse, T., Miyamoto, H., Komatsu, G., Sugita, S., Okada, T., Namiki, N., Arakawa, M., Ishiguro, M., Abe, M., Gaskell, R., Palmer, E., Barnouin, O. S., Michel, P., French, A. S., McMahon, J. W., Scheeres, D. J., Abell, P. A., Yamamoto, Y., Tanaka, S., Shirai, K., Matsuoka, M., Yamada, M., Yokota, Y., Suzuki, H., Yoshioka, K., Cho, Y., Tanaka, S., Nishikawa, N., Sugiyama, T., Kikuchi, H., Hemmi, R., Yamaguchi, T., Ogawa, N., Ono, G., Mimasu, Y., Yoshikawa, K., Takahashi, T., Takei, Y., Fujii, A., Hirose, C., Iwata, T., Hayakawa, M., Hosoda, S., Mori, O., Sawada, H., Shimada, T., Soldini, S., Yano, H., Tsukizaki, R., Ozaki, M., Iijima, Y., Ogawa, K., Fujimoto, M., Ho, T.-M., Moussi, A., Jaumann, R., Bibring, J.-P., Krause, C., Terui, F., Saiki, T., Nakazawa, S., and Tsuda, Y. (2019). Hayabusa2 arrives at the carbonaceous asteroid 162173 Ryugu—A spinning top–shaped rubble pile. *Science*, 364(6437):268–272.

Weidenschilling, S. J. and Cuzzi, J. N. (2006). Accretion Dynamics and Timescales: Relation to Chondrites. *Meteorites and the Early Solar System II*, 943:473–485.

Weidenschilling, S. J., Marzari, F., and Hood, L. L. (1998). The Origin of Chondrules at Jovian Resonances. *Science*, 279(5351):681–684.

Wilcox, B. B., Robinson, M. S., Thomas, P. C., and Hawke, B. R. (2005). Constraints on the depth and variability of the lunar regolith. *Meteoritics & Planetary Science*, 40(5):695–710.

Wilhelms, D. E. and Squyres, S. W. (1984). The martian hemispheric dichotomy may be due to a giant impact. *Nature*, 309(5964):138–140.

Woolfson, M. M. (2019). Planet formation and the evolution of the Solar System. *Physica Scripta*, 94(11):113001.

Woolfson, M. M. and Lipson, H. S. (1964). A capture theory of the origin of the Solar System. *Proceedings of the Royal Society of London. Series A. Mathematical and Physical Sciences*, 282(1391):485–507.

Wünnemann, K., Collins, G. S., and Melosh, H. J. (2006). A strain-based porosity model for use in hydrocode simulations of impacts and implications for transient crater growth in porous targets. *Icarus*, 180(2):514–527.

Wünnemann, K. and Ivanov, B. A. (2003). Numerical modelling of the impact crater depth-diameter dependence in an acoustically fluidized target. *Planetary and Space Science*, 51:831–845.

Wünnemann, K., Morgan, J., and Jödicke, H. (2005). Is Ries crater typical for its size? An analysis based upon old and new geophysical data and numerical modeling. In *Large Meteorite Impacts III*. Geological Society of America.

Wünnemann, K., Zhu, M.-H., and Stöffler, D. (2016). Impacts into quartz sand: Crater formation, shock metamorphism, and ejecta distribution in laboratory experiments and numerical models. *Meteoritics & Planetary Science*, 51(10):1762–1794.

Wünnemann, K. and Lange, M. A. (2002). Numerical modeling of impact-induced modifications of the deep-sea floor. *Deep Sea Research Part II: Topical Studies in Oceanography*, 49(6):969–981.

Yamamoto, S., Hasegawa, S., Suzuki, A. I., and Matsunaga, T. (2017). Impact velocity dependence of transient cratering growth. *Journal of Geophysical Research: Planets*, 122(5):1077–1089.

Yamamoto, S., Okabe, N., Kadono, T., Sugita, S., and Matsui, T. (2005). Measurements of Ejecta Velocity Distribution by a High-Speed Video Camera. volume 36.

Yang, W. and Ahrens, T. J. (1995). Impact Jetting of Geological Materials. *Icarus*, 116(2):269–274.

Yano, H., Kubota, T., Miyamoto, H., Okada, T., Scheeres, D., Takagi, Y., Yoshida, K., Abe, M., Abe, S., Barnouin-Jha, O., Fujiwara, A., Hasegawa, S., Hashimoto, T., Ishiguro, M., Kato, M., Kawaguchi, J., Mukai, T., Saito, J., Sasaki, S., and Yoshikawa, M. (2006). Touchdown of the Hayabusa Spacecraft at the Muses Sea on Itokawa. *Science*, 312(5778):1350–1353.

Yeomans, D. K., Barriot, J.-P., Dunham, D. W., Farquhar, R. W., Giorgini, J. D., Helfrich, C. E., Konopliv, A. S., McAdams, J. V., Miller, J. K., Owen, Jr., W. M., Scheeres, D. J., Synnott, S. P., and Williams, B. G. (1997). Estimating the Mass of Asteroid 253 Mathilde from Tracking Data During the NEAR Flyby. *Science*, 278:2106.

Zel'dovich, Y. B. and Raizer, Y. P. (2002). *Physics of Shock Waves and High-Temperature Hydrodynamic Phenomena*. Courier Corporation.

Zellner, B., Tholen, D. J., and Tedesco, E. F. (1985). The eight-color asteroid survey: Results for 589 minor planets. *Icarus*, 61(3):355–416.